



JAEA-Review

2007-018



JP0750238

JAEA-Review

**研究炉(JRR-3 及び JRR-4)利用における研究成果集
(平成17年度)**

Activity Report on the Utilization of Research Reactors (JRR-3 and JRR-4)
(Japanese Fiscal Year, 2005)

(編) 研究炉利用課

(Ed.) Research Reactor Utilization Section

東海研究開発センター
原子力科学研究所
研究炉加速器管理部

Department of Research Reactor and Tandem Accelerator
Nuclear Science Research Institute
Tokai Research and Development Center

March 2007

Japan Atomic Energy Agency

日本原子力研究開発機構

本レポートは日本原子力研究開発機構が不定期に発行する成果報告書です。
本レポートの入手並びに著作権利用に関するお問い合わせは、下記あてにお問い合わせ下さい。
なお、本レポートの全文は日本原子力研究開発機構ホームページ (<http://www.jaea.go.jp/index.shtml>)
より発信されています。このほか財団法人原子力弘済会資料センター*では実費による複写頒布を行っ
ております。

〒319-1195 茨城県那珂郡東海村白方白根2番地4
日本原子力研究開発機構 研究技術情報部 研究技術情報課
電話 029-282-6387, Fax 029-282-5920

*〒319-1195 茨城県那珂郡東海村白方白根2番地4 日本原子力研究開発機構内

**This report is issued irregularly by Japan Atomic Energy Agency
Inquiries about availability and/or copyright of this report should be addressed to
Intellectual Resources Section, Intellectual Resources Department,
Japan Atomic Energy Agency
2-4 Shirakata Shirane, Tokai-mura, Naka-gun, Ibaraki-ken 319-1195 Japan
Tel +81-29-282-6387, Fax +81-29-282-5920**

© Japan Atomic Energy Agency, 2007

研究炉（JRR-3 及び JRR-4）利用における研究成果集（平成 17 年度）

日本原子力研究開発機構 東海研究開発センター 原子力科学研究所
研究炉加速器管理部
（編）研究炉利用課

（2007 年 2 月 14 日受理）

平成 17 年度、研究炉 JRR-3 は 7 サイクルの運転（1 サイクル：26 日連続運転）、JRR-4 については、37 サイクル（デイリー運転：137 日）の施設共用運転を行なった。

JRR-3 は、中性子散乱、即発ガンマ線分析、中性子ラジオグラフィなどの実験利用及び、放射化分析、原子炉燃料材料、ラジオアイソトープ製造、フィッシュントラック年代測定照射利用等、様々な目的に利用されている。

JRR-4 については、医療照射（Boron Neutron Capture Therapy：BNCT）、即発ガンマ線分析、放射線測定器の感度試験、原子炉研修運転実習等の実験利用、及び放射化分析、ラジオアイソトープ製造、フィッシュントラック年代測定のための照射利用等、様々な目的に利用されている。

本報告書は、研究炉の利用者（原子力機構外を含む）から成果の提出を受け、中性子散乱 9 分野（構造、磁性、超伝導など）、中性子ラジオグラフィ、即発ガンマ線分析、放射化分析、ラジオアイソトープ製造、原子炉燃料材料、その他、の分野別に研究成果を取りまとめたものである。

Activity Report on the Utilization of Research Reactors (JRR-3 and JRR-4)
(Japanese Fiscal Year, 2005)

(Ed.) Research Reactor Utilization Section

Department of Research Reactor and Tandem Accelerator
Nuclear Science Research Institute
Tokai Research and Development Center
Japan Atomic Energy Agency
Tokai-mura, Naka-gun, Ibaraki-ken

(Received February 14, 2007)

In the fiscal year 2005, The research reactor JRR-3 was operated 7 cycles (cycle operation : 26days/cycle) for utilization sharing of the facility. And JRR-4 was operated 37 cycles (daily operation : 137 days).

JRR-3 is used for the purposes below;

- Experimental studies such as neutron scattering, prompt gamma-ray analyses, neutron radiography
- Irradiation for activation analyses, radioisotope (RI) productions, fission tracks
- Irradiation test of reactor materials
- etc.

JRR-4 is used for the purposes below;

- Medical irradiation (Boron Neutron Capture Therapy : BNCT)
- Prompt gamma-ray analyses
- Sensitivity measurement of radiation detectors
- Experiment in the nuclear reactor training
- Practice of Reactor operation
- Irradiation for activation analyses, RI productions, fission tracks
- etc.

The volume contains 100 activity reports, which are categorized into the fields of neutron scattering (9 subcategories), neutron radiography, neutron activation analyses, RI productions, prompt gamma-ray analyses, and others submitted by the users in JAEA and from other organizations.

Keywords: JRR-3, JRR-4, Research Reactor, Neutron Scattering, Neutron Radiography, Neutron Activation Analysis, Neutron Beam, Irradiation

目 次

はじめに	1
研究成果一覧	3
1. 中性子散乱	13
1) 構造・励磁	13
2) 磁 性	31
3) 超伝導現象	57
4) 高分子	63
5) 生物学	73
6) 基礎物理学・中性子光学	85
7) 装 置	91
8) 残留応力	107
9) その他	119
2. 中性子ラジオグラフィ	125
3. 即発ガンマ線分析	137
4. 放射化分析	145
5. ラジオアイソトープ製造	155
6. 原子炉燃料材料	159
7. その他	163
おわりに	169
謝 辞	170
付 録	171

Contents

Preface	1
Research Reports	3
1. Neutron Scattering	13
1) Structure·Excitation	13
2) Magnetism	31
3) Superconductivity	57
4) Polymer	63
5) Biology	73
6) Fundamental Physics·Neutron Optics	85
7) Instrument	91
8) Residual Stress	107
9) Others	119
2. Neutron Radiography	125
3. Prompt Gamma-ray Analyses	137
4. Neutron Activation Analyses	145
5. Production of Radio Isotopes	155
6. Irradiation Test of Reactor Materials	159
7. Others	163
Conclusion	169
Acknowledgments	170
Appendixes	171

はじめに

平成17年度には、JRR-3において7サイクルの施設共用運転、JRR-4において37サイクルの施設共用運転が行なわれ、これに伴いさまざまな利用が行われた。

本報告書は研究炉（JRR-3及びJRR-4）を利用した研究開発等の成果を公開することを目的とし、利用者（原子力機構内、千葉県環境研究センター、大阪府立大学など）から当該利用の研究成果の提出を受け、分野別に取りまとめたものである。

提出して頂いた成果の件数は、中性子散乱77件、中性子ラジオグラフィ8件、即発ガンマ線分析5件、放射化分析6件、RIの製造1件、原子炉燃料材料1件、その他2件で合計100件であった。

本報告書が、研究炉利用の現状報告にとどまらず、新たな研究分野の開発検討にも役立つ事を期待します。

研究炉利用課長
楠 剛

This is a blank page.

研究成果一覽



Research Reports

This is a blank page.

No.	「 Title 」	Page
<i>Neutron Scattering - Structure - Excitation -</i>		
1-1-1	Hexagonal-to-squared Vortex Lattice Transition in the Mixed State of Nb₃Sn R.Kadono, K. H. Satoh, A. Koda, T. Nagata, H. Kawano-Furukawa, J. Suzuki, M.Matsuda K. Ohishi, W. Higemoto, S. Kuroiwa, H. Takagiwa, J. Akimitsu	15
1-1-2	The Change in Nano-scaled Microstructure Measurement during Plastic Deformation by SANS-J for High Nitrogen Steel K. Ikeda, Y. Tomota, J. Suzuki	16
1-1-3	Neutron Scattering Study of LiNiO₂ K. Basar, Xianglian, H. Honda, T. Sakuma, H. Takahashi, O. Abe, N. Igawa, Y. Ishii	17
1-1-4	Difference of Dynamic Structure Factor between Methane Hydrate and Ice Ih T. Kamiyama, N. Seki, Y. Kiyonagi, T. Uchida, T. Ebinuma, H. Narita, N. Igawa, H. Yamauchi Y. Ishii	18
1-1-5	Structural Transition of K_{0.5}CoO₂ Y. Mori, M. Soda, M. Sato, N. Igawa, K. Kakurai	19
1-1-6	Structural Studies of Pyrochlore-related Spin-1/2 System Ag₂Cu₂O₃ D. Uematsu, M. Soda, M. Sato, N. Igawa, K. Kakurai	20
1-1-7	Neutron Diffraction Study on Hydrogen-bonding Networks in Disodium Uridine 5'-monophosphate Heptahydrate S. Yamamura, Y. Sugawara, T. Ohhara, I. Tanaka, N. Niimura	21
1-1-8	Diffuse Scattering and Lattice Dynamics in Relaxor KLT S. Wakimoto, G.A. Samaru, R. K. Grubbs, E. L. Venturini, L. A. Boatner, G. Xu, G. Shirane S.-H. Lee	22
1-1-9	Crystal Structure of Ba₃Ca_{1.18}Nb_{1.82}O_{8.73} T. Shimoyama, J. Sagiya, T. Tojo, H. Kawaji, T. Atake, N. Igawa, Y. Ishii	23
1-1-10	Crystal Structure of Carbon Dioxide Hydrate N. Igawa, T. Taguchi, Y. Ishii	24
1-1-11	Location of Deuterium Atoms in BaSn_{0.5}In_{0.5}O_{2.75} by Neutron Powder Diffraction at 10K T. Ito, T. Nagasaki, K. Iwasaki, M. Yoshino, N. Igawa, Y. Ishii	25
1-1-12	Growth Process of Methane Hydrate from Powder Ice A. Hoshikawa, H. Fukazawa, N. Igawa, H. Yamauchi, Y. Ishii	26
1-1-13	Magnetic Field-induced Martensitic Transformation of Heusler-type Off-stoichiometric Ni₂MnGa Single Crystal K. Inoue, Y. Yamaguchi, Y. Ishii, H. Yamauchi, T. Shishido	27
1-1-14	The Growth and Structure of Ferroelectric Ice XI H. Fukazawa, A. Hoshikawa, N. Igawa, H. Yamauchi, Y. Ishii	28
1-1-15	Intrinsic Dielectric Loss of LaAlO₃ at Microwave Frequency T. Shimada, H. Yamauchi, Y. Ishii, J. Breeze, N. McN Alford	29

No.	「 Title 」	Page
<i>Neutron Scattering - Magnetism -</i>		
1-2-1	Polarized Neutron Inelastic Scattering Study of Anisotropic Magnetic Fluctuations in Quasi-1D Ising-like Antiferromagnet TlCoCl_3 A. Oosawa, K. Kakurai, Y. Nishiwaki, T. Kato	33
1-2-2	Spherical Neutron Polarimetry Study of Magnetic Structure in Distorted-triangular-lattice Ising-like Antiferromagnet TlCoCl_3 A. Oosawa, K. Kakurai, M. Takeda, Y. Shimojo, Y. Nishiwaki, T. Kato	34
1-2-3	Magnetic-field Induced Commensurate Spin State in Multiferroic Compound of HoMn_2O_5 H. Kimura, Y. Kamada, Y. Noda, K. Kaneko, N. Metoki, K. Kohn	35
1-2-4	Magnetic Structure of the Kagome Staircase Compound $\text{Co}_3\text{V}_2\text{O}_8$ Y. Yasui, Y. Kobayashi, M. Sato, N. Igawa, K. Kakurai	36
1-2-5	Magnetic Behavior of Frustrated $S=1/2$ System of the Pyrochlore Lattice $\text{Hg}_2\text{Cu}_2\text{F}_6\text{S}$ S. Kawabata, Y. Yasui, Y. Kobayashi, M. Sato, N. Igawa, K. Kakurai	37
1-2-6	Search for Magnetic Fluctuations in $\text{Na}_x\text{CoO}_2 \cdot y\text{H}_2\text{O}$ by Neutron Scattering T. Moyoshi, M. Soda, Y. Yasui, M. Sato, K. Kakurai	38
1-2-7	Magnetic Structure of YBaCo_4O_7 with Kagome and Triangular Lattice M. Soda, Y. Yasui, M. Moyoshi, M. Sato, N. Igawa, K. Kakurai	39
1-2-8	Determination of Magnetic Structure under High Pressure in KCuCl_3 K. Goto, M. Fujisawa, A. Oosawa, T. Osakabe, K. Kakurai, H. Tanaka	40
1-2-9	Magnetic Excitations in $\text{Cu}_2\text{Fe}_2\text{Ge}_4\text{O}_{13}$ T. Masuda, K. Kakurai, M. Matsuda	41
1-2-10	Magnetic Structure of Shastry-Sutherland Type Frustration System ErB_4 under Magnetic Fields K. Ohoyama, F. Iga, N. Katoh, S. Katano, S. Michimura	42
1-2-11	Magnetic Excitations in $\text{Cu}_2\text{Fe}_2\text{Ge}_4\text{O}_{13}$ II T. Masuda, K. Kakurai, M. Matsuda, K. Kaneko, N. Metoki	43
1-2-12	Successive Magnetic Phase Transitions in $\alpha\text{-Tb}_2\text{S}_3$ Studied by Neutron Diffraction Technique M. Matsuda, K. Kakurai, S. Ebinu, S. Nagata	44
1-2-13	Magnetic Excitations from the Singlet Dimerized State in $\text{Na}_2\text{Co}_2(\text{C}_2\text{O}_4)_3(\text{H}_2\text{O})_2$ M. Matsuda, Z. Honda, S. Wakimoto, K. Kakurai, K. Yamada	45
1-2-14	Magnetic Structure in the Half-magnetization Plateau State in a Heisenberg Pyrochlore Antiferromagnet HgCr_2O_4 M. Matsuda, H. Ueda, Y. Ueda, S.-H. Lee	46
1-2-15	Small-angle Neutron Scattering Study of Magnetic Structure of Transition Metal Nanoparticles T. Shinohara, Y. Oba, T. Sato, T. Oku, J. Suzuki	47
1-2-16	Low Energy Magnetic Excitation in TbMnO_3 R. Kajimoto, Y. Mitsui, H. Yoshizawa, H. Shintani, T. Kimura, Y. Tokura	48
1-2-17	Magnetic Structure of $\text{CuCr}_{1-x}\text{Mg}_x\text{O}_2$ R. Kajimoto, M. Matsuda, T. Okuda	49
1-2-18	Magnetization Process of Co-Pd-Si-O Nanogranular Soft Magnetic Film Studied by Polarized Small-angle Neutron Scattering M. Ohnuma, J. Suzuki, S. Ohnuma	50
1-2-19	High-pressure Neutron Diffraction Study on the Filled Skutterudite $\text{PrFe}_4\text{P}_{12}$ T. Osakabe, D. Kawana, K. Kuwahara	52
1-2-20	Effect of Substitution of Sr for Ba in Co_2Z-type Hexaferrite on Magnetic Moment Orientation and Its Temperature Dependence Y. Takada, T. Nakagawa, M. Tokunaga, T. Tanaka, T. A. Yamamoto, T. Tachibana, S. Kawano, Y. Ishii, N. Igawa	53
1-2-21	Long Period, Incommensurate Longitudinal SDW State in UCu_2Si_2 F. Honda, N. Metoki, T. D. Matsuda, Y. Haga, Y. Onuki	54
1-2-22	The Detailed Temperature Dependence of Phase Slip Transition in $\text{Cr}(001)/\text{Sn}$ Epitaxial Film M. Takeda, K. Kakurai, K. Mibu	56

No.	「 Title 」	Page
<i>Neutron Scattering - Superconductivity -</i>		
1-3-1	Incommensurate Lattice Distortion in the HTT Phase of LSCO S. Wakimoto, H. Kimura, M. Fujita, K. Yamada, Y. Noda, G. Shirane, G. Gu H.-K Kim, R.J. Birgeneau	59
1-3-2	Polarized Neutron Scattering Study of Spin Excitations in LSCO S. Wakimoto, K. Kakurai, M. Takeda, M. Matsuda	60
1-3-3	Ni-Impurity Effects on Incommensurate Spin Correlations in Hole-doped Superconductor $\text{La}_{2-x}\text{Sr}_x\text{CuO}_4$ in the vicinity of Superconductor-insulator Boundary H. Hiraka, S. Ohta, S. Wakimoto, M. Matsuda, K. Yamada	61

No.	「 Title 」	Page
<i>Neutron Scattering - Polymer -</i>		
1-4-1	<i>In-situ</i> and Real-time Observation for Star Polymer Formation in Ru(II)-Catalyzed Living Radical Polymerization by Small Angle Neutron Scattering(SANS) T. Terashima, R. Motokawa, M. Kamigaito, S. Koizumi, M. Sawamoto, T. Hashimoto	65
1-4-2	<i>In-situ</i> and Time-resolved Small-angle Neutron Scattering Observation for Reversible Addition-fragmentation Chain Transfer Living Radical Polymerization of Poly(Methyl Methacrylate)-<i>block</i>-Polystyrene R. Motokawa, Y. Zhao, T. Hashimoto, S. Koizumi	67
1-4-3	The First Success of Detailed Structure Analysis of a Giant Polymer Single Crystal by Wide-angle Neutron Diffraction Data Collected with a 2-dimensional Imaging Plate Detector K. Tashiro, M. Hanesaka, T. Ohhara, K. Kurihara, R. Kuroki, T. Tamada, S. Fujiwara, I. Tanaka, N. Niimura	69
1-4-4	<i>In-situ</i> Small-angle Neutron Scattering Studies of Mesoporous Silica Films I. Itoh, N. Miyamoto, H. Miyata, T. Noma, T. Watanabe, S. Koizumi, T. Hashimoto	71

No.	「 Title 」	Page
<i>Neutron Scattering - Biology -</i>		
1-5-1	Neutron Crystallographic Analysis of Endopolygalacturonase I from <i>Stereum Purpureum</i> at a 1.5 Å Resolution M. Sato, T. Shimizu, T. Nakatsu, H. Kato	75
1-5-2	The Influence of Oxidation Stress on the Abnormal Tau Aggregation S. Naito, H. Mochizuki, T. Yasuda, Y. Mizuno, M. Furusaka, S. Ikeda, M.H. Shimizu J. Suzuki, S. Fujiwara	76
1-5-3	Hydration Water Dynamics at Protein Dynamical Transition H. Nakagawa, Y. Joti, A. Kitao, K. Shibata, N. Go, M. Kataoka	77
1-5-4	Neutron Structure Analysis on Water Nano-tube Cluster Stabilized by Molecule-based Porous Crystal M. Tadokoro, K. Kurihara, T. Ohhara, I. Tanaka, R. Kuroki	78
1-5-5	Neutron Fiber Diffraction of Muscle Thin Filaments Containing Deuterated Troponin I S. Fujiwara, F. Matsumoto	80
1-5-6	Neutron Diffraction Experiment of TAKA Amylase Y. Morimoto, T. Tamada, K. Kurihara, T. Ohhara, K. Inaka, R. Kuroki	81
1-5-7	Neutron Diffraction Study of Porcine Pancreatic Elastase with Its Inhibitor T. Tamada, K. Kurihara, T. Ohhara, T. Kinoshita, T. Tada, R. Kuroki	82
1-5-8	pH Dependence Study of Insulin Structure by Neutron Crystallographic Analysis T. Ishikawa, Y. Oonishi, I. Tanaka, T. Chatake, K. Kurihara, T. Tamada, R. Kuroki N.Niimura	83

No.	「 Title 」	Page
<i>Neutron Scattering - Fundamental Physics - Neutron Optics -</i>		
1-6-1	Neutron Interferometry at PNO Y. Hasegawa, K. Aizawa	87
1-6-2	Current Status of the Neutron Beta Decay Experiment in JRR-3 S. Yamada, K. Mishima, H. Sato, T. Shinohara, T. Oku, J. Suzuki, H. M. Shimizu	88
1-6-3	Neutron Scattering Study on DyRhIn₂ Single Crystal N. V. Hieu, S. Jonen, N. Metoki, K. Sugiyama, R. Settai, T.D. Matsuda, Y. Haga, T. Takeuchi M. Hagiwara, Y. Ōnuki	89
1-6-4	The Magnetic Structure Study of NpPtGa₅ by Neutron Scattering S. Jonen, N. Metoki, F. Honda, K. Kaneko, D. Aoki, Y. Homma, E. Yamamoto, Y. Shiokawa Y. Ōnuki	90

No.	「 Title 」	Page
<i>Neutron Scattering - Instrument -</i>		
1-7-1	The Improvement of Triple-axis Spectrometer at JAEA: The New Double Bent PG Monochromator for TAS-1 S. Jonen, N. Metoki	93
1-7-2	Concept and Establishment of Extended Biconcave Lens for Cold Neutrons T. Adachi, T. Shinohara, K. Ikeda, K. Hirota, H. M. Shimizu, T. Oku, H. Sasao S. Yamada, J. Suzuki	94
1-7-3	Development of a Magnetic Neutron Lens Based on an Extended Halbach-type Permanent Sextupole Magnet T. Oku, S. Yamada, H. Sasao, J. Suzuki, T. Shinohara, K. Hirota, K. Ikeda, H.M. Shimizu	95
1-7-4	Development of a Highly Efficient Neutron Polarizing Device Based on a Quadrupole Magnet T. Oku, S. Yamada, J. Suzuki, K. Mishima, T. Shinohara, K. Hirota, K. Ikeda H. Sato, H.M.shimizu	96
1-7-5	Development of Flatpanel Anger Detector K. Hirota, S. Satoh, H.M.Shimizu, T. Shinohara, T. Oku, J. Suzuki	97
1-7-6	Experimental Study on Neutron Control by Using Piezoelectric Single Crystals S. Kawamura, J.H.Kaneko, K. Tanabe, K. Aizawa, A. Homma, Y. Otake, H. Fujimoto F. Fujita, M. Furusaka	98
1-7-7	Development of a Hybrid-anvil Type High-pressure Device for Magnetic Neutron Diffraction Studies T. Osakabe	100
1-7-8	Development of a High-resolution Two-dimensional MicroStrip Gas Chamber H. Takahashi, P. Siritprussamee, K. Fujita, T. Oku, J. Suzuki	101
1-7-9	A New Tandem Crystal System for Bonse-Hart Ultra-small-angle Neutron Scattering Spectrometer at JAEA D. Yamaguchi, S. Koizumi, R. Motokawa, T. Kumada, K. Aizawa, T. Hashimoto	102
1-7-10	Introduction of the 3-D Polarization Analysis Device CRYOPAD on TAS-1 at JRR-3 I. New Polarizing Monochromator and Analyser System on TAS-1 M. Takeda, M. Nakamura, Y. Shimojo, P. Courtois, K.H. Andersen, K. Kakurai	103
1-7-11	Introduction of the 3-D Polarization Analysis Device CRYOPAD on TAS-1 at JRR-3 II. Construction and Installation of the CRYOPADUM M. Takeda, M. Nakamura, A. Oosawa, Y. Shimojo, E. Lelievre-Berna, F. Tasset, L.-P. Regnault, K. Kakurai	105

No.	「 Title 」	Page
<i>Neutron Scattering - Residual Stress -</i>		
1-8-1	Effect of Lamellar Spacing on Internal Stress of a Pearlite Steel T. Shinozaki, S. Morooka, Y. Shiota, T. Suzuki, Y. Tomota	109
1-8-2	Neutron Diffraction Profile Analysis to Determine Dislocation Density and Grain Size for Drawn Steel Wires S. Ryuhuku, T. Shiratori, Y. Shiota, Y. Tomota, H. Suzuki, A. Moriai	110
1-8-3	Influence of Triaxial Stress State on the Neutron Stress Measurement using Neutron Image Plate(NIP) T. Sasaki, Y. Morii, N. Minakawa	111
1-8-4	Formation of Texture and Intergranular Strain in Cold Rolled Austenitic Plate H. Suzuki, T.M. Holden, B. Clausen, Y. Shiota, Y. Tomota	112
1-8-5	Stress Measurement of Austenitic Butt Weld using Neutron Diffraction H. Suzuki, T.M. Holden	113
1-8-6	Fatigue Damage Mechanism in Ultrafine- and Nano-grained Material Investigated by Neutron Diffraction Method Y. Akiniwa, H. Kimura, K. Tanaka, H. Suzuki, Y. Morii	114
1-8-7	Residual Stress Measurements beneath the Surface of Laser Peened Steel K. Akita, H. Tanaka, K. Takahashi, Y. Sano, H. Suzuki, A. Moriai	115
1-8-8	Stress Measurement of Cast Aluminum Components using the Neutron Diffraction Method with the Oscillation Technique S. Yamashita, K. Onishi, M. Morikawa, H. Suzuki, A. Moriai	116

No.	「 Title 」	Page
<i>Neutron Scattering - Others -</i>		
1-9-1	Positional Structure Scanning by Neutron Diffraction Measurement S. Shamoto, S. Iikubo, K. Kodama, H. Suzuki, H. Iikura, A. Moriai, M. Matsubayashi, N. Igawa	121
1-9-2	Application of Neutron Topography to Protein Crystals H. Koizumi, N. Ohya, M. Koishi, M. Tachibana, K. Kojima, K. Kurihara, R. Kuroki	123

No.	「 Title 」	Page
<i>Neutron Radiography</i>		
2-1	Quantitative Neutron Radiography System with Honeycomb Collimator for Controls of Scattered Neutron and γ-ray Effects M. Tamaki	127
2-2	Observation of Hydrogen Distribution in Hydrogen Storage Alloys Tank by using Neutron-radiography Technique H. Iikura, R. Yasuda, M. Matsubayashi, T. Ebisawa, H. Kawano, H. Arashima H. Ito	128
2-3	Water Movement Analysis in a Rose by Neutron Radiography T.M. Nakanishi, Y. Ichimaru, H. Iikura, M. Matsubayashi	129
2-4	Brief Void Fraction Measurement of Boiling Flow in Tight-lattice Rod Bundle M. Kureta	131
2-5	Visualization of Oil Behavior Inside Air Conditioner Compressor by Neutron Radiography S. Yamashita, K. Onishi, M. Matsubayashi, H. Iikura	132
2-6	Development of Neutron Imaging Techniques for Proton Exchange Membrane Fuel Cells(PEMFC) M. Matsubayashi, H. Iikura, R. Yasuda	133
2-7	Installation of a Cooled-CCD Camera Imaging System at the JRR-3 Cold Neutron Radiography Facility M. Matsubayashi, H. Iikura, R. Yasuda	134
2-8	Trial of neutron detection with GafChromic film N. Nariyama, S. Ohnishi	135

No.	「 Title 」	Page
<i>Prompt Gamma-ray Analysis</i>		
3-1	Characterization of Boron Species in Apple Fruit by Doppler Broadening of Prompt γ-ray Y. Sakai, Y. Watanabe, M.K. Kubo, H. Matsue	139
3-2	Non-destructive Analysis of the Ancient Egyptian Glass Relics by Neutron S. Yoshida, K. Yamahana, H. Matsue	140
3-3	Development of Neutron In-beam Mossbauer Spectrometer M.K. Kubo, Y. Tsuruoka, Y. Kobayashi, Y. Yamada, Y. Watanabe, Y. Sakai, H. Shoji W. Sato, H. Matsue	141
3-4	Focusing Neutron Beam Induced Prompt Gamma-ray Analysis at JAEA H. Matsue, M. Segawa, Y. Sekiya, S. Yamada, T. Shinohara, H. Sasao, T. Oku J. Suzuki, H.M. Shimizu	142
3-5	Comparison of Date Sorting Methods in MPGA Y. Toh, M. Oshima, M. Koizumi, A. Kimura	144

No.	「 Title 」	Page
<i>Neutron Activation Analysis</i>		
4-1	Application of Fission track Method to Particle Analysis of Environmental Sample for Safeguards C.G. Lee, K. Iguchi, J. Inagawa, D. Suzuki, F. Esaka, M. Magara, S. Sakurai, S. Usuda	147
4-2	Characterization of Aerosol in Kanto Air Basin (XXV) S. Naito, S. Yonemochi	149
4-3	The effect of soil contamination in feed on dioxyn concentration in cow milk K. Nishimura, N.Kihou	150
4-4	Irradiation of lithium amalgam K. Manabe, S. Yokoyama, A. Endo	151
4-5	Neutron Activation Analysis of Trace Elements in Rice and Sesame K. Kushita	152
4-6	Ratio of ionic calcium to elemental calcium in the atmospheric aerosols N. Ito, A. Mizohata	153


No.	「 Title 」	Page
<i>Production of Radio Isotopes</i>		
5-1	Simplification of procedure for radiochemical analysis of solidified products—Separation method of ^{14}C— K. Ishimori, K.Ooki, Y. Kameo, H. Takaizumi, M. Nakajima, Y. Ooki, K. Isogai	157

No.	「 Title 」	Page
<i>Irradiation Test of Reactor Materials</i>		
6-1	Characteristics of Polonium Adhesion Produced from Lead-Bismuth on Nickel T. Obara, T. Koga, T. Miura, H. Sekimoto	161

No.	「 Title 」	Page
<i>Others</i>		
7-1	Boron Neutron Capture Therapy for Recurrent Head and Neck Malignancies T. Aihara, J. Hiratsuka, N. Morita, H. Kumada, K. Ono, T. Harada	165
7-2	Improvement of DAP plastic detector for fission track dating (Part 2) H. Iwano, T. Danhara, H. Kobayashi, T. Tsuruta	167

This is a blank page.

1. 中性子散乱 1) 構造・励磁



1. Neutron Scattering 1) Structure・Excitation

This is a blank page.

研究テーマ：中性子小角散乱による第二種超伝導体の磁束格子状態の研究
 表題：Nb₃Sn の混合状態における三角-四角磁束格子転移

1-1-1

Hexagonal-to-squared Vortex Lattice Transition in the Mixed State of Nb₃Sn

R. Kadono, K. H. Satoh, A. Koda, T. Nagata¹, H. Kawano-Furukawa¹, J. Suzuki²,
 M. Matsuda², K. Ohishi³, W. Higemoto³, S. Kuroiwa⁴, H. Takagiwa⁴ and J. Akimitsu⁴

Institute of Materials Structure Science, KEK, Tsukuba, Ibaraki 305-0801

¹*Department of Physics, Ochanomizu University, Tokyo 112-8610*

²*Quantum Beam Science Directorate, JAEA, Tokai, Ibaraki 319-1195*

³*Advanced Science Research Center, JAEA, Tokai, Ibaraki 319-1195*

⁴*Department of Physics, Aoyama Gakuin University, Sagamihara, Kanagawa 229-8558*

We report on the study of vortex (flux line) state in Nb₃Sn using small-angle neutron scattering (SANS). The magnetic field dependence of the SANS diffraction pattern was obtained at 2.6(1) K. Figure 1 shows the typical SANS-J data at 2.6(1) K after subtracting background data obtained at 30 K ($> T_c$), where scattered neutrons from an incident beam with a mean wavelength $\lambda_0 = 6.5$ Å are detected by a position-sensitive detector at a distance of 10 m (1–2 T) or 4 m (3–4 T) from the specimen. The cryostat (including the magnet) and specimen are rotated slightly ($\pm 0.2^\circ$, in several steps) around the vertical axis to obtain a sum of diffraction patterns over Bragg angles for both triangular and square FLL structure. It is clear in Fig. 1 that there is a difference in the pattern of angles between data at 1–2 T and those at 3–4 T. Since the patterns at lower fields suggests an overlap of two (possibly distorted) hexagonal domains due to the tetragonal crystal structure, their change into the nearly four-fold symmetric pattern at higher fields demonstrate the occurrence of triangular-to-square lattice transformation at 2–3 T. The field range of transformation is considerably higher than that in V₃Si, where the transition to square lattice is nearly complete at 1.5 T (with $H \parallel \{0,0,1\}$).¹⁾ The apex angle of the real space unit cell is evaluated to be close to 60° and 90° for the respective data. Furthermore, the spots on the $\{1,0,0\}$ axis at high fields (Figs. 1c, d) is absent at lower

fields. This clearly indicates that the diagonal of the real space rhombic unit cell, which is aligned to $\{1,1,0\}$ or $\{1,\bar{1},0\}$ direction in each domain, rotates to a $\{1,0,0\}$ direction with increasing field. A similar domain structure at lower field has been observed in V₃Si.^{1,2)} The present result was used together with μ SR data to reconstruct a detailed field profile in the mixed state of Nb₃Sn.³⁾

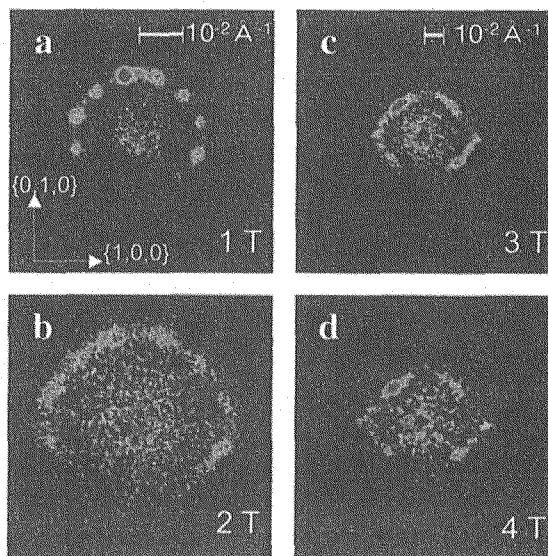


Figure 1: SANS diffraction patterns obtained by subtracting the background data at 30 K from the data taken at 2.6(1) K.

References

- 1) M. Yethiraj, *et al.*: "Phys. Rev. Lett.", **82**, 5112 (1999).
- 2) D. K. Christen, *et al.*: "Physica", **135B**, 369 (1985).
- 3) R. Kadono, *et al.*: "Phys. Rev. B", in press.

原子炉：JRR-3 装置：SANS-J(C3-2) 分野：中性子散乱（構造）

研究テーマ：鉄鋼の加工熱処理に伴うマイクロ組織形成および残留応力発生の中性子回折測定
 表題：中性子その場小角散乱測定を用いた高窒素鋼の内部構造解析

1-1-2

The Change in Nano-scaled Microstructure Measurement during Plastic Deformation by SANS-J for High Nitrogen Steel

K. Ikeda¹, Y. Tomota² and J. Suzuki³

¹ Graduate student of Ibaraki University, Hitachi, Ibaraki 316-8511

² Graduate School of Science and Engineering, Ibaraki University, Hitachi, Ibaraki 316-8511

³ Quantum Beam Science Directorate, JAEA, Tokai, Ibaraki 319-1195

1. Introduction

Nitrogen addition to austenitic steel is well known to improve several mechanical and chemical properties¹⁾. For instance, the yield strength and work-hardening are increased with increasing of nitrogen concentration. The effect of nitrogen on strength is much effective than carbon. However, the relationship between strengthening mechanism and nano-sized microstructure has not been made clear. In this study, the change in nano-scaled microstructure during plastic deformation was examined by using a small angle neutron scattering (SANS-J).

2. Experimental Procedure

The chemical compositions of materials used are shown in Table 1. The specimens were quenched into water after solution treatment to obtain single austenite structure. Change in nano-structure was examined in situ during tensile deformation by using SANS-J.

Table 1: Chemical compositions of materials used

	C	Si	Mn	Cr	Ni	N
N1	0.048	0.33	0.80	25.1	19.8	0.023
N3	0.048	0.31	0.84	25.0	20.1	0.325

3. Results and Discussion

The result of the small angle neutron scattering is shown in Fig. 1. As seen, the scattering intensity increases with increasing of tensile strain at q^{-1} indicating the evolution of dislocation structure in a low nitrogen bear-

ing steel (N1). On the other hand, in case of a high nitrogen bearing steel (N3), the intensity decreases with strain in the beginning and then increases. There seems to be two contributing factors to the scattering intensity: one is evolution dislocation of structure and the other is destruction of nano-sized cluster. The size, shape and amount of the clusters will be analysed quantitatively in a near future.

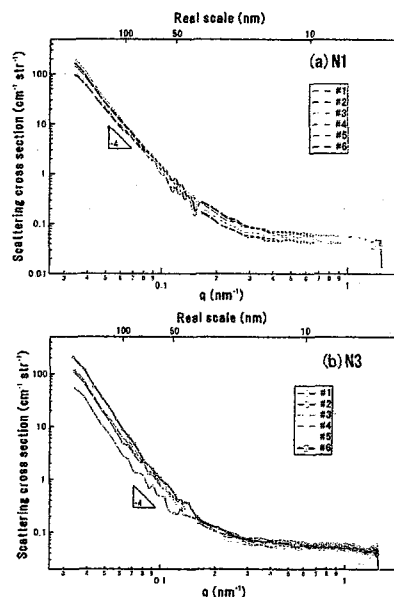


Figure 1: Scattering profiles of N1:(a) and N3:(b) obtained by in situ SANS-J measurement during tensile deformation.

References

- 1) U. K. Mudali and B. Raj: "High Nitrogen Steels and Stainless Steels", Alpha Science (2004).

研究テーマ：二次電池正極材料 LiCoO_2 のサイズ効果
表題： LiNiO_2 の中性子回折

1-1-3

Neutron Scattering Study of LiNiO_2

K. Basar, Xianglian, H. Honda, T. Sakuma, H. Takahashi¹, O. Abe², N. Igawa³ and Y. Ishii³

Institute of Applied Beam Science, Ibaraki University, Mito 310-8512, Japan

¹*Institute of Applied Beam Science, Ibaraki University, Hitachi 316-8511, Japan*

²*Faculty of Engineering, Ibaraki University, Hitachi 316-8511, Japan*

³*Japan Atomic Energy Agency, Tokai 319-1195, Japan*

LiNiO_2 and LiCoO_2 are important materials that can be applied as cathode materials for lithium-ion batteries¹⁾. Presently, based on its advantages LiNiO_2 becomes particularly attractive as cathode material in lithium-ion batteries. In this study we report the neutron scattering study of LiNiO_2 . The average crystallite size of LiNiO_2 is discussed and the amount of crystalline LiNiO_2 produced in the annealing process is estimated.

The sample was prepared by dry mixing of starting materials LiOH and NiO then milled by high-energy planetary milling for 3 hours at frequency 3 Hz to perform a ground product. After that, the mixture was heated at temperature 400°C for 5 hours. The whole sample was divided into three parts: sample A which had no further heating process, sample B annealed at 500°C for 5 hours and sample C annealed at 650°C for 5 hours. Neutron scattering measurements at room temperature have been performed for LiNiO_2 composites (sample A, B and C) by HRPD installed at JRR-3 in JAEA. The data were collected in the 2θ range from 10° to 150° with step angle 0.05° .

Figure 1 shows the neutron scattering intensity from LiNiO_2 composites (sample A, B and C). Rietveld analysis has been performed on the neutron scattering intensities of sample A, B and C using RIETAN-2000²⁾. The crystal of LiNiO_2 is assumed to belong to hexagonal type structure with space group $R\bar{3}m$ ^{3,4)}. The average crystallite sizes of LiNiO_2 which were calculated using Scherrer equation for

three different samples A, B and C are about 3, 4 and 13 nm, respectively. Assuming that 100% of starting materials change to crystalline LiNiO_2 in the sample C, the percentage of crystalline LiNiO_2 formation in sample A and B are about 61 and 87%, respectively.

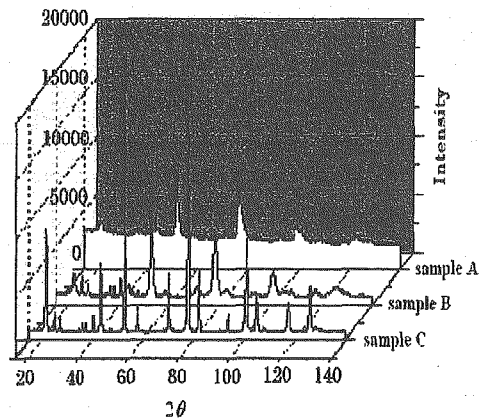


Figure 1: Neutron scattering intensities of LiNiO_2 composites at room temperature.

References

- 1) J. R. Dahn, U. von Sacken and C. A. Michal: "Solid State Ionics", **44**, 87 (1990).
- 2) F. Izumi and T. Ikeda: "Mater. Sci. Forum", **321-324**, 198 (2000).
- 3) V. Bianchi, D. Caurant, N. Baffier, C. Belhomme, E. Chappel, G. Chouteau, S. Bach, J. P. Pareira-Ramos, A. Sulpice and P. Wilmann: "Solid State Ionics", **140**, 1 (2001).
- 4) W. Li, J. N. Reimers and J. R. Dahn: "Phys. Rev.", **46**, 3236 (1992).

研究テーマ：包接水和物の動的特性の研究

表題：メタンハイドレートと氷 Ih の動的構造因子の差

1-1-4

Difference of Dynamic Structure Factor between Methane Hydrate and Ice Ih

T. Kamiyama, N. Seki, Y. Kiyonagi, T. Uchida, T. Ebinuma¹, H. Narita¹,
N. Igawa², H. Yamauchi² and Y. Ishii²

Graduate School of Engineering, Hokkaido University, Sapporo 060-8628

¹Institute for Energy Utilization, National Institute of Advanced Industrial Science and Technology,
Sapporo 062-8517

²Quantum Beam Science Directorate, JAEA, Tokai, Ibaraki 319-1195

The unique cage structure of methane hydrate (MH) gives interesting physical properties such as thermal conductivity¹⁾. The properties can be affected its host-guest interactions. For a correct understanding of such phenomena we need exact information of the host and guest molecular dynamics. In our previous experiments using TAS-1 and TAS-2 the rotational motion of methane molecule coincides with almost free quantum rotation of spherical top shape molecular, and there exist some $S(Q,E)$ peaks assigned as methane translational motions hindered by the water cages. The latter motions appear as the intense broad peaks under 10 meV region, which can separate from $S(Q,E)$ using the free rotation model of a methane molecule.

In this experiment we tried to appear the existence of such hidden peaks which characterizes the hydrate structure. The host framework constructed light water molecules shows almost same lattice and librational peak positions with light water ice. In the normal ice the lattice and librational modes are separated clearly, but the MH spectrum can be seen that there are some modes between ice lattice and librational mode. The purpose of this experiment was to separate these unknown peaks from $S(Q,E)$ using TAS-1.

The prepared MH ($\text{CH}_4\text{-D}_2\text{O}$) sample had 80% of the methane inclusion density. Figure 1 shows the experimental $S(Q,E)$ at $Q = 6 \text{ \AA}^{-1}$ for $\text{CH}_4\text{-D}_2\text{O}$ with TAS-1 and for D_2O ice with MARI at ISIS. As shown in the figure

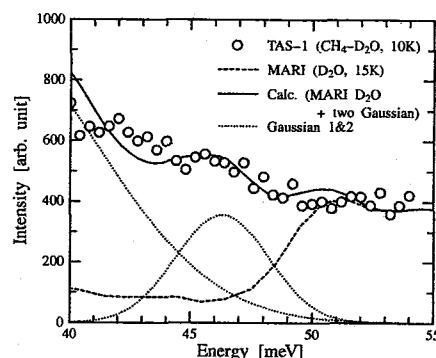


Figure 1: An example of peak analysis of $S(Q,E)$ at 10 K obtained by TAS-1.

the gap between lattice and librational modes in the ice is filled up in the MH. The subtraction of the D_2O ice spectrum from the present $S(Q,E)$ leaves the excess peaks in the difference. The excess peaks are fitted with two Gaussian function. In the fitting result the lower energy peak position corresponds with the TO mode in the ice lattice. The higher energy peak at 46.5 meV is a new peak which is characteristic in MH obviously. The position of this peak is on a Q^2 -line calculated with the effective inertial mass of CH_4 molecule. This suggests a possibility that the peak origin comes from the CH_4 rotation, although the intensity has large discrepancy with the CH_4 free rotation model.

References

- 1) J. S. Tse and M. A. White: "J. Phys. Chem.", **92**, 5008 (1988).

研究テーマ：新超伝導物質 $\text{Na}_x\text{CoO}_2 \cdot y\text{D}_2\text{O}$ の磁気励起スペクトル
表題： $\text{K}_{0.5}\text{CoO}_2$ の構造転移

1-1-5

Structural Transition of $\text{K}_{0.5}\text{CoO}_2$ Y. Mori, M. Soda, M. Sato, N. Igawa¹ and K. Kakurai¹*Department of Physics, Nagoya University, Chikusa-ku, Nagoya 464-8602*¹*Quantum Beam Science Directorate, JAEA, Tokai, Ibaraki 319-1195*

$\text{K}_{0.5}\text{CoO}_2$ with the triangular lattice of Co atoms exhibits two transitions accompanied with magnetic anomalies at temperatures $T_{c1} \sim 60$ K and $T_{c2} \sim 20$ K. K ions order at $T_{c0} \sim 550$ K.¹⁾ These transitions are very similar to those of $\text{Na}_{0.5}\text{CoO}_2$. For $\text{Na}_{0.5}\text{CoO}_2$, the structures both above and below T_{c0} have been reported and it has been presumed that the order of Na ions play an important role to two phase transitions at T_{c1} and T_{c2} .

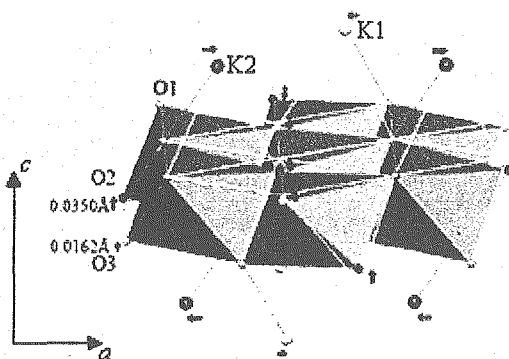
In the present work, neutron diffraction studies have been carried out on a polycrystal sample of $\text{K}_{0.5}\text{CoO}_2$ to investigate its detailed structures at 423 and 573 K using the high-resolution powder diffractometer (HRPD) installed at JRR-3 of JAEA in Tokai.

A number of superlattice peaks arising from the potassium order were observed at 423 K. These peaks can be indexed by using the orthorhombic space group $Pnmm$, as for $\text{Na}_{0.5}\text{CoO}_2$. Then, the diffraction patterns were taken at 573 K. At the temperature, the superlattice peaks observed at 423 K disappear and all reflections can be indexed by the hexagonal space group $P6_3/mmc$. At both temperatures of 423 and 573 K, the error bars of the positional parameters of K atoms (at 6h sites of the space group $P6_3/mmc$ at 573 K and 2a and 2b sites of the space group $Pnmm$ at 423 K) obtained by the fitting were rather large, though the positions of O atoms can be determined well.

In Fig. 1, the structure of $\text{K}_{0.5}\text{CoO}_2$ determined by the present Rietveld analyses is shown, where K1 and K2 and O1, O2, and O3 represent crystallographically distinct K and

O sites, respectively. K1 atoms are on the lines along c through the center of gravity of a triangle formed by three Co atoms within a CoO_2 plane and K2 atoms lie above the Co atoms (or on the same line along c through the Co atoms). The arrows indicate the atomic shifts from the positions corresponding to the hexagonal symmetry described by thin bonds. In the figure, because the atomic shifts of oxygen atoms along c are very small as compared to those of potassium atoms, they are drawn five times longer than the actual ones.

In the present experiments, we could determine the structure of $\text{K}_{0.5}\text{CoO}_2$ system above and below T_{c0} and we found that this system has the qualitatively similar order pattern to that of $\text{Na}_{0.5}\text{CoO}_2$. Although there are some differences between two systems, these may be explained by the difference between the distances of CoO_2 layers.

Figure 1: Structure of $\text{K}_{0.5}\text{CoO}_2$.

References

- 1) H. Watanabe *et al.*: "J. Phys. Soc. Jpn.", **75**, 034716 (2006).

原子炉：JRR-3 装置：HRPD(1G) 分野：中性子散乱（構造）

研究テーマ：フラストレートした量子スピン系 $\text{Hg}_2\text{Cu}_2\text{F}_6\text{X}$ ($\text{X}=\text{O}, \text{S}$) の磁氣的挙動
 表題：スピン 1/2 擬パイロクロア格子系 $\text{Ag}_2\text{Cu}_2\text{O}_3$ の構造

1-1-6

Structural Studies of Pyrochlore-related Spin-1/2 System $\text{Ag}_2\text{Cu}_2\text{O}_3$ D. Uematsu, M. Soda, M. Sato, N. Igawa¹ and K. Kakurai¹*Department of Physics, Nagoya University, Furo-cho, Chikusa-ku, Nagoya 464-8602*¹*Quantum Beam Science Directorate, JAEA, Tokai, Ibaraki 319-1195*

In $\text{Ag}_2\text{Cu}_2\text{O}_3$, edge-linked CuO_4 squares form the CuO_2 chains with their square-planes parallel to the ac - (or bc -) planes, and the chains align parallel to the a - (or b -) axis. We can also see a network of corner sharing Cu_4 tetrahedra, or a pyrochlore-related lattice, in which the geometrical frustration is expected to induce strong magnetic fluctuations, if the exchange coupling energies J among the spins ($S=1/2$) of these Cu^{2+} ions are antiferromagnetic.

In order to study the relationship between the structural and magnetic properties of this pyrochlore-related system $\text{Ag}_2\text{Cu}_2\text{O}_3$, neutron and X-ray Rietveld analyses and measurements of the magnetic susceptibility χ and specific heat C have been carried out. Samples were prepared by the co-precipitation method.

Powder neutron diffraction measurements were performed by using a high resolution powder diffractometer (HRPD) in JRR-3 of JAEA in Tokai with the neutron wavelength of 1.8233 Å.

In the Rietveld refinements at several temperatures by using the tetragonal space group $I4_1/amd$ (origin choice 2) reported previously¹⁾, all hkl peaks with nonzero h and k have the slightly broader widths than the corresponding resolution ones, while those of the $h0l$ and $0kl$ peaks have the resolution widths. Especially at 10 K, where temperature $T < T_N$, the width of the hkl reflections with nonzero h and k are much larger than the calculated widths, while the widths of the $h0l$ and $0kl$ peaks are T -independent and resolution limited. This clearly indicates that the mono-

clinic distortion is enhanced at low T . In the analyses of this distorted structure, we have found that $C2/c$ is the appropriate space group to the present system, though further detailed considerations are required to obtain satisfactory results at 10 K, as described later. In the actual analyses, we adopted one of the choices in the space group $C2/c$, $I112/b$ (unique axis c or $\gamma \neq 90^\circ$; choice 3) in order to make it easy to compare the atomic positions with those of the above tetragonal cell.

We have found that the monoclinic distortion begins to increase rapidly with decreasing T at the magnetic transition temperature $T_N \sim 70$ K. Because the system undergoes the magnetic ordering at T_N , it is quite plausible that the structural distortion and the magnetic transition couple to each other.

Observing the T -dependence of the γ value, one can realize that the Cu_4 tetrahedron is more twisted about the c axis at $T < T_N$ than above T_N . We think that the release of the geometrical frustration inherent in the present spin systems is induced by the twisting of the tetrahedra.

In the present experiment, we have not detected the magnetic reflections within the experimental accuracy so that we do not know the actual ordering pattern of the spins below T_N . It is desirable to search the magnetic reflections by using single crystals, though it is difficult to prepare them by the co-precipitation method.

References

- 1) P. Gomez-Romero *et al.*: "Angew. Int. Ed.", **38**, 524 (1999).

原子炉：JRR-3 装置：HRPD(1G) 分野：中性子散乱 (構造)

研究テーマ：ヌクレオチド結晶の高水和状態における水和構造の解析

表題：中性子回折法によるウリジン 5'-リン酸二ナトリウム七水和物の水素結合網の解析

1-1-7

Neutron Diffraction Study on Hydrogen-bonding Networks in Disodium Uridine 5'-monophosphate Heptahydrate

S. Yamamura, Y. Sugawara, T. Ohhara¹, I. Tanaka² and N. Niimura³

School of Science, Kitasato University, Sagamihara, Kanagawa 228-8555

¹Quantum Beam Science Directorate, JAEA, Tokai, Ibaraki 319-1195

²Faculty of Engineering, Ibaraki University, Hitachi, Ibaraki 316-8511

³Graduate School of Science and Engineering, Ibaraki University, Hitachi, Ibaraki 316-8511

Phase transitions of nucleoside and nucleotide hydrates are induced by humidity or temperature, where reconstruction of hydrogen-bonding networks participates. In the case of disodium uridine 5'-monophosphate ($C_9H_{11}N_2O_9PNa_2$, Na_2UMP) heptahydrate, disorder of sodium ions and crystal water molecules is observed at room temperature (RT) and a phase transition, which would be related with the ordering of hydrogen-bonding networks, proceeds around -50 °C. Thus neutron diffraction analysis of Na_2UMP heptahydrate at RT was carried out following the previous work for disodium cytidine 5'-monophosphate (Na_2CMP) hydrate¹⁾.

Na_2UMP was crystallized from deuterated aqueous solution in order to reduce incoherent scattering from hydrogen atoms. An as-grown crystal with approximate dimensions of $1.6 \times 1.4 \times 1.1$ mm³ was sealed in a quartz capillary tube. The neutron intensity data were collected using a BIX-III diffractometer installed at 1G-A port of JRR-3 in JAERI (Tokai) with the wavelength of 1.51 Å. Crystal data are; orthorhombic, $P2_12_12_1$, $a = 22.987(4)$, $b = 8.890(1)$, $c = 58.091(8)$ Å, $Z = 24$. Hydrogen positions were determined by iteration of difference Fourier syntheses starting from the coordinates of non-hydrogen atoms obtained by X-ray analysis using non-deuterated sample. The R factor is 0.25 for 13734 observed reflections ($|F_o| > 4\sigma(F_o)$) up to 0.85 Å at the present stage.

The crystal structure is shown in Fig. 1. There are six UMP molecules and 48 sites of 42 crystal water molecules in an asymmetric unit. All hydrogen atoms of UMP molecules and 51 hydrogen atoms of 34 crystal water sites were determined. All exchangeable hydrogen atoms such as bonded with N and O in UMP molecules and those of all crystal water molecules were deuterated. Further refinement is in progress.

References

- 1) S. Yamamura, *et al.*: "Progress Report on Neutron Science", 2005-045, 114 (2005).

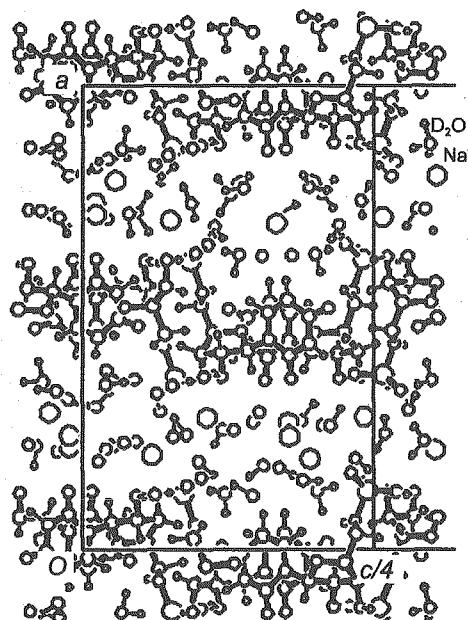


Figure 1: Crystal structure of Na_2UMP heptahydrate.

原子炉：JRR-3

装置：BIX-3(1G-A)

分野：中性子散乱（構造）

研究テーマ：先端偏極中性子散乱によるスピン-格子物性の研究
表題：リラクサー強誘電体 KLT の散漫散乱と格子振動の研究

1-1-8

Diffuse Scattering and Lattice Dynamics in Relaxor KLT

S. Wakimoto, G. A. Samara¹, R. K. Grubbs¹, E. L. Venturini¹, L. A. Boatner², G. Xu³,
G. Shirane³ and S.-H. Lee⁴

Quantum Beam Science Directorate, JAEA, Tokai, Ibaraki 319-1195

¹*Sandia National Laboratories, Albuquerque, New Mexico 87185, USA*

²*Oak Ridge National Laboratory, Oak Ridge, Tennessee 37831, USA*

³*Brookhaven National Laboratory, Upton, New York 11973, USA*

⁴*Department of Physics, University of Virginia, Charlottesville, Virginia 22904, USA*

Li doping into a quantum paraelectric KTaO_3 induces relaxor behavior. Though it is expected that a large off-center displacements of Li ions trigger polarized nano-regions (PNR's) and hence the relaxor behavior, detailed study of the lattice dynamics and atomic displacements in $\text{K}_{1-x}\text{Li}_x\text{TaO}_3$ (KLT) has been sparse.

We have performed neutron scattering experiments at the TAS-1 and LTAS spectrometers using a single crystal of $\text{K}_{0.95}\text{Li}_{0.05}\text{TaO}_3$ where a small amount of a Ca impurity (~ 15 ppm) was incorporated during the single crystal growth. From dielectric measurements, dynamics of Li ions which is order-disorder type nature, has been observed as a relaxation starting below ~ 200 K. Neutron scattering experiments reveal that diffuse scattering ridges appear around the nuclear Bragg peaks along the $[100]$ direction below ~ 150 K (Fig. 1) and phonon line broadening starts to appear at even higher temperatures ~ 200 K. These facts suggest that PNR's start to form around 200 K accompanying with the relaxational behavior of the Li ions. From analyses of the diffuse intensities at different zones, we have derived atomic displacements inside PNR's. We find that the displacements include a uniform phase shift of all of the atoms in addition to the condensation of the TO soft ferroelectric mode, that is analogous to the prototypical relaxor material $\text{Pb}(\text{Mg}_{1/3}\text{Nb}_{2/3})\text{O}_3$.

In summary, we draw the following picture

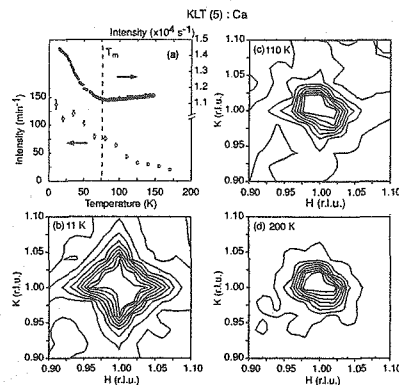


Figure 1: (a) Temperature dependence of the $(2, 0, 0)$ nuclear Bragg peak (black circles) and the diffuse scattering intensity measured at $(1.05, 1, 0)$. (b)-(d) Contour maps of the diffuse intensity around $(1, 1, 0)$.

for KLT. At the Burns temperature ~ 200 K, PNR's start to form triggered by off-center displacements of the Li ions. The ionic displacements consist of the displacements associated with the soft FE mode superimposed on a uniform phase shift, which should be an energy barrier to the bulk FE transition. Below the Burns temperature, the dynamics of Li atoms appears as the relaxational behavior in the dielectric response. As temperature decreases dipolar fluctuations are reduced and stronger correlations develop among the PNR's that grow in volume, as evidenced by the growth of diffuse scattering intensity.

原子炉：JRR-3 装置：TAS-1(2G), LTAS(C2-1) 分野：中性子散乱 (構造)

研究テーマ：中性子散乱による機能材料構造の研究
表題：Ba₃Ca_{1.18}Nb_{1.82}O_{8.73} の結晶構造

1-1-9

Crystal Structure of Ba₃Ca_{1.18}Nb_{1.82}O_{8.73}

T. Shimoyama¹, J. Sagiya¹, T. Tojo¹, H. Kawaji¹, T. Atake¹, N. Igawa² and Y. Ishii²

¹Materials and Structures Laboratory, Tokyo Institute of Technology, Yokohama 226-8503

²Quantum Beam Science Directorate, JAEA, Tokai, Ibaraki 319-1195

Ba₃Ca_{1+x}Nb_{2-x}O_{9-3x/2} is a candidate for high temperature proton-conducting electrolyte, since a large amount of water/hydrogen can be solved and the electrical conductivity would be comparable to that of the best oxygen-ion conductors. The proton solubility and the conductivity have been studied extensively. However, the mechanism of the conductivity has not been clarified yet. In the present study, the effects of the water/hydrogen dissolution on the crystal structure have been studied by the neutron diffraction measurements.

Polycrystalline sample of Ba₃Ca_{1.18}Nb_{1.82}O_{8.73} (BCN18) was synthesized by a solid state reaction method. BaCO₃ (RARE METALLIC Co., Ltd., 99.99 %), Nb₅O₂ (MITSUI MINING SMELTING Co., Ltd., 99.99 %) and CaCO₃ (RARE METALLIC Co., Ltd., 99.99 %) were weighed in stoichiometrically ratio and mixed in an alumina mortar with small amount of ethanol. The mixture was dried in the air and pressed into disks, and then calcined in an alumina crucible at 1000 °C for 20 h. The product was ground, pressed into disks, and then sintered at 1500 °C for 24 h in the air. The dry sample (no water/hydrogen; denoted as dry BCN18) was prepared by heating the specimen at 900 °C for 20 h in vacuum. The deuterated water-solved sample (BCN18-D) was prepared by holding the dry sample in D₂O vapor of about 3 kPa (saturated vapor pressure of water at room temperature) at 350 °C for 60 h. The amount of D₂O solved in the sample was determined to be 26.0 mol% by the weight measurements.

The powder neutron diffraction measurements were carried out using the high resolution powder diffractometer (HRPD) installed at the Japan Research Reactor 3 of the Japan Atomic Energy Agency (JAEA) with a wavelength of 1.8233 Å. The neutron diffraction data were collected with constant monitor counts and a step angle of 0.05° over the 2θ range of 2.5°- 160°.

The results of diffraction patterns obtained at room temperature for dry BCN18 and deuterated water-solved sample (BCN18-D) are shown in Fig. 1. The peaks of BCN18-D are shifted to lower angles compared to those of dry BCN18. The relative intensity is also different in between the two, which should be caused by the introduction of oxide ions at the oxygen vacancy sites and the deuterons at in the interstitial sites of BCN18-D. The lattice constant and the atomic displacement parameter *B* of BCN18-D are larger than those of the dry BCN18. The detailed analysis using Rietveld method is under way.

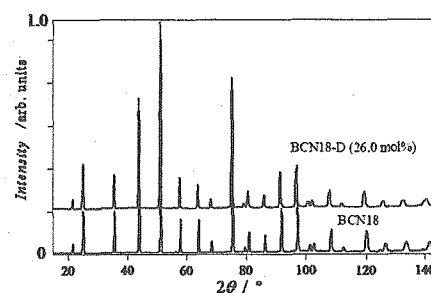


Figure 1: Neutron diffraction patterns of dry BCN18 and BCN18-D(26.0 mol%).

原子炉：JRR-3 装置：HRPD(1G) 分野：中性子散乱 (構造)

研究テーマ：中性子散乱による機能材料構造の研究
表題：炭酸ガスハイドレートの結晶構造解析

1-1-10

Crystal Structure of Carbon Dioxide Hydrate

N. Igawa, T. Taguchi and Y. Ishii

Quantum Beam Science Directorate, JAEA, Tokai, Ibaraki 319-1195

Clathrate hydrates are solid-state substances and consists of two types of cages (called "large" and "small" cages) formed by water molecules that are hydrogen-bonded in a manner similar to ice and trapped encaging gas molecules inside each cage. Although many studies on the clathrate hydrate including carbon dioxide hydrate were carried out, no detailed crystallographic property has yet been cleared. The purpose of this study is the precise crystal structural analysis of carbon dioxide hydrate, one of those clathrate hydrates, focused on the temperature dependence on the motion behaviors of the inclusion carbon dioxide gas molecule in the two types of cages.

Powder sample of carbon dioxide hydrate was synthesized from powdered ice and pressurized carbon dioxide. Instead of H_2O , D_2O was used to synthesize the sample for the reduction of the high incoherent neutron scattering from H atom. The neutron diffraction patterns of carbon dioxide hydrate were measured by using a High Resolution Powder Diffractometer (HRPD) installed at JRR-3, JAEA in the temperature range from 10 K to 185 K. The powder sample was contained in a vanadium cylinder of 10 mm in diameter and 40 mm-high, and the cylinder was set in an Al container filled with He gas, which was attached to the Displex type refrigerator. A neutron wavelength of 0.1823 nm was used and diffraction data were collected in the 2θ range from 20° to 165° with a step-angle of approximately 0.05° . Obtained diffraction patterns were analyzed by the Rietveld method using the program "RIETAN-2000".¹⁾

Figure 1 shows the result of a profile refine-

ment of the neutron diffraction pattern at 10 K. The top and bottom rows of tick marks in the figure represent calculated peak positions for the carbon dioxide and for carbon dioxide hydrate, respectively. There are some extra peaks in the profile; all of those extra peaks were attributed to the crystal of carbon dioxide which is a starting material gas and remained in the sample. The experimental patterns attributed to the carbon dioxide hydrate are fitted well to the model with the space group $Pm\bar{3}n$ and a lattice constant $a = 1.1815$ nm at 10 K: the reliable factors are $R_{wp} = 3.86\%$, $R_I = 6.07\%$ and "goodness-of-fit" indicator $S = 1.37$. We estimated that both the cages are almost fully occupied by a carbon dioxide molecule at 10 K. The precious analyses are in progress.

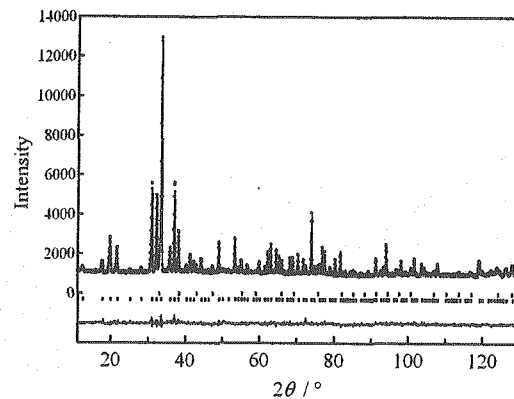


Figure 1: Profile refinement of carbon dioxide hydrate at 10 K.

References

- 1) F. Izumi and T. Ikeda: "Mater. Sci. Forum", **198**, 321 (2000).

研究テーマ：ペロブスカイト型酸化物プロトン伝導体中の水素占有位置（2）
表題：10 Kにおける粉末中性子回折による $\text{BaSn}_{0.5}\text{In}_{0.5}\text{O}_{2.75}$ 中の重水素位置の決定

1-1-11

Location of Deuterium Atoms in $\text{BaSn}_{0.5}\text{In}_{0.5}\text{O}_{2.75}$
by Neutron Powder Diffraction at 10 K

T. Ito¹, T. Nagasaki², K. Iwasaki¹, M. Yoshino¹, N. Igawa³ and Y. Ishii³

¹Department of Materials, Physics and Energy Engineering, Graduate School of Engineering,
Nagoya University, Nagoya 464-8603

²EcoTopia Science Institute, Nagoya University, Nagoya 464-8603

³Quantum Beam Science Directorate, JAEA, Tokai, Ibaraki 319-1195

Aliovalently-doped perovskite oxides often show significant proton conductivity in a humid atmosphere at high temperature¹⁾. To understand the state and transport of hydrogen in these materials, it is essential to locate protons in them. While several computational approaches²⁾ have yielded consistent results with respect to the hydrogen site, none of the neutron diffraction studies^{3,4)} have verified the results. In the present study, we try to locate deuterium atoms in D_2O dissolved $\text{BaSn}_{0.5}\text{In}_{0.5}\text{O}_{2.75}$ by neutron powder diffraction at 10 K. The data are analyzed by the maximum entropy method (MEM, program PRIMA) as well as the Rietveld method (program RIETAN-2000)^{5,6)}.

The $\text{BaSn}_{0.5}\text{In}_{0.5}\text{O}_{2.75}$ samples were prepared by the solid-state reaction of BaCO_3 , In_2O_3 and SnO_2 powders at 1673 K for 20+20 h in a dry oxygen flow. The $\text{BaSn}_{0.5}\text{In}_{0.5}\text{O}_{2.75}$ powder was loaded in a thermobalance and held at 673 K in a wet oxygen flow containing 12.8 kPa D_2O . The deuterium concentration in the sample was evaluated to be 0.15 D/Ba. The sample without dissolved D_2O was prepared by the same procedure, except that the final heating was done in a dry oxygen flow instead of a wet one. The neutron powder diffraction data ($\lambda = 1.823 \text{ \AA}$) of the samples were collected at 10 K using the High Resolution Powder Diffractometer (HRPD).

The diffraction data were analyzed first by the ordinary Rietveld method and then by the iterative procedure named REMEDY cy-

cle^{5,6)}, which includes MEM-based whole pattern fitting. Figure 1 shows the distribution of neutron scattering length density of the samples obtained by the final MEM analysis. We conclude that the deuterium atoms occupy the $12h$ site of the cubic perovskite structure ($Fm\bar{3}m$) with an O-D distance of 0.97 \AA . This hydrogen position is similar to those suggested by the previous computational studies²⁾.

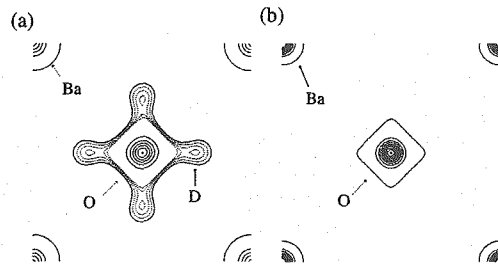


Figure 1: Distribution of nuclear scattering length density on (100) plane of $\text{BaSn}_{0.5}\text{In}_{0.5}\text{O}_{2.75}$ (a) with and (b) without dissolved D_2O .

References

- 1) H. Uchida *et al.*: "Solid State Ionics", **34**, pp. 103-110 (1989).
- 2) For example, M. Yoshino *et al.*: "Solid State Ionics", **162-163**, pp. 127-133 (2003).
- 3) K.S. Knight: "Solid State Ionics", **127**, pp. 43-48 (2000).
- 4) T. Ito *et al.*: "Solid State Ionics", to be published.
- 5) F. Izumi *et al.*: "Mater. Sci. Forum", **321-324**, pp. 198-205 (2000).
- 6) F. Izumi *et al.*: "Recent Research Developments in Physics, Vol. 3, Part II", Transworld Research Network, p. 699 (2002).

原子炉：JRR-3 装置：HRPD(1G) 分野：中性子散乱（構造）

研究テーマ：中性子散乱による機能材料構造の研究
表題：粉末氷からのメタンハイドレート形成過程

1-1-12

Growth Process of Methane Hydrate from Powder Ice

A. Hoshikawa, H. Fukazawa, N. Igawa, H. Yamauchi and Y. Ishii

Quantum Beam Science Directorate, JAEA, Tokai, Ibaraki 319-1195

There is less quantitative information concerning nucleation of gas hydrates from ice relative to nucleation from water. We measured growth process of methane hydrate from D_2O ice particles under pressurized CH_4 gas by in situ neutron powder diffraction.

The neutron diffraction measurements were carried out on HRPD installed at JRR-3. A single-crystal sapphire cell was used as a high-pressure sample cell. The Bragg peaks of the sapphire cell were excluded by the 3rd collimator of HRPD.

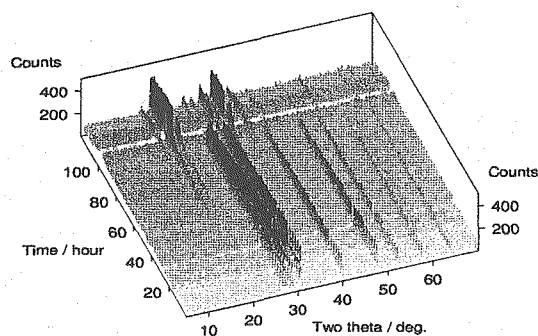


Figure 1: In situ time resolved diffraction patterns.

Figure 1 shows time resolved diffraction patterns of methane hydrate. Each measurement was done for 45 min. The background increased according to introducing CH_4 gas because H atoms show strong incoherent scattering. Analysis was based on the previous crystal structure data^{1,2)}. The temperature and pressure dependence of mass fraction was obtained as shown in Fig. 2.

To avoid melting ice, the CH_4 gas was gradually applied at 240 K as isothermal process. The diffraction peaks of methane hy-

drate were observed at 2 MPa. The pressure was kept at 2 MPa for several hours. After that, the pressure was increased until 6 MPa. However, the growth rate of methane hydrate did not change. Accordingly, the pressure did not affect the growth rate under the sufficient pressure for the growth.

Following, the temperature was changed under nearly isobaric process (6–7 MPa). When temperature was changed from 265 K to 270 K, an increase of the growth rate was observed. At 275 K, the D_2O ice was melted and the growth rate drastically increased. After 4 hours, almost all of the D_2O ice was changed to methane hydrate. It was successful to observe the growth process from the ice to methane hydrate.

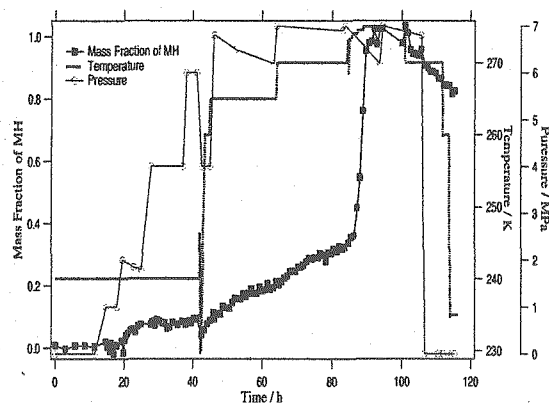


Figure 2: Mass fraction of methane hydrate.

References

- 1) A. Hoshikawa, N. Igawa, H. Yamauchi, and Y. Ishii: "J. Phys. Chem. Solid.", **66**, 1810-1814 (2005).
- 2) A. Hoshikawa, N. Igawa, H. Yamauchi, and Y. Ishii: "J. Chem. Phys.", **125**, 034505 (2006).

研究テーマ：ホイスラー型 Ni_2MnGa 系合金単結晶の磁場誘起マルテンサイト変態
 表題：ホイスラー型 Ni_2MnGa 系合金単結晶の磁場誘起マルテンサイト変態

1-1-13

Magnetic Field-induced Martensitic Transformation of Heusler-type Off-stoichiometric Ni_2MnGa Single Crystal

K. Inoue, Y. Yamaguchi¹, Y. Ishii², H. Yamauchi² and T. Shishido¹

Faculty of Science and Technology, Ryukoku University, Otsu 520-2194

¹IMR, Tohoku University, Sendai 980-8577

²Quantum Beam Science Directorate, JAEA, Tokai, Ibaraki 319-1195

Magnetic field effect on a martensitic transformation of a Heusler-type off-stoichiometric $\text{Ni}_{2.16}\text{Mn}_{0.78}\text{Ga}_{1.06}$ single crystal has been investigated. This off-stoichiometric alloy has a martensitic transformation temperature around 293 K, which is coincident with a Curie temperature. It is paramagnetic in the mother phase and ferromagnetic in the martensitic phase. By temperature dependent powder neutron diffraction we have observed a cubic Heusler structure ($Fm\bar{3}m$) in the mother phase and coexistent structures of tetragonal ($I4/mmm$) and orthorhombic ($Pbca$) in the martensitic phase. In the present experiment a single crystal of $2 \times 6 \times 10 \text{ mm}^3$ and triple-axis neutron spectrometer, TAS-2, were used. Behavior of peaks around cubic (200) on the reciprocal plane, cubic ($h k 0$), due to increase in magnetic field up to 8 [T], was investigated at 293 K. The results are shown in Fig. 1, where the vertical axes are enlarged, to see precisely the change of small peaks around cubic (200). We see that a small peak corresponding to the martensitic structure is recognized even in no magnetic field. This small peak and the other newly appearing peaks become stronger according to the increase in magnetic field. These peaks are all due to the martensitic structures. After removing the field, all new peaks again disappear and the pattern returns to the original one before applying the field. The result shows that the magnetic field causes the martensitic transformation. Comparing the transformation process

with a usual transformation process caused by temperature decrease, which was measured by triple-axis neutron spectrometer, AKANE (Tohoku univ.), we can conclude that the process of the transformation caused by the increase in magnetic field is quite similar to the process caused by the decrease in temperature.

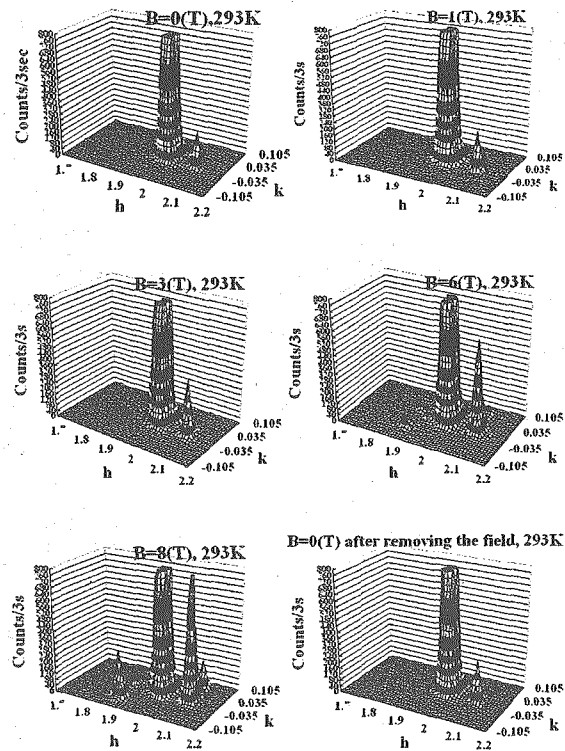


Figure 1: Magnetic field dependence of the peaks around cubic (200) on the reciprocal plane of cubic ($h k 0$).

研究テーマ：中性子散乱による機能材料構造の研究
表題：氷 XI の成長と構造

1-1-14

The Growth and Structure of Ferroelectric Ice XI

H. Fukazawa, A. Hoshikawa, N. Igawa, H. Yamauchi and Y. Ishii

Quantum Beam Science Directorate, JAEA, Tokai, Ibaraki 319-1195

The complex behavior of water and the unusual properties of proton ordering in ferroelectric ice crystal continue to attract much interest. Neutron diffraction studies provide firm structural evidences that at high-pressure ices VIII and IX, which are the proton ordered phases of ices VII and III, exist as stable low-temperature phases. The disordered protons of the high-pressure ices move to ordered positions as ices are cooled. On the other hand, structure analysis about proton arrangements in ice XI, which is considered to exist as the proton-ordered phase of normal ice Ih at atmospheric pressure, has not succeeded because of lack of a bulk crystal of ice XI. The difficulty in obtaining the bulk of ice XI is due to a difficulty in the transition from ice Ih to XI.

Why is the transition so difficult? This is directly related to the intrinsic nature of ice at low temperatures. The interesting properties of ice XI has been long discussed in the condensed matter physics. In addition, surface scientists tried to reveal the nature of the proton ordering in thin ice film on specific metal. Furthermore, the existence of ice XI on outer planets recently becomes an important subject in planetary science. We have revealed the growth and structure of ice XI using our high resolution powder diffractometer, HRPD.

In 05' we measured neutron powder diffraction from ice doped with minute impurities (0.001-M and 0.01-M KOD, 0.001-M and 0.01-M NaOD, 0.001-M and 0.01-M LiOD, 0.001-M ND₃, 0.001-M DCl, etc). We repeatedly measured diffraction from the doped ice samples at several temperatures, and sought for

a suitable condition to get a large amount of ice XI. We happily obtained a well ordered ice. More than half of the ice sample becomes ice XI when the growth was finished by 5 days annealing. It is the highest value in previous neutron studies. Our result provides the reliable evidence of the proton ordering in the doped ice. Furthermore, since the mass fraction of ice XI is much higher than the mole fraction of the impurity, the dopant is considered to act as a catalyst. Thus, we conclude that ice XI is stable form of ice at low temperature^{1,2)}.

The evidence of the ferroelectric structure in doped ice obtained by our neutron diffraction suggests the existence of ferroelectric ice in the universe. We expect that planetary exploration will find ferroelectric ice XI in the solar system. A millimetre-sized particle of ice XI has a ten thousand volt charge. Ice XI on outer planets should become a huge source of electric field. The real dangerous ice in our solar system will become a shocking news item, as a fictional ice in Kurt Vonnegut's novel.

References

- 1) H. Fukazawa, A. Hoshikawa, H. Yamauchi, Y. Yamaguchi, Y. Ishii : "J. Cryst. Growth", **151**, 251-259 (2005).
- 2) H. Fukazawa, *et al.* : "Physica B", (in press).

研究テーマ：中性子非弾性散乱測定によるアルミン酸ランタンの誘電損失に関する研究
表題：中性子非弾性散乱測定によるアルミン酸ランタンの誘電損失に関する研究

1-1-15

Intrinsic Dielectric Loss of LaAlO_3 at Microwave Frequency

T. Shimada, H. Yamauchi¹, Y. Ishii¹, J. Breeze² and N. McN Alford²

R&D Center, NEOMAX, Osaka Shimamoto 618-0013, Japan

¹Quantum Beam Science Directorate, JAEA, Tokai, Ibaraki 319-1195, Japan

²London South Bank University, London SE1 0AA, UK

A millimeter wave wireless communication will be perfectly realized within 10 years. In the same time, the loss problem in the dielectric materials will be also picked up. Then it is expected to clear the mechanism of the dielectric loss at millimeter wave frequencies. In the present study, we chose the single crystal LaAlO_3 as a target material and measured inelastic neutron scattering. Also low temperature dielectric loss was measured to compare between the obtained dispersion curves and the temperature dependence of the dielectric loss.

LaAlO_3 single crystals were prepared by Czochralski method. The microwave dielectric properties were measured by TE₀₁ δ resonant mode in dielectric resonator. Also the neutron inelastic scattering data collected using TAS-1 equipped in JRR-3 of JAEA.

It is known that LaAlO_3 shows extremely low dielectric loss at microwave frequency and its loss is strongly depend on the incidence direction of electromagnetic wave in the crystal and the difference between the dielectric losses measured in the disc crystals having different top surface was found¹⁾. Also Spark *et al.* reported that phonon creation at the Brillouin zone boundary of the material contributed to the dielectric loss at microwave frequency²⁾. Figure 1 shows the phonon dispersion curve of the LaAlO_3 measured by TAS-1. Figure 2 also shows the temperature dependence of the dielectric loss of the LaAlO_3 . It is inferred that the loss peak at 220 K is corresponding to the excitation of the acoustic phonon having energy of 25 meV at

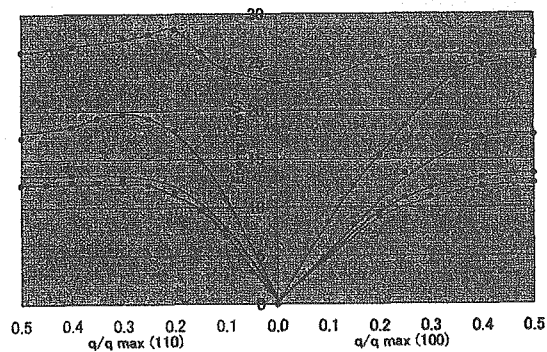


Figure 1: Phonon dispersion of LaAlO_3 at 100 and 110 directions.

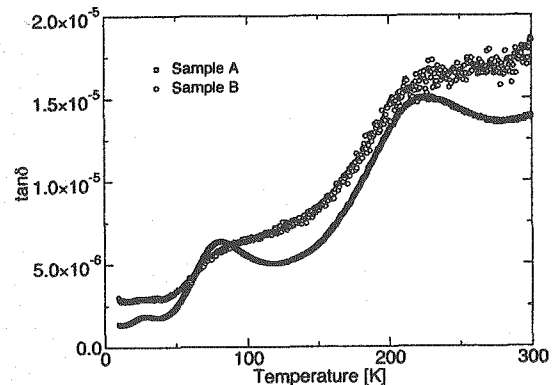


Figure 2: Temperature dependence of the dielectric loss of a LaAlO_3 single crystal.

the Brillouin zone boundary to the optical phonon. In this stage it is not cleared why the dielectric loss increased at 75 K. In order to clear the cause of this dielectric loss, it is necessary to collect the furthermore phonon data in the future.

References

- 1) T. Shimada : "J. Eur. Ceram. Soc.", **25**, pp.2901-2905 (2004).
- 2) M. Spark *et al.*: " Phys. Rev. B ", **33**, 4213 (1986).

原子炉：JRR-3 装置：TAS-1(2G) 分野：中性子散乱 (構造)

This is a blank page.

1. 中性子散乱 2) 磁性



1. Neutron Scattering 2) Magnetism

This is a blank page.

研究テーマ：偏極中性子散乱を用いた擬一次元イジング型反強磁性体 TlCoCl_3 及び関連物質の磁性の研究

表題：偏極中性子非弾性散乱による擬一次元イジング型反強磁性体 TlCoCl_3 の異方的磁気揺らぎの研究

1-2-1

Polarized Neutron Inelastic Scattering Study of Anisotropic Magnetic Fluctuations in Quasi-1D Ising-like Antiferromagnet TlCoCl_3

A. Oosawa, K. Kakurai¹, Y. Nishiwaki² and T. Kato³

Department of Physics, Sophia University, 7-1 Kioi-cho, Chiyoda-ku, Tokyo 102-8554

¹*Quantum Beam Science Directorate, Japan Atomic Energy Agency, Tokai, Ibaraki 319-1195*

²*Department of Physics, Tokyo Institute of Technology, Oh-okayama, Meguro-ku, Tokyo 152-8551*

³*Faculty of Education, Chiba University, 1-33 Yayoi-cho, Inage-ku, Chiba 273-8522*

In 1D Ising-like antiferromagnets, it is known that the transverse magnetic fluctuation $S_{xx}(\mathbf{Q}, \omega)$ and the longitudinal magnetic fluctuation $S_{zz}(\mathbf{Q}, \omega)$ are quite anisotropic due to the Ising anisotropy¹. For the spin-wave excitation continuum, the $S_{zz}(\mathbf{Q}, \omega)$ could not be observed so far in unpolarized neutron inelastic scattering experiments because the intensity of $S_{zz}(\mathbf{Q}, \omega)$ is much smaller than that of $S_{xx}(\mathbf{Q}, \omega)$ such that $S_{zz}(\mathbf{Q}, \omega)$ is masked by $S_{xx}(\mathbf{Q}, \omega)$ out of the scattering plane which is always observed.

In a year ago, we demonstrated the advantages of polarized neutron inelastic scattering experiments, which enables the separation of $S_{xx}(\mathbf{Q}, \omega)$ and $S_{zz}(\mathbf{Q}, \omega)$, and reported on a polarized neutron inelastic scattering investigation of quasi-1D Ising-like antiferromagnet TlCoCl_3 ². However, the statistical error of the obtained data is large so that we could not conclude the existence of the $S_{zz}(\mathbf{Q}, \omega)$ for the spin-wave excitation continuum in TlCoCl_3 . Because the new polarized neutron monochromator and analyzer have been recently installed in TAS-1³, we retry the investigation with the same sample and experimental conditions as the previous experiments².

Figure 1 shows the energy dependence of the SF scattering intensity and the NSF scattering intensity multiplied by 0.13 at $\mathbf{Q} = (1.5, 1.5, 1)$. The observed intensities in the present experiments are much larger than those in the previous experiments². At $\mathbf{Q} = (1.5, 1.5, 1)$, we can expect that the

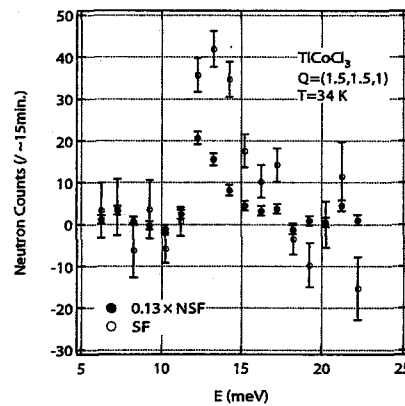


Figure 1: Energy dependence of SF intensity and NSF intensity multiplied by 0.13 at $\mathbf{Q} = (1.5, 1.5, 1)$. Both intensities are subtracted by background.

intensities corresponding to $S_{xx}(\mathbf{Q}, \omega)$ and $0.13S_{xx}(\mathbf{Q}, \omega) + 0.87S_{zz}(\mathbf{Q}, \omega)$ are observed for NSF and SF scatterings, respectively². We can see the difference between the SF scattering intensity and the NSF scattering intensity multiplied by 0.13 in Fig. 1, which is attributed to the $0.87S_{zz}(\mathbf{Q}, \omega)$. We compared the obtained intensities with those calculated by Ishimura and Shiba¹, and could conclude the existence of the weak longitudinal magnetic fluctuation $S_{zz}(\mathbf{Q}, \omega)$ and find a semi quantitative agreement between them. The details are presented in Ref. 4.

References

- 1) N. Ishimura and H. Shiba: "Progr. Theor. Phys", **63**, 743 (1980).
- 2) A. Oosawa *et al.*: "JAERI-Review", **45**, 92 (2005).
- 3) M. Takeda *et al.*: "JAERI-Review", **45**, 159 (2005).
- 4) A. Oosawa *et al.*: "J. Phys. Soc. Jpn.", **75**, 074719 (2006).

原子炉：JRR-3 装置：TAS-1(2G) 分野：中性子散乱 (磁性)

研究テーマ：偏極中性子散乱を用いた擬一次元イジング型反強磁性体 TlCoCl_3 及び関連物質の磁性の研究

表題：三次元偏極中性子解析による歪んだ三角格子イジング型反強磁性体 TlCoCl_3 の磁気構造の研究

1-2-2

Spherical Neutron Polarimetry Study of Magnetic Structure in Distorted-triangular-lattice Ising-like Antiferromagnet TlCoCl_3

A. Oosawa, K. Kakurai¹, M. Takeda¹, Y. Shimojo¹, Y. Nishiwaki² and T. Kato³

Department of Physics, Sophia University, 7-1 Kioi-cho, Chiyoda-ku, Tokyo 102-8554

¹*Quantum Beam Science Directorate, Japan Atomic Energy Agency, Tokai, Ibaraki 319-1195*

²*Department of Physics, Tokyo Institute of Technology, Oh-okayama, Meguro-ku, Tokyo 152-8551*

³*Faculty of Education, Chiba University, 1-33 Yayoi-cho, Inage-ku, Chiba 273-8522*

TlCoCl_3 has a CsNiCl_3 -type hexagonal crystal structure at room temperature, in which magnetic Ising Co ions form linear chains along the c -axis and these chains make a triangular lattice in the c -plane. From magnetization measurements, two anomalies were observed at $T_{N1}=29.5$ K and $T_{N2} = 15$ K¹). The magnetic Bragg reflections indicative of the *up-up-down-down*-type magnetic structure have been observed below T_{N1} at $Q = (\frac{h}{8}, \frac{h}{8}, l)$ with odd h and odd l , while no changes of the magnetic Bragg reflections were observed at T_{N2} by means of the neutron diffraction measurements²). Recently, it was suggested that the ordering of weak transverse magnetic moments may occur at T_{N2} . Such weak ordered moments can be hardly detected in diffraction measurements. In order to detect the weak ordered moments, we performed spherical neutron polarimetry experiments using CRYOPAD on TAS-1³).

The scattering plane is (h, h, l) in the present experiments so that the z -direction is perpendicular to c -axis. $P_{yy} \cong -P_{zz} \cong -P_{xx}$ indicates that there is large ordered moments along the c -axis. When the ordering of weak transverse magnetic moments occurs together with the large moments along the c -axis, we can expect that the polarizations P_{yz} and P_{zy} also become finite. As shown in Fig. 1, finite polarizations were observed for P_{yz} and P_{zy} . However, no magnetic structure with overall agreement of polarizations observed at various Q was found. Moreover, the finite polarizations for P_{yz} and P_{zy} were also observed at $T = 20$ K, which is above T_{N2} . The observed finite polarizations for P_{yz} and P_{zy} have to be investigated in more detail.

References

- 1) Y. Nishiwaki *et al.*: "J. Phys. Soc. Jpn.", **72**, 2608 (2003).
- 2) Y. Nishiwaki *et al.*: "J. Phys. Soc. Jpn.", **75**, 034707 (2006).
- 3) M. Takeda *et al.*: "Physica B", **356**, 136 (2005).

Figure 1 shows the summary of the spherical neutron polarimetry results of TlCoCl_3 .

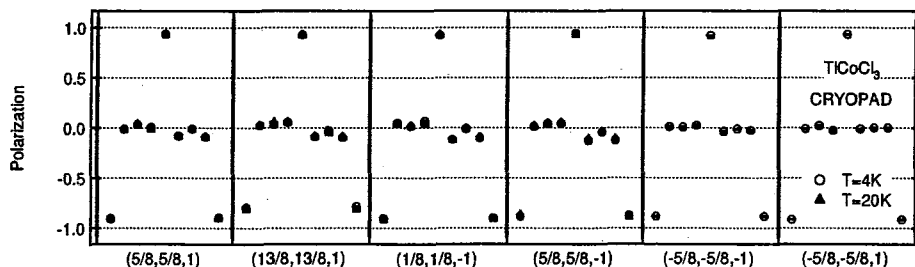


Figure 1: Summary of the spherical neutron polarimetry results of TlCoCl_3 . The open circles and full triangles denote the data at $T = 4$ and 20 K, respectively. The data points indicate the measured nine polarizations P_{xx} , P_{xy} , P_{xz} , P_{yx} , P_{yz} , P_{zx} , P_{zy} , P_{zz} for each magnetic Bragg reflections at $Q = (h, h, l)$.

原子炉：JRR-3 装置：TAS-1(2G) 分野：中性子散乱 (磁性)

研究テーマ：強誘電反強磁性物質 RMn_2O_5 (R:希土類) の高磁場下での磁気秩序
表題：マルチフェロイック物質 HoMn_2O_5 における磁場誘起格子整合スピン状態の観測

1-2-3

Magnetic-field Induced Commensurate Spin State in Multiferroic Compound of HoMn_2O_5

H. Kimura, Y. Kamada, Y. Noda, K. Kaneko¹, N. Metoki¹ and K. Kohn²

Institute of Multidisciplinary Research for Advanced Materials, Tohoku University, Sendai 980-8577

¹*Advanced Science Research Center, JAEA, Tokai, Ibaraki 319-1195*

²*Department of Physics, Waseda University, Tokyo 169-8555*

Recent discovery of a colossal magneto-electric (CME) effect in manganese oxides of RMnO_3 and RMn_2O_5 ($R = \text{rare earth elements}$)^{1,2)} opens a possibility of new candidates for multifunctional devices such as a magnetically controlled ferroelectric memory. These systems show a multiferroic behavior where an antiferromagnetic order and a ferroelectric order coexist, which might be relevance with the CME effect. However, microscopic mechanisms of the CME effect is not fully understood yet. We have conducted neutron diffraction measurements under high magnetic fields in the multiferroic HoMn_2O_5 and found unambiguous relation between the microscopic magnetism and the field-induced ferroelectricity.

Neutron diffraction measurements were performed using the thermal neutron triple-axis spectrometer TAS-2. The single crystal of HoMn_2O_5 was mounted on the $(h\ 0\ l)$ scattering plane with a vertical-field superconducting magnet, which results in applying a field up to 13 T along the b -axis. The incident and final energies of neutrons were fixed at 14.3 meV.

We have found in the present study that with applying the magnetic field, a first order phase transition from the incommensurate magnetic (ICM) order to the commensurate magnetic (CM) one occurs, where a spontaneous electric polarization arises³⁾. Figure 1 shows magnetic (H) – temperature (T) phase diagram for ICM and CM states in HoMn_2O_5 , obtained in the present study. In this figure,

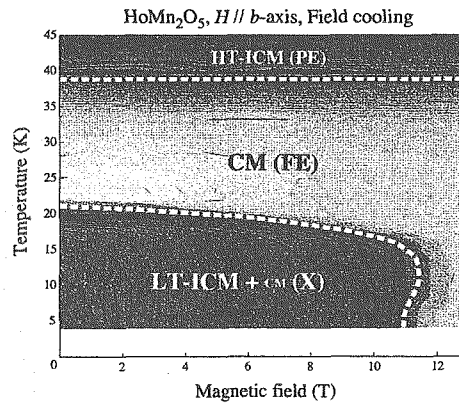


Figure 1: $H - T$ phase diagram for ICM and CM states in HoMn_2O_5 , shown as the contour map of intensity for ICM and CM magnetic signals. The dielectric phase diagram taken by Higashiyama *et al.*³⁾ is superposed in this figure.

$H - T$ phase diagram for dielectric property reported in Ref. 3) is superposed, showing that the ferroelectric (FE) state is only induced in the CM phase. This one to one correspondence between the magnetic phase diagram and the dielectric phase diagram under magnetic field clearly indicates that the electric polarization is magnetically induced and the commensurate magnetic structure is indispensable to the ferroelectricity in the multiferroic RMn_2O_5 system.

References

- 1) T. Kimura, *et al.*: "Nature (London)", **426**, 55 (2003).
- 2) N. Hur, *et al.*: "Nature (London)", **429**, 392 (2004).
- 3) D. Higashiyama, *et al.*: "Phys. Rev. B", **72**, 064421 (2005).

原子炉：JRR-3 装置：TAS-2(T2-4) 分野：中性子散乱（磁性）

研究テーマ：酸素欠損型 $\text{RBaCo}_2\text{O}_{5+\delta}$ ($\text{R}=\text{Nd}, \text{Tb}, \text{Ho}, \text{Y}$) の電荷秩序と磁気相転移
表題：階段状カゴメ格子系 $\text{Co}_3\text{V}_2\text{O}_8$ の磁気構造

1-2-4

Magnetic Structure of the Kagome Staircase Compound $\text{Co}_3\text{V}_2\text{O}_8$

Y. Yasui, Y. Kobayashi, M. Sato, N. Igawa¹ and K. Kakurai¹

Department of Physics, Nagoya University, Furo-cho, Chikusa-ku, Nagoya 464-8602

¹Quantum Beam Science Directorate, JAEA, Tokai, Ibaraki 319-1195

$\text{Co}_3\text{V}_2\text{O}_8$ is an insulating system with Co^{2+} ions (spin $S=3/2$) arranged in a kagome staircase or in a buckled kagome plane. It is interesting to investigate the magnetic behavior of this two-dimensional spin system at low temperature, because it has the geometrical frustration inherent in its crystal structure.

By measuring the magnetic susceptibility χ and specific heat C on single crystals of $\text{Co}_3\text{V}_2\text{O}_8$, three phase transitions have been found at $H=0$ and the transition temperatures are 11.2 K, 8.8 K, and 6.0-7.0 K. We call these temperatures T_{c1} , T_{c2} , and T_{c3} , respectively. At T_{c1} and T_{c2} , a small drop of χ with decreasing T and an anomaly in the C - T curve have been observed, indicating that the system undergoes the second order transition to antiferromagnetic phases. At T_{c3} , the system undergoes the first order transition to ferromagnetic phases with decreasing T . The occurrence of the successive transitions are considered to be due to the geometrical frustration. The iso-structural system $\text{Ni}_3\text{V}_2\text{O}_8$ has turned out to be multiferroic, *i.e.*, the phase is not only magnetically but also ferroelectrically-ordered.¹⁾ Because the origin of the appearance of the multiferroic phase is proposed in relation to the incommensurate magnetic structure,^{1,2)} it is expected that it exhibits the multiferroic phase transition for $\text{Co}_3\text{V}_2\text{O}_8$. Here, the magnetic structure of $\text{Co}_3\text{V}_2\text{O}_8$ has been investigated by powder neutron diffraction studies down to 2.7 K at the high resolution powder diffractometer (HRPD) of JRR-3 of JAERI in Tokai.

Neutron powder patterns were taken at 2.7 K, 7.0 K, 8.9 K and 30 K, where parts of

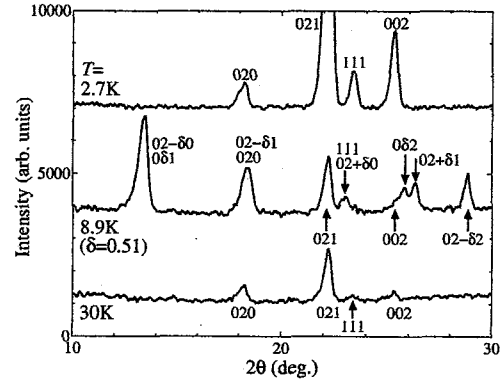


Figure 1: Neutron powder diffraction patterns of $\text{Co}_3\text{V}_2\text{O}_8$ at 2.7 K, 8.9 K and 30 K.

the obtained pattern are shown in Fig. 1. In the T -region of $T_{c3} \leq T \leq T_{c1}$, superlattice reflections $0k \pm \delta l$ ($k=\text{even}$) have been found, besides the fundamental ones. The magnetic structure seems to be spiral in the ac -plane. With decreasing T , δ (or periodicity of the spiral) changes from the incommensurate (IC) value to the commensurate ($=0.5$; C) one at T_{c2} . In the data at 2.7 K, all the superlattice reflections disappear and additional intensities at fundamental Bragg points appear. At 2.7 K, the Co moments have the collinear ferromagnetic structure parallel to the a -axis. These results indicate that the T -regions of $T < T_{c3}$, $T_{c3} < T < T_{c2}$ and $T_{c2} < T < T_{c1}$ correspond to the ferromagnetic, antiferromagnetic C- and antiferromagnetic IC- phases, respectively.

References

- 1) G. Lawes *et al.*: "Phys. Rev. Lett", **95**, 087205 (2005).
- 2) M. Mosotovy: "Phys. Rev. Lett", **96**, 067601(2006).

原子炉：JRR-3 装置：HRPD(1G) 分野：中性子散乱 (磁性)

研究テーマ：フラストレートした量子スピン系 $\text{Hg}_2\text{Cu}_2\text{F}_6\text{X}$ ($\text{X}=\text{O}, \text{S}$) の磁氣的挙動
 表題： $s=1/2$ スピン系を持つパイロクロア型化合物 $\text{Hg}_2\text{Cu}_2\text{F}_6\text{S}$ の磁氣的挙動

1-2-5

Magnetic Behavior of Frustrated $s=1/2$ System of the Pyrochlore Lattice $\text{Hg}_2\text{Cu}_2\text{F}_6\text{S}$

S. Kawabata, Y. Yasui, Y. Kobayashi, M. Sato, N. Igawa¹ and K. Kakurai¹

Department of Physics, Nagoya University, Furo-cho, Chikusa-ku, Nagoya 464-8602

¹Quantum Beam Science Directorate, JAEA, Tokai, Ibaraki 319-1195

Pyrochlore oxides $\text{A}_2\text{B}_2\text{O}_6\text{O}'$ have the *fcc* structure with the space group $Fd\bar{3}m$, in which two individual 3-dimensional networks of corner-sharing A_4 or B_4 tetrahedra are formed. Because these networks can be considered to be the 3-dimensional version of the triangular lattice, effects of the strong magnetic frustration are expected, if spins with the antiferromagnetic nearest neighbor interaction exist at the corners of the tetrahedra. However, there have not ever been found ideal pyrochlore compounds for the study of the frustrate quantum spin ($s=1/2$) systems. We have prepared iso-structural system $\text{Hg}_2\text{Cu}_2\text{F}_6\text{S}$ which has Cu^{2+} ions with $s=1/2$ ($3d^9$). Polycrystalline samples of $\text{Hg}_2\text{Cu}_2\text{F}_6\text{S}$ were prepared by a solid reaction in a similar manner to that described in Ref. 1. They were checked by X-ray measurements, where no impurity peaks were detected. In order to obtain the magnetic and structural information at low temperatures, we have carried out the powder neutron diffraction studies down to 2.4 K at the high resolution powder diffractometer (HRPD) of JRR-3 of JAERI in Tokai. Rietveld analyses were carried out by using the computer program Rietan 2000.

The magnetic susceptibility χ exhibits Curie-Weiss-like behavior with Weiss temperature $\theta \sim 100$ K in the high temperature (T) region, which indicates that the exchange interaction among Cu spins is antiferromagnetic. In the low T region, χ exhibits a rather rapid increase with decreasing T . From the specific heat data, we have found no experimental indication of a structural and/or mag-

netic phase transition(s) down to 3 K much lower than θ . By the powder neutron Rietveld analysis, we have found followings. Hg and Cu sites seem to have no defect, whereas F and S sites may have slight amounts of defects. The Debye-Waller factors seem to be slightly larger than those of other pyrochlore compounds. No indication of the structural change and magnetic phase transition has been found down to 2.4 K, which indicates that the geometrical frustration is not released down to the lowest temperature studied.

To extract microscopic information, we have also carried out ^{19}F -NMR. The Knight shift ^{19}K increases slightly with decreasing T from room temperature and then decreases after having a broad maximum at around 100 K, as the short-range spin correlation grows. The different T -dependences between χ and ^{19}K indicate that the χ -increase observed with decreasing T in the low T region is not intrinsic. The frustrated $s=1/2$ pyrochlore system $\text{Hg}_2\text{Cu}_2\text{F}_6\text{S}$ has been studied by the neutron diffraction and ^{19}F -NMR and measurements of the magnetic susceptibility χ and specific heat C . No indication of magnetic phase transitions and structural distortions has been observed down to 2.4 K much lower than the Weiss temperature θ (~ 100 K). It seems to be important to prepare clean samples for the accumulation of ideal behaviors of this geometrically frustrated spin system.

References

- 1) D. Bernard, J. Pannetier and J. Lucas : "J. Solid State Chem.", **14**, 328 (1975).

原子炉：JRR-3 装置：HRPD(1G) 分野：中性子散乱 (磁性)

研究テーマ：新超伝導物質 $\text{Na}_x\text{CoO}_2 \cdot y\text{D}_2\text{O}$ の磁気励起スペクトル
 表題：中性子散乱による $\text{Na}_x\text{CoO}_2 \cdot y\text{D}_2\text{O}$ の磁気揺らぎ探索

1-2-6

Search for Magnetic Fluctuations in $\text{Na}_x\text{CoO}_2 \cdot y\text{H}_2\text{O}$ by Neutron Scattering

T. Moyoshi, M. Soda, Y. Yasui, M. Sato, and K. Kakurai¹

Department of Physics, Nagoya University, Chikusa-ku, Nagoya 464-8602

¹*Quantum Beam Science Directorate, JAEA, Tokai, Ibaraki 319-1195*

$\text{Na}_{1.3}\text{CoO}_2 \cdot 1.3\text{H}_2\text{O}$ exhibits the superconducting transition at 4.5K.¹⁾ Because the strong magnetic fluctuation expected for correlated electrons on the 2-dimensional triangular lattice may play an important role in realizing superconductivity, the system, which may have such electrons attracts much interest.

In the present work, neutron scattering studies have been carried out on aligned single crystals of $\text{Na}_x\text{CoO}_2 \cdot y\text{D}_2\text{O}$ containing bi-layer ($y \sim 1.3$), monolayer ($y \sim 0.6$) and non-deuterated ($x \sim 0.44$) phases. The volume fractions of systems were estimated to be 64, 10 and 26%. Neutron measurements were carried out using the spectrometer TAS-1 with the triple-axis condition installed at JRR-3 of JAEA in Tokai. The [110] and [001] axes were aligned in the scattering plane.

The data taken at 5.5 K by scanning along $(1/2, 1/2, l)$ with $\Delta E=2.5$ meV show a very weak modulation, which has a periodicity of c^* of the non-deuterated parts. It becomes maximum at points with odd l 's and minimum at even l 's, indicating that the magnetic correlation in the non-deuterated parts is antiferromagnetic both in-plane and inter-plane directions. The scattering intensity obtained by the elastic scan along $(1/2, 1/2, l)$ exhibits a modulation with a periodicity of c^* of the bi-layer system. It can be understood as the D_2O short-range order. (Analyses of the D_2O short-range order are discussed in ref. 2.) By the h -scans along (h, h, l) at fixed l 's for $\Delta E=2.5$ meV at 5.5 and 50 K, we have found two peaks around $h=1/2$ and these peaks spread widely along l and pre-

vent us from searching antiferromagnetic fluctuations by the h -scans.

Then, we have carried out h -scans along $(h, h, 2.4)$ at 5.5, 50 and 100 K, where a peak has been observed at $h \sim 0$. It seemed, at first sight, to be due to the in-plane ferromagnetic fluctuations. However, both the width and height of the peak remain constant with increasing T at least up to 100 K. It indicates, for the following reasons, that the peak is not magnetic. If it is magnetic, the T -independent behavior of the integrated intensity should be understood by the cancellation of the increasing Bose factor and the decreasing spectral weight $\chi''(\mathbf{Q}, \omega=\Delta E)$. Therefore, with increasing T from 5.5 K to 100 K, $\chi''(\mathbf{Q}, \omega=2.5$ meV) have to be changed by a factor of 4, indicating that the magnetic correlation are changing rather drastically with T . However, we have not observed the appreciable change of the profile width, even though the resolution width is much smaller than the observed peak width. This probably excludes the possibility that the peak has a magnetic origin.

The present results indicate that magnetic fluctuations are rather weak in $\text{Na}_x\text{CoO}_2 \cdot y\text{D}_2\text{O}$ which exhibits superconducting transition, if any. It can be said especially for ferromagnetic fluctuations. For a much more quantitative estimation of the strength of the magnetic fluctuations in $\text{Na}_x\text{CoO}_2 \cdot y\text{D}_2\text{O}$, further studies have to be carried out.

References

- 1) K. Takada *et al.*: "Nature", **422**, 53 (2003).
- 2) T. Moyoshi *et al.*: "J. Phys. Soc. Jpn.", **75**, 074705 (2006).

原子炉：JRR-3 装置：TAS-1(2G) 分野：中性子散乱 (磁性)

研究テーマ：酸素欠損型 $\text{RBaCo}_2\text{O}_{5+\delta}$ ($\text{R}=\text{Nd}, \text{Tb}, \text{Ho}, \text{Y}$) の電荷秩序と磁気相転移
表題：カゴメ格子と三角格子を持つ YBaCo_4O_7 の磁気構造

1-2-7

Magnetic Structure of YBaCo_4O_7 with Kagome and Triangular Lattice

M. Soda, Y. Yasui, M. Moyoshi, M. Sato, N. Igawa¹ and K. Kakurai¹

Department of Physics, Nagoya University, Furo-cho, Chikusa-ku, Nagoya 464-8602

¹Quantum Beam Science Directorate, JAEA, Tokai, Ibaraki 319-1195

RBaCo_4O_7 ($\text{R}=\text{Ca}, \text{Y}$ and rare earth elements) with the alternating stack of the kagome and triangular lattices of CoO_4 tetrahedra along the c -axis presents us an opportunity to study a question how the magnetic correlation grows in this geometrically frustrated system with decreasing temperature T .^{1,2)}

In the neutron diffraction studies on a single crystal of YBaCo_4O_7 , superlattice reflections have been observed at Q -points $(h'/2, 0, l')$ and $(h'/2, h'/2, l')$ (Q -group A), $(h''/3, h''/3, l'')$ ($l''=\text{odd}$; Q -group B_1) and $(h''/3, h''/3, l'')$ ($l''=\text{even}$; Q -group B_2) in the reciprocal space of the hexagonal unit cell ($a=b \sim 6.2982 \text{ \AA}$, $c \sim 10.2467 \text{ \AA}$) at low T ($\sim 10 \text{ K}$).

The reflections at Q -group A appear at $T_{c2} \sim 105 \text{ K}$ with decreasing T and their profiles consist of two components, (narrow) Gaussian and (broad) Lorentzian ones. The reflections at Q -group B_1 , which have only the Gaussian component, are observed below $T_{c1} \sim 70 \text{ K}$. The reflections at Q -group B_2 have only the Lorentzian component in the region $T_{c1} < T < T_{c2}$ and the Gaussian component appears at T_{c1} with decreasing T .

From the $|Q|$ -dependence of the integrated intensities, the Gaussian and Lorentzian components can be regarded to have nuclear and magnetic origins, respectively. In the present studies and the detail structural analyses using the high resolution powder diffractometer HRPD, we have found that the Gaussian components at Q -group A and at Q -group B_1 and B_2 are associated with the distortions of the kagome and triangular lattices, respectively.

The Lorentzian (magnetic) components of

the reflections at Q -group A and B_2 begin to grow gradually at around T_{c2} with decreasing T . These reflections do not grow up to sharp Bragg reflections even at T_{c1} . Even at 10 K , the correlation lengths estimated by using the widths of the Lorentzian profiles at both Q -group A and B_2 are $\sim 150 \text{ \AA}$.

With decreasing T , the structural transition at T_{c2} is expected to release, more or less, the geometrical frustration through the distortions of the triangles and enhances the magnetic correlation. The structural transition at T_{c1} is also expected to enhance, with decreasing T , the growth rate of the magnetic short-range order. The existence of the correlated behaviors between the occurrence of the structural transitions and the growths of the magnetic reflections with the Lorentzian shape suggests that couplings of the lattice distortions with the magnetic correlation are important in the present system.

At 10 K , the patterns of the magnetic short-range order have been determined for both sites of the kagome and triangular lattices. In the present analyses, a model is used, where the Lorentzian components at Q -group A and B_2 can be considered as the contributions from the moments on the kagome and triangular lattices, respectively. We have found that the moments on the triangular lattice have the 120° structure and that the structure of the kagome lattice is closely related with the 120° structure at 10 K .

References

- 1) M. Valldor, *et al.*: "Solid State Sci.", **4**, 923 (2002).
- 2) M. Soda, *et al.*: "J. Phys. Soc. Jpn.", **75**, 054707 (2006).

原子炉：JRR-3 装置：TAS-1(2G) 分野：中性子散乱 (磁性)

研究テーマ：スピンギャップ磁性体及びフラストレート磁性体の素励起と相転移
表題：KCuCl₃ の高圧下における磁気構造の決定

1-2-8

Determination of Magnetic Structure under High Pressure in KCuCl₃

K. Goto, M. Fujisawa¹, A. Oosawa², T. Osakabe³, K. Kakurai³ and H. Tanaka

Department of Physics, Tokyo Institute of Technology, Meguro-ku, Tokyo 152-8550

¹*Department of Physics, Kobe University, Kobe, Hyogo 657-8501*

²*Department of Physics, Sophia University, Chiyoda-ku, Tokyo 102-8554*

³*Quantum Beam Science Directorate, JAEA, Tokai, Ibaraki 319-1195*

Recently, it has been observed that the spin gap in TlCuCl₃ collapses under applied hydrostatic pressure, so that this system undergoes quantum phase transition (QPT) from a gapped singlet state to an antiferromagnetic state at a critical pressure P_c .¹⁻⁴ This study is concerned with a pressure-induced QPT in KCuCl₃, which is a three-dimensionally coupled spin dimer system with a gapped ground state and has the same crystal structure as TlCuCl₃. We have performed magnetization measurements on KCuCl₃ up to 10 kbar applied pressure, and the pressure dependence of the gap up to $P_c = 8.2$ kbar was obtained. To investigate the antiferromagnetic ordered state for $P > P_c$, we performed neutron elastic scattering experiments on KCuCl₃ under hydrostatic pressure.

The sample of single KCuCl₃ crystal with volume of $\sim 0.2\text{cm}^3$ was set in a McWhan-type high pressure cell.⁵ A mixture of Fluorinert FC70 and FC77 was used as pressure transmitting medium. The hydrostatic pressures $P = 11, 14,$ and 21 kbar were applied at helium temperatures. The pressure was determined from the pressure dependence of the lattice constant of NaCl crystal placed in the sample space. Neutron elastic scattering measurements were performed using the TAS-1 spectrometer installed at JRR-3 in JAEA, Tokai. The sample was mounted in the cryostat with its a^* - and c^* -axes in the scattering plane.

Above P_c , Bragg reflections indicative of antiferromagnetic ordering were observed at $Q = (h, 0, l)$ with the integer h and odd l , which are equivalent to those reciprocal points where we observe the lowest magnetic excitation at ambient pressure. This confirms that the pressure-induced magnetic ordering

observed arises from the closing of the spin gap energy. The magnetic structures, very similar to those of the pressure induced magnetic ordering in TlCuCl₃, were determined and the pressure dependence of the transition temperature was obtained (for details see Ref.6). The transition temperature increased with increasing pressure as shown in Fig.1.

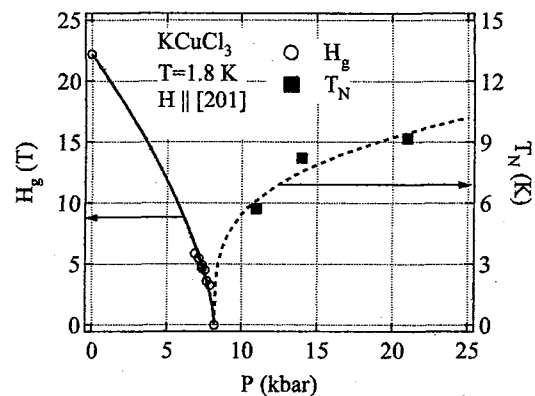


Figure 1: Pressure dependence of critical field H_g and critical temperature T_N .

References

- 1) K. Goto, M. Fujisawa, T. Ono, H. Tanaka and Y. Uwatoko: "J. Phys. Soc. Jpn.", **73**, 3254 (2004).
- 2) A. Oosawa, M. Fujisawa, T. Osakabe, K. Kakurai and H. Tanaka: "J. Phys. Soc. Jpn.", **72**, 1026 (2003).
- 3) A. Oosawa, K. Kakurai, T. Osakabe, M. Nakamura, M. Takeda and H. Tanaka: "J. Phys. Soc. Jpn.", **73**, 1446 (2004).
- 4) Ch. Rüegg, A. Furrer, D. Sheptyakov, Th. Strässle, K. W. Krämer, H. -U. Güdel and L. Mélési: "Phys. Rev. Lett.", **93**, 257201 (2004).
- 5) D. B. McWhan, C. Vettier, R. Youngblood and G. Shirane: "Phys. Rev. B", **20**, 4612 (1979).
- 6) K. Goto, M. Fujisawa, H. Tanaka, Y. Uwatoko, A. Oosawa, T. Osakabe, and K. Kakurai: "J. Phys. Soc. Jpn.", **75**, 064703 (2006).

原子炉：JRR-3 装置：TAS-1(2G) 分野：中性子散乱（磁性）

研究テーマ : $\text{Fe}_2\text{Cu}_2\text{Ge}_4\text{O}_{13}$ における磁気励起
表題 : $\text{Fe}_2\text{Cu}_2\text{Ge}_4\text{O}_{13}$ における磁気励起

1-2-9

Magnetic Excitations in $\text{Cu}_2\text{Fe}_2\text{Ge}_4\text{O}_{13}$ T. Masuda, K. Kakurai¹ and M. Matsuda¹

International Graduate Schools of Arts and Sciences, Yokohama City University

¹Quantum Beam Science Directorate, JAEA, Tokai, Ibaraki 319-1195

$\text{Cu}_2\text{Fe}_2\text{Ge}_4\text{O}_{13}$ is known for weakly coupled spin chains and dimers compound¹⁾. In the cooperative ground state the Cu^{2+} dimers are strongly bound to singlet ground state and disordered by quantum fluctuation. In addition the magnetic staggered field is applied by the neighboring Fe ions. Therefore this material is rare experimental realization of $S = 1/2$ spin dimers model in the staggered field.

The material includes two subsystems: Fe chains and Cu dimers. The energy scales are well separated. The excitations up to 10 meV is explained by effectively coupled Fe chains. On the other hand, narrow band excitation that could be ascribed to Cu dimers was observed by using powder sample²⁾. In this note we report the observation of Cu dimers mode by using single crystal.

As is shown in Fig. 1 well defined sharp peaks are observed at $\hbar\omega \sim 25$ meV where the scattering vector is $(h 0 1.65)$. The intensity dramatically changes with q . The peak position is almost the same for all scans. The narrow band excitation suggests that the peak is due to Cu dimers. Indeed the energy scale is consistent with previous study on powder sample²⁾. Figure 2 shows constant energy scan at $\hbar\omega = 26.3$ meV. Enhanced modulation is observed in wide q range. The data is well reproduced by spin dimers model assumed from crystallographical consideration (solid line).

References

- 1) T. Masuda *et al.*, "Phys. Rev. Lett.", **93**, pp. 077202 (2004).
- 2) T. Masuda *et al.*, "Phys. Rev. B.", **72**, pp. 094434 (2005).

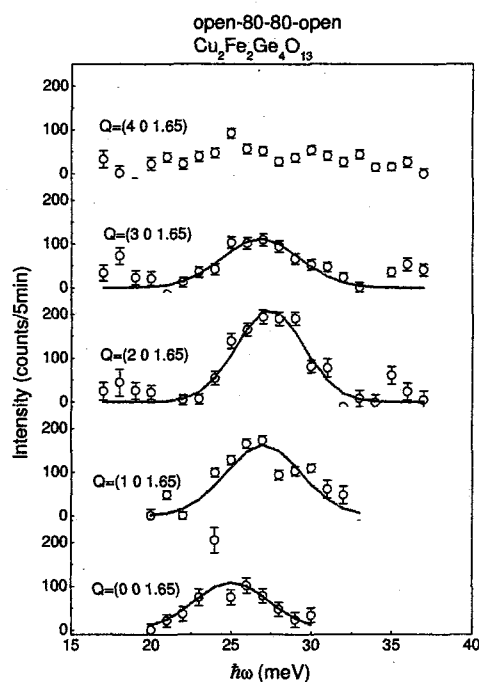
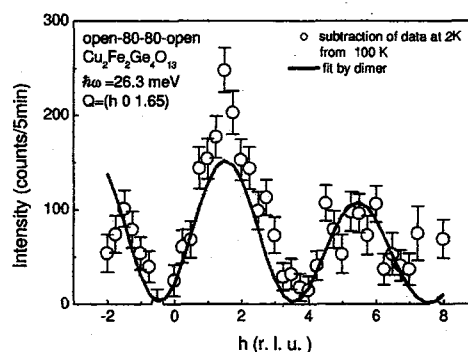
Figure 1: Constant q scans in $\text{Cu}_2\text{Fe}_2\text{Ge}_4\text{O}_{13}$.

Figure 2: Intensity modulation.

原子炉 : JRR-3 装置 : TAS-1(2G) 分野 : 中性子散乱 (磁性)

研究テーマ：幾何学フラストレーション系 RB_4 での磁性

表題：Shastry-Sutherland 型フラストレーション系 ErB_4 での磁場中磁気構造

1-2-10

Magnetic Structure of Shastry-Sutherland Type Frustration System ErB_4 under Magnetic Fields

K. Ohoyama, F. Iga¹, N. Katoh, S. Katano² and S. Michimura¹

Institute for Materials Research Tohoku Univ. Sendai 980-8577

¹*Advanced Science Research Center, JAEA, Tokai, Ibaraki 319-1195*

²*Graduate School of Advanced Sciences of Matter, Hiroshima Univ. Hiroshima, 739-8530*

Geometrical spin frustration causes various anomalous magnetic behaviour. RB_4 (R: rare earth) system, which has the tetragonal ThB_4 type structure, attracts our interests recently because the arrangement of rare earth atoms in the c-plane can be treated as a Shastry-Sutherland lattice¹⁾, in which spin frustration between R-R dimers is caused. ErB_4 is a simple antiferromagnet ($T_N = 15.4\text{K}$) under zero magnetic field;²⁾ the magnetic moments, which are parallel to the c-axis, has the $++-$ type alignment with $k=(1,0,0)$.³⁾ Recently, Michimura *et al.* reported that ErB_4 shows some anomalous behaviour in magnetisation: (1) 1/2 plateau of $M-H$ for $H//[001]$, (2) the complicated $M-T$ phase diagram for $H//[110]$.⁴⁾

To determine magnetic structures in each phase in ErB_4 , we performed neutron diffraction experiments under magnetic field on the triple axis spectrometer, TAS-2, of JAEA. Magnetic field was applied along $[001]$ and $[110]$ directions with a He free 10T superconducting magnet developed by JAEA.

We observed magnetic reflection at 3 T at 4.7K where the 1/2 plateau was observed; all the observed magnetic reflections can be indexed with $k=(1,0,0)$, which is the same as that below $H=2\text{T}$. This directly indicates that the magnetic unit cell in the 1/2 plateau phase is the same as the crystal unit cell; therefore, the 1/2 plateau is caused by flip of one magnetic moments which is antiparallel to the magnetic field below $H=2\text{T}$. However, the intensity of the mag-

netic reflections can not be represented by any spin flip models. Figure 1 shows the temperature dependence of the magnetic reflections of (100), (010) and (110) for $H//[001]$. As shown in Fig.1, the intensity changes at $H=2\text{T}$, and rapidly decreases above 4 T. Note that anomalous enhancement were observed at $H=2\text{T}$. A possible reason of the anomalous enhancement fields is extinction effect of the single crystal, which may be suppressed by spin fluctuation around the transition points. Magnetic structure refinement is in progress.

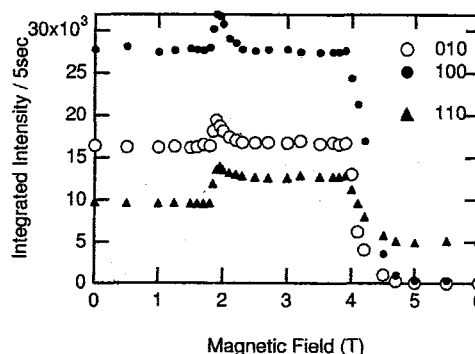


Figure 1: Magnetic field dependence of magnetic reflections of ErB_4 at $T=4.7\text{K}$ for $H//[001]$.

References

- 1) B. S. Shastry and B. Sutherland : "Physica B", **108**, 1069 (1981).
- 2) Z. Fisk, *et al.*: "Solid State Commu.", **39**, 1189 (1981).
- 3) G. Will, *et al.*: "J. Less Common Met.", **82**, 349 (1981).
- 4) S. Michimura, *et al.*: "Proc. of the 60th Annual Meeting of JPSJ", 25aPS-83 (2005).

原子炉：JRR-3 装置：TAS-2(T2-4) 分野：中性子散乱 (磁性)

研究テーマ : $\text{Fe}_2\text{Cu}_2\text{Ge}_4\text{O}_{13}$ における磁気励起
表題 : $\text{Fe}_2\text{Cu}_2\text{Ge}_4\text{O}_{13}$ における磁気励起

1-2-11

Magnetic Excitations in $\text{Cu}_2\text{Fe}_2\text{Ge}_4\text{O}_{13}$ II

T. Masuda, K. Kakurai¹, M. Matsuda¹, K. Kaneko², and N. Metoki²

International Graduate Schools of Arts and Sciences, Yokohama City University

¹Quantum Beam Science Directorate, JAEA, Tokai, Ibaraki 319-1195

²Advanced Science Research Center, JAEA, Tokai, Ibaraki 319-1195

$\text{Cu}_2\text{Fe}_2\text{Ge}_4\text{O}_{13}$ is bicomponent compound that combines classical Fe^{3+} chains and quantum Cu^{2+} dimers¹⁾. As is shown in Fig. 1, crankshaft chains of Fe^{3+} ions run in b direction. Cu^{2+} dimers are located between Fe chains. The energy scale of chains and dimers are well separated. From neutron inelastic experiment, it is estimated that $J_{\text{Cu}} \sim 25$ meV, $J_{\text{Fe}} = 1.6$ meV, and $J'_{\text{Fe}} = 0.12$ meV²⁾. $J_{\text{Cu-Fe}}$ and J^{eff} are *indirectly* estimated to be small by neutron diffraction measurement. If the estimate is correct, the Cu dimers between Fe chains behave as media that transfer exchange integral and consequently the low energy excitation can be explained by effectively coupled Fe chains in a direction. To verify this scenario, we performed neutron inelastic scattering experiment to obtain the dispersion in a^* direction.

Figure 2 shows typical constant q scans. Well defined sharp peaks are observed. At AF zone center of $q = (2\ 1\ -0.5)$, anisotropy gap is observed at $\hbar\omega \sim 1$ meV. Two peaks at 1.0 meV and 2.4 meV is explained by the twinning of the crystal. As is reported in Ref. 2 two domains share a common $a^* - b^*$ plane. Peak at low energy is slightly wider than resolution limited. This can be explained by anisotropy in the exchange interaction. We assumed empirical neutron crosssection for effectively coupled chains in a direction and do the fitting by the model with resolution convolution (solid curves). Twinned crystal effect, anisotropy gap, and anisotropy exchange interaction are included. The calculation reproduce the data very well. Hence the disper-

sion in a^* direction is well explained by weakly coupled spin chains model.

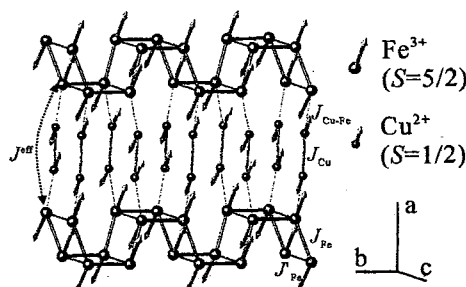


Figure 1: Crystal structure of $\text{Cu}_2\text{Fe}_2\text{Ge}_4\text{O}_{13}$.

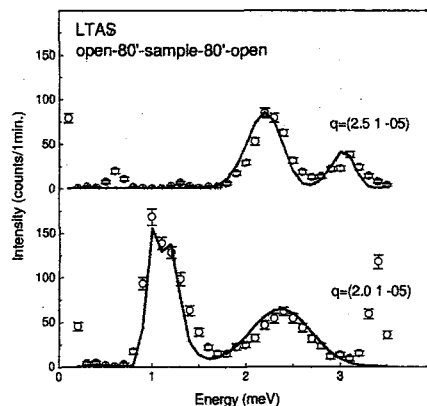


Figure 2: Constant q scans.

References

- 1) T. Masuda *et al.*, "Phys. Rev. Lett. ", **93**, pp. 077202 (2004).
- 2) T. Masuda *et al.*, "Phys. Rev. B. ", **72**, pp. 094434 (2005).

原子炉 : JRR-3 装置 : LTAS(C2-1) 分野 : 中性子散乱 (磁性)

研究テーマ：先端偏極中性子散乱によるスピン-格子物性の研究
表題：中性子回折法による α -Tb₂S₃ の逐次磁気相転移の研究

1-2-12

Successive Magnetic Phase Transitions in α -Tb₂S₃ Studied by Neutron Diffraction Technique

M. Matsuda, K. Kakurai, S. Ebisu¹ and S. Nagata¹

Quantum Beam Science Directorate, JAEA, Tokai, Ibaraki 319-1195

¹Department of Materials Science and Engineering, Muroran Institute of Technology,
27-1 Mizumoto-cho, Muroran, Hokkaido 050-8585

α -R₂S₃ (R=Gd, Tb and Dy) consists of a stacking of square lattice R1 and triangular lattice (TL) R2 planes.¹⁾ Matsuda *et al.* previously carried out a neutron diffraction study on a powder sample of α -Gd₂S₃, in which there is no orbital degree of freedom.²⁾ It was found that the magnetic structure is collinear with easy axis along the *b*-axis. The structure is unexpectedly simple in spite of the TL structure, which may cause frustrating interactions in the magnetic system.

Recently, macroscopic magnetic properties of α -Tb₂S₃ were investigated using single crystal.³⁾ It was reported that α -Tb₂S₃ shows anomalies in magnetic susceptibility at $T_{N1} \sim 13$ K and $T_{N2} \sim 4$ K, indicating successive magnetic phase transitions.³⁾ It was also found that the susceptibility is anisotropic ($\chi_{\parallel b} > \chi_{\perp b}$) above T_{N1} . Even below T_{N1} , the susceptibility is still highly anisotropic. $\chi_{\parallel b}$ decreases below $\sim T_{N1}$, while $\chi_{\perp b}$ keeps increasing without anomaly and finally decreases below $\sim T_{N2}$. This behavior is quite different from that in α -Gd₂S₃.

Neutron diffraction measurements on a powder sample of α -Tb₂S₃ were performed on TAS-1.⁴⁾ It was found that the Tb1 and Tb2 moments behave quite independently. The Tb1 moments show a collinear antiferromagnetic ordering at ~ 12 K with the magnetic unit cell same as the chemical one. On the other hand, the Tb2 moments start to order at ~ 3.5 K without affecting the magnetic order of the Tb1 moments. The magnetic structure is noncollinear with a magnetic unit cell

double of the chemical one along the *a*- and *c*-axes. The ordered moments of the Tb1 and Tb2 moments are $\sim 8\mu_B$, similar to the full moment for the free Tb³⁺ ion. These results indicate that the Tb1 and Tb2 moments are completely decoupled due to an orbital contribution, which probably gives rise to a non-collinear structure in the TL plane.

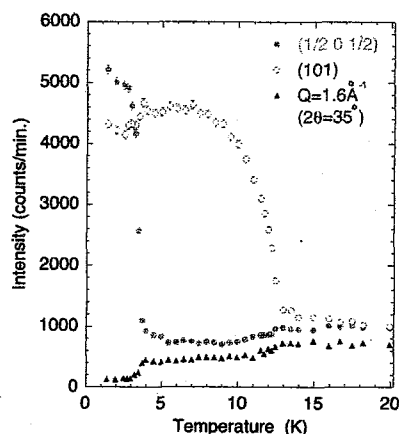


Figure 1: The temperature dependence of the peak intensities at the (1 0 1) and $(\frac{1}{2} 0 \frac{1}{2})$ magnetic reflections. The intensity, which mostly consists of a paramagnetic component, was also measured at $Q=1.6 \text{ \AA}^{-1}$.

References

- 1) S. Ebisu, Y. Iijima, T. Iwasa and S. Nagata: J. Phys. Chem. Solids **65**, 1113 (2004).
- 2) M. Matsuda, A. Kikkawa, K. Katsumata, S. Ebisu and S. Nagata: J. Phys. Soc. Jpn. **74**, 1412 (2005).
- 3) S. Ebisu, M. Gorai, K. Maekawa and S. Nagata: to be published in AIP Conf. Proceedings.
- 4) M. Matsuda, K. Kakurai, S. Ebisu and S. Nagata: J. Phys. Soc. Jpn. **75**, 074710 (2006).

原子炉：JRR-3 装置：TAS-1(2G) 分野：中性子散乱 (磁性)

研究テーマ：先端偏極中性子散乱によるスピン-格子物性の研究
表題： $\text{Na}_2\text{Co}_2(\text{C}_2\text{O}_4)_3(\text{H}_2\text{O})_2$ におけるダイマー状態の磁気励起

1-2-13

Magnetic Excitations from the Singlet Dimerized State in $\text{Na}_2\text{Co}_2(\text{C}_2\text{O}_4)_3(\text{H}_2\text{O})_2$

M. Matsuda, Z. Honda¹, S. Wakimoto, K. Kakurai and K. Yamada¹

Quantum Beam Science Directorate, JAEA, Tokai, Ibaraki 319-1195

¹Faculty of Engineering, Saitama University, Urawa, Saitama 338-8570

Low-dimensional spin system exhibits various interesting phenomena originating from quantum fluctuations. Magnetism of spin-ladder has attracted much attention because the spin-ladder is a system between one- and two-dimensional. ¹⁾ Interestingly, the ground state depends on the number of legs. The antiferromagnetic ladder with even numbers of legs shows a singlet ground state with a spin gap. On the other hand, the antiferromagnetic ladder with odd numbers of legs shows a gapless ground state.

Recently, macroscopic magnetic properties have been measured in $\text{Na}_2\text{Co}_2(\text{C}_2\text{O}_4)_3(\text{H}_2\text{O})_2$ (abbreviated to SCO, hereafter), which consists of two-leg ladders of Co^{2+} ions. ^{2,3)} It was reported that SCO can be well described as the fictitious 1/2 system with anisotropic g values and exchange interactions at low temperatures. Therefore, SCO is a model compound for the two-leg ladder with an Ising anisotropy. Susceptibility measurements show a broad maximum around 20 K and show an exponential decay down to ~ 5 K. Below ~ 5 K, the susceptibility is almost independent of temperature. No anomaly was observed in heat capacity measurements. In Ref. 2 the results were discussed in the context of the quantum phase transition. It was suggested that a magnetic ordering occurs because the inter-ladder coupling is slightly larger than the critical value in SCO.

In order to clarify the ground state in SCO, it is important to measure the magnetic properties from a microscopic point of view. We carried out neutron scattering experiments on

TAS-2 and LTAS using polycrystalline sample to study the magnetic correlations and the energy level scheme of the Co^{2+} moments. Since the excited state were found to be almost dispersionless, we could get useful information on the magnetic excitations even with the polycrystalline sample. Typical magnetic excitation spectra are shown in Fig. 1. We found that the system is well described by an almost isolated dimer model, in which dimers are formed between spins along the rung direction and the interaction along the rung direction is much larger than that along the leg direction. The intra-dimer coupling constant is determined to be 5.2 meV. Other interactions were found to be very small.

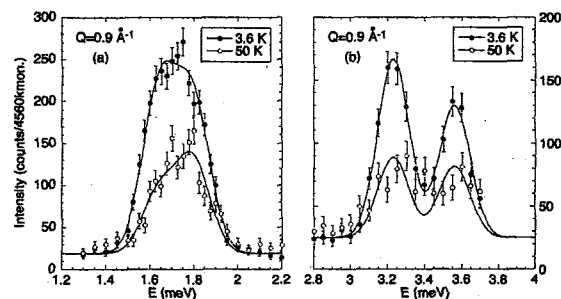


Figure 1: Magnetic excitation spectra in polycrystalline SCO measured on LTAS with $\Delta E \sim 0.2$ meV at $Q=0.9 \text{ \AA}^{-1}$ and at $T=3.6$ and 50 K.

References

- 1) For a review see E. Dagotto and T. M. Rice: Science **271**, 618 (1996).
- 2) Z. Honda, K. Katsumata, A. Kikkawa and K. Yamada: Phys. Rev. Lett. **95**, 087204 (2005).
- 3) D. J. Price, A. K. Powell and P. T. Wood: J. Chem. Soc. Dalton Trans. **2000**, 3566 (2000).

原子炉：JRR-3

装置：TAS-2(T2-4), LTAS(C2-1)

分野：中性子散乱 (磁性)

研究テーマ：先端偏極中性子散乱によるスピン格子物性の研究

表題：ハイゼンベルグパイロクロア反強磁性体 HgCr_2O_4 のプラトー状態における磁気構造

1-2-14

Magnetic Structure in the Half-magnetization Plateau State in a Heisenberg Pyrochlore Antiferromagnet HgCr_2O_4

M. Matsuda, H. Ueda¹, Y. Ueda¹ and S.-H. Lee²

Quantum Beam Science Directorate, JAEA, Tokai, Ibaraki 319-1195

¹Institute for Solid State Physics, The University of Tokyo, Kashiwa, Chiba 277-8581

²Department of Physics, University of Virginia, Charlottesville, Virginia 22904-4714, USA

Geometrically frustrated magnets exhibit interesting properties at low temperatures because of their macroscopic ground state degeneracies. Cr-based spinel compounds ACr_2O_4 ($A=\text{Mg, Zn, Cd}$ and Hg) are so far the best model systems for a network of corner-sharing tetrahedrons with isotropic nearest-neighbor antiferromagnetic interactions. The systems exhibit novel spin-Peierls-like phase transitions from cubic spin liquid to non-cubic Néel states at low temperatures. Recent bulk magnetization studies on CdCr_2O_4 and HgCr_2O_4 revealed the magnetic field-induced half magnetization plateau states that are stable over a wide range of field.^{1,2)} It was theoretically proposed that the plateau phase is induced by spin-lattice couplings.³⁾

We performed neutron diffraction measurements using a powder sample of HgCr_2O_4 on TAS-2 to determine magnetic structures both at ambient and high magnetic fields. The measurements in magnetic fields were performed up to 13.5 T using a new type of split-pair superconducting magnet cooled by cryocoolers. Upon cooling without field, HgCr_2O_4 undergoes an orthorhombic distortion with $Fddd$ symmetry at 6 K.²⁾ Elastic magnetic neutron scattering data obtained with zero field shows that in the low temperature orthorhombic phase the spins order long range with two characteristic magnetic wave vectors $\mathbf{Q}=(1/2, 0, 1)$ and $(1, 0, 0)$. Strikingly, above ~ 10 T the $\{1/2, 0, 1\}$ magnetic peaks that were present at $H=0$ have

completely disappeared, while the $\{1, 0, 0\}$ magnetic peaks became stronger, as shown in Fig. 1. Furthermore, new magnetic peaks appeared at several nuclear Bragg reflection points such as $(1, 1, 1)$, $(1, 3, 1)$, and $(2, 2, 2)$ but not at other nuclear Bragg reflection points such as $(2, 2, 0)$. From the magnetic structural analysis, it was found that a ferrimagnetic structure with a collinear three spin-up and one spin-down configuration of each Cr^{3+} tetrahedron is realized. Among possible structures, we determined one with $P4_332$ symmetry.

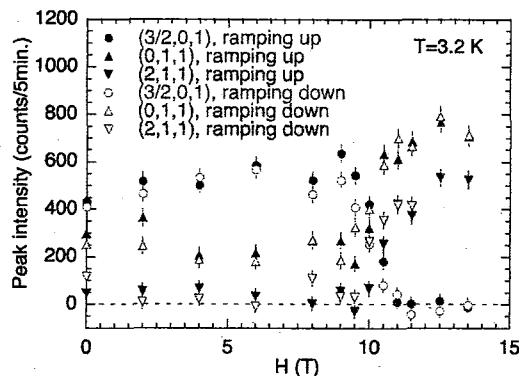


Figure 1: H -dependence of the neutron scattering intensities at $(3/2, 0, 1)$, $(0, 1, 1)$ and $(2, 1, 1)$ measured at 3.2 K.

References

- 1) H. Ueda, H. Mitamura, T. Goto and Y. Ueda: Phys. Rev. B **73**, 094415 (2006).
- 2) H. Ueda, H. Aruga-Katori, H. Mitamura, T. Goto and H. Takagi: Phys. Rev. Lett. **94**, 047202 (2005).
- 3) K. Penc, N. Shannon and H. Shiba: Phys. Rev. Lett. **93**, 197203 (2004).

原子炉：JRR-3 装置：TAS-2(T2-4) 分野：中性子散乱（磁性）

研究テーマ：集光型偏極中性子小角散乱法による遷移金属ナノ粒子内部の磁気構造の研究
表題：中性子小角散乱法による遷移金属ナノ粒子の磁気構造に関する研究

1-2-15

Small-angle Neutron Scattering Study of Magnetic Structure of Transition Metal Nanoparticles

T. Shinohara, Y. Oba¹, T. Sato¹, T. Oku and J. Suzuki

Quantum Beam Science Directorate, JAEA, Tokai, Ibaraki 319-1195

¹Department of Science and Technology, Keio University, Yokohama, Kanagawa 223-8522

The magnetic properties of nanoparticle system are significantly affected by the surface. Because a large number of atoms are located near the surface of a particle, changes in electronic and crystal structures occurred at the surface sometimes cause a different magnetic properties from the core of a particle. However, in many case, the details of intraparticle magnetic structure such as the thickness of surface magnetic layer or the magnetic volume of a nanoparticle is not clear, due to the difficulty in the direct observation. For the investigation of the magnetic structure, a neutron scattering experiment is most powerful method. Furthermore, small-angle neutron scattering (SANS) contains fruitful information of structures in the size between nano meter and micro meter, so that SANS measurement is very suitable to study the magnetic structure of nanoparticle. In this work, we performed SANS measurements of transition metal magnetic nanoparticles, to clarify the intraparticle magnetic structure.

SANS experiments were performed using a SANS spectrometer, SANS-J, of JRR-3 in JAEA. As the samples, we selected two metal nanoparticles, one is Pd nanoparticle¹⁾ and another is FePt nanoparticle²⁾, which is one of the most promising material for the ultra high-density recording media due to its strong magnetic anisotropy. Pd nanoparticles were confirmed to show the ferromagnetic properties by the magnetization measurements, and the magnetic ordering was believed to appear in the surface of a particle. From SANS measurements using unpolarized

neutron beam on Pd nanoparticle, we could not obtain the meaningful magnetic scattering intensity. This is because the sample condition was not good in addition to the very small intensity of the magnetic scattering relative to the nuclear scattering. Therefore, SANS experiments using polarized neutrons are in progress. Then, for FePt nanoparticle, the mean nanoparticle size of 6nm was derived from the q dependence of SANS intensity. The magnetic scattering contribution F_M^2 is 1/10 of nuclear scattering intensity F_N^2 (Fig. 1). Based on the chemical composition of nanoparticle sample and nuclear scattering length, the averaged magnetic moment of particle was estimated to be about $1.1 \mu_B/\text{atom}$.

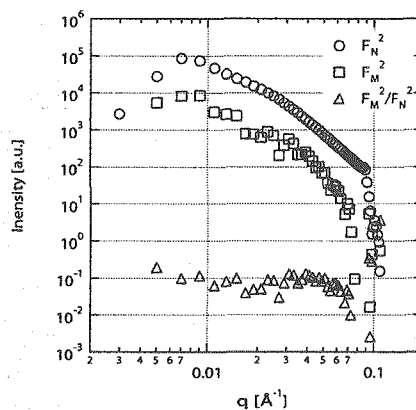


Figure 1: $I(q)$ profiles of FePt nanoparticles.

References

- 1) T. Shinohara, *et al.*: "Phys. Rev. Lett.", **91**, 197201 (2003).
- 2) H. Kura, *et al.*: "J. Appl. Phys.", **96**, 5771 (2004).

原子炉：JRR-3 装置：SANS-J(C3-2) 分野：中性子散乱（磁性）

研究テーマ：中性子利用実験装置の開発研究
表題：TbMnO₃の低エネルギー磁気励起

1-2-16

Low Energy Magnetic Excitation in TbMnO₃

R. Kajimoto, Y. Mitsui¹, H. Yoshizawa¹, H. Shintani², T. Kimura³ and Y. Tokura²

Quantum Beam Science Directorate, Japan Atomic Energy Agency, Tokai, Ibaraki 319-1195

¹Neutron Science Laboratory, ISSP, University of Tokyo, Tokai, Ibaraki 319-1106

²Department of Applied Physics, University of Tokyo, Bunkyo-ku, Tokyo 113-8656

³Bell Laboratories, Lucent Technologies, 600 Mountain Avenue, Murray Hill, NJ 07974, USA

TbMnO₃ shows a sinusoidal spin ordering with a characteristic wave vector $q_{\text{spin}} = 0.29b^*$ below $T_N = 42$ K. Below $T_C = 28$ K, the magnetic structure changes into an elliptically distorted spiral ordering with $q_{\text{spin}} = 0.28b^*$.¹⁾ Recently, this compound has much attention because the spontaneous ferroelectric polarization appears concomitantly with the appearance of the spiral spin ordering.²⁾ In our previous neutron scattering study using a thermal-neutron spectrometer, we have found that in TbMnO₃, a magnetic excitation exists over a whole Brillouin zone of the A-type antiferromagnetic spin ordering at 10 K ($< T_C$). Its dispersion relation can be well explained by a Heisenberg model with finite next-nearest-neighbor coupling except for a region around $q = q_{\text{spin}}$. There seemed to be a complicated structure in the excitation at $q \sim q_{\text{spin}}$, but we could not see its details because of the insufficient energy resolution.³⁾

In the present study, we have studied magnetic excitations at $q \sim q_{\text{spin}}$ using the cold-neutron triple-axis spectrometer LTAS to elucidate detailed structure of the excitation with a higher energy resolution. We have found an unusual magnetic excitation with three excitation branches at 10 K, as shown in Fig. 1. The branches with the highest energy smoothly increases its energy as q increases, and it extends to the zone boundary. On the other hand, the lower two branches have minimum energies at $q = q_{\text{spin}}$. They have appreciable intensities around $q = 0$ and $q = q_{\text{spin}}$, but they rapidly lose intensities

LTAS: $E_f=3.5\text{meV}$, G-M-open-80'-80'

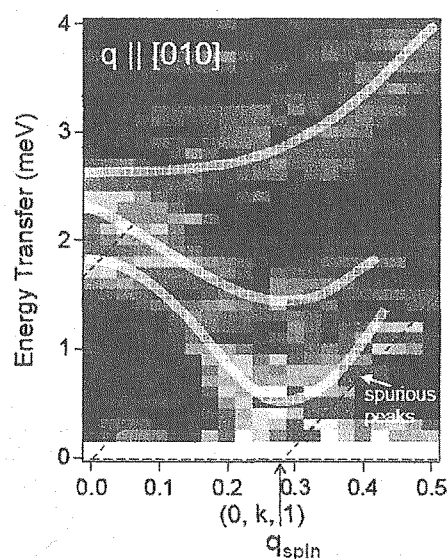


Figure 1: Intensity map on a q - ω plane with $q \parallel b^*$. Solid lines are guides to the eye.

as q gets away from q_{spin} . The origin of this unusual low energy excitation may be the peculiar magnetic structure of the elliptical spiral ordering. Alternatively, it may have some coupling with the local symmetry of the lattice that causes the electric polarization.

References

- 1) M. Kenzelmann *et al.*: "Phys. Rev. Lett.", **95**, 087206 (2005).
- 2) T. Kimura *et al.*: "Nature (London)", **426**, 55 (2003); "Phys. Rev. B", **71**, 224425 (2005).
- 3) R. Kajimoto *et al.*: "J. Phys. Soc. Jpn.", **74**, 2430 (2005).

原子炉：JRR-3 装置：LTAS(C2-1) 分野：中性子散乱（磁性）

研究テーマ：中性子利用実験装置の開発研究
表題：CuCr_{1-x}Mg_xO₂ の磁気構造

1-2-17

Magnetic Structure of CuCr_{1-x}Mg_xO₂

R. Kajimoto, M. Matsuda and T. Okuda¹

Quantum Beam Science Directorate, Japan Atomic Energy Agency, Tokai, Ibaraki 319-1195

¹Department of Nano-structures and Advanced Materials, Kagoshima University, Kagoshima 890-0065

CuCrO₂ has a delafossite structure, where Cr³⁺ ions form a triangular lattice. $S = 3/2$ spins of the Cr³⁺ ions form a 120° structure in the ac plane below $T_N = 26$ K.^{1,2)} By substitution of Cr³⁺ ions by Mg²⁺ ions (Cr_{1-x}Mg_x), holes are introduced. It was found recently that only a few percent of the Mg doping drastically decreases the resistivity.²⁾ Though T_N does not change by the doping, observation of a kink structure in the resistivity at T_N and that of a magnetoresistance effect below T_{cross} ($T_{\text{cross}} = 144$ K for $x = 0.03$) evidence the coupling between the doped holes and the spins of Cr ions. In the present study, we performed a neutron diffraction study on powder samples of CuCr_{1-x}Mg_xO₂ to see whether the magnetic structure is affected by the Mg doping. The measurement was performed using the triple-axis spectrometer TAS-2 with an incident energy $E_i = 14.7$ meV.

Figure 1 shows powder diffraction profiles of the $x = 0$ sample and the $x = 0.03$ sample measured at ~ 10 K. In $x = 0$, magnetic reflections are observed at the positions indicated by vertical bars. These positions are indexed as $\frac{1}{3}\frac{1}{3}l$ or $\frac{2}{3}\frac{2}{3}l$ with $l = \text{integer}$ reflecting the 120° magnetic structure as revealed by Kadowaki *et al.*¹⁾ In $x = 0.03$, we observed that the positions of the magnetic peaks are identical to those of $x = 0$. This indicates the size of the magnetic unit cell is identical for both samples. However, intensities of the magnetic peaks show considerable changes by the Mg doping. In $x = 0.03$, magnetic peaks with small l (e.g. $\frac{1}{3}\frac{1}{3}0$) lose intensity, while those with large l (e.g. $\frac{1}{3}\frac{1}{3}4$) gain intensity. This

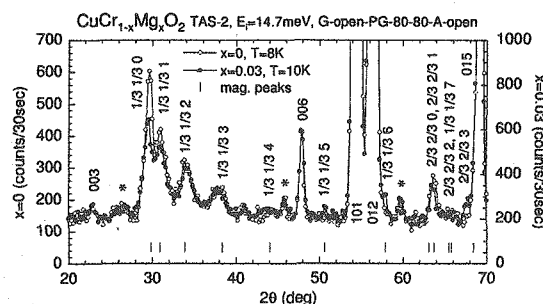


Figure 1: Powder diffraction profiles of CuCrO₂ (open symbols) and CuCr_{0.97}Mg_{0.03}O₂ (closed symbols) measured at ~ 10 K. Vertical bars indicate positions of magnetic reflections. Ranges of the ordinates are scaled so that the nuclear Bragg peaks (e.g. 006) of each sample superpose each other. Peaks with asterisks may be due to contaminations in the samples.

suggests that the Mg doping rotates the directions of the spins probably to the ab plane. We also measured the $x = 0.01$ sample, and the result is very similar to that of $x = 0.03$.

Present results indicate that the directions of Cr³⁺ spins in CuCr_{1-x}Mg_xO₂ are very susceptible to the Mg doping. One of the possible origins of the spin rotation is coupling between the doped holes and the spins. However, another role of the Mg doping is to introduce non-magnetic ions into the Cr sites. To clarify which is the origin of the spin rotation, a measurement with a sample doped by non-magnetic trivalent ions, such as Al³⁺, should be required.

References

- 1) H. Kadowaki *et al.*: "J. Phys.: Condens. Matter", **2**, 4485 (1990).
- 2) T. Okuda *et al.*, "Phys. Rev. B", **72**, 144403 (2005).

原子炉：JRR-3 装置：TAS-2(T2-4) 分野：中性子散乱（磁性）

研究テーマ：中性子小角散乱によるナノヘテロ構造を有する実用金属材料の微細構造の解明
 表題：偏極中性子小角散乱による高周波軟磁性材料 Co-Pd-Si-O グラニューラ膜の磁化過程

1-2-18

Magnetization Process of Co-Pd-Si-O Nanogranular Soft Magnetic Film Studied by Polarized Small-angle Neutron Scattering

M. Ohnuma, J. Suzuki¹ and S. Ohnuma²

Quantum beam center, NIMS, Tsukuba 305-0047

¹Quantum Beam Science Directorate, JAEA, Tokai 319-1195

²The Research Institute for Electric and Magnetic Materials, Sendai 982-0807

Metal-nonmetal nanogranular soft-magnetic film is one of the most promising soft-magnetic materials in high-frequency region due to their high- B_s , large electric resistivity and large induced magnetic anisotropy (H_k). The induced anisotropy is almost ten times larger than the one in conventional nanocrystalline soft magnetic materials (ex. FINEMET). Because it is difficult to explain such large anisotropy by well-known Neel-Taniguchi theory, some new mechanisms must be underlying in it. For making it clear, we are studying the response of magnetic domain structure in the field smaller than H_k using Po-SANS.

Pd chip were sputtered on the Si substrate in the Ar + O₂ atmosphere in the field of 0.01T¹⁾. Si is preferentially oxidized and forms amorphous oxide matrix. Remaining part forms Co(Pd) ferromagnetic particles which is embedded in amorphous oxide matrix. Chemical micro-structure were characterized by Mo-SAXS in NIMS. Using local-monodisperse hard sphere model²⁾, the average particle size is evaluated as $D=3.1$ nm. A minimum interparticle distance is almost same with the particle size, indicating that the magnetic particles contact each other. Therefore, the film shows soft-magnetic property because the magnetic coupling occurs by physical contacts and the magneto-crystalline anisotropy is averaged out.

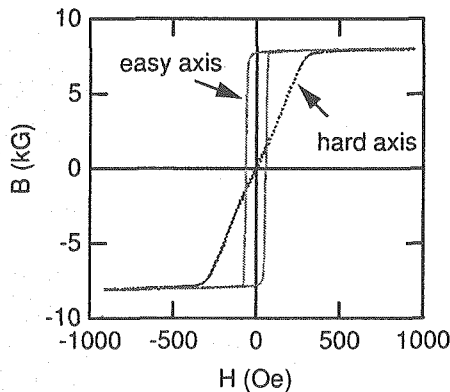


Figure 1: Magnetization curves of as-deposited Co₅₉Pd₁₁Si₈O₂₂ nanogranular films.

The composition of studied film is Co₅₉Pd₁₁Si₈O₂₂ which was made by the following way; The Co-Si alloy target with

Figure 1 shows magnetization curve of the as-deposited film. Although the H_k reaches about 240 Oe (= 24 mT), any indication of anisotropy in microstructure has been observed by SAXS. Therefore, the magnetic domain structure has been studied using Po-SANS to discuss the origin of the magnetic anisotropy. Figures 2 and 3 show the two dimensional scattering patterns measured in the field lower than H_k (0, 10 and 20 mT) in the q region of $0.1 \leq q \leq 1$ nm⁻¹ and the angular distribution of the intensity at $q = 0.12$ nm⁻¹, respectively. Because the easy axis was settled along the horizontal axis, the magnetization direction in zero field locates along the horizontal direction. Despite of this geometric condition, the strong

原子炉：JRR-3 装置：SANS-J(C3-2) 分野：中性子散乱（磁性）

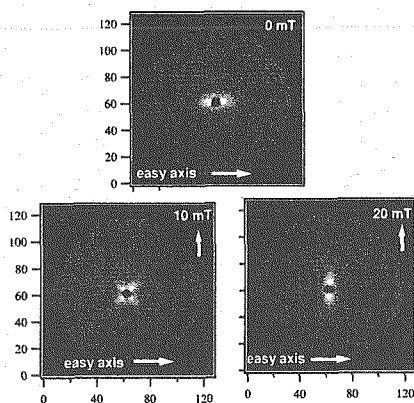


Figure 2: Two dimensional Po-SANS patterns of as-deposited $\text{Co}_{59}\text{Pd}_{11}\text{Si}_8\text{O}_{22}$ nanogranular films measured in the field of 0, 10 and 20 mT.

anisotropic scattering was observed parallel to the horizontal direction (Fig.2 and 3), which is unexpected from the normal relation between magnetization and scattering vector, q expressed as

$$I(q) = I_{\text{nuclear}}(q) + I_{\text{magnetic}}(q) \sin^2 \alpha \quad (\alpha: \text{angle between magnetization direction and } q).$$

When the magnetic field of 10 mT was applied to vertical direction, the intensity maxima split into two and aligned about 45° from horizontal direction. In the 20 mT, the intensity maxima converged into one but it arrayed along horizontal axis; again, parallel to the magnetization direction. These results indicate that the magnetic moment of each magnetic domain has two components; the major component is parallel to the magnetization direction and the minor component is aligned from 90° from the main one. The shape of these scattering patterns is independent of spin flipper conditions, possibly suggesting that the polarity of minor components is random and hence the total magnetization along this direction is zero. The anisotropic intensity became weak in 60 mT and disappeared in 0.6 T as shown in Fig. 2 and 3. They indicate that the

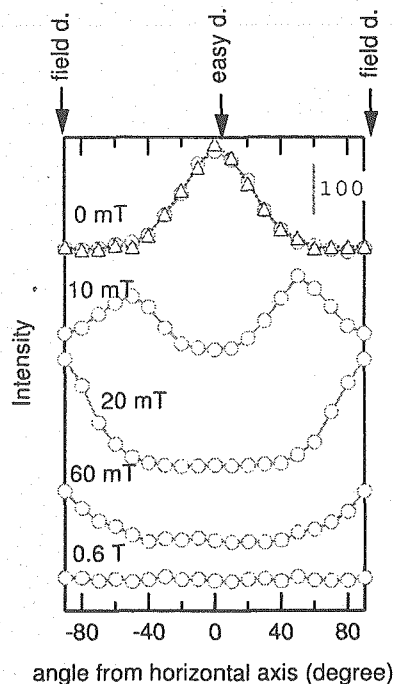


Figure 3: Angular distribution of the intensity at $q=0.12 \text{ nm}^{-1}$ of as-deposited $\text{Co}_{59}\text{Pd}_{11}\text{Si}_8\text{O}_{22}$ nanogranular films measured in the field of 0, 10 and 20 mT.

minor component is also ordered in the high field, which is normal behavior of the magnetization process.

As we described above, the behavior below H_k is quite complex and unusual which has not been reported before. Therefore, it can be related to the origin of the large H_k of the metal-nonmetal nanogranular soft-magnetic films. For confirming it, we are now studying the magnetization behavior below H_k for other soft-magnetic materials and granular films.

References

- 1) S. Ohnuma, H. Fujimori, S. Mitani and T. Masumoto : "J. Appl. Phys.", **79**, 5130 (1996).
- 2) J. S. Pedersen : "J. Appl. Cryst.", **27**, 595 (1994).

研究テーマ：先端偏極中性子散乱によるスピン-格子物性の研究

表題：高圧力下中性子回折による充填スクッテルダイト $\text{PrFe}_4\text{P}_{12}$ の研究

1-2-19

High-pressure Neutron Diffraction Study on the Filled Skutterudite $\text{PrFe}_4\text{P}_{12}$

T. Osakabe, D. Kawana¹ and K. Kuwahara¹

Quantum Beam Science Directorate, JAEA, Tokai, Ibaraki 319-1195

¹Tokyo Metropolitan Univ., Minami-Osawa, Hachioji, Tokyo 192-0397

Filled skutterudite compounds RT_4X_{12} (R = rare earth, T = transition metal, X = pnictogen) have attracted much attention because of their various physical properties such as magnetic ordering, multipolar ordering, heavy electron state, superconductivity and metal-insulator transition. One of these compounds, metallic $\text{PrFe}_4\text{P}_{12}$ shows a non-magnetic phase transition at $T_A = 6.5$ K at ambient pressure, which is thought to be caused by a multipolar ordering. Recent electrical resistivity measurements under pressure have revealed that T_A decreases gradually with increasing pressure up to 2.4 GPa. Above 2.4 GPa, the non-magnetic transition is completely suppressed and instead an insulator phase appears at low temperature¹⁾. In order to elucidate the order parameter of this pressure-induced insulating phase, we have performed high-pressure neutron diffraction experiments using the triple-axis spectrometer TAS-1 installed at 2G beam port of JRR-3 at JAEA in Tokai. The high-pressure was generated up to 3.2 GPa by a newly-developed hybrid-anvil device composed of a large sapphire anvil and a tungsten carbide anvil. The pressure transmitted by the glycerin medium was hydrostatic well above 3.0 GPa. The sample size was about $0.8 \times 0.6 \times 0.2$ mm³. The pressure was applied along the $[0,0,1]$ direction of the sample. As shown in Fig. 1, in spite of a small sample, we have successfully observed the distinct magnetic Bragg peak at $(1,0,0)$ reciprocal lattice point at 3.2 GPa in the insulating phase. The peak corresponds to an antiferromagnetic long-range ordering of $q = (1,0,0)$. The magnetic moments are 2.0

μ_B /Pr ions, which are align along the $[0,0,1]$ direction. The inset in the figure shows the temperature dependence of the $(1,0,0)$ magnetic intensity. From the figure, T_N is estimated to be 9 K at 3.2 GPa. This agrees well with the metal-insulator transition temperature T_{MI} ¹⁾. These result indicates that the insulating phase corresponds to the antiferromagnetically ordered phase and the 4f electronic states of Pr ions are magnetically degenerate in low energy region.

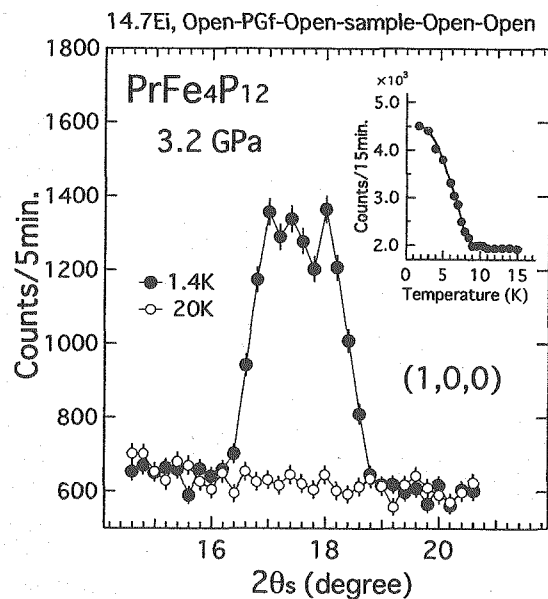


Figure 1: $(1,0,0)$ magnetic Bragg reflection at 3.2 GPa. The inset shows temperature dependence of the $(1,0,0)$ peak intensity.

References

- 1) H. Hidaka, I. Ando, H. Kotegawa, T. Kobayashi, H. Harima, M. Kobayashi, H. Sugawara and H. Sato: "Phys. Rev. B", **71**, 073102-1 - 4 (2005).

研究テーマ：中性子回折による六方晶 Ba フェライトの磁気構造とその温度依存性の研究
表題：Co₂Z 型六方晶フェライトの Ba-Sr 置換が磁気モーメントの方位やその温度依存性に与える効果

1-2-20

Effect of Substitution of Sr for Ba in Co₂Z-type Hexaferrite on Magnetic Moment Orientation and Its Temperature Dependence

Y. Takada, T. Nakagawa, M. Tokunaga, T. Tanaka, T. A. Yamamoto, T. Tachibana¹,
S. Kawano², Y. Ishii³ and N. Igawa³

Graduate School of Engineering, Osaka University, 2-1 Yamadaoka, Suita, Osaka 565-0871

¹NEOMAX Co. Ltd., 2-15-17 Egawa, Shimamoto-cho, Mishima-gun, Osaka 618-0003

²Kyoto University Research Reactor Institute, Noda, Kumatori-cho, Sennan-gun, Osaka 590-0494

³Quantum Beam Science Directorate, JAEA, Tokai, Ibaraki 319-1195

1. Introduction

Co₂Z-type ferrite Ba₃Co₂Fe₂₄O₄₁ (Ba₃Z) has the easy magnetization direction lies in the basal plane (*c*-plane)¹. Therefore this material maintains a high permeability even in the UHF region and is regarded as a candidate for EM noise absorber in this region. Substitution of Sr for Ba induce the changes in direction and size of magnetic moments and their temperature dependence. The moments in Ba₃Z and Ba_{1.5}Sr_{1.5}Co₂Fe₂₄O₄₁ (Ba_{1.5}Sr_{1.5}Z) lie in the *c*-plane at room temperature and turn significantly from the direction parallel to the *c*-plane to the *c*-axis in the temperature range from 523 to 573 K. On the other hand, moments in Sr₃Co₂Fe₂₄O₄₁ (Sr₃Z) deviate from the *c*-plane at room temperature and turn in the range from 473 to 523 K². In our present work, the temperature dependence of moment directions in Ba_{1.0}Sr_{2.0}Co₂Fe₂₄O₄₁ (Ba_{1.0}Sr_{2.0}Z) and Ba_{0.5}Sr_{2.5}Co₂Fe₂₄O₄₁ (Ba_{0.5}Sr_{2.5}Z) and the effect of substitution of Sr for Ba on magnetic structure were investigated by high-temperature neutron diffraction.

2. Experimental

Powder samples of Ba_{1.0}Sr_{2.0}Z and Ba_{0.5}Sr_{2.5}Z were prepared by ceramic method. Sintering conditions were as follows; [Ba_{1.0}Sr_{2.0}Z: *T*=1513 K and *P*_{O₂}=101.3 kPa] and [Ba_{0.5}Sr_{2.5}Z: *T*=1483 K and *P*_{O₂}=21.3 kPa]. High-temperature neutron diffraction patterns were obtained using HRPD at JRR-3 up to 773 K. Neutron wavelength was 0.1823 nm.

3. Results and Discussion

Figure 1 shows the temperature dependence of moment angles with *c*-axis of Ba_{1.5}Sr_{1.5}Z, Ba_{1.0}Sr_{2.0}Z, Ba_{0.5}Sr_{2.5}Z and Sr₃Z determined from the Rietveld analyses. The magnetic moments in Ba_{1.0}Sr_{2.0}Z mostly lie in the *c*-plane at room temperature and turn significantly from the direction parallel to the *c*-plane to the *c*-axis in the temperature range from 498 to 523 K. On the other hand, the magnetic moments in Ba_{0.5}Sr_{2.5}Z deviate from the *c*-plane at room temperature and turns in the range from 473 to 498 K. These results indicate that the substitution of Sr for more than the half of Ba induces the gradual decrease in temperature range in which magnetic moments turn to the direction parallel to the *c*-axis.

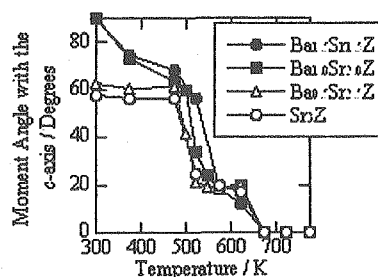


Figure 1: Temperature dependence of moment angles with *c*-axis of sample.

References

- 1) J. Smit, *et al.*: "Ferrites", ed. N. V. Philips (Philips Technical Library, Eindhoven, 1959) pp. 257.
- 2) Y. Takada, *et al.*: "J. Appl. Phys." (in press).

研究テーマ：中性子散乱によるウラン化合物の物性研究
 表題：UCu₂Si₂における長周期、不整合反強磁性構造

1-2-21

Long Period, Incommensurate Longitudinal SDW State in UCu₂Si₂

F. Honda¹, N. Metoki¹, T. D. Matsuda¹, Y. Haga¹, and Y. Onuki^{1,2}

¹Advanced Science Research Center, Japan Atomic Energy Agency, Tokai, Ibaraki 319-1195

²Graduate school of Science, Osaka University, Toyonaka, 560-0043

UCu₂Si₂ crystallizes in the body-centered tetragonal ThCr₂Si₂-type (I4/mmm) structure. The magnetic structures and the phase diagram of UCu₂Si₂ were controversial and mysterious for a long time.¹⁾ Recently, a high quality single crystal of UCu₂Si₂ was grown by a Sn-flux method and the magnetic susceptibility measurement revealed the antiferromagnetic (AFM) ordering below 106 K, and the transition to a ferromagnetic (FM) ground state at 100 K.²⁾ The AFM structure of UCu₂Si₂ has not been confirmed yet. In order to investigate the magnetism of UCu₂Si₂, we carried out neutron diffraction experiments.³⁾

The high quality sample allows us to perform reliable neutron diffraction experiments even such a small sample. The experiments were carried out on the cold and thermal neutron triple-axis spectrometers LTAS and TAS-2 installed in the guide hall of research reactor JRR-3 at the Japan Atomic Energy Agency (JAEA).

Figure 1 shows the (1 0 l) scattering profile of UCu₂Si₂ measured in (a) paramagnetic (PM) at 110 K, (b) AFM at 101 K, and (c) FM phases at 10 K. At 101 K, we observed the resolution limited first and third-order magnetic satellite reflections at (1 0 1 ± δ) and (1 0 1 ± 3δ), respectively, indicating the incommensurate AFM state where δ slightly depends on temperature. FM scattering is observed on (1 0 1) nuclear reflection below 100 K. The broad feature around l = 1.3 which is seen whole temperature ranges is an unknown polycrystalline signal.

The intensity of the third order satellite, ≈ 25 cts/600 s, is less than 1 % of the first order

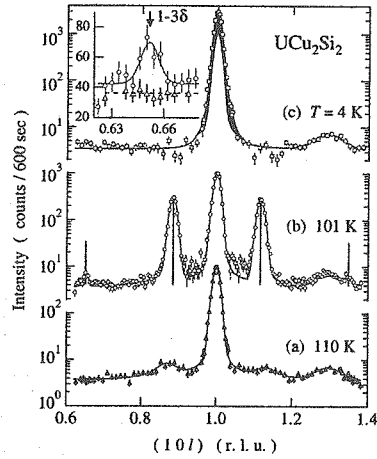


Figure 1: Line scan profile around (1 0 l).

satellite peak, ≈ 3000 cts/600 s. In case of the anti-phase structure, remarkable third-order satellites as large as 10% of the first order one should be observed, which is shown as bars in Fig. 1(b). The observed intensity for the third order satellite is one order of magnitude smaller than that for the case of anti-phase structure. Thus, the AFM phase is an incommensurate longitudinal spin-density-wave (SDW) state with a nearly sinusoidal magnetic amplitude modulation. The solid line in Fig. 1(b) is the result of a model calculation with the periodicity $\Lambda = 85.7 \text{ \AA}$ ($q = [0 0 \delta]$, $\delta = 0.116$) and a modulation amplitude $\mu_1 = 1.3 \mu_B/U$ and $\mu_3 = 0.1 \mu_B/U$ for the first and third Fourier components, respectively.

The determined magnetic structures of (a) FM and (b) AFM in UCu₂Si₂ are shown in Fig. 2, which are confirmed by a careful analysis of the integrated intensity of magnetic

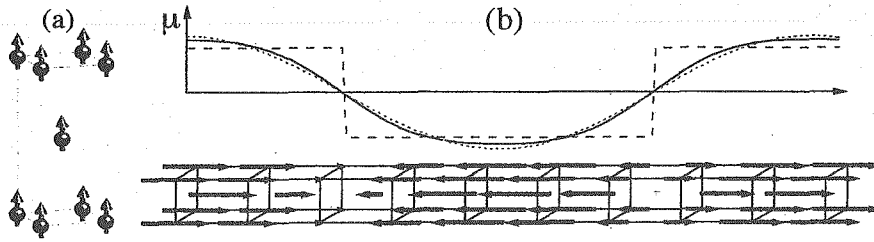


Figure 2: Magnetic structures in UCu_2Si_2 at (a) FM and (b) AFM phases.

peaks. The moment amplitude is indicated by the solid curve in the upper part of Fig. 2 (b). The remarkable feature of the AFM structure are the long periodicity $\Lambda = 85.7$ Å corresponding to roughly 17 uranium basal plane layers. In AFM phase, there is a large FM region in each half period consisting of more than 8 layers of uranium. Moreover, the long-period incommensurate modulation appears only in a very narrow region in the magnetic phase diagram and it turns to be a FM phase with further cooling and/or applying very small magnetic field (≤ 1 kOe). Thus it is evident that the ferromagnetic interactions play a dominant role in this compound.

Figure 3 shows the temperature dependence of the magnetic scattering intensities of the first order satellite. The magnetic satellite peak appears below $T_N = 106$ K, and increases continuously with decreasing temperature down to 100 K. The inset shows the

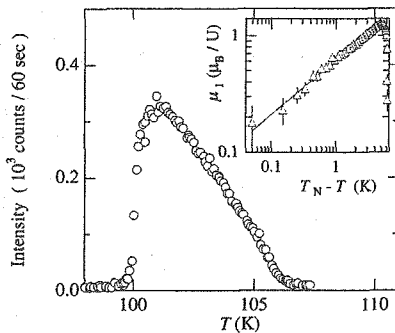


Figure 3: T dependence of order parameter.

sublattice magnetic moment (μ_1) calculated from the magnetic reflection intensity with respect to $T_N - T$ in a logarithmic scale. The obtained critical exponent of the order parameter, β , is $0.48(4)$. The mean field-like temperature dependence, $\beta = 0.5$, of the order parameter reminds us a SDW state with a gap as occasionally found in the itinerant $3d$ electron system like a chromium, implying the SDW/CDW state in UCu_2Si_2 .

A similar but rather short periodicity incommensurate modulation is reported in UPd_2Si_2 and UNi_2Si_2 , where the magnetic structures are interpreted with ANNNI (Axial Next Nearest Neighbor Ising) type model based on frustrated short range interaction between “localized” $5f$ electrons. However, there is no way to explain the long sinusoidal modulation in UCu_2Si_2 with ANNNI model because of the long periodicity. The electronic properties of these three compounds should be more or less similar, thus we suggest the strong “itinerant” character of $5f$ electron as a origin of the SDW state in UT_2Si_2 system.

References

- 1) M. Kuznietz :“J. Phys.: Condens. Matter.”, **15**, 8957 (2003)and references therein.
- 2) T.D. Matsuda *et al.*:“J. Phys. Soc. Jpn.”, **74**, 1552 (2005).
- 3) F. Honda *et al.*:“J. Phys.: Condens. Matter.”, **18**, 479 (2006).

研究テーマ：先端偏極中性子散乱によるスピン-格子物性の研究
表題：磁性薄膜・人工格子の特異な磁気構造の研究

1-2-22

The Detailed Temperature Dependence of Phase Slip Transition in Cr(001)/Sn Epitaxial Film

M. Takeda, K. Kakurai, and K. Mibu¹

Quantum Beam Science Directorate, JAEA, Tokai, Ibaraki 319-1195

¹ Graduate School of Engineering, Nagoya Institute of Technology, Showa-ku, Nagoya, Aichi, 466-8555

In epitaxial Cr(001)/Sn multilayers with periodically embedded monatomic Sn layers an exotic spin-density-wave (SDW) is realized below Néel temperature^{1,2}. For example a film with multilayer structure of [Cr(10.0 nm)/Sn(0.2 nm)] \times 24 has a commensurate antiferromagnetic (CAF) structure at 300 K. The phase transition from the CAF to incommensurate SDW (ISDW) occurs with decreasing temperature as shown in Fig. 1.

The wavelength of the ISDW is governed by the artificial periodicity, $\Lambda = 10.2$ nm as a result of competition between the nesting vector of the Fermi surface and the artificial period. Since the antinodes of this ISDW are pinned by the nonmagnetic Sn layers, another type of phase transition between different number of the node (between $N = 1$ and 3) was observed in the ISDW state. This transition was called phase slip transition. The CAF peak is denoted by "C peak", the satellite peak originating in ISDW with $N = 1$ by "S1", and that with $N = 3$ by "S3" in Fig. 1.

We measured detailed temperature dependence of this phase slip transition by using TAS-1 and TAS-2 in the 2-axis mode. The scans were done along [00L] direction through the (010) reciprocal point of the bct structure. The change of peak height are plotted as insets in each figure. Hysteresis was observed in every peak, and the "S1" peak is the most intense at 150 K during cooling process while the intensity of the "S3" peak does not have clear peaks. We are going to measure the other samples which do not show the phase slip transition. These two results will

elucidate the detailed mechanism of the phase slip transition.

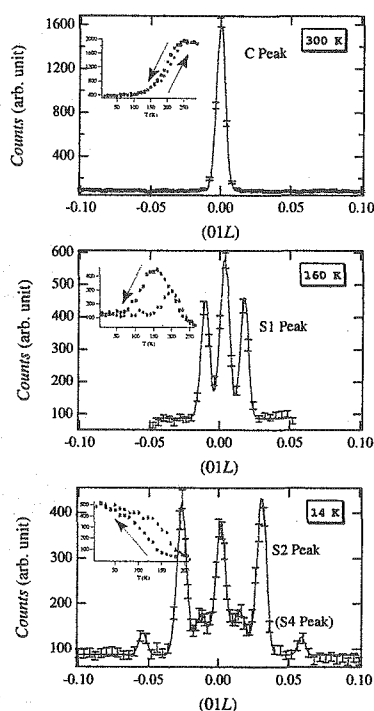


Figure 1: Temperature dependence of [01L] scans of [Cr(10.0nm)/Sn(0.2nm)] \times 24 epitaxial film at 300, 160 and 14 K. Note that the scales of vertical axes of these figures are different from one another. Insets are the temperature dependence of peak height corresponding to each peak.

References

- 1) K. Mibu, M. Takeda, J. Suzuki, A. Nakanishi, T. Kobayashi, Y. Endoh and T. Shinjo: "Phys. Rev. Lett.", **89**, 287202 (2002).
- 2) M. Takeda, K. Mibu, T. Shinjo, and Y. Endoh: "Phys. Rev. B.", **70**, 104488 (2004).

原子炉：JRR-3

装置：TAS-1(2G), TAS-2(T2-4)

分野：中性子散乱 (磁性)

1. 中性子散乱 3) 超伝導現象



1. Neutron Scattering 3) Superconductivity

This is a blank page.

研究テーマ：先端偏極中性子散乱によるスピン-格子物性の研究
 表題：高温超伝導体 LSCO の高温正方晶での格子非整合散漫散乱

1-3-1

Incommensurate Lattice Distortion in the HTT Phase of LSCO

S. Wakimoto, H. Kimura¹, M. Fujita², K. Yamada², Y. Noda¹, G. Shirane³, G. Gu³,
 H.-K. Kim⁴, R. J. Birgeneau⁵

Quantum Beam Science Directorate, JAEA, Tokai, Ibaraki 319-1195

¹Institute of Multidisciplinary Research for Advanced Materials, Tohoku University, Sendai 980-8577

²Institute for Material Research, Tohoku University, Katahira, Sendai 980-8577

³Brookhaven National Laboratory, Upton, New York 11973, USA

⁴Department of Physics, University of Toronto, Toronto, Ontario, Canada M5S 1A7

⁵Department of Physics, University of California, Berkeley, Berkeley, California 94720-7300, USA

Structural inhomogeneity in high- T_c 214 compounds has been reported by various experimental probes. In particular, by neutron scattering, Kimura *et al.*¹⁾ have observed a local LTO-type distortion in the HTT phase of $\text{La}_{2-x}\text{Sr}_x\text{CuO}_4$ (LSCO) with $x = 0.12$ and 0.18 , evidenced by incommensurate diffuse (ICD) peaks appearing around the LTO superlattice peak position. In addition, no such incommensurate diffuse feature can be detectable in the non-superconducting $x = 0.05$ sample.²⁾ We have extended the study of the ICD feature in the HTT phase to a wider concentration range using LSCO with $x = 0.07$, 0.15 , and 0.20 , and LBCO with $x = 0.125$.

Neutron scattering experiments have been performed at LTAS and TAS-2 for $x = 0.07$ and 0.20 , while at TOPAN for the others. For all compositions, a sharp superlattice peak of the LTO structure is replaced by a pair of ICD peaks above the LTO-HTT transition temperature T_s . The incommensurate modulation direction is parallel to the CuO_6 octahedral tilting direction, that is, the diagonal Cu-Cu direction of the CuO_2 plane. By comparison of the structure factors at different zones, we conclude that the ICD peaks originate from LTO type displacements, which suggests that a LTO type local lattice distortion remains in a one-dimensionally modulated form in the HTT phase.

The temperature dependences of the incommensurability δ for all samples scale ap-

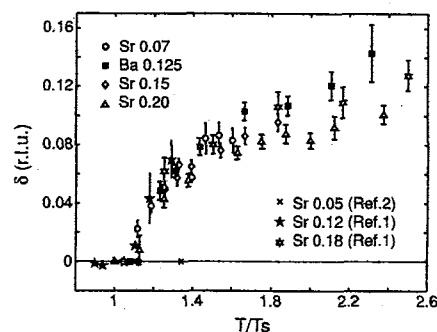


Figure 1: Incommensurability δ for all of the present samples as a function of normalized temperature T/T_s , together with data of Sr $x = 0.12$ and 0.18 from Kimura *et al.*, and of $x = 0.05$ from Wakimoto *et al.*

proximately as T/T_s (Fig. 1), while those of the integrated intensity of the ICD peaks scale as $(T - T_s)^{-1}$. Though understanding of a coupling between the ICD feature and the superconductivity requires more research, these observations together with absence of ICD peaks in the non-superconducting $x = 0.05$ sample evince a universal incommensurate lattice instability of hole-doped 214 cuprates in the superconducting regime (See Ref. 3 for details).

References

- 1) H. Kimura *et al.*: "J. Phys. Soc. Jpn.", **69**, 851 (2000).
- 2) S. Wakimoto *et al.*: "J. Phys. Soc. Jpn.", **73**, 3413 (2004).
- 3) S. Wakimoto *et al.*: "J. Phys. Soc. Jpn.", **75**, 074714 (2006).

原子炉：JRR-3 装置：LTAS(C2-1), TAS-2(T2-4) 分野：中性子散乱 (超伝導)

研究テーマ：先端偏極中性子散乱によるスピン-格子物性の研究
 表題：高温超伝導体の磁気揺らぎの異方性の研究

1-3-2

Polarized Neutron Scattering Study of Spin Excitations in LSCO

S. Wakimoto, K. Kakurai, M. Takeda and M. Matsuda

Quantum Beam Science Directorate, JAEA, Tokai, Ibaraki 319-1195

It is widely accepted that magnetic fluctuation plays a central role for the high- T_c superconductivity. However, apparent differences in magnetic response in different cuprates had provided a major challenge. Recent discovery of the universal “hour-glass” shaped magnetic dispersion observed in several hole-doped cuprates have connected the low-energy incommensurate magnetic excitation which is intimate to the superconductivity in LSCO compounds and the commensurate resonance feature which is dominant in YBCO compounds. The origin of the hour-glass dispersion is still controversial, however, information of anisotropy of the low energy incommensurate spin fluctuation should contribute to the understanding.

We have performed polarized neutron scattering experiments at the TAS-1 spectrometer using the LSCO with $x = 0.08$. The spectrometer was operated in a uniaxial polarization mode. A vertically focusing Heusler monochromator and a double-focusing Heusler analyzer are used. Inelastic measurements were done with fixed final energy at 14.7 meV and hence a spin-flipper and a PG filter are placed after the sample.

Figure 1 shows profiles of low energy (4 meV) incommensurate magnetic peaks at 2.7 K observed in vertical-field (VF) non-spin-flip (NSF) and spin-flip (SF) channels. Solid lines are results of fits to a resolution convoluted two-dimensional Lorentzian function, which give almost same intensity for the NSF and SF channels. Considering that the VF-NSF channel probes fluctuation along the z -axis and the VF-SF channel probes that along the y -axis, the results demonstrate that the

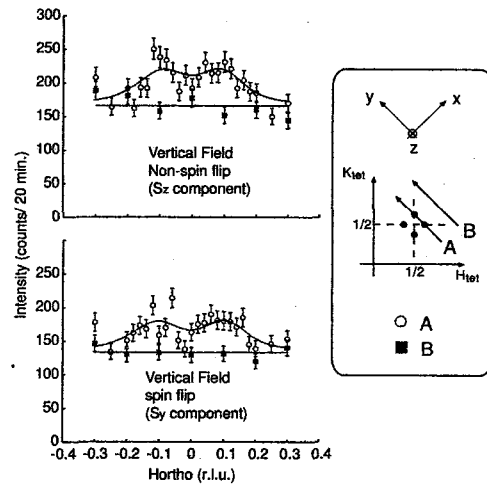


Figure 1: Incommensurate peak profiles for LSCO $x = 0.08$ with energy transfer $\omega = 4$ meV at 2.7 K. Data for vertical-field non-spin-flip and spin-flip channels are shown. Scan trajectories are depicted in the right.

low-energy spin fluctuation in the underdoped $x = 0.08$ sample is isotropic.

Current results shed new lights on the high- T_c research. First, we demonstrate that the inelastic magnetic signal of the high- T_c compound is detectable by the polarized neutron scattering which had been hardly successful due to the low intensity. We believe that the double-focusing Heusler analyzer made a major contribution. Second, the isotropic fluctuation implies that the in-plane spin-gap, which is estimated to be ~ 4 meV in non-doped LCO, is somewhat reduced in underdoped samples. In this aspect, a comparison to a stripe-ordered LBCO 1/8 sample should be interesting. This is currently in progress.

研究テーマ：先端偏極中性子散乱によるスピン-格子物性の研究

表題：ホールドーブ型超伝導体 $\text{La}_{2-x}\text{Sr}_x\text{CuO}_4$ の超伝導体-絶縁体近傍における格子非整合スピン相関への Ni 不純物効果

1-3-3

Ni-impurity Effects on Incommensurate Spin Correlations in Hole-doped Superconductor $\text{La}_{2-x}\text{Sr}_x\text{CuO}_4$ in the Vicinity of Superconductor-insulator Boundary

H. Hiraka¹, S. Ohta¹, S. Wakimoto², M. Matsuda², and K. Yamada

Institute for Materials Research, Tohoku University, Sendai 980-8577

¹*Graduate School of Science, Tohoku University, Sendai 980-8578*

²*Quantum Beam Science Directorate, JAEA, Tokai, Ibaraki 319-1195*

Doped high- T_c cuprates, one of the most fruitful examples of doped Mott insulators, provide us rich information on the interplay between the doped carriers and the spin correlations commonly underlying on the Cu-O square lattices. In the superconducting (SC) phase, the so-called parallel spin-density modulation (P-SDM) persists entirely in hole-doped $\text{La}_{2-x}\text{Sr}_x\text{CuO}_4$ (LSCO),¹⁾ while the so-called diagonal spin-density modulation (D-SDM) takes place in the insulating spin-glass (SG) phase.²⁾ The detailed study in the vicinity of the boundary between SG and SC phases confirmed a D- to P-SDM transition at the boundary.^{3,4)} To clarify the origin of the D-SDM, Matsuda *et al.* studied the impurity effect in the SG phase.⁵⁾ The results show that Ni doping quickly destroys the incommensurability and restores the Neel ordering, indicating a strong effect on hole localization.

We further explored the Ni-impurity effects in the SC phase to study whether the strong hole-localization effect of Ni-impurity commonly exists in the entire superconducting phase. In the present neutron scattering experiments, Ni-impurity effects on the static spin correlations were investigated particularly in the vicinity of the SG-SC boundary of LSCO. Single crystals of $\text{La}_{1.94}\text{Sr}_{0.06}\text{Cu}_{1-y}\text{Ni}_y\text{O}_4$ with $y = 0.03$ and 0.06 were prepared. Magnetic neutron-diffraction measurements were carried out on the cold-neutron triple-axis spectrometer LTAS installed in the guide hall of JRR-3 at

the Japan Atomic Energy Agency.

Similar to the result in the SG phase,⁵⁾ we observed a drastic impurity effect in the SC phase. Upon dilute Ni substitution of $y = 0.03$, both P-SDM and D-SDM considerably shrink in incommensurability, associated with degradation of bulk superconductivity. Subsequent Ni doping up to $y = 0.06$ induces a bulk three-dimensional antiferromagnetic order with the same spin structure without Ni-impurity. This suggests that Ni is doped as Ni^{3+} or as Ni^{2+} with a hole forming a strongly bound state. Based on the hypothesis of the reduction of the effective hole concentration by Ni-impurity, we propose that the previously studied impurity effects can be simply interpreted.

References

- 1) K. Yamada, C. H. Lee, K. Kurahashi, J. Wada, S. Wakimoto, S. Ueki, H. Kimura, Y. Endoh, S. Hosoya, G. Shirane, R. J. Birgeneau, M. Greven, M. A. Kastner, and Y. J. Kim : "Phys. Rev. B", **57**, 6165 (1998).
- 2) S. Wakimoto, R. J. Birgeneau, M. A. Kastner, Y. S. Lee, R. Erwin, P. M. Gehring, and S.-H. Lee, M. Fujita, K. Yamada, Y. Endoh, K. Hirota and G. Shirane : "Phys. Rev. B", **61**, 3699 (2000).
- 3) M. Matsuda, M. Fujita, K. Yamada, R. J. Birgeneau, M. A. Kastner, H. Hiraka, Y. Endoh, S. Wakimoto and G. Shirane : "Phys. Rev. B", **62**, 9148 (2000).
- 4) M. Fujita, K. Yamada, H. Hiraka, P. M. Gehring, S.-H. Lee, S. Wakimoto and G. Shirane : "Phys. Rev. B", **65**, 064505 (2002).
- 5) M. Matsuda, M. Fujita and K. Yamada : "Phys. Rev. B", **73**, 140503R (2006).

原子炉：JRR-3 装置：LTAS(C2-1) 分野：中性子散乱（超伝導）

This is a blank page.

1. 中性子散乱 4) 高分子



1. Neutron Scattering 4) Polymer

This is a blank page.

研究テーマ：中性子散乱によるリビングラジカル重合における星型ポリマーの形成過程の解析
 表題：中性子小角散乱によるリビングラジカル重合における星型ポリマー形成過程のその場・
 実時間観察

1-4-1

In-situ and *Real-time* Observation for Star Polymer Formation in
 Ru(II)-Catalyzed Living Radical Polymerization by
 Small Angle Neutron Scattering (SANS)

T. Terashima¹, R. Motokawa², M. Kamigaito³, S. Koizumi²,
 M. Sawamoto¹ and T. Hashimoto²

¹Department of Polymer Chemistry, Graduate School of Engineering,
 Kyoto University, Kyoto 615-8510

²Soft Matter & Neutron Scattering Group, JAEA, Tokai, Ibaraki 319-1195

³Department of Applied Chemistry, Graduate School of Engineering,
 Nagoya University, Nagoya 464-8603

Introduction. Living radical polymerization is among the best methods for the synthesis of polymers with well-defined structures, such as block, graft, and star polymers. In conjunction with our Ru(II)-catalyzed living radical polymerization, for example, we have already synthesized a variety of star polymers via the polymer linking method¹⁾. The synthesis is considered to follow the mechanism schematically illustrated in Fig. 1: (i) Generation of linear living chains (2; "arms"); (ii) *In-situ* addition of a small amount of a divinyl compound (3; linking agent) to as-formed arms 2; (iii) Formation of "block" polymers (4) via one of the two vinyl groups in 2, while the other vinyl group dangling in the pendant; (iv) Inter- and intra-molecular "linking" of 4 via the growing ends and the pendent vinyl groups, to form star polymers (5) with a microgel ("core") on which multiple arm chains are attached. Though proposed a long time ago and seemingly consistent with some observations, the linking mechanism has not yet been established nor confirmed.

Thanks to the high material permeability and the low energy of neutron²⁾, small angle neutron scattering (SANS) is powerful for observation of the phase transition and the self-assembling of polymers, and it occurred to us that it may also be applied to *in-situ* and *real-time* direct observation of chemical reactions including the star polymer formation.

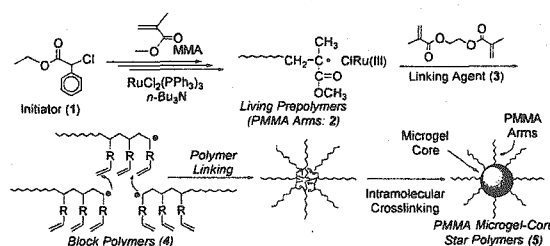


Figure 1: Synthesis of PMMA microgel-core star polymers via Ru(II)-catalyzed living radical polymerization.

In this report, the formation of microgel-core star polymers in the Ru(II)-catalyzed living radical polymerization was followed *in-situ* by *real-time* SANS, to shed a new light to the polymer linking mechanism.

Results and Discussion. *Star Polymer Synthesis.* Methyl methacrylate (MMA) was polymerized with a three-component initiating system, ethyl 2-chloro-2-phenylacetate (1) (initiator), RuCl₂(PPh₃)₃ (catalyst), and *n*-Bu₃N (additive), in toluene-*d*₈ at 80 °C (Fig. 2). The polymerization smoothly proceeded, to give linear living polymers (2: PMMA arm) with relatively narrow molecular weight distributions (MWDs) and controlled number-average molecular weights (e.g., $M_n \cong 11600$; $M_w/M_n = 1.33$; conv. 91 %; 49 h). A small amount of linking agent 3 ([3]/[1] =

10/1) was then added to induce the linking reaction. The products at +5 h showed a bimodal MWD with a slightly higher molecular weight, indicating the formation of block polymers 4. Upon leaving the mixture unquenched (≥ 10 h), the MWD further shifted to higher molecular weights, eventually giving star polymers 5 in high yield (89%; 50 h).

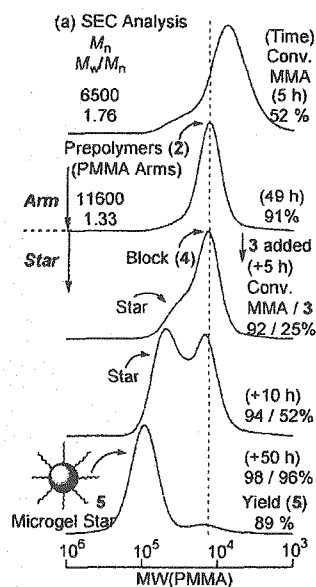


Figure 2: SEC analysis of microgel-core star polymer formation in the Ru(II)-catalyzed living radical polymerization. Polymerizations: $[MMA]_0/[1]_0/[RuCl_2[(PPh_3)_3]_0/[n-Bu_3N]_0 = 2000/20/10/40$ mM in toluene at 80 °C; Linking: $[3] = 200$ mM (2/3 = 2/1 v/v).

In-Situ SANS. The identical reactions were followed *in-situ* in toluene- d_8 at 80 °C by *real-time* SANS in a quartz cell (2 mm thickness) connected to a glass tubing and a three-way stopcock and set into the neutron beam path (Fig. 3). During the initial linear arm formation (*Region 1*; ≤ 7 h), the q -profiles exhibited an Ornstein-Zernike type scattering attributed to a disordered PMMA solution. The scattering intensity increased with conversion due to the expansion of the polymer chains (*Region 2*; ≥ 13 h). Upon subsequent addition of **3** into **2**, the q -profiles initially changed

little (*Region 3*), consistent with the block copolymerization where polymer size hardly changes. As **3** was further consumed (*Region 4*), the scattering intensity clearly increased, indicating the arm linking into star polymers **5**. The profile further changed in *Region 5* (≥ 29 h), developing a distinct peak possibly due to some interaction among star polymers. The peak maximum (q_{max}) shifted to higher q as the linking proceeded, suggesting tighter packing (or shorter distance of gravity) of star polymers.

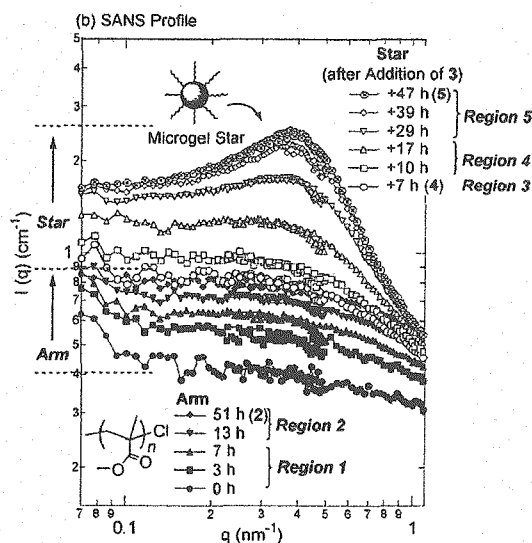


Figure 3: SANS profiles (absolute scattering intensity) for microgel-core star polymer formation in the Ru(II)-catalyzed living radical polymerization. Conditions: See Fig. 2.

Conclusions. For the first time to our knowledge, *in-situ* and *real-time* SANS observations of microgel-core star polymer formation were achieved in living radical polymerization to clarify the linking mechanism.

References

- 1) T. Terashima, *et al.* : "J. Am. Chem. Soc.", **125**, 5288-5289 (2003).
- 2) K. Yamauchi, *et al.* : "Macromolecules", **39**, 4531-4539 (2006).

研究テーマ：中性子散乱によるソフトマターの構造と機能の研究

表題：リビングラジカル重合によるポリメタクリル酸メチル-ポリスチレンジブロック共重合体合成過程の中性子小角散乱によるその場観察

1-4-2

***In-situ* and *Time-resolved* Small-angle Neutron Scattering Observation for Reversible Addition-fragmentation Chain Transfer Living Radical Polymerization of Poly(Methyl Methacrylate)-*block*-polystyrene**

R. Motokawa, Y. Zhao, T. Hashimoto and S. Koizumi

Research Group of Neutron-scattering Soft Matter, Advanced Science Research Center, Japan Atomic Energy Agency, Tokai-mura, Ibaraki-ken, 319-1195, Japan

We investigate living radical polymerization process of Poly(methyl methacrylate)-*block*-polystyrene (PMMA-*block*-PS), i.e., reversible addition-fragmentation chain transfer (RAFT) radical polymerization method, which is observed by *in-situ* and *time-resolved* small-angle neutron scattering (*tr*-SANS) measurements.

RAFT polymerization method has been developed in the past decade, which can be used to synthesize narrowly-dispersed and well-defined sequential block copolymer. The living process is achieved by employing a special chain transfer reagent, so-called RAFT reagent having dithioester function in its chemical structure. Here, cumyl dithiobenzoate was used as a RAFT reagent. There exist a lot of researches about the polymerization and kinetics for the RAFT systems, however, the meso-scale structure appeared in polymerization process ("polymerization-induced molecular self-assembly") have never investigated up to now. *tr*-SANS is extremely powerful method to explore the polymerization process¹⁾ because of low energy and high permeability of incident cold neutrons for the sample specimens. In this study, we aim to elucidate the relationship between the propagation reactions occurring at around local chain end radical and "polymerization-induced molecular self-assembly" formed by reaction products.

To obtain PMMA-*block*-PS, as a first step, PMMA having the dithioester function at chain end was synthesized in ben-

zene at 60°C in the presence of initiator, 2,2-Azobisisobutyronitrile (AIBN), where the number averaged molecular weight (M_n) and polydispersity (M_w/M_n) of PMMA are 17,000 and 1.1 at the monomer conversion of 34%. In the second step, the isolated PMMA mixture obtained from first step, 1.19 g was dissolved in 15.7 g (0.14 mol) of Styrene- d_8 in a 100-mL round bottom flask. After conducting degas operation by freeze-thaw method, diblock copolymerization was carried out at 130°C under a bulk condition without initiator. Then styrene monomer was polymerized from radically activated chain end. Radicals generate from a self-initiation of styrene dimer. The molar ratio of [MMA]/[Styrene- d_8] segment was adjusted for 1/10. In order to acquire sufficient difference of scattering length density between PMMA and PS block chains for *tr*-SANS experiment, deuterated styrene monomer was used. Next, a typical *tr*-SNAS operation was carried out by following procedure. The prior polymerization solution, 1.5 mL of PMMA/Styrene- d_8 mixture, was introduced into quartz cell (2 mm thickness) connected a glass tubing and three-way stopcock under Ar stream by a syringe, and then set into the heat block at 130°C. Immediately, by irradiating on quartz cell with cold neutrons monochromatized with a velocity selector to have a mean wavelength $\lambda=0.65$ nm and $\Delta\lambda/\lambda = 13\%$. *In-situ* and *time-resolved* observations were started with the SANS-J-II spectrometer installed at 20 MW JRR-3 research reactor at JAEA, Tokai, Japan.

原子炉：JRR-3 装置：SANS-J(C3-2) 分野：中性子散乱（高分子）

Pinhole type small-angle neutron scattering (PSANS) spectrometer mode enables us to cover a q -range of $0.03 < q < 0.25 \text{ nm}^{-1}$ and $0.1 < q < 1.65 \text{ nm}^{-1}$ at two detector positions 10 m and 2.5 m, respectively. The scattered neutrons were detected by a two-dimensional position-sensitive ^3He detector of 0.58 m diameter. The data were corrected for counting efficiency, instrumental background, and air scattering. After circular averaging, we converted the scattering intensity to absolute intensity unit of cm^{-1} using a secondary standard of irradiated Al. Focusing ultra-small-angle neutron scattering (F-USANS) spectrometer mode with *SANS-J-II* is capable of accessing a lower q -region of $0.005 < q < 0.04 \text{ nm}^{-1}$ by using MgF_2 lenses to collimate incident neutrons, where the set-up is very powerful method to investigate mesoscopic length scale structures²⁾.

In the first step, q -profiles obtained by *tr*-SANS are well reproduced by Ornstein-Zernike (OZ) formula during polymerization, indicating that polymerization of PMMA proceeds in the disordered solution state from first to last of reaction. Figure 1 shows scattering q -profiles obtained by *tr*-SANS measurements in second step. These q -profiles can be exhibited four regions, which are defined by Region 1 to 4 with proceeding di-block copolymerization. In Region 1, an OZ type scattering originated from disordered PMMA/styrene- d_8 mixture at initial stage of polymerization was observed. In Region 2, the q -profiles exhibited scattering broad maximum due to a correlation hole effect³⁾ for intramolecular interaction of PMMA-*block*-PS, gradually moving peak position toward lower q -region. In Regions 3 and 4, the scattering upturn abruptly appeared at lower q -region ($q < 0.5 \text{ nm}^{-1}$). It seems that the macrophase separation between PMMA-*block*-PS and PS homopolymer (sub-products) is occurred, and then the turbid solution was confirmed by eyes. Here, it should be noted that the

propagation rate constant abruptly decrease with appearing upturn of scattering profile at lower q -region interestingly. At the almost same time, scattering maximum at around $q=0.15 \text{ (nm}^{-1}\text{)}$ and its higher order peaks originated from microdomain structure were clearly observed, suggesting that the disorder-order transition occurred due to exceeding critical values of χN as a consequence of increase of both M_n and concentration in solution, where the χ and N are Flory interaction parameter and degree of polymerization.

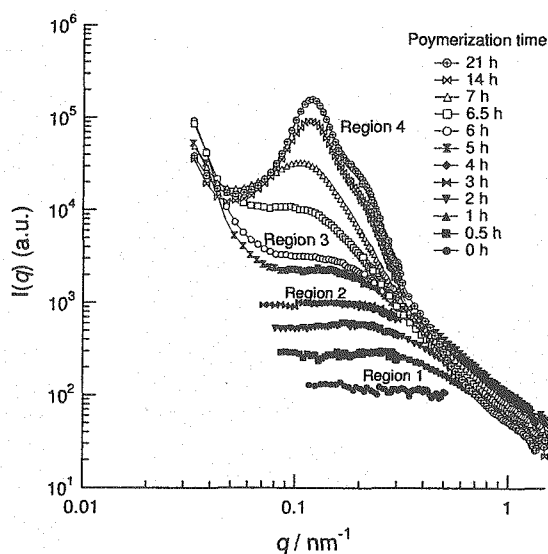


Figure 1: Polymerization time dependence of the *tr*-SANS profiles during the RAFT polymerization of PMMA-*block*-PS.

References

- 1) K. Yamauchi, H. Hasegawa, T. Hashimoto, H. Tanaka, R. Motokawa, S. Koizumi: "Macromolecules", **39**, 4531 (2006).
- 2) S. Koizumi, H. Iwase, J. Suzuki, T. Oku, R. Motokawa, H. Sasao, H. Tanaka, D. Yamaguchi, H. Shimizu, T. Hashimoto "Physica B" in press.
- 3) L. Leibler: "Macromolecules", **13**, 1602 (1980).

研究テーマ：中性子イメージングプレートを利用した合成高分子-溶媒複合システムの構造解析と溶媒効果の解明

表題：2次元広角中性子回折データを用いた巨大高分子単結晶構造解析の初めての成功例

1-4-3

The First Success of Detailed Structure Analysis of a Giant Polymer Single Crystal by Wide-angle Neutron Diffraction Data Collected with a 2-dimensional Imaging Plate Detector

K. Tashiro, M. Hanesaka, T. Ohhara¹, K. Kurihara¹, R. Kuroki¹,
T. Tamada¹, S. Fujiwara¹, I. Tanaka² and N. Niimura²

Department of Future Industry-oriented Basic Science and Materials, Toyota Technological Institute, Tempaku, Nagoya 468-8511

¹*Quantum Beam Science Directorate, JAEA, Tokai, Ibaraki 319-1195*

²*Faculty of Engineering, Ibaraki University, Hitachi, Ibaraki 316-8511*

In these several years we have collected the neutron diffraction diagrams of uniaxially-oriented synthetic polymer samples using a 2-dimensional imaging plate detector system (BIX-3) installed in the JRR-3 of Japan Atomic Energy Research Institute. For example, we succeeded for the first time in the highly-accurate determination of hydrogen atomic positions in the crystal lattice of orthorhombic polyethylene by using the uniaxially-oriented fully-deuterated (and hydrogenous) polyethylene samples¹). The determination of hydrogen atomic positions in polymer crystal lattice is absolutely necessary for the precise and quantitative prediction of physical properties. The neutron diffraction data from the deuterated polymer samples are useful for this purpose. However, we sometimes encounter the serious problem of crystal structure analysis of polymers: a general polymer gives only small number of broad reflections because of small and imperfect crystallites. This situation is seen in both of the X-ray and neutron diffraction measurements. The best way of getting the most precise structure information is to use the single crystal with the size treatable by hand. But, there have been reported quite limited number of giant single crystals so far, the crystal structures of which were analysed only by the X-ray diffraction method²). Therefore the determination of hydrogen atomic positions is not

enough reliable. In the present study we have been challenged for the first time in analyzing the crystal structure of these giant single crystals by the neutron diffraction method including the determination of hydrogen atoms. The thus determined crystal structure can be compared with the X-ray diffraction result. This comparison allows us to estimate the electron cloud distribution because neutron is scattered by atomic nuclei while X-ray is scattered by electron cloud. In the present study we report the structure analysis results obtained for polydiacetylene single crystal based on the X-ray diffraction and neutron diffraction methods. It might be valuable to emphasize here that our trial is the first success in the direct comparison of the structural information obtained by these two different methods for the synthetic polymer substance.

The sample utilized here is poly (1, 6-di(N-carbazolyl) -2, 4-hexadiyne or PDCHD, which was prepared by irradiating γ -ray onto a single crystal of the corresponding monomers. The large single crystal of ca. 5 mm \times 5 mm \times 0.5 mm was set on the goniometer head of BIX-3 cylindrical camera built up in JRR-3 reactor hall of the Japan Atomic Energy Agency. The wavelength of incident neutron beam is 1.51 Å. The diffraction patterns were taken by oscillating the sample at every 2° for 30 min for one shot. The thus collected reflections were analyzed using a software DENZO

for indexing and evaluation of integrated intensities. The structural analysis was made using a software Shelx. The reliable factor was 0.113 for 1654 reflections and 0.122 for 1822 reflections with $F \geq 4\sigma(F)$ where F is a structure factor and σ is the standard deviation. The X-ray reflections were taken using a RIGAKU R-axis Rapid X-ray diffractometer system with an imaging plate detector. The reliable factor was 0.035 for 1055 reflections and 0.109 for 2363 reflections with $F \geq 4\sigma(F)$. The unit cell parameters are $a = 12.840$ (6) Å, b (fiber axis) = 4.880 (2) Å, $c = 17.304$ (10) Å and $\beta = 108.31$ (2)° with the space group $P2_1/c - C_{2h}^5$. Figure 1 shows the crystal structure viewed along the chain axis. Using the atomic coordinates of C and N atoms determined by X-ray diffraction method, the hydrogen atoms were extracted clearly as negative peaks in Fig. 1. From the thus obtained initial structure we could refine the structure with the reliable factor of 0.113 (The relatively high factor might come from the sample quality.) As mentioned above, the neutron diffraction data should give us the positions of atomic nuclei, while the X-ray analysis corresponds to the electron density distribution. We compared the atomic density map obtained by the neutron diffraction data with the electron density map or the Fo-Fc density map calculated on the basis of X-ray diffraction data. The result is shown in Fig. 2 which is the z-axis projection of Fo-Fc electron density map compared with the atomic positions. The detailed interpretation of this map is now being made in parallel with the quantum chemical calculation of the electron density distribution.

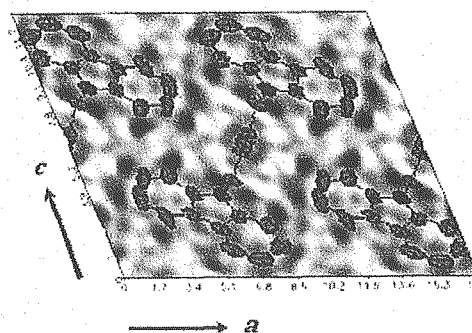


Figure 1: Crystal structure of PDCHD analyzed by neutron diffraction data.

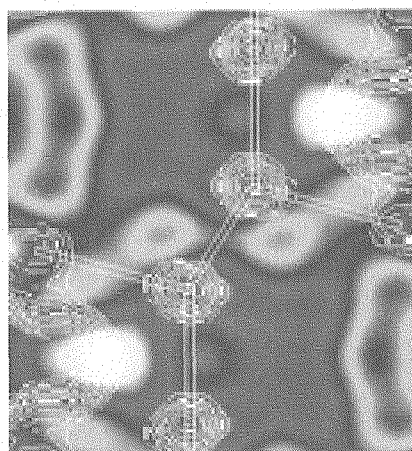


Figure 2: Fo - Fc map calculated from the X-ray diffraction data (z-axis projection).

References

- 1) K. Tashiro, I. Tanaka, Y. Oohara, N. Niimura, S. Fujiwara and T. Kamae : "Macromolecules", **37**, 4109 (2004).
- 2) K. Tashiro, H. Nishimura and M. Kobayashi : "Macromolecules", **29**, 8188-8196 (1996).

研究テーマ：リビング重合反応、及び水熱合成反応の *in-situ* 中性子散乱による反応機構解明
 表題：メソポーラスシリカ薄膜の中性子小角散乱によるその場観察

1-4-4 *In-situ* Small-angle Neutron Scattering Studies of Mesoporous Silica Films

H. Itoh, N. Miyamoto¹, H. Miyata, T. Noma, T. Watanabe, S. Koizumi¹ and T. Hashimoto¹

Canon Research Center, Canon Inc., Tokyo 146-8501, Japan

¹Advanced Science Research Center, Japan atomic energy agency, Ibaraki 319-1195, Japan

Mesoporous silica films prepared through self-assembly of surfactants are promising materials for future applications in optical and electronic molecular devices because of their high transparency and high structural regularity on macroscopic scale. Recently, Miyata *et al.* succeeded in the preparation of a three-dimensional (3-D) hexagonal mesoporous structure (space group of $P6_3/mmc$), in which the in-plane arrangement of the mesopores is macroscopically controlled¹⁾. They have proposed a model that a two-dimensional (2-D) hexagonal mesoporous structure, which is initially formed on a rubbing-treated polyimide surface, is transformed to the 3-D hexagonal structure. In the present study, an *in-situ* small-angle neutron scattering (SANS) has been performed to investigate the formation mechanism of the mesoporous structure. High transmittance of neutron beam compared to X-ray beam allows *in-situ* observation of the formation process of the aligned mesoporous films in an aqueous reactant solution.

SANS experiments were performed on SANS-J-II at research reactor JRR-3 of Japan Atomic Energy Agency (JAEA), Tokai. SANS-J-II covers a q -range of $0.14 \text{ nm}^{-1} < q < 1.16 \text{ nm}^{-1}$ at the detector position 2.35 m and with the incident neutron of $\lambda = 0.65 \text{ nm}$ ($\Delta\lambda/\lambda = 13\%$). The scattered neutrons were detected by a ³He position-sensitive detector of 0.58 m diameter. Silica glass substrates with 200 μm thickness coated with a rubbing-treated polyimide were introduced into a rectangular quartz cell with dimensions 10 mm \times 10 mm \times 45 mm. A precursor solution with a composition of polyoxyethylene 10 cetyl ether (Brij56) 0.012 polyoxyethylene 20 cetyl ether (Brij58) 0.006: tetraethoxysilane 1.0: D₂O 396: HCl 12.2 were filled in the cell. The sample temperature was controlled at 60 °C by circulating water bath within the accuracy of 0.1 °C.

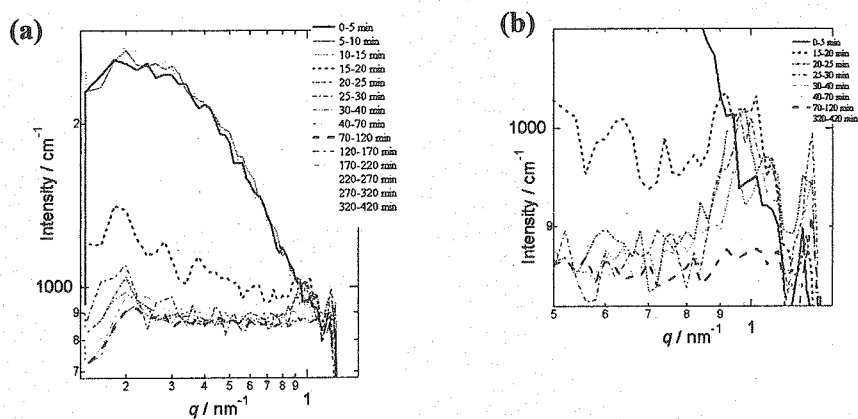


Figure 1: Time resolved scattering q -profiles at 60 °C. Figure (b) is an enlargement of figure (a) in the q -range between 0.5 and 1.3 nm⁻¹.

原子炉：JRR-3

装置：SANS-J (C3-2)

分野：中性子散乱 (高分子)

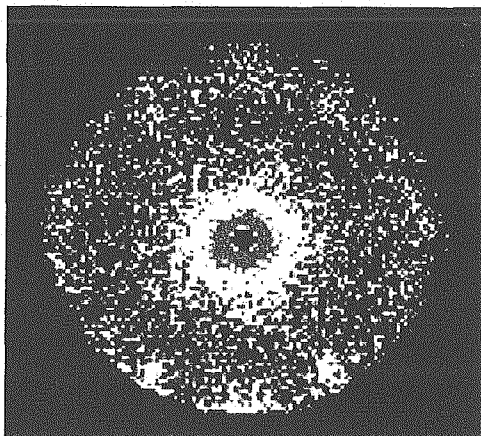


Figure 2 : The 2-D scattering pattern for the five substrates after draining the reactant solution.

Figure 1 shows the time-resolved q -profiles at 60 °C from the cell containing the five substrates and the solution. A broad scattering band in a low- q region was observed until 15 minutes, and then the intensity drastically decreased from 15 to 20 minutes. Subsequently, a peak at 1.05 nm^{-1} , which indicates a lattice distance of 6.0 nm, was observed at 20 minutes. This suggests that initially formed spherical micelles in the solution assemble to the ordered mesostructure in a relatively early stage of the film formation. To confirm the 3-D hexagonal mesoporous

structure with a controlled in-plane arrangement on the substrates, a 2-D scattering pattern was obtained from the substrates after draining the solution. In Fig. 2, the 2-D scattering pattern shows diffraction spots with a 60° interval indicating the oriented mesoporous structure.

Reference

- 1) H. Miyata, T. Suzuki, A. Fukuoka, T. Sawada, M. Watanabe, T. Noma, K. Takada, T. Mukaide, and K. Kuroda, "Nature Mater.", **3**, 651 (2004).

1. 中性子散乱 5) 生物学



1. Neutron Scattering 5) Biology

This is a blank page.

研究テーマ：Stereum purpureum 由来 Endopolygalacturonase I の中性子結晶構造解析
 表題：リング銀葉病菌由来エンドポリカラグツロナーゼの 1.5 Å 分解能中性子結晶構造解析

1-5-1

Neutron Crystallographic Analysis of Endopolygalacturonase I from *Stereum Purpureum* at a 1.5 Å Resolution

M. Sato, T. Shimizu¹, T. Nakatsu¹ and H. Kato¹

Graduate School of Integrated Science, Yokohama City University

¹Graduate School of Pharmaceutical Sciences, Kyoto University

Endopolygalacturonases (endoPGs, EC 3.2.1.15) are α -inverting glycosidases and catalyze the hydrolysis of the α -1, 4-glycosidic linkages between adjacent α -D-galacturonic acid residues within the pectin main chain. Reaction catalyzed by the inverting glycosidase proceeds by a general acid base catalysis, in which a general acid catalyst donates a proton to the glycosidic oxygen and a catalytic base guides the nucleophilic attack of water molecule on the anomeric carbon of the galacturonate. The X-ray crystal structure analyses of endoPG I from *Stereum purpureum* in complex with GalpA (β -D-galactopyranuroic acid) and GalfA (β -D-galactofuranuroic acid) have identified catalytic residues and proposed for general acid-base catalysis of the enzyme¹⁾.

To identify the general base and acid, we carried out the neutron crystallographic analysis of endoPG I in complex with GalpA. The single crystals of endoPG I were prepared at pH 5.0 with hanging-drop vapor diffusion method using PEG4000 as the precipitant, and grown by macroseeding. The crystals were then soaked for 30 days in a D₂O-prepared reservoir solution, containing 2% GalpA, 25 % PEG-4000 and 10% MPD, and then subjected to neutron experiment.

Neutron diffraction data were collected at room temperature using a single-crystal diffractometer (BIX-4) at JRR-3 in JAEA, Tokai, and processed using Denzo-Scalepack program. The initial structure was obtained from X-ray analysis¹⁾, and refined using the program SHELXS. Figure 1 shows a typical 1.5 Å resolution 2Fo-Fc neutron map. Crystallographic data and current refinement statistics are given in Table 1. Structural analysis of the complex is now in progress.

Table 1: Crystal data and current refinement statistics

Space Group	P1
Cell Dimensions	
<i>a</i> / <i>b</i> / <i>c</i>	47.1 Å / 52.6 Å / 37.7 Å
α / β / γ	107.6° / 109.9° / 70.9°
Z	1
Resolution	20.0 Å -1.5 Å
No. of reflections	
Work set	41,976
Test set	2,202
R	22.5%
R _{free}	26.2%
No. of atoms	
C, O, N, S	2,385
H/D	1,702/111

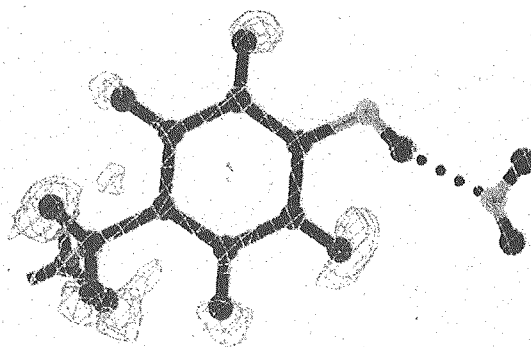


Figure 1: 1.5 Å resolution neutron map (2Fo-Fc) of Tyr243 of endoPG I and a water molecule.

Reference

- 1) T. Shimizu, T. Nakatsu, K. Miyairi, T. Okuno and H. Kato: "Biochemistry", **41**, 6651-6659 (2002).

研究テーマ：細胞における蛋白質の高次構造化不全と細胞の異常死に関する研究 (II)
 表題：中性子溶液散乱によるタウ蛋白質の構造研究

1-5-2 The Influence of Oxidation Stress on the Abnormal Tau Aggregation

S. Naito^{1,2}, H. Mochizuki², T. Yasuda², Y. Mizuno², M. Furusaka³, S. Ikeda¹,
 M. H. Shimizu¹, J. Suzuki⁴ and S. Fujiwara⁴

¹KEK, Tsukuba, Ibaraki 305-0801, ²Dept. of Neurol., Juntendo Univ. Sch. of Med., ³Dept. of Mech. Intell. Eng., Grad. School of Eng., Hokkaido Univ., Kita 13, Nishi 8, Kita-ku, Sapporo 060-8628, ⁴Japan Atomic Energy Agency, Ibaraki 319-1195

Tau is one of the microtubule-associated proteins. Mainly, 4-repeat tau (4Rtau) containing two cysteine residues and 3-repeat tau (3Rtau) lacking one repetition domain containing one cysteine residue are expressed in normal brain. The abnormal aggregation of tau often observed in Alzheimer's disease brain causes cellular degeneration and death. We are examining the influence of post-translational modifications, e.g., oxidation, phosphorylation, and proteolysis, on the formation of the abnormal aggregation. Here, we report the influence of oxidation stress on the 4Rtau and 3Rtau (Fig.1) by dynamic light scattering (DLS) and small-angle neutron scattering (SANS).

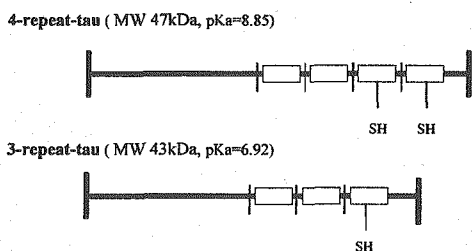


Figure 1: Diagram of 4-repeat-tau and 3-repeat-tau.

We prepared the tau aqueous solution suggesting the monomeric dispersion¹⁾ by DLS and confirmed that the conformation was unchanged if reductive atmosphere was maintained. Figure 2 shows the variation of the characteristic decay time distribution after loading oxidation stress by adding excess hydrogen peroxide (H₂O₂). 4Rtau and 3Rtau form huge clusters comprising of several thousands molecules before oxidation. The size distribution of 4Rtau was small compared to that of 3Rtau. A growth of cluster size was observed on only 3Rtau during loading oxidation stress. SANS were conducted at SANS-J and at SWAN situated at the KENS to elucidate the variation of

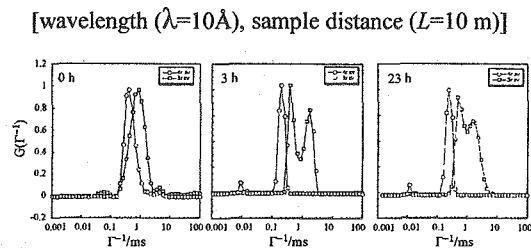


Figure 2: The variation of characteristic decay time distribution function, $G(\Gamma^{-1})$, of 4Rtau and 3Rtau after loading oxidation stress.

the shape of the tau aggregates. Figure 3 shows the SANS profiles of 4Rtau and 3Rtau before and after loading oxidation stress.

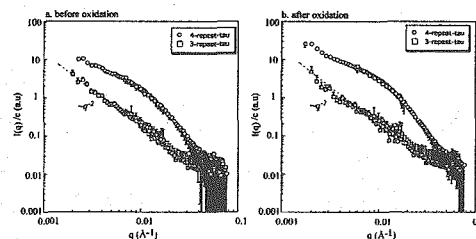


Figure 3: SANS profiles of 4Rtau and 3Rtau before/after loading oxidative stress.

Before oxidation, 4Rtau may form a huge cluster ($R_g = ca. 230\text{\AA}$), on the other hand, 3Rtau may form random coil ($slope = -2$). After oxidation, the cluster size of 4Rtau was scarcely changed and the variation of the cluster size of 3Rtau could not be unfortunately estimated in this q range although the growth of cluster size could be detected by DLS. It was obvious that 3Rtau was subject to be oxidized and changed the size of network. We will clear further the shape and the size of tau clusters by ultra-SANS this year.

Reference

- 1) S. Naito, et al. : "JAEARI-Review" 2005-045, 56 (2005).

研究テーマ：シミュレーション計算を利用した生体分子機能の解明研究
表題：タンパク質動力学転移における水和水のダイナミクス

1-5-3

Hydration Water Dynamics at Protein Dynamical Transition

H. Nakagawa, Y. Joti¹, A. Kitao¹, K. Shibata, N. Go and M. Kataoka²

Quantum Beam Science Directorate, Japan Atomic Energy Agency, Tokai, Ibaraki, 319-1195

¹Institute of Molecular and Cellular Biosciences, The University of Tokyo, Yayoi, Tokyo, 113-0032

²Graduate School of Materials Science, Nara Institute of Science and Technology, Nara, 630-0192

A protein dynamical transition around 180–240 K has been observed for the hydrated protein¹⁾. It is reported for various proteins that function is suppressed with the loss of anharmonic dynamics by dehydration or by cooling down below the transition temperature. It is essential to elucidate the role of water at the protein-water interface to understand protein dynamics and function properly. The incoherent neutron scattering has been used to study hydration related protein pico-nano second dynamics with D₂O-hydrated protein. The scattering from the hydration water on the protein can be selectively estimated by the subtraction of the scattering profile of a D₂O-hydrated protein from that of a H₂O-hydrated protein. The neutron elastic scattering experiments were performed with the triple axis spectrometer, LTAS, in the JRR-3 reactor in Tokai, which has an energy resolution of 170 μeV. The Q-range covered was from 0.4 to 2.0 Å⁻¹. The data were then collected from 10 K to 300 K. The mean-square displacements were estimated with the dehydrated sample and the hydrated samples with the hydration level of h=0.08, 0.16, 0.26 and 0.45 (g H₂O/g protein). The dynamical transition was observed at ~240 K above h=0.26 hydration level. Figure shows the temperature dependent changes of the mean-square displacement of the protein and its hydration water at h=0.16 and 0.26. With lower hydration, the mean-square displacement of hydration water is almost the same as protein. With higher hydration, the displacement of water is again almost the same as that of pro-

tein in the lower temperature range, while it deviates significantly from that of protein at the protein dynamical transition temperature ~240 K. It was reported that a relaxation time of the protein-water hydrogen bond network is 18ps at 300 K²⁾, which is within the experimentally observable time scale ~24ps. This suggests that such a network relaxation is involved in the hydration water dynamics. It is also indicated that the hydration affects the protein collective modes^{3,4)}. Therefore, we conclude that the couplings between hydration water dynamics and protein collective modes are essential for the protein dynamical transition.

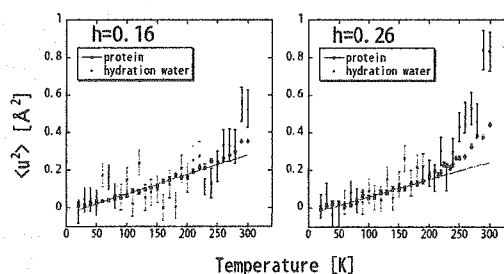


Figure 1: Mean-square displacement of protein and hydration water at h=0.16 and 0.26 hydration levels.

References

- 1) W. Doster, *et al.* : "Nature", **337**, 754 (1989).
- 2) M. Tarek, *et al.* : "Phys. Rev. Lett.", **88**, (1989).
- 3) Y. Joti, *et al.* : "J. Am. Chem. Soc.", **127**, 8705 (2005).
- 4) H. Nakagawa, *et al.* : (in preparation).

研究テーマ：分子性ポーラス結晶で安定化された巨大水分子クラスターの中性子線構造解析
 表題：分子性ポーラス結晶で安定化された巨大水分子クラスターの中性子線構造解析

1-5-4

Neutron Structure Analysis on Water Nano-tube Cluster Stabilized by Molecule-based Porous Crystal

M. Tadokoro, K. Kurihara¹, T. Ohhara¹, I. Tanaka² and R. Kuroki¹

Department of Chemistry, Faculty of Science, Tokyo University of Science, Shinjuku-ku, Tokyo 162-8601

¹*Neutron Biology Research Center, Quantum Beam Science Directorate, Japan Atomic Energy Agency, Tokai, Ibaraki 319-1195*

²*Department of Biomolecular Functional Engineering, College of Engineering, Ibaraki University, Hitachi, Ibaraki 316-8511*

The dynamics and structure of water clusters confined to nanometer-scale surroundings are different from those of bulk water and ice under ambient pressure. We have programmed the creation of a new nanometer-scale water cluster in the molecule-based nano-porous crystal in order to inspect the dynamics and behaviors of water molecules under the specific conditions.

We already placed nanometer-scale water clusters, a unit of which is constructed from 60 water molecules, inside a porous crystal formed from specially designed molecular blocks ($[\text{Co}^{\text{III}}(\text{H}_2\text{bim})_3]^{3+}$ and $[\text{TMA}]^{3-}$) to investigate the molecular dynamics of the confined water molecules. ¹⁾ X-ray crystallography of a crystal filled with water has revealed that the water clusters (a water nanotube) found in a one-dimensional nano channel with approximately 1.4 nm diameter comprise a multi-layered water structure with hydrogen bonding networks. The water nanotubes exhibit dynamics that resemble a water-ice transition, which produces an "ice nanotube" state below ca. -38°C .

In the ice state, we observed fragments of water clusters in a cubic ice phase Ic of similar structure. Each fragment was recognized as a distinct structural model of the crystal embryo in heterogeneous nucleation on an ice phase Ic (Fig. 1).

The existence of confined H_2O (1) or D_2O (2) molecules was also confirmed by ther-

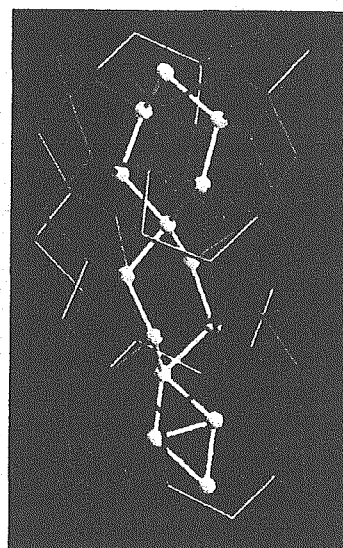


Figure 1: The structure of an ice nanotube obtained by X-ray crystal analysis below the phase transition temperature. The spheres of hydrogen-bonded water oxygens were connected with the lines.

mogravimetry (TG) measurements, which were carried out after coating the fragile crystals 1 and 2 with paraffin liquid in air. As a result, the number of H_2O and D_2O molecules for $[\text{Co}^{\text{III}}(\text{H}_2\text{bim})_3](\text{TMA})$ and $[\text{Co}^{\text{III}}(\text{D}_2\text{bim})_3](\text{TMA})$ units in crystals 1 and 2 are determined to be more than twenty, respectively. Further, the differential scanning calorimetry (DSC) thermograms were performed between -10°C and -60°C at a scan rate of 10°C per minute. We observed

原子炉：JRR-3 装置：BIX-3(1G-A) 分野：中性子散乱（生物）

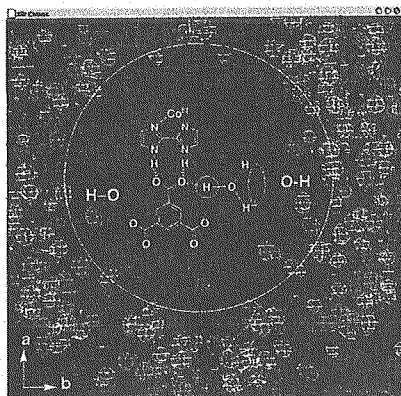


Figure 2: A view of an electron density map for the $[\text{Co}^{\text{III}}(\text{H}_2\text{bim})_3](\text{TMA})_n$ crystal along the c axis: a white circle indicates approximately the width of a channel, in which a water nanotube exists. In the channel, the net parts of the electron densities represent oxygen atoms of the water, and the hydrogen-bonded protons in the circle.

a reversible phase transition for 1 and 2 that showed exothermic peaks at -38.8 °C and -33.4 °C during cooling and endothermic peaks at -28.3 °C and -22.8 °C during heating, respectively. The difference in the temperatures of these phase transitions for 1 and 2 are almost comparable to the isotope effect (ca. 5 °C under ambient pressure) on the freezing and melting of H_2O and D_2O . This similarity suggests that the peaks of the phase transitions in DSC are related to the condensation and fusion of water molecules inside the channels. The irreversible endothermic peaks of 1 and 2 were also observed at 101.7 °C and 105.0 °C, respectively. The values of the freezing enthalpies of 1 (65.89 cal/mol) and 2 (58.22 cal/mol) were rather low compared with that of bulk ice (1436.3 cal/mol), indicating that only a limited number of water molecules in the channels participate in the water-ice transition. Therefore, the strong H-bonded water molecules in the primary water tube probably play a less important role in this transition, since in the primary domain, these molecules are strongly H-bonded with the oxygen atoms of TMA^{3-} on the surface of the channels.

In this study, we have measured a neu-

tron structure analysis for the water nanotube crystal at room temperature in order to reveal some proton positions of hydrogen bonding water molecules stabilizing a water nanotube in the channel. Water nanotube is constructed from intrinsic disordered water molecules, and those around a central axis of the tube were not observed because of heavy disordering. However, the water molecules near an outer wall in the channel were observed as relatively localized electron density by X-ray analysis. Therefore, we have investigated by a neutron structure analysis that whether protons of the water molecules have hydrogen bonded with the outer wall or not. As the results, existence of the protons connecting water oxygens with trimesic acid oxygens containing into the porous frameworks was revealed. The hydrogen bonded water molecules would be contributed in stabilizing the water nanotube clusters.

References

- 1) M. Tadokoro, S. Fukui, T. Kitajima, Y. Nagao, S. Ishimaru, H. Kitagawa, K. Isobe and K. Nakasuji : Structures and Phase Transition of Multilayered Water Nanotube Confined to Nanochannel, " Chem. Commun. ", pp.1274 (2006).

研究テーマ：中性子を用いた生体物質の構造に関する研究

表題：重水素化トロポニンIを含む筋肉の細いフィラメントの中性子繊維回折

1-5-5

Neutron Fiber Diffraction of Muscle Thin Filaments Containing Deuterated Troponin I

S. Fujiwara and F. Matsumoto

Quantum Beam Science Directorate, JAEA, Tokai, Ibaraki 319-1195

Muscle contraction occurs by sliding of the “thin” filaments and the “thick” filaments in muscle cells. Ca^{2+} -sensitive regulation of contraction in skeletal and cardiac muscles is conducted through the interactions of the thin filament based proteins, troponin (Tn) C, TnI, TnT, tropomyosin, and actin. To understand this regulatory mechanism, it is important to obtain information of the structure of these proteins within the thin filaments.

We studied the structure of TnC within the thin filament by neutron scattering¹⁾ and diffraction²⁾, and showed that conformational changes of TnC occur by binding of Ca^{2+} . We also measured neutron scattering patterns of deuterated TnI within the thin filaments with and without Ca^{2+} , and obtained the results suggesting large conformational changes³⁾. Here we employed neutron fiber diffraction to obtain information on the arrangement of TnI within the Tn-complex. TnI was deuterated and reconstituted into the thin filaments purified from cardiac muscles. These reconstituted thin filaments containing deuterated TnI (dTnI-RTF) and the native thin filaments (NTF) were sealed in quartz capillaries, and oriented in magnetic field of 18 Tesla. Neutron fiber diffraction patterns of these oriented samples were measured with SANS-J instrument at the guide hall of JRR-3 in Japan Atomic Energy Agency.

Obtained patterns were processed by tilt correction, isotropic background subtraction, and quadrant folding. Intensity distributions of meridional reflections from Tn were then extracted. Figure 1 shows the intensity distribution obtained. Analysis with model cal-

ulation of projected density to the orientation axis suggested relative movements of the domains of TnI as well as TnI within the Tn-complex. The detailed analysis is currently underway.

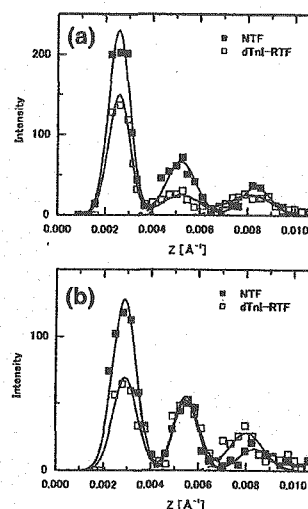


Figure 1: Meridional intensity distributions of Tn reflections (a) without Ca^{2+} , and (b) with Ca^{2+} .

Supported in part by Special Coordination Funds for Promoting Science and Technology from the Ministry of Education, Culture, Sports, Science and Technology, the Japanese Government, and also supported by the Ministry of Education, Science, Sports and Culture, Grant-in-Aid for Exploratory Research, 16657032, 2004.

References

- 1) F. Matsumoto *et al.*: “J. Mol. Biol. ”, **342**, 1209 (2004).
- 2) S. Fujiwara *et al.*: “JAERI-Review”, **2005-045**, 59 (2005).
- 3) F. Matsumoto *et al.*: “JAERI-Review”, **2005-045**, 60 (2005).

原子炉：JRR-3 装置：SANS-J(C3-2) 分野：中性子散乱（生物）

研究テーマ：中性子構造解析によるアミラーゼファミリーの構造・機能相関
表題：タカアミラーゼの中性子回折実験

1-5-6

Neutron Diffraction Experiment of TAKA Amylase

Y. Morimoto, T. Tamada¹, K. Kurihara¹, T. Ohhara¹, K. Inaka² and R. Kuroki¹

Research Reactor Institute, Kyoto University, Kumatori, Osaka 590-0494

¹Quantum Beam Science Directorate, JAEA, Tokai, Ibaraki 319-1195

²Mol-logics, inc., Yamato-koriyama, Nara 639-1123

α -amylase (α -1,4-glucan-4-glucanohydrolase, EC 3.2.1.1) catalyses the hydrolysis of internal α -1,4 glycosidic linkages of amylose. Neutral α -amylase from *Aspergillus oryzae* (TAKA amylase) is a glycoprotein consisting of a single polypeptide chain of 478 amino acids. Although the tertiary structure has been investigated by X-ray structure analysis, hydration and hydrogen structures has not been determined experimentally. Neutron structure analysis is the only method to determine hydrogen and hydration of protein structures at medium resolution range. In order to investigate the role of hydrogen and hydration on the function of TAKA amylase, we carried out the neutron diffraction study of TAKA amylase.

Crystals of TAKA amylase were prepared using counter-diffusion device composed of only a silicon capillary and the agarose gel inside.¹⁾ Single crystals were grown to the maximum size of 0.7 mm³ (3.9 × 0.9 × 0.2 mm) under 40 % PEG4000 and 2 mM CaCl₂ in 0.1 M acetate buffer (pH6.0). After the crystal was soaked into D₂O solution (pD6.0) during three months for neutron diffraction experiment, the crystal was sealed in quartz capillary for the neutron diffraction study (Fig. 1). Diffraction images were collected at room temperature using monochromatic neutron beam ($\lambda = 2.9 \text{ \AA}$) and recorded on a neutron imaging plate on a single-crystal diffractometer (BIX-3) at JRR-3 in JAEA²⁾. The crystal of TAKA amylase belongs to the space group $P2_12_12_1$ with cell dimensions of $a = 51$, $b = 67$, $c = 133 \text{ \AA}$. Some

diffraction spots were observed beyond 3.1 \AA resolution after six hours irradiation. Full data collection was stopped because several beam dumps occurred during assigned beam time at JRR-3. Since present data set was insufficient to determine hydrogen and hydration structures in detail, production of larger crystals aimed to re-collection of data set is in progress.

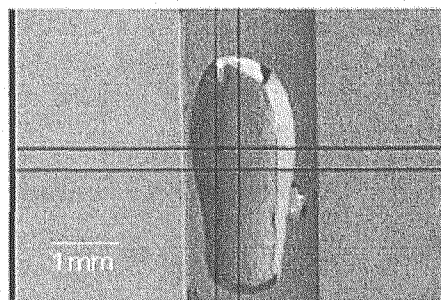


Figure 1: TAKA amylase crystal used for neutron diffraction study.

References

- 1) H. Tanaka, K. Inaka, S. Sugiyama, S. Takahashi, S. Sano, M. Sato, S. Yoshitomi: "J. Synchrotron Rad.", **11**, 45 (2004).
- 2) I. Tanaka, K. Kurihara, T. Chatake, N. Niimura: "J. Appl. Cryst.", **35**, 35 (2002).

研究テーマ：中性子を用いた生体物質の構造に関する研究
表題：ブタ膵臓エラスターゼ/阻害剤複合体の中性子回折

1-5-7

Neutron Diffraction Study of Porcine Pancreatic Elastase with Its Inhibitor

T. Tamada, K. Kurihara, T. Ohhara, T. Kinoshita¹, T. Tada¹ and R. Kuroki

Quantum Beam Science Directorate, JAEA, Tokai, Ibaraki 319-1195

¹Graduate School of Science, Osaka Prefecture University, Sakai, Osaka 599-8531

Porcine pancreatic elastase (PPE) is a serine protease classified in the chymotrypsin family that is possibly the most destructive enzymes having the ability to degrade virtually all of the connective components in the body. Uncontrolled proteolytic degradation by pancreatic elastase (EC 3.4.21.36) causes the fatal disease pancreatitis. Inhibitor for PPE is typical subject of development by structure based drug design (SBDD) because some elastases have similar structures of active sites. Nevertheless, many inhibitors designed by SBDD using X-ray structures still have side effects. More detailed structure including hydrogen and hydration information is useful to develop highly selective inhibitors. Neutron structure analysis is the only method to determine hydrogen and hydration of protein structures at medium resolution range. We carried out the neutron diffraction analysis of PPE with its inhibitor.

The single crystals of PPE were prepared under 0.2 M sodium sulfate in D₂O solution (pD 5.0) using sitting-drop vapor diffusion method. The crystal was grown to the size of 1.8 mm³ for neutron diffraction experiment by repeating macro-seeding of the crystal, and then sealed in quartz capillary for the diffraction study. Diffraction data were collected at room temperature using monochromatic neutron beam ($\lambda = 2.9/2.6$ Å) and recorded on a neutron imaging plate on a single-crystal diffractometer (BIX-3/4) at JRR-3 in JAEA.¹⁾ The crystal of PPE belongs to the space group $P2_12_12_1$ with cell dimensions of $a = 51$, $b = 58$, $c = 76$ Å. The total rotation ranges of 178.5° and 88.5° (around

Table 1: Data collection and processing statistics

Resolution (Å)	2.4 (2.49-2.40)
No. of reflections	
observed	27,386
independent	7,605
Redundancy	3.6 (2.5)
Completeness (%)	82.6 (70.6)
Mean $I/\sigma(I)$	13.0 (7.7)
R_{merge}	0.130 (0.221)

another axis) were covered by 595 and 295 still images with exposure time of 50 min./frame by step scanning method at BIX-3 and 4, respectively. Data were processed with the programs DENZO and SCALEPACK.²⁾ Data set was integrated and scaled to 2.4 Å resolution. Data collection and processing statistics are shown in Table 1. Structural analysis is now in progress. Production of larger crystals is also proceeding to collect higher resolution data.

References

- 1) I. Tanaka, K. Kurihara, T. Chatake, N. Niimura : "J. Appl. Cryst.", **35**, 35 (2002).
- 2) Z. Otwinowski and W. Minor : "Methods Enzymol.", **276**, 307 (1997).

原子炉：JRR-3 装置：BIX-3(1G-A) 分野：中性子散乱 (生物)

研究テーマ：タンパク質および有機化合物の水素・水和構造の高度な中性子解析

表題：中性子結晶解析によるインスリン構造のpH依存性

1-5-8

pH Dependence Study of Insulin Structure by Neutron Crystallographic Analysis

T. Ishikawa¹, Y. Oonishi^{1,2}, I. Tanaka¹, T. Chatake³, K. Kurihara⁴, T. Tamada⁴,
R. Kuroki⁴ and N. Niimura¹

¹Ibaraki Univ., Hitachi, Ibaraki 316-8511

²Kaken Co. Ltd., Mito, Ibaraki 310-0903

³Chiba Scie.Univ., Choshi, Chiba 288-0025

⁴JAEA, Tokai, Ibaraki 319-1195

Insulin is one of the well-known and important hormones. Because it regulates glucose in metabolism, it is used as one of medical treatments for diabetes. It has about 5700 Da per a monomer, which is composed of two peptide chains; A-chain (21 a.a.) and B-chain (30 a.a.). This protein is synthesized and stored in the pancreas as a hexamer with zinc ions and secreted from there. In general, biomacromolecules functions under various local conditions related to aqueous environments; such as hydrogen ion concentration (pH/pD), solvent concentration and so on. Some X-ray structure analyses under various pHs indicated that one of amino acids of insulin from porcine, His10 in B-chain, undergoes a change of conformation according to a change of pH. Recent neutron structural analysis of the same insulin under pD9 reveals that both N atoms of His10 in B-chain are protonated and only one N of His 5 in B-chain protonated¹⁾. The aim of this study is to confirm these protonation states and conformation changes of His5 and His10 in B-chain under other pHs such as pD6 and 7, and to compare the structures between these pDs and pD9. Sample was porcine insulin and it was purchased from SIGMA(I-5523). Using crystallization phase diagrams, metastable region was mapped. Under the condition of the metastable region, large single crystals are certainly grown. At first, crystals were grown under pH9, then soaked into D₂O buffer for pD6 and 7 for some weeks to exchange H₂O for D₂O, respectively. As a result, large single crystals of 2.7 mm³ were obtained when a precipitant was Na₂HPO₄ and an additive was EDTA at 298 K under both pD6 and 7, respectively. With these crystals, neutron diffraction experiments were done at BIX-4 at JRR-3, JAEA. Neutron wavelength was 2.6

Å, step-scanned by 0.3°, exposure time were about 90 min per one frame and 320 frames (96°) were obtained for both pDs' samples. DENZO was used for data reduction. Finally, for pD6 crystal, the crystal system was I2₁3, a=79.0 Å(cubic), and 2339 independent reflections were identified up to 2.5 Å resolution. For pD6 data, structural analysis has been carried out by CNS and Xtalview from PDB ID:1B2A X-ray data (1.7 Å) as an initial model. At present, it is at the stage of R-factor = 23.2%, R-free=24.5% at 3.0 Å resolution. 2|Fo|-|Fc| nuclear density maps around B5His and B10His were obtained as Fig. 1. From these result the protonation states of these Histidines under pD6 are the same as those of pD9. Further analysis on pD6 crystal and the analysis on pD7 will soon follow this.

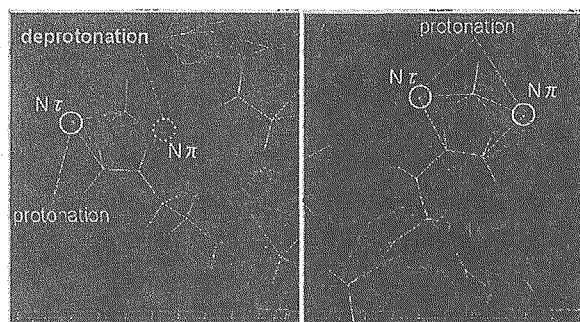


Figure 1: 2|Fo|-|Fc| nuclear density map of B5His(left) and B10His(right).


References

- 1) M. Maeda, *et al.* : "J. Synchr. Rad.", **11**, 41-44 (2004).

原子炉：JRR-3 装置：BIX-4(1G-B) 分野：中性子散乱（生物）

This is a blank page.

1. 中性子散乱 6) 基礎物理学・中性子光学



**1. Neutron Scattering 6) Fundamental Physics
Neutron Optics**

This is a blank page.

研究テーマ：中性子光学の基礎研究と応用研究
表題：PNOにおける中性子干渉計実験

1-6-1

Neutron Interferometry at PNO

Y. Hasegawa^{1,2} and K. Aizawa³

¹PRESTO, Japan Science and Technology Agency (JST), Kawaguchi, Saitama 332-0012

²Atominstytut der Österreichischen Universitäten, A-1020 Wien, Austria

³Quantum Beam Science Directorate, JAEA, Tokai, Ibaraki 319-1195

Since its advent, neutron interferometric experiments have provided elegant demonstrations of the effects related to the fundamental aspects of quantum physics¹⁾. In particular, investigations of the property of spin-1/2 system, *i.e.*, one of the simplest quantum two-level system, have been done in a superior manner with the use of neutron interferometer. In order to carry out experiments of precise neutron optics (PNO), we have developed a special multi-purpose apparatus, called PNO-apparatus, at JRR-3. The performance of the neutron interferometer experiments were already reported together with several coherent neutron scattering length measurements^{2,3)}.

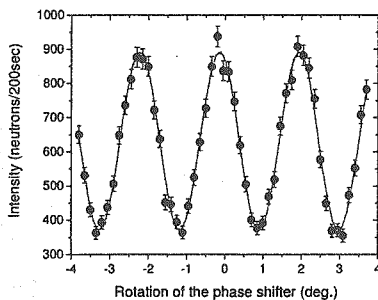


Figure 1: Typical sinusoidal intensity modulation obtained by tuning the relative phase of the two beams.

Bell's inequalities together with the EPR-paradox have aroused considerable interests for many decades^{4,5)}. Beyond locality, a more general concept, *i.e.*, contextuality, is expected to describe striking phenomena predicted by quantum theory. (Non-contextuality is a simple classical deduction

for the quantum phenomena and implies the independent results of measurements between mutually commuting observables.) One of the authors has accomplished a polarized neutron optical experiment to demonstrate the violation of a Bell-like inequality in the study of the quantum contextuality⁶⁾.

After an absence of neutron interferometer experiments of late, a neutron interferometer, which was used in the former experiments, was again tested at PNO. The intensity of the interfering beam is expected to exhibit a sinusoidal modulation as

$$I(\phi) = \bar{I} \cdot (1 + C \cos \phi) \quad (1)$$

where C and ϕ represent a contrast and a relative phase in the interferometer. Typical interference oscillation is shown in Fig.1. A contrast of higher than 40% was achieved.

We have now prepared two other new interferometers of larger dimension and going to test them at PNO. These interferometers are expected to be used for further quantum optical experiments at the J-PARC.

References

- 1) H. Rauch and S.A. Werner: "Neutron Interferometry", Clarendon, Oxford, (2000).
- 2) H. Tomimitsu, Y. Hasegawa, K. Aizawa and S. Kikuta: "Nucl. Instr. Meth. A", **420**, 453 (1999).
- 3) H. Tomimitsu, Y. Hasegawa and K. Aizawa: "Phys. Lett. A", **274**, 175 (2000).
- 4) A. Einstein, B.Podolsky and N. Rosen: "Phys. Rev.", **47**, 777 (1935).
- 5) J.S. Bell: "Speakable and Unspeakable in Quantum Mechanics", Cambridge University Press, Cambridge, (1987).
- 6) Y. Hasegawa, R. Loidl, G. Badurek, M. Baron and H. Rauch: "Nature", **425**, 45 (2003).

原子炉：JRR-3 装置：PNO(3G) 分野：中性子散乱（基礎物理）

研究テーマ：中性子光学素子の開発と中性子分光法の研究
表題：JRR-3 での中性子ベータ崩壊実験

1-6-2

Current Status of the Neutron Beta Decay Experiment in JRR-3

S. Yamada, K. Mishima¹, H. Sato¹, T. Shinohara, T. Oku, J. Suzuki and H. M. Shimizu²

Quantum Beam Science Directorate, JAEA, Tokai, Ibaraki 319-1195

¹*RIKEN, Wako, Saitama 351-0198*

²*KEK, Tsukuba, Ibaraki 305-0801*

Neutron beta decay measurements have been served as a probe for fundamental physics via the weak interaction between d and u quarks during the reaction. From the decay parameters, such as lifetime or energy spectra of decay products, we can obtain V_{ud} , a matrix element of Cabibbo-Kobayashi-Maskawa (CKM) matrix, which describes the mixing between quark mass eigenstates and weak eigenstates. The CKM matrix element obeys unitarity in the standard model of particle physics. Our research goal is to determine the CKM matrix element V_{ud} precisely to check the unitarity by measuring the proton energy spectrum in the neutron beta decay.

Before the measurement of the proton spectrum, we have performed a preliminary experiment¹⁾ in which we aimed at measuring neutron beta decay events from a thermal neutron beam. This experiment was taken place at the T1-4-5 NBD port in JRR-3, where we had introduced straight and parabolic supermirror guides to increase a beam flux.²⁾ The experimental setup is shown in Fig. 1(a). We used a channel electron multiplier (CEM) as a proton detector and a plastic scintillator with a photomultiplier (PMT) as an electron detector. These two detectors are placed at the both sides of the neutron beam. We measured arrival time of signals from both the detectors and used the correlation between them to eliminate the background events. We also measured an energy spectrum by the electron detector to identify the neutron beta decay events.

In Fig. 1(b), the difference of the arrival time between CEM and PMT signals is shown. A sharp peak at 0 ns indicates simultaneous events which come from gamma ray background. A small peak in the region of 50-400 ns is due to neutron beta decay. The arrival time of the peak can be explained by the difference between the proton and electron velocities. After this successful measurement of the beta decay events, we have prepared for the measurement of the proton energy spectrum with a newly developed superconducting detector.

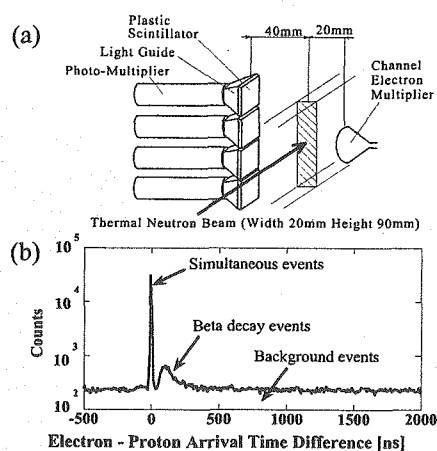


Figure 1: (a) Schematic view of the experimental setup. (b) Spectrum of the arrival time difference between CEM and PMT signals.

References

- 1) K. Mishima, *et al.*: "Proc. Int. Conf. on Neutron Scattering 2005", to be published in *Physica B*.
- 2) S. Yamada, *et al.*: "Proc. Int. Conf. on Neutron Scattering 2005", to be published in *Physica B*.

原子炉：JRR-3 装置：NBD(T1-4-5) 分野：中性子散乱（基礎物理）

研究テーマ：中性子散乱によるウラン化合物の物性研究
 表題：中性子散乱による DyRhIn₅ の磁気構造の研究

1-6-3

Neutron Scattering Study on DyRhIn₅ Single Crystal

N. V. Hieu¹, S. Jonen², N. Metoki², K. Sugiyama^{1,3}, R. Settai¹, T. D. Matsuda², Y. Haga²,
 T. Takeuchi², M. Hagiwara³ and Y. Ōnuki^{1,2}

¹Graduate School of Science, Osaka University, Toyonaka, Osaka 560-0043

²Advanced Science Research Center, JAEA, Tokai, Ibaraki 319-1195

³KYOKUGEN, Osaka University, Toyonaka, Osaka 560-8531

⁴Low Temperature Center, Osaka University, Toyonaka Osaka, 560-0043

DyRhIn₅ is one of the isostructural derivative of the heavy fermion superconductors CeTIn₅ (T= Rh, Co, Ir)¹⁻³. DyRhIn₅ is an antiferromagnetic compound with the Néel temperature $T_N = 28.1$ K. The magnetic susceptibility indicates an easy-axis along the [001] direction. A characteristic metamagnetic transition with two steps has been reported for $H \parallel [001]$ ⁴.

In order to reveal the ground state magnetic structure for DyRhIn₅, neutron scattering experiments have been carried out with use of TAS-2 spectrometer. Nuclear and magnetic scattering intensities were measured by triple axis mode with PG monochromator and analyzer at the neutron energy $E = 14.7$ meV. We found an antiferromagnetic structure with $q_1 = (\frac{1}{2} 0 \frac{1}{2})$ in the ground state⁵. The intensity of the $(\frac{1}{2} 0 \frac{1}{2})$ and $(\frac{1}{2} 0 \frac{3}{2})$ reflection shows a continuous temperature dependence of the magnetic order parameter as shown in Fig. 1. From the reflection intensities, we determined the magnetic structure as shown in Fig. 2. The estimated moment size was $8(1) \mu_B$. The magnetic structure of DyRhIn₅ is the same as NdRhIn₅⁶ and TbRhIn₅⁷.

- 5) N. V. Hieu *et al.*: Submitted to " J. Phys. Soc. Jpn."
- 6) S. Chang *et al.*: " Phys. Rev. B.", **66**, 132417 (2002).
- 7) R. Lora-Serrano *et al.*, cond-mat/0602612 (2006).

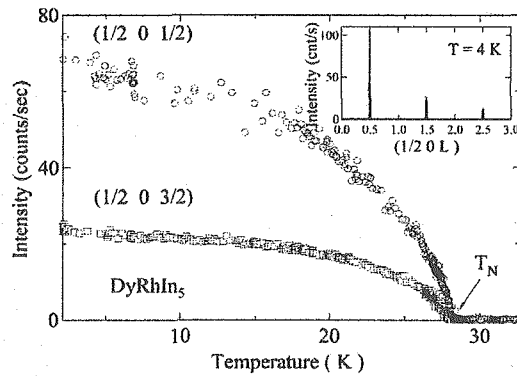


Figure 1: Temperature dependence of $(\frac{1}{2} 0 \frac{1}{2})$ and $(\frac{1}{2} 0 \frac{3}{2})$ peak intensity. The inset shows the magnetic peaks in $(\frac{1}{2} 0 L)$ scan.

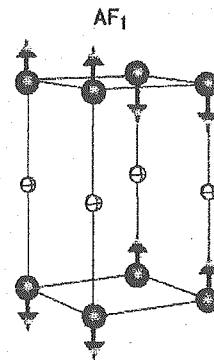


Figure 2: Magnetic structure of DyRhIn₅.

References

- 1) H. Hegger *et al.*: " Phys. Rev. Lett.", **84**, 4986 (2000).
- 2) R. Movshovich *et al.*: "Phys. Rev. Lett.", **86**, 5152 (2001).
- 3) C. Petrovic *et al.*: "Europhys. Lett.", **53**, 354 (2001).
- 4) N. V. Hieu *et al.*: " J. Phys. Soc. Jpn.", **75**, 074708 (2006).

研究テーマ：中性子散乱によるウラン化合物の物性研究
 中性子散乱実験による NpPtGa₅ の磁気構造の研究

1-6-4

The Magnetic Structure Study of NpPtGa₅ by Neutron Scattering

S. Jonen¹, N. Metoki^{1,2}, F. Honda¹, K. Kaneko¹, D. Aoki³,
 Y. Homma³, E. Yamamoto¹, Y. Shiokawa^{1,3} and Y. Ōnuki^{1,4}

¹Advanced Science Research Center, Japan Atomic Energy Agency, Tokai, Naka, Ibaraki, 319-1195, Japan

²Department of Physics, Tohoku University, Sendai 980-8578, Japan

³Institute for Materials Research, Tohoku University, Oarai, Ibaraki 311-1313, Japan

⁴Graduate School of Science, Osaka University, Toyonaka, Osaka 560-0043, Japan

Recently, systematic neutron experiments in NpTGa₅ ($T = \text{Fe, Co, Ni and Rh}$)¹⁻⁴ revealed a wide variety of magnetic structure, and the successive phase transition of 5*f* electronic state in NpRhGa₅³) and NpNiGa₅⁴). The NpTGa₅ crystallize in the same crystal structure as unconventional superconductor PuCoGa₅⁵). The successive phase transition observed at NpRhGa₅ and NpNiGa₅ was discussed theoretically by Kiss *et al.*⁶) in terms of localized 5*f* electron picture. They suggest that the 5*f* electronic state transition might be the consequence of the competing magnetic and quadrupolar interactions in the multi-5*f* orbital.

The NpPtGa₅ is antiferromagnet below $T_N = 27$ K. The magnetic field, applied parallel to the [100] direction, induces a second phase transition in the temperature dependence of magnetic susceptibility. Neutron scattering measurements have been performed to clarified the nature of the field induced phase transition, and to determine the magnetic structure of NpPtGa₅.

The high quality single crystal sample of NpPtGa₅ was grown by the Ga-flux methods. Neutron scattering experiments were carried out at thermal and cold triple axis spectrometers TAS-2 and LTAS installed at the research reactor JRR-3 in JAEA. Neutron scattering measurements under magnetic field up to 5 T have been carried out by using the superconducting magnet.

The magnetic structure of NpPtGa₅ have been clarified by elastic neutron scattering measurements. For temperature below T_N , the NpPtGa₅ exhibits an *A*-type antiferromagnetic structure with propagation vector $\vec{q}=(0\ 0\ 1/2)$, namely the Np magnetic moment of $0.4\ \mu_B$ is parallel to the $\langle 100 \rangle$ direction in the basal plane. This structure can be described with a ferromagnetic layer on a basal plane, stacked along the tetragonal *c*-axis in an antiferromagnetic sequence.

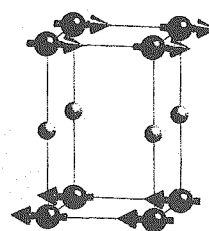


Figure 1: Magnetic structure of NpPtGa₅.

The neutron scattering measurements under application of magnetic field parallel to the [100] direction, revealed that the field induced phase transition observed in the magnetic susceptibility is due to a change of an antiferromagnetic domain structure, from multi-domain to single-domain case. The most intrigued result in this study is the necessity of high magnetic field above 10 T at $T = 1$ K, observed in the magnetic susceptibility, to change the magnetic domain structure to single-domain. Similar results have been observed in NpRhGa₅, where the antiferromagnetic domain became single-domain at 6 T ($T=3$ K)³. The NpPtGa₅ exhibits a identical magnetic structure as NpRhGa₅, with magnetic moment parallel to the basal plane at low temperature. The coexistence of ferroquadrupolar order with antiferromagnetic order in the NpRhGa₅, predicted theoretically by Kiss⁶), might be the hint to understand this problem.

References

- 1) F. Honda *et al.*: "Physica B", **359-361**, 1147 (2005).
- 2) N. Metoki *et al.*: "Phys. Rev. B", **72**, 14460 (2005).
- 3) S. Jonen :submitted to "Phys. Rev. B".
- 4) F. Honda :submitted to "Phys. Rev. B".
- 5) J. L. Sarrao *et al.*: "Nature", **420**, 297 (2002).
- 6) A. Kiss and Y. Kuramoto : "J. Phys. Soc. Jpn.", **75**, 034709 (2006).

1. 中性子散乱 7) 装 置

1. Neutron Scattering 7) Instrument

This is a blank page.

研究テーマ：中性子散乱によるウラン化合物の物性研究

表題：熱中性子 3 軸分光器 TAS-1 の高性能化

1-7-1

The Improvement of Triple-axis Spectrometer at JAEA: The New Double Bent PG Monochromator for TAS-1

S. Jonen¹ and N. Metoki^{1,2}

¹ASRC, Japan Atomic Energy Agency, Tokai, Naka, Ibaraki, 319-1195, Japan

²Department of Physics, Tohoku University, Sendai 980-8578, Japan

Instrumental improvement of the triple-axis spectrometers (TAS), installed in Research Reactor, JRR-3 at JAEA, is in progress for the study of strongly correlated electron systems such as actinide compounds and high T_C superconductors by neutron scattering. JAEA has installed three characteristic TAS spectrometers at JRR-3: TAS-1 at reactor room, provides a high flux thermal neutron beam with polarization / polarimetry option; The low background and high resolution are the advantage of TAS-2 installed at guide hall; whereas cold source neutron spectrometer LTAS has a high energy resolution.

High energy excitation and/or magnetic form factor can be measured only at TAS-1, where the incident beam for $E > 30$ meV is available. Therefore improvement of the high energy neutron flux at TAS-1 spectrometer is very important. For this propose, a new double bent PG monochromator is under construction.

The new double bent PG monochromator was designed with *Monte Carlo* simulation using the software McStas (Risø National Laboratory / Institute Laue-Langevin)^{1,2}. The size of monochromator and the focusing condition have been optimized by simulation. The simulation was carried out by using 9 columns \times 5 rows PG crystal array, (PG crystal - 30×20 mm²). The total size of monochromator with 270×100 mm² is necessary to use more efficiently the incident neutron flux at high energy region. From simulation results, we are expecting a gain of neutron flux around 9 times as larger as the flat

monochromator with the same size by using the double focusing. Figure 1 shows the projected double bent 9×5 PG monochromator, where the vertical and horizontal focus will be controlled independently by two step-motors.

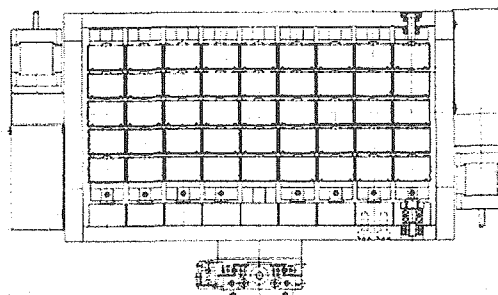


Figure 1: The projected double bent monochromator with 9×5 PG crystal array.

The new double bent PG monochromator will be installed at the new monochromator drum for TAS-1, with two others type of monochromators: The double bent Cu monochromator for high energy; and a flat Cu monochromator for magnetic form factor measurements up to high- Q range.

References

- 1) K. Lefmann and K. Nielsen : "Neutron News", **10**, 20 (1999).
- 2) P. Willendrup, E. Farhi and K. Lefmann : "Physica B", **350**, 735 (2004).

原子炉 : JRR-3 装置 : TAS-1(2G) 分野 : 中性子散乱 (装置)

研究テーマ：中性子光学の基礎研究と応用研究

表題：冷中性子用二重両凹面レンズによる中性子利用効率向上の実証

1-7-2

Concept and Establishment of Extended Biconcave Lens for Cold Neutrons

T. Adachi¹, T. Shinohara^{1,3}, K. Ikeda¹, K. Hirota¹, H. M. Shimizu^{1,2},
T. Oku³, H. Sasao³, S. Yamada³ and J. Suzuki³

¹ RIKEN, Wako, 351-0198

² High Energy Accelerator Research Organization, Tsukuba, 305-0801

³ Quantum Beam Science Directorate, JAEA, Tokai, 319-1195, Japan

Recent development of neutron optical devices has raised efficiency of neutron utilization¹⁻³). Simple biconcave lens works as focusing device for neutrons because of negative refractive index. The biconcave lenses were used for focusing geometry small angle neutron scattering instruments^{4,5}). Merit of biconcave lens in several neutron optical devices is comparatively fine focusing profile because of its simple shape. However, the biconcave shape whose outer side is thicker causes a demerit of less transmission of neutron beam. Therefore, the biconcave shape is unsuitable for large aperture lens. So far aperture of the biconcave lens was less than 25 mm in diameter practically. We have developed a ring-like lens composing a concentric circle with the biconcave lens as shown in Fig. 1. The aperture of the lens was enlarged up to 45 mm in diameter and loss of neutrons absorbed should be reduced because thickness of outer part of the lens decrease compared with single large aperture lens. We obtained 1.5 times better intensity than the usual biconcave lens as shown in Fig. 2. Comparison of performances between these two systems was summarized in Table 1. This can be one of the methods to improve utilizing efficiency of neutrons.

References

- 1) T. Oku and H. M. Shimizu: "Physica B", **283**, 314 (2000).
- 2) H. M. Shimizu, T. Oku and T. Adachi: "Physica B", **311**, 123 (2002).
- 3) H. M. Shimizu: "Appl. Phys. A", **74**, S326 (2002).
- 4) M. R. Eskildsen *et al.*: "Nature", **391**, 563 (1998).
- 5) S.-M. Choi *et al.*: "J. Appl. Cryst.", **33**, 793 (2000).

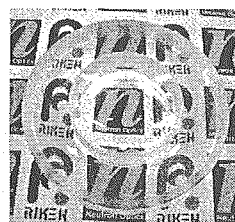


Figure 1: Photograph of double biconcave lens.

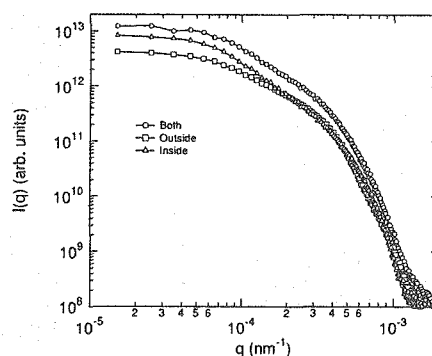


Figure 2: Beam profile of intensity v.s. momentum-transfer, q .

Table 1: Comparison of performances

	Inside	Outside	Both
Radius (mm)	0-13.5	16.5-23	0-13.5, 16.5-23
Transmission	0.41	0.29	0.35
FWHM (mm)	2.2	2.4	2.4
Relative Area	1	1.4	2.4
Relative intensity	1	0.5	1.5

原子炉：JRR-3

装置：SANS-J(C3-2)

分野：中性子散乱（装置）

研究テーマ：中性子利用実験装置の開発研究
 表題：永久六極磁石型中性子磁気レンズの開発

1-7-3

Development of a Magnetic Neutron Lens Based on an Extended Halbach-type Permanent Sextupole Magnet

T. Oku, S. Yamada, H. Sasao, J. Suzuki, T. Shinohara¹, K. Hirota¹,
 K. Ikeda¹ and H. M. Shimizu¹

Quantum Beam Science Directorate, JAEA, Tokai, Ibaraki 319-1195

¹RIKEN, Wako, Saitama 351-0198

We have developed a magnetic neutron lens (MNL) based on an extended Halbach-type permanent sextupole magnet for the application to focusing-geometry small-angle neutron scattering (FSANS) experiments¹⁾. In this study, we investigated the neutron focusing property of the MNL by using pulsed polarized neutrons. Figure 1 (a) shows the schematic cross section of the MNL. The sextupole magnetic field distribution $|\mathbf{B}| = (G/2)r^2$ with the magnetic field gradient coefficient $G = 10,660 \pm 530 \text{ T/m}^2$ is generated inside the MNL. The experiment was carried out at the beam line of C3-1-2-1 (NOP) of JRR-3 in Japan Atomic Energy Agency (JAEA). The experimental setup is shown in Fig. 1 (b). The neutron beam pulsed by a chopper was polarized by using a quadrupole magnet. The neutron wavelengths were determined by the time-of-flight method with wavelength resolution $\Delta\lambda/\lambda = 0.03$ in FWHM around $\lambda = 8 \text{ \AA}$. Figure 2 shows the radial average of the measured neutron intensity distribution on the detector plane. The intensity peak became sharpest when the focal condition was satisfied at $\lambda =$

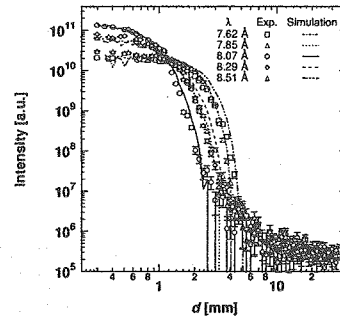


Figure 2: Radial distribution of the focused beam intensity.

8.07 Å. The intensity peak with the ratio of the peak height to the background level of $\sim 4 \times 10^5$ was observed at the focal condition, so that the MNL was considered as the applicable focusing device to the FSANS experiments.

References

- 1) T. Oku, *et al.* : "Physica B" (2006) in press.

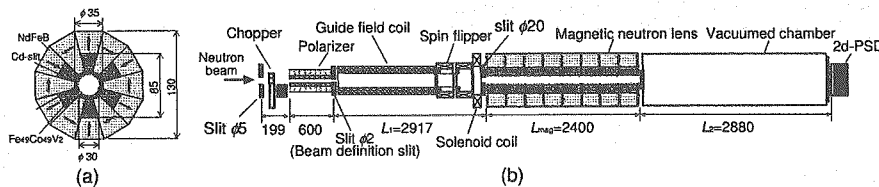


Figure 1: (a) A schematic cross section of the extended Halbach-type sextupole magnet. (b) The experimental setup.

原子炉：JRR-3 装置：NOP(C3-1-2-1) 分野：中性子散乱（装置）

研究テーマ：中性子利用実験装置の開発研究
 表題：四極磁石を用いた高性能中性子偏極装置の開発

1-7-4

Development of a Highly Efficient Neutron Polarizing Device Based on a Quadrupole Magnet

T. Oku, S. Yamada, J. Suzuki, K. Mishima¹, T. Shinohara¹, K. Hirota¹,
 K. Ikeda¹, H. Sato¹ and H. M. Shimizu¹

Quantum Beam Science Directorate, JAEA, Tokai, Ibaraki 319-1195

¹RIKEN, Wako, Saitama 351-0198

We have developed a neutron polarization device based on a Halbach-type permanent quadrupole magnet (HQM) (Fig. 1 (a)). The HQM consists of 12 segments of strong permanent magnet NdFeB, and has an aperture size of 5 mm in diameter and the length of 600 mm (Fig. 1 (a)). Neutron absorbing Cadmium (Cd) cylinders with inner diameter of 3.5 mm were inserted into the HQM aperture for the suppression of neutron reflection on the inner surface of the HQM. According to the magnetic field measurement, the magnetic field gradient $\partial|B|/\partial r = 791.9 \pm 8.3$ T/m is realized in the HQM aperture. By passing through the aperture of the HQM, positive and negative polarity neutrons are accelerated in opposite directions and are spatially separated due to the magnetic field gradient. Then, by extracting one spin component, we can obtain a polarized neutron beam.

A cold neutron polarization experiment was performed at the beamline of C3-1-2-1(NOP) of JRR-3 in Japan Atomic Energy Agency (JAEA). The experimental setup is shown in Fig. 1 (b). A neutron beam with wavelength

$\lambda = 9.5 \pm 0.3 \text{ \AA}$ and size of 2 mm in diameter is incident into the aperture of the HQM. In this experimental condition, negatively polarized neutrons are accelerated away from the HQM center axis, and then expected to hit the Cd cylinders, resulting in being absorbed. On the other hand, positively polarized neutrons are accelerated toward the HQM center axis, and expected to pass through the HQM. The polarization degree of the neutrons passing through the HQM was measured by using the superconducting sextupole magnet (SSM)¹⁾ and the 2-dimensional position sensitive detector (2d-PSD)²⁾ (Fig. 1 (b)). As a result, an extremely high polarization degree of $P = 0.9993 \pm 0.0059$ was obtained in spite of the fact that the obtained value included the influence of the depolarization effect due to the imperfect adiabatic field condition along the neutron beam axis.

References

- 1) J. Suzuki *et al.* : "J. Appl. Cryst." **36**, 795-799 (2003).
- 2) K. Hirota *et al.* : "Phys. Chem. Chem. Phys.", **7**, 1836-1838 (2005).

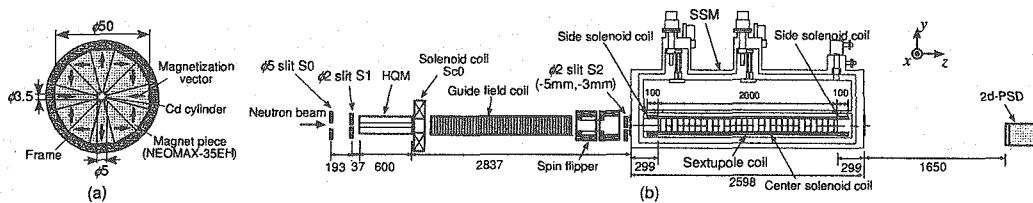


Figure 1: (a) A schematic of the cross section of the Halbach-type quadrupole magnet. (b) The experimental setup.

原子炉：JRR-3 装置：NOP(C3-1-2-1) 分野：中性子散乱 (装置)

研究テーマ：中性子光学の基礎研究と応用研究

表題：シンチレーターを用いた中性子2次元検出器の開発

1-7-5

Development of Flatpanel Anger Detector

K. Hirota, S. Satoh¹, H. M. Shimizu¹, T. Shinohara², T. Oku² and J. Suzuki²

Riken, Wako, Saitama 351-0198

¹*KEK, Tsukuba, Ibaraki 305-0801*

²*Quantum Beam Science Directorate, JAEA, Tokai, Ibaraki 319-1195*

Neutron optical devices such as a neutron magnetic lens and material lens for a cold neutron beam have been developed ¹⁾ recently. These devices need good spatial resolution of less than 1mm² for the detector. We have developed scintillation detectors ²⁾, which is called RPMT. This RPMT detector has good performances for spatial resolution, high signal-to-noise ratio and user friendliness, but it is difficult to expand larger effective area. Therefore we have started to develop a new neutron detector, called flatpanel Anger detector.

This detector consists of neutron sensor, DAQ system and a monitoring PC. A 64-channel flatpanel PMT (FPMT), Hamamatsu H8500 and ZnS(Ag)/⁶LiF scintillator are used for the neutron sensor. The data taking system is constructed using 10-bit 100 MHz FADC and Xilinx FPGA chips. The 64 anodes and a dynode output signals are pulse-shaped by amplifier and digitalized by FADC chips in parallel. The trigger timing is used by the dynode signal. The effective area of this detector is around 25 cm², and it is easy to expand larger area with small dead space by multi-FPMT's system. A 'center of the light yield position' calculation is used on the pulse height data of 9 pixels of the FPMT including the brightest central pixel and its surrounding 8 pixels. In the case of the brightest pixel is in peripheral of the FPMT, the position is decided by the ratio of the brightest pixel and the next pixel.

The two-dimensional image of cold neutron beam is shown in Fig. 1. This figure shows

collimated neutron beam with a 5 mm-gap-comb-shaped cadmium slit. Neutron detecting counts of the central region is the highest because the neutron beam is not uni-field.

The spatial resolution was measured using a cadmium collimator with a diameter of 0.5 mm and thickness of 1 mm. This measured spatial resolution is originated from both collimator size and detector resolution. The neutron beam wavelength was 0.95 nm. The measured spatial resolution is typically 0.8 mm FWHM in central region and getting worse to around 1.5 mm in the peripheral pixel region. This measurement is consistent with the result of Fig. 1. This is because the calculating method is not so suitable in peripheral pixel region, and we should develop new analyzing method.

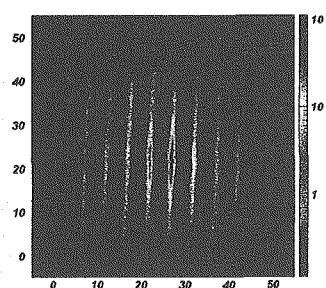


Figure 1: Two-dimensional image of cold neutron beam.

References

- 1) H. M. Shimizu *et al.*: "Physica B", **311**, 23 (2002).
- 2) Katsuya Hirota *et al.*: "Phys. Chem. Chem. Phys.", **7**, 1836 (2007).

原子炉：JRR-3

装置：NOP(C3-1-2-1)

分野：中性子散乱（装置）

研究テーマ：圧電性結晶による中性子制御の実験的研究

表題：圧電性結晶による中性子制御の実験的研究

1-7-6

Experimental Study on Neutron Control by Using Piezoelectric Single Crystals

S. Kawamura¹, J. H. Kaneko¹, K. Tanabe¹, K. Aizawa², A. Homma², Y. Otake³,
H. Fujimoto⁴, F. Fujita¹ and M. Furusaka¹

¹Hokkaido University, N13 W8, Kita-ku, Sapporo, 060-8628, Japan

²JAEA, Tokai, Naka, Ibaraki 319-1195, Japan

³Riken, 2-1 Hirosawa, Wako, Saitama 351-0198, Japan

⁴AIST, Umezono 1-1-1, Tsukuba 305-8563, Japan

D-spacing of piezoelectric-crystal varies with applying electric field. We have been trying to develop novel neutron-optical-devices using piezoelectric-crystals. As the first step of this study, we carried out a experiment using $(1-x)(\text{Pb}(\text{Mg}_{1/3}\text{Nb}_{2/3})\text{O}_3)-x(\text{PbTiO}_3)$ (PMN-PT) single-crystal whose piezoelectricity is about 1000 times larger than α -quartz single crystals. The sample used in the experiment was purchased from MTI Corp and its dimension was $10 \times 8 \times 0.5 \text{ mm}^3$. The surface of sample was parallel to the planes (001) and the piezoelectric coefficient d_{33} was 2000 pC/N. Aluminium electrodes of about $1 \mu\text{m}$ thickness were evaporated on both faces of the sample and $25 \mu\text{m}$ diameter gold wires were attached to the electrodes. The sample was poled at $180 \text{ }^\circ\text{C}$ for 30 min under a loaded electric field of 14 kV/cm and then field-cooled to room temperature¹⁾.

Diffraction experiment was carried out using the PNO instrument equipped at the JRR-3 reactor of the Japan Atomic Energy Agency. The schematic diagram of experimental setup is shown Fig. 1. The entire setup was situated on the optical bench of the PNO and monochromatic neutrons of 2.0 \AA were used for the experiment. Rocking curves (RC) of the crystal were obtained under various voltages from 100 V to 700 V, which correspond to electric fields between 2 kV/cm and 14 kV/cm. A ^3He proportional detector was used and the statistical er-

rors at each measuring point near the peak were about 1.2 %.

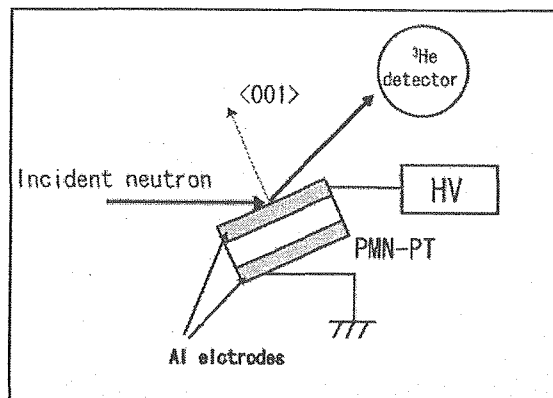


Figure 1: Experimental layout of PNO. Monochromatic neutrons of 2.0 \AA were used and rocking curves of PMN-PT were measured before and after applying the electric fields.

As shown in Fig. 2, the angular position of the diffraction peaks was changed by the electric field. Changes in its full width at half maximum were observed. The angular position of the diffraction peaks related to the rocking curve measurements showed time-dependent variation after the applied electric field was changed from one value to another. As shown in Fig. 3, each variation was well described by a single exponential decay function limiting to a saturated value. The time constants had different values when applied electric fields were changed, but they were on

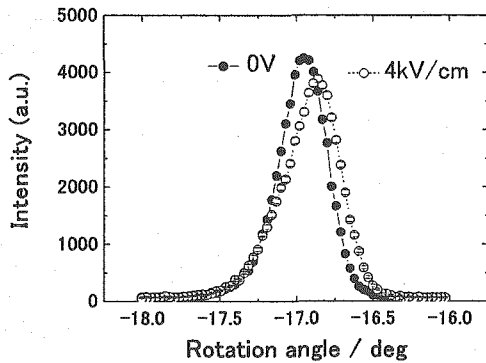


Figure 2: Rocking curve at electric field 0 V/cm and 4 kV/cm.

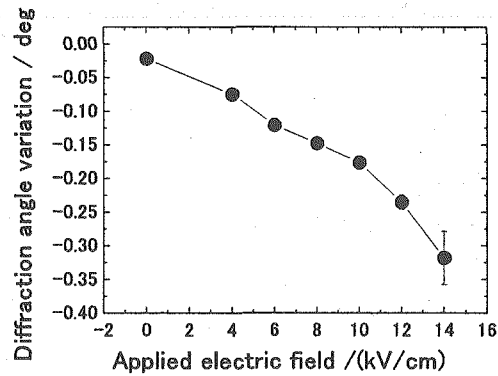


Figure 4: Saturated value of diffraction angle variation for different values of the applied electric field.

the order of hours. The origin of this time-dependent variation of the diffraction angle is considered to occur through a slow relaxation of the domain configuration induced by the electric field applied to the crystals.

Saturation values of the angular position of the peaks of the rocking curves that were obtained from curve-fitting are shown in Fig. 4. A maximum diffraction-angle change of about 0.32 was obtained.

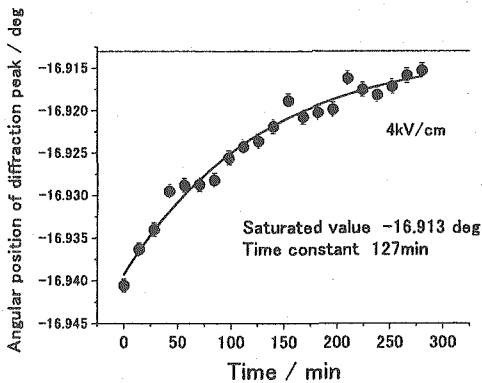


Figure 3: Time-dependent variations of the peak position on the rocking curve after changing the electric field of 0-4 kV/cm.

Dramatic changes of the d-spacing in the piezoelectric single-crystal (PMN-PT) were confirmed in this experiment. The Bragg-angle variations attributable to the applied electric field are sufficiently large and present the possibility of the crystal's use as a novel neutron optical device. Further experiments aimed at improving the characteristics of the device are in progress. First, the form factor of the (001)-reflection is intrinsically small because of the titanium it contains, which has a negative scattering length. The following experiments will be concentrated on the (111)-reflection, which has a much larger form factor. Furthermore, some dynamic experiments that apply a high-frequency electric field of megahertz order are planned for the near future.

References

1) T. Y. Koo and S- W. Cheong : "Appl. Phys. Lett.", 80, 4205 (2002).

研究テーマ：先端偏極中性子散乱によるスピン格子物性の研究
表題：中性子磁気散乱実験のためのハイブリッドアンビル技術の開発

1-7-7

Development of a Hybrid-anvil Type High-pressure Device for Magnetic Neutron Diffraction Studies

T. Osakabe

Quantum Beam Science Directorate, JAEA, Tokai, Ibaraki 319-1195

We have newly developed a hybrid-type anvil device (HA) for high-pressure neutron scattering studies beyond 3 GPa. The device is composed of a sapphire anvil and a WC anvil. Figure 1 shows a schematic drawing of the HA. The essential point is a hollow in the center of the culet of the WC anvil. This hollow highly suppresses deformation of the gasket sandwiched between the two anvils, since a part of the gasket is strongly caught by the edge of the hollow when the gasket is pressed. This gives three important effects. One is preventing the sapphire anvil from cracking. Another is enlarging the sample chamber and the other is improving the pressure generation efficiency. As a matter of course, the sapphire is transparent for neutron and generates low background. Furthermore, we can easily measure the pressure value by a ruby-fluorescence method through the sapphire anvil.

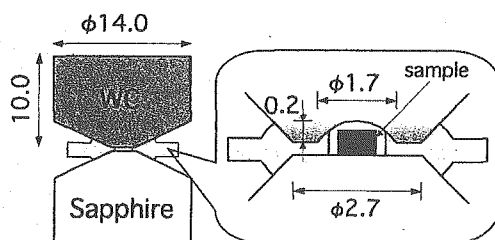


Figure 1: Schematic drawings of a hybrid-anvil device.

Figure 2 shows the result of the feasibility test of the HA and the sapphire-anvil device (SA) for comparison ¹⁾. The test conditions are as follows. For the HA, the diameter of the culet, the pressure medium and the gasket material are 2.7 mm, glycerin and Al al-

loy (JIS A2017P, tensile strength : 0.38 GPa), respectively. On the other hand, for the SA, those are 2.35 mm, Daphne 7373 oil and brass (JIS C6782B, 0.49 GPa), respectively. As clearly seen in Fig. 2, the pressure generation efficiency of the HA is superior to that of the SA. Furthermore, the available sample volume determined by the initial diameter of the sample chamber and the final distance between two anvils is about 2.5 times larger than that of the SA. In the test, the pressure of 5 GPa was generated easily by the HA without cracks in the anvils.

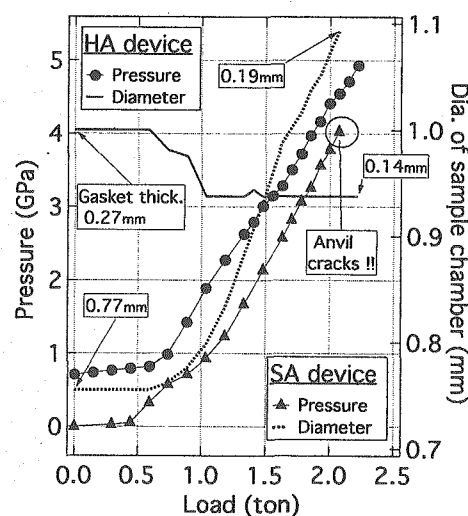


Figure 2: Generated pressure and diameter of the chamber versus applied load for the HA and the SA.

References

- 1) T. Osakabe, M. Kohgi, D. Kawana, K. Soyama and H. Kitazawa: "J. Magn. Magn. Matt.", **272-276**, 2157-2158 (2004).

研究テーマ：高効率・高分解能マイクロストリップガス計数管の開発
 表題：高効率・高分解能マイクロストリップガス計数管の開発

1-7-8

Development of a High-resolution Two-dimensional MicroStrip Gas Chamber

H. Takahashi, P. Siritiprussamee, K. Fujita, T. Oku¹ and J. Suzuki¹

Department of Nuclear Engineering and Management, Graduate School of Engineering, The University of Tokyo 113-8656

¹Quantum Beam Science Directorate, JAEA, Tokai, Ibaraki 319-1195

High-resolution neutron imaging detectors are required for future high-intensity neutron sources. We are developing a high-resolution gaseous neutron detector by using multi-grid-type MSGC with floating pad readout method¹⁾. Nowadays, Microstrip Gas Chambers are successfully used in neutron applications. However, conventional MSGCs with the virtual cathode readout still have limited performance at the high counting rate applications. A floating pad readout method does not require a conducting glass whose resistivity should be controlled between the lower limit (for dark current) and the upper limit (for counting rate performance) for the virtual cathode readout method. In our floating pad readout method, readout pads are separated from the anode and induced charge is transmitted through the insulator layer. Therefore, the resistivity control is not a crucial issue in our detector. We are testing detectors of several different geometry and the electrode configuration. Due to the pin limitation of the pressure vessel, we used a charge-division readout method for position localization. The experiment was performed at the NOP beam line of the JAERI JRR-3 neutron scattering facility. A collimated neutron beam of 0.5 mm diameter was incident on the detector. For a 3cm × 3cm MSGC filled with 5 bar CF₄ and 0.5 bar ³He, we could achieve a measured position resolution of 0.6 mm (FWHM) including the beam size and the parallax error (see Fig. 1). Example of the image is shown in Fig. 2. The Global-Local readout principle²⁾ can also be combined with this method.

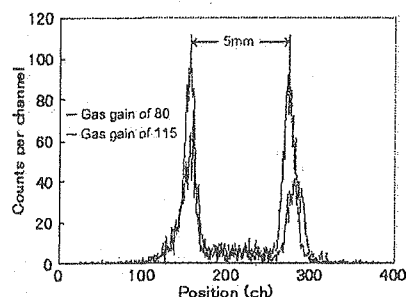


Figure 1: Obtained neutron resolution at different gas gain.

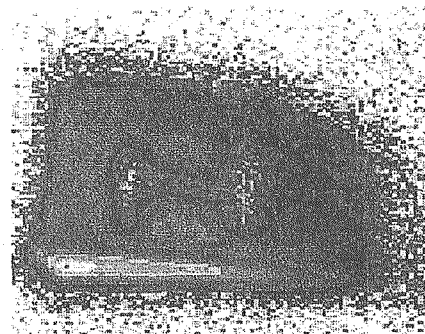


Figure 2: Sample neutron image taken with Cd plate.

References

- 1) H. Takahashi, P. Siritiprussamee, *et al.*: "Nucl. Instr. and Meth.", **A529**, 348 (2004).
- 2) P. Siritiprussamee, H. Takahashi, *et al.*: "IEEE Trans. on Nucl. Sci.", **53**, No.1, 326 (2006).

研究テーマ：中性子散乱によるソフトマターの構造と機能の研究
表題：JAEA 超小角中性子散乱装置におけるタンデム検出系の構築

1-7-9

A New Tandem Crystal System for Bonse-Hart Ultra-small-angle Neutron Scattering Spectrometer at JAEA

D. Yamaguchi, S. Koizumi, R. Motokawa, T. Kumada, K. Aizawa¹ and T. Hashimoto

Advanced Science Research Center, JAEA, Tokai, Ibaraki 319-1195

¹*Quantum Beam Science Directorate, JAEA, Tokai, Ibaraki 319-1195*

A new tandem channel-cut crystal system was introduced on Bonse-Hart ultra-small-angle neutron scattering (USANS) spectrometer at research reactor JRR-3, Tokai, Japan. For conventional Bonse-Hart setup ¹⁾, it consumes a considerable time (20hrs) to measure a scattering profile of whole q-range ($2 \times 10^{-4} \leq q \leq 7 \times 10^{-2} \text{ (nm}^{-1}\text{)}$, where q denotes magnitude of scattering vector) due to the step scan system. To improve this situation, two analyzer channel-cut silicon (Si) perfect crystals were settled in tandem and operated simultaneously and consequently the measurement time was reduced to half. As schematically illustrated in Fig. 1, a new tandem optical system consists of three triple-bounce Si [111] channel-cut crystals and the third one is employed for the second analyzer crystal. The two analyzer crystals play different parts in collecting the scattering; one is for the smaller scattering angles whose corresponding q value ranges $2 \times 10^{-4} \leq q \leq 4 \times 10^{-3} \text{ (nm}^{-1}\text{)}$ and the other is for the larger scattering angles of $2 \times 10^{-3} \leq q \leq 7 \times 10^{-2} \text{ (nm}^{-1}\text{)}$. In Fig. 2 an example of tandem measurement is compared with conventional one. The specimen employed for the measurements was a polymer blend film, which has phase separated structures of micrometer scale and gives considerable scattering intensity at the q-range of USANS. By comparison of two kinds of measurements shown in Fig. 2, we discern that tandem measurement gives nearly the same scattering profile with the conventional measurement within half of the measurement time.

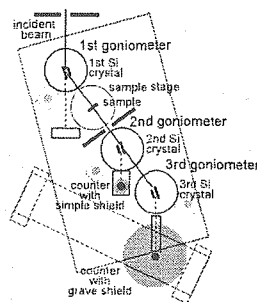


Figure 1: New tandem USANS set-up.

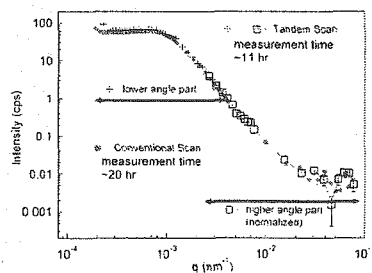


Figure 2: Example of tandem measurement. Symbols of + mark and open square represent the data of tandem scan, while symbol of filled circle represents the data of conventional scan.

References

- 1) K. Aizawa, H. Tomimitsu :Design and use of a double crystal diffractometer for very small angle neutron scattering at JRR-3M, "Physica B", 213/214, 884 (1995).

研究テーマ：先端偏極中性子散乱によるスピン-格子物性の研究
表題：新偏極モノクロメータとアナライザの製作と設置

1-7-10

Introduction of the 3-D Polarization Analysis Device CRYOPAD on TAS-1 at JRR-3

I. New Polarizing Monochromator and Analyser System on TAS-1

M. Takeda, M. Nakamura, Y. Shimojo, P. Courtois¹, K. H. Andersen¹ and K. Kakurai

Quantum Beam Science Directorate, JAEA, Tokai, Ibaraki 319-1195

¹*Institut Laue-Langevin, BP 156, Cedex 9, F-38042 Grenoble, France*

Recently the functional materials, such as giant magneto-resistance and multiferroic materials, are being widely investigated by both the experimental and theoretical condensed matter physicists. In these materials the spin, charge and orbital degrees of freedom often interact in intriguing ways to display their macroscopic functional characteristics. The neutron scattering sensitive both to statics and dynamics of the spin and lattice systems is an ideal tool to gain fundamental understandings of these interesting systems often relevant to applications. Especially the use of polarized neutrons is expected to play a key role due to the sensitivity to the nuclear-magnetic interference term. The Polarized Neutron Magnetism Group in the Quantum Beam Science Directorate of Japan Atomic Energy Agency (JAEA), former Research Group for Neutron Scattering Studies on Spin-Lattice Correlations in the Advanced Science Research Center, has therefore been upgrading the polarized neutron capability of the thermal neutron triple-axis spectrometer TAS-1 over the last five years. The two main objectives of this upgrade program were

- 1) the construction and installation of the new polarizing monochromator and analyser, to improve the polarized neutron flux and detectability, and
- 2) the construction and installation of the third generation CRYOPAD, called CRYOPADUM, to enable the 3-dimensional polarization analysis on TAS-1.

To replace the old flat Cu_2MnAl Heusler

monochromator and analyser a pair of doubly focusing Heusler polarizing monochromator and analyser has been constructed and installed. The magnetic circuits for the devices were carefully designed by using a 3D finite-element-calculation program. The detailed specifications such as reflecting area, bent angles for each crystal have been optimized by using the neutron ray-trace simulation package, McStas, assuming a sample size of 10 mm diameter and 20 mm height. The high-quality Heusler crystals with the dimensions approximately $20 \times 21 \times 6 \text{ mm}^3$ were produced at ILL¹⁾ and were carefully checked individually on their mosaicity, reflectivity and polarizing efficiency on TAS-1. All the crystals confirmed to have single grain and showed flipping ratios of 15-30 for 14.7 meV neutrons. The averaged reflectivity was 25% at peak position of the rocking scan. The crystals were then ranked by the quality factor $P \times I$, where P is the polarizing efficiency and I is the integrated intensity. Figure 1 shows the rocking curves of the highest and lowest ranked crystal used for the monochromator. In both devices 5 Heusler crystals are mounted on 7 columns with fixed vertical curvature optimized for 30.5 meV neutrons.

After assigning the better quality crystals to the near center positions of the reflecting area, the crystals were finally cut into a specific shape according to their positions to make the composite vertical curvature without air gap between the crystals. The horizontal curvature can be varied by rotating

原子炉：JRR-3 装置：TAS-1(2G) 分野：中性子散乱 (装置)

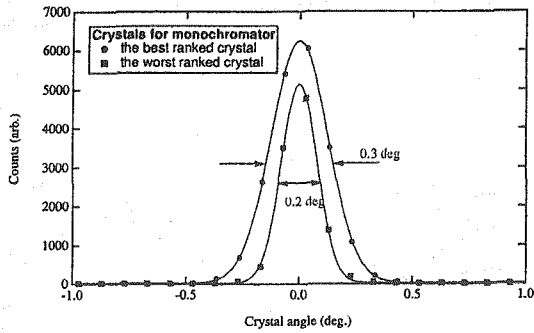


Figure 1: The rocking scans for the best and lowest ranked Heusler monochromator crystal.

the outer three columns on each side (see Fig. 2). The performance of the new polarizing monochromator including the horizontal focusing performance was reported earlier²⁾.

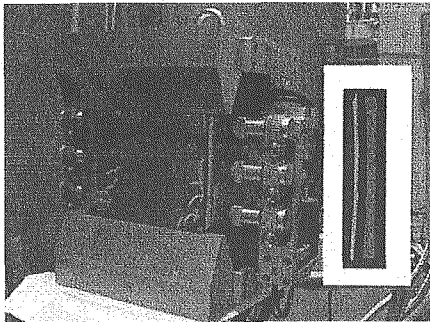


Figure 2: The doubly focusing polarizing monochromator for TAS-1. The inset picture shows the curved boron nitride column plate with the crystals glued on.

Figure 3 depicts the comparison of the vanadium incoherent scattering intensities as measured with the old and new polarizing and analyzing Heusler systems with $E_i=14.7$ meV. The polarization under the same condition is determined to be 92% by the flipping ratio measurement on the (004) pyrolytic graphite (PG) Bragg reflection. Hence an overall gain factor of 30 is clearly achieved without loss of the neutron polarization. The energy resolutions for two different incident energies are shown in Fig. 4 with optimized horizontal focusing.

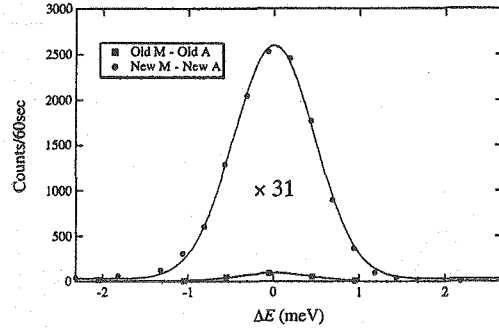


Figure 3: Comparison of the vanadium incoherent scattering intensities as measured with the old and new polarizing and analyzing systems.

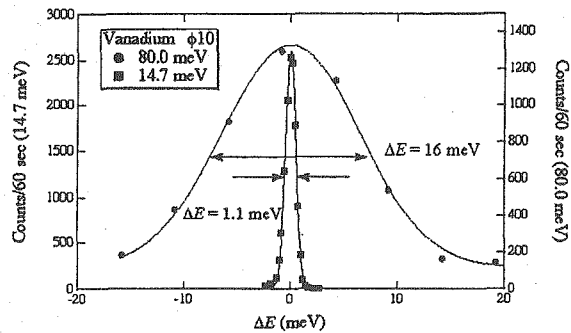


Figure 4: Energy resolutions for two different incident neutron energies as measured using vanadium incoherent scattering with the new system with horizontal focusing.

In summary the increased flux and improved detectability of the polarized neutrons by the new polarizing and analyzing system enable the introduction of the elastic and especially inelastic spherical polarimetry on TAS-1, as will be reported in the following report.

References

- 1) P. Courtois : " Physica B", 267-268, 363 (1999).
- 2) M. Nakamura, M. Takeda, Y. Shimojo and K. Kakurai: PROGRESS REPORT ON NEUTRON SCATTERING RESEARCH March 2004, "JAERI-Review 2004-005", pp. 140-141 (2004).

研究テーマ：先端偏極中性子散乱によるスピン格子物性の研究
表題：CRYOPADUMの開発と設置

1-7-11

Introduction of the 3-D Polarization Analysis Device CRYOPAD on TAS-1 at JRR-3

II. Construction and Installation of the CRYOPADUM

M. Takeda, M. Nakamura, A. Oosawa¹, Y. Shimojo, E. Lelievre-Berna², F. Tasset²,
L.-P. Regnault³ and K. Kakurai

Quantum Beam Science Directorate, JAEA, Tokai, Ibaraki 319-1195

¹*Dep. of Physics, Sophia University, Chiyoda-ku, Tokyo 102-8554*

²*Institut Laue-Langevin, BP 156, Cedex 9, F-38042 Grenoble, France*

³*CEA-Grenoble, SPSMS-MDN, F-38054 Grenoble Cedex 9, France*

In the CRYogenic Polarization Analysis Device, CRYOPAD, as proposed by Tasset¹⁾, the different spin control magnetic field regimes and the zero-field chamber are most effectively separated by the Niobium shields cooled into the Meissner superconducting state and the vectorial control of neutron polarization at high momentum transfer Q could be achieved. In the historical CRYOPAD (Cryopad-I) the precession angles were controlled with small vertical coils, one being moved inside the cryostat in order to intercept the scattered beam. In the second generation CRYOPAD (Cryopad-II) a monolithic system based on a superposition of two horizontal superposed toroidal coils was developed. This second system was giving satisfaction to within 2° of absolute precision when intercepting an incoming beam less than 2 cm in diameter. But, due to the very weak scattering cross-sections involved in inelastic investigations we now seek at larger divergence for the incoming beam and there is a corresponding need to increase the size of the homogeneous region in the Larmor coil intercepting the incident beam. According to recent computer simulations at ILL by M. Thomas it is possible to achieve a high homogeneity in compact coils by combining Meissner shields and μ -metal yokes in their construction. This new design will also remove the systematic errors due to the superposition of the primary

and secondary fields present in the design of Cryopad-II. This third generation CRYOPAD Using μ -metal, CRYOPADUM, has been developed within the frame of the ILL millennium programme, the European ENPI network and the ILL/ASRC/JAERI Memorandum of Understanding and three copies are built for D3/ILL diffractometer, the IN22/CEA and TAS-1/JAEA (former JAERI) triple-axis spectrometers. The aim of this collaboration is to open new fields of investigation exploiting spherical neutron polarimetry in elastic and inelastic scattering experiments^{2,3)}.

To check the interference the CRYOPADUM is rotated by 135° from the normal position, where the primary coils faces the incident beam. As can be seen in the inset of Fig. 1, using $E_i=14.5$ meV and PG(004) $2\theta=90^\circ$ Bragg reflection, both the

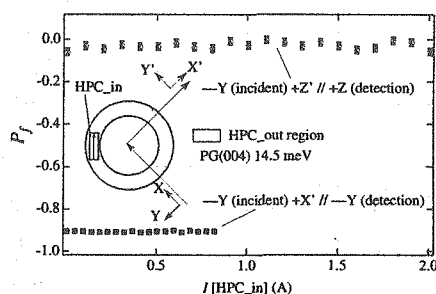


Figure 1: The final polarization versus primary coil current.

原子炉：JRR-3 装置：TAS-1(2G) 分野：中性子散乱 (装置)

incident and scattered neutrons pass only the secondary coil. The final polarization P_f was measured as a function of primary coil current. If the field produced by the primary coil would interfere with the secondary coil precession field, the P_f would change by the parasitic field of the primary coil. Figure 1 clearly indicates that there is no coupling between the primary and secondary precession fields.

Successful elastic polarimetric investigation of CdCr_2O_4 , a frustrated pyrochlor antiferromagnet, revealing the existence of an elliptical magnetic ground state has been already reported⁴⁾. Here we show inelastic scattering results demonstrating the potential of the CRYOPADUM for spherical polarimetry on spin excitations. As an example the spin excitation in $\text{SrCu}(\text{BO}_3)_2$, an orthogonal dimer system, so called Shastry-Sutherland system is looked at. In this system an almost dispersionless excitation is observed at 3 meV energy transfer, when observed with an energy resolution of 1 meV, a typical energy resolution of the thermal neutron spectroscopy. Figure 2 shows the spin flip and non spin flip scattering of the spin excitation at $Q=(1.5, 0.5, 0)$ when polarization is along the scattering vector, i.e. along x direction. The excitation is interpreted as a non-propagating triplet excitation due to the frustrated interdimer exchange between the orthogonally arranged neighbouring dimers. Figure 3 depicts all the nine polarization matrix elements for the 3 meV excitation measured at $Q=(1.5, 0.5, 0)$. One can clearly recognize the purely magnetic character of this excitation, because $P_{xx}=-0.9$, 90% being the instrument polarization in accord with the results shown in Fig. 2. Within the accuracy of the measurements there is no transverse component of the scattered polarization, which are perpendicular to the initial direction. The finite value in P_{yy} may indicate a slight deviation of the isotropic fluctuation, which would cause a full depolar-

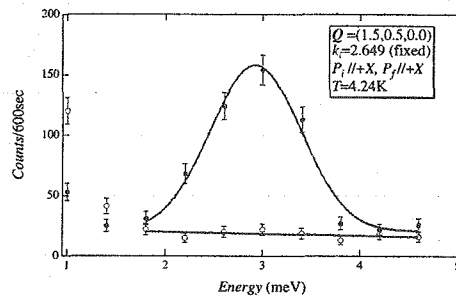


Figure 2: The spin flip and non spin flip scattering intensity of the spin excitation at $Q=(1.5, 0.5, 0)$.

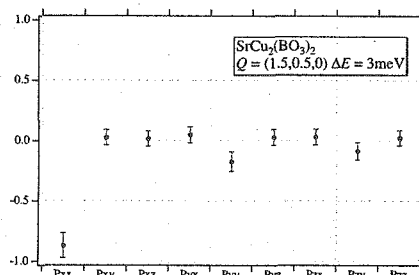


Figure 3: The nine polarization matrix elements for the 3 meV excitation measured at $Q=(1.5, 0.5, 0)$.

ization in P_{yy} and P_{zz} . A more detailed investigation of the anisotropy of the triplet excitation and transverse component at different reciprocal positions are under consideration.

In summary the above results impressively demonstrate the high performance of the new CRYOPADUM on TAS-1 and its potential to open new fields of investigation in the condensed matter magnetism.

References

- 1) F. Tasset: "Physica B", **156-157**, 627 (1999).
- 2) K. Kakurai: "Annual Report on Neutron Science 2004, Highlights in Research at JAERI", pp. 9 (2004).
- 3) M Takeda *et al.*: PROGRESS REPORT ON NEUTRON SCATTERING RESEARCH March 2005, "JAERI-Review", **2005-013**, pp. 124 (2004).
- 4) K. Kakurai: "Annual Report on Neutron Science 2005, Highlights in Research at JAERI", pp. 11 (2004).

1. 中性子散乱 8) 残留応力



1. Neutron Scattering 8) Residual Stress

This is a blank page.

研究テーマ：パーライトパテント材の引張試験中中性子その場測定
表題：パーライト鋼の内部応力に及ぼすラメラ間隔の影響

1-8-1

Effect of Lamellar Spacing on Internal Stress of a Pearlite Steel

T. Shinozaki, S. Morooka¹, Y. Shiota¹, T. Suzuki² and Y. Tomota³

Graduate student of Ibaraki University, Hitachi, Ibaraki 316-8511

¹*Graduate student of Ibaraki University, Hitachi, Ibaraki 316-8511*

²*Superplasticity Research Center, Ibaraki University, Hitachi, Ibaraki 316-8511*

³*Graduate School of Science and Engineering, Ibaraki University, Hitachi, Ibaraki 316-8511*

1. Introduction

In a pearlitic steel, phase and intergranular stresses are yielded due to inhomogeneous plastic flow between ferrite and cementite and among differently oriented ferrite blocks, respectively. Such internal stresses must be dependent on microstructural factors. In this study, we examined the effect of lamellar spacing on internal stress after tensile test by means of neutron diffraction.

2. Experimental Procedures

The chemical compositions of steels used are 0.801C-0.01Mn-0.01Si-0.01P-0.01S in mass%. Specimens were austenitised at 1173K followed by holding at 673K (specimen A) or 823K (B) for 3.6 ks to complete isothermal transformation from austenite to pearlite. The average lamellar spacings (S_0) determined from SEM micrographs are 68nm(A) and 101nm(B). These specimens were given a tensile strain of approximately 3.6% by tensile tests. After tensile tests, specimens for the measurement of residual strains were prepared by cutting from their parallel part. The residual strains in the ferrite matrix were measured along five directions by using RESA at JAEA. Peak positions of the diffraction profiles were determined by curve fitting with a Gaussian function.

3. Results and Discussion

Figure 1 shows the residual lattice strain of the specimen A and B. Lattice planes of

ferrite (211) were measured, where a specimen was rotated by 0, 22.5, 45, 67.5 and 90 degrees with respect to the tensile direction as illustrated in the insert in Fig. 1. As seen, the residual lattice strain is compressive in the axial direction (0 degree) while tensile in the transverse direction (90 degrees). It is noted that the absolute values of the intergranular residual strains are increased with an increase in S_0 from comparison between specimens A and B.

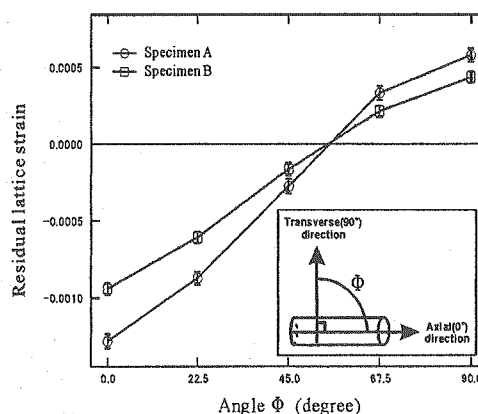


Figure 1: (211) residual lattice strain as a function of the angle between the measuring and the tensile direction for specimen A and B, where the geometrical arrangement for residual strain measurement is shown in the insert.

原子炉：JRR-3 装置：RESA(T2-1) 分野：中性子散乱（残留応力）

研究テーマ：鉄鋼の加工熱処理に伴うミクロ組織形成および残留応力発生の中性子回折測定
表題：中性子回折プロファイル解析による伸線鋼の転位密度と粒径の決定

1-8-2

Neutron Diffraction Profile Analysis to Determine Dislocation Density and Grain Size for Drawn Steel Wires

S. Ryuhuku, T. Shiratori, Y. Shiota, Y. Tomota¹, H. Suzuki² and A. Moriai²

Graduate student of Ibaraki University, Hitachi, Ibaraki 316-8511

¹Graduate School of Science and Engineering, Ibaraki University, Hitachi, Ibaraki 316-8511

²Japan Atomic Energy Agency (JAEA), Tokai, Ibaraki 319-1195

1. Introduction

The changes in dislocation density and cell size as a function of plastic strain and carbon concentration in steel wires is needed to measure quantitatively for development of stronger wire. The ρ and d are usually determined by using TEM observations, but the macroscopic averages are difficult to obtain. Hence, in this study, diffraction profiles for bundles of steel wires with different carbon contents were obtained by means of neutron diffraction. The ρ and d were determined by a profile analysis based on the integral breadth method. The results were compared with those by another profile fitting program and TEM observations.

2. Experimental procedures

The specimens were subjected to about the same drawing strain (true strain of 4.0), for ferrite (0C) and pearlite (0.4C to 0.9C) steels. Neutron diffraction measurements were performed with RESA at JAEA by the angular dispersion method. The (211) diffraction profile was chosen for the analysis because it was hardly influenced by cementite peaks. TEM observations were performed for the determination of d . The integral breadth method was based on De Keijser *et al.* (1982). And the Fourier coefficients method was based on Kuwano (1977) referring to Warren Averbach and Garrod Auld. Lukas *et al.* (1997) have proposed a transformation model fitting method which belongs to the former group.

3. Results and Discussion

An example of profile fitting is presented in

Fig.1 where a ferrite steel annealed at 923 K for 10.8 ks was used for a standard material. The dislocation density and crystallite size in drawn steels were determined by the profile analyses developed in this work using the integral breadth method and the Fourier coefficients method. Calculated d was found to be similar to those measured from TEM observations shown in Fig. 2. Considering Pearson product-moment correlation coefficients, both the Bailey-Hirsch relation and the Hall-Petch relation have similar sensitivity in the drawn wire conditions. Hence, these relation were simultaneously confirmed in pearlite drawn wires with different drawn strains and different carbon contents.

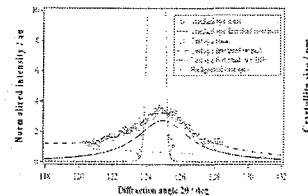


Figure 1: Example of profile fitting.

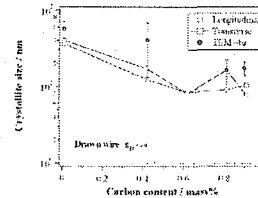


Figure 2: Change of crystallite size with carbon content.

原子炉：JRR-3 装置：RESA(T2-1) 分野：中性子散乱（残留応力）

研究テーマ：中性子IPを応用した工業材料の残留応力測定
 表題：中性子IPによる応力測定への材料板厚の影響

1-8-3

Influence of Triaxial Stress State on the Neutron Stress Measurement using Neutron Image Plate (NIP)

T. Sasaki, Y. Morii¹ and N. Minakawa¹

Department of Materials Science and Engineering, Kanazawa University, Kanazawa 920-1192

¹Quantum Beam Science Directorate, JAEA, Tokai, Ibaraki 319-1195

The authors have been trying to develop an area detector type neutron stress analysis technique for industrial applications. A fundamental attempt has been done to study the possibility of the method through a simple experiment. In the experiment, a steel plate with the thickness of 5 mm was used for the tensile test. Stress in the specimen was analyzed by applying the $\cos \alpha$ method to the neutron diffraction ring detected with a neutron image plate (NIP). As a result, it was found that stress obtained with an NIP corresponds to applied stress involving constant misfit stress. The misfit stress was understood as to be caused by the penetration depth of neutron beams larger than that of X-ray beams. It was also found that the misfit stress can be easily corrected using diffraction data obtained from a sample in stress free state. A numerical simulation was also conducted to make sure of the validity of the experiment on the wide range of measurement conditions. The result showed that the former authors' experiment was adequate to much wider measurement conditions.

On the contrary, the method will be required to be applicable to samples in triaxial stress state in order to increase the worth of the authors method in practical use. Since the experiment on triaxial stress state is not easy from the point of view of the facility, the authors conducted a numerical simulation using the similar way as the plane stress analysis simulation mentioned above. The X-ray triaxial stress analysis method for an area detector type method, which was firstly proposed

by Sasaki *et al.* in 1995¹⁾ for X-ray stress analysis, was applied to stress determination. As a result, the stresses obtained also showed misfit stress as similar as the plane stress analysis, but indicated the regularity against the applied stresses. However, the correction method which is effective in the plane stress analysis was not enough for the triaxial stress analysis. So the other new correction method was tried. The correction method which was finally succeeded was as follows. The diffraction data are obtained first from both a target sample and stress free sample. Then, strains are calculated for both results using assumed lattice constant in stress free state. Since the neutron diffraction ring does not become a circle even if in stress free state due to huge penetration depth, strains obtained from each part of the diffraction ring does not become to be zero. So, strains of the target sample are then be subtracted from those of stress free sample. Then, calculate stress using these strains applying the Sasaki *et al.* method. As a result, the triaxial stress components obtained by this process showed good agreement with initial stresses.

References

- 1) T. Sasaki and Y. Hirose: "J. Soc. Mat. Sci. Jpn.", 44, No.504, 1138-1143 (1995).

研究テーマ：中性子散乱による産業用物質材料の構造解析の開発研究

表題：冷間圧延したオーステナイト系ステンレス鋼の集合組織発達と第二種ひずみの形成

1-8-4

Formation of Texture and Intergranular Strain in Cold Rolled Austenitic Plate

H. Suzuki, T. M. Holden¹, B. Clausen², Y. Shiota³ and Y. Tomota³

Quantum Beam Science Directorate, JAEA, Tokai, Ibaraki 319-1195

¹Northern Stress Technologies, Ontario, Canada

²Los Alamos National Laboratory, Los Alamos, NM, 87545, USA

³Ibaraki University, Hitachi, Ibaraki, 316-8511, Japan

The formations of the texture and intergranular strain in cold rolled type-316 austenitic stainless steel plate were evaluated by measuring the intergranular strain pole figures using neutron diffraction.

Samples were prepared in the received condition and after reducing the thickness by rolling by 25 % and 75 %. Discs with 10 mm diameter and 1 mm thickness were cut from the center of the cold rolled plates with 25 % and 75 % reductions by using the wire electric discharge machining. These were then stacked and glued together preserving the orientation of the discs. The only quarter pole figure was measured in both of texture and strain pole figures.

Figure 1 shows the gradation images of the intergranular strain pole figure superimposed on the texture contour map in each reflection

of the 25 % reduction. In the 200 reflection, there is a ridge of tension around $\chi=45^\circ$ with local maxima on the RD-ND and TD-ND loci, not much at all at the ND and compression along TD-RD peaking near $\eta=30^\circ$. The 220 reflection has a valley where 200 reflection has a ridge around $\chi=45^\circ$. There is tension at the ND and at $\eta=45^\circ$ along RD-TD. The 111 reflection has less structure but a valley around $\chi=75^\circ$ and tension at higher and lower χ angles. This relation of intergranular strains among three reflections is very similar with the relation of those with uniaxial deformation. The low strains for the 111 reflection were in line with the recommendations of the standard measurement method.

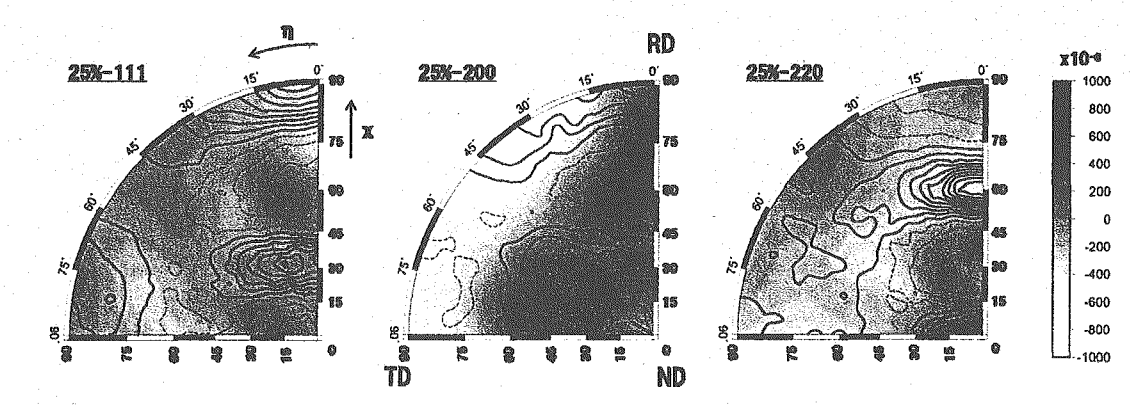


Figure 1: Gradation images of the intergranular strain pole figure superimposed on the texture contour map (lines) for each reflection at 25 % reduction. Contour separation for the texture is 0.25 and dotted-lines indicate levels below 1.0.

原子炉：JRR-3

装置：RESA(T2-1)

分野：中性子散乱（残留応力）

研究テーマ：中性子散乱による産業用物質材料の構造解析の開発研究

表題：中性子回折によるオーステナイト系ステンレス鋼突合せ溶接材の残留応力評価

1-8-5

Stress Measurement of Austenitic Butt Weld using Neutron Diffraction

H. Suzuki and T. M. Holden¹

Quantum Beam Science Directorate, JAEA, Tokai, Ibaraki 319-1195

¹Northern Stress Technologies, Ontario, Canada

The residual stress distribution in a double-V butt weld plate of austenitic stainless steel (SUS304) was measured using the neutron diffraction technique, and the importance of consideration of intergranular effects on the stress measurement of weldment is discussed.

The double-V butt weld samples with size of 100 mm×100 mm×10 mm were fabricated by TIG welding with 308-type stainless steel welding rod. To check for chemistry related shifts in the weld metal and for intergranular effects, 2×2×2 mm³ coupons were wire-cut from the mid-thickness of a companion weld at distances of 2, 4, 6, 10, 20, 30 and 49 mm from the weld centerline. In these coupons, the macroscopic stress field is destroyed, but chemical effects and intergranular effects are retained, and then these are considered to give an accurate, though not in general stress-free reference.

Figure 1 shows the variations of lattice parameter derived from each reflection in the three directions. The lattice parameter for the 002 reflection in the LD direction strongly increases near the weld centre which definitely affects the stress evaluation of the weldment. There appear to be no changes in the lattice parameter for the 111 and 220 reflections near the weld although there is some scatter probably due to the large grain size. It was concluded that the intergranular effects were not significant for these reflections. The fact that only the 002 reflection has this behaviour suggests that chemistry is not the origin of the increase in the weld center.

In order to correct for the intergranular strains in this sample, the residual stress dis-

tributions were calculated by using the observed lattice parameter of the coupons. Figure 2 shows the result of the longitudinal stress distribution after correction. The residual stresses derived from 111, 002 and 220 reflections overlapped within the scattered band of approximately ± 35 MPa which was less than twice the standard error of each measurement. The consideration of intergranular effects thus improves the accuracy of neutron stress measurements of weldments.

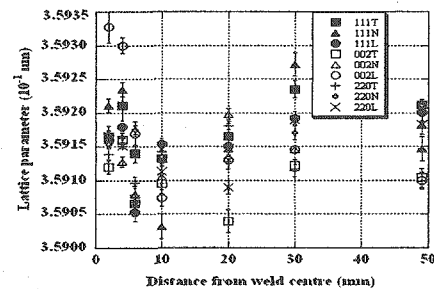


Figure 1: Lattice parameter distributions.

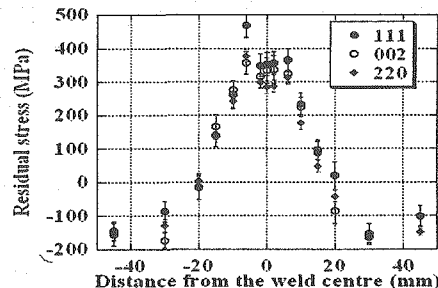


Figure 2: Residual stress distributions in longitudinal direction.

原子炉：JRR-3 装置：RESA(T2-1) 分野：中性子散乱（残留応力）

研究テーマ：中性子回折法によるナノ結晶材料の変形および疲労損傷機構の解明
 表題：中性子回折法による超細粒・ナノ結晶材料の変形および疲労損傷機構の解明

1-8-6

Fatigue Damage Mechanism in Ultrafine- and Nano-grained Material Investigated by Neutron Diffraction Method

Y. Akiniwa, H. Kimura, K. Tanaka, H. Suzuki¹ and Y. Morii¹

Department of Mechanical Science and Engineering, Nagoya University, Nagoya 464-8306

¹*Quantum Beam Science Directorate, JAEA, Tokai, Ibaraki 319-1195*

1. Introduction

Nanocrystallization of metals by severe plastic deformation techniques yields high strength and toughness without embrittlement. Compared with conventional strengthening by the addition of alloying elements or the composition of reinforcing materials, nanocrystallization is considered to be superior in terms of the reduction in the production cost and improvement in the recyclability and weldability. While most of severe plastic deformation techniques introduce nanocrystals only on the specimen surface, equal channel angular pressing (ECAP) can produce large bulk samples with little residual porosity¹⁾. Materials processed by ECAP consist of nanocrystals and ultrafine grains. The deformation and fatigue damage mechanism in the characteristic microstructure, especially in the nanocrystalline region, is not clarified. Some reports on nanocrystals under tensile load revealed that the value of full width at half maximum in the diffraction profile recovered to the initial level after unloading even in the plastically deformed region. This unique phenomenon is attributed to the plastic deformation based on the grain boundary sliding without leaving transgranular strain. The deformation mechanism of ECAP-processed materials is considered to be influenced by both grain boundary sliding in nanocrystalline region and accumulation of transgranular strain in relatively coarse ultrafine-grained region. However, the deformation mechanism is unknown especially in the microscopic level. X-ray diffraction measurement is applicable to the analysis of nanocrystalline materials because most of nanocrystals produced by severe plastic deformation exist only on the surface of the materials, with the typical depth of about 10 micrometer. On the other hand, bulk samples of ECAP-processed materials, with the dimension more than 10 mm, are ultrafine-grained or nano-grained even in the middle of the sample. Therefore, the neutron diffraction technique

is necessary to understand the deformation behavior inside of the specimen. With the help of atomic force microscopy and EBSD²⁾ on the specimen surface, the deformation and damage mechanism of the ECAP-processed materials will be clarified. In this study, the change of the neutron diffraction profile of ECAP-processed copper was investigated at the fatigue crack tip.

2. Material and measurement

Annealed pure Cu was processed by ECAP with 12 rout Bc passes. A specimen with a single-edge notch was fatigued to introduce a crack. The neutron facility of JAERI (RESA) was used with the size of the incident beam confined to 0.3×15 mm in order to measure the detailed distribution around the crack tip. The diffraction plane of Cu(111) was employed under the wave length of 0.2087 nm.

3. Experimental results and conclusion

The value of full width at half maximum in the diffraction profile was calculated at 0, 0.3, 0.6, 1.0, 1.5, 2.0, 3.0 and 5.2 mm from the crack tip. Even though the material has experienced severe plastic deformation around the crack tip from 0 to 0.6 mm, the value dose not differ from that at the other end at 5.2 mm without plastic deformation. This result is in contrast to the conventional copper with large grains, indicating that the transgranular strain distribution is different and that grain rotation occurs in the nanocrystalline region resulting in the decrease in FWHM value. With the same measurements during loading and surface analysis by AFM and EBSD, the deformation and fatigue mechanism will be clarified.

References

- 1) R. Z. Valiev : " Mat. Sci. Eng. A.", **137**, 35 (1991).
- 2) H. Kimura : " JSME Int. J., A.", **47-3**, 331 (2004).

研究テーマ：レーザーピーニングした配管内面における残留応力分布測定
表題：レーザーピーニングした鉄鋼における内部残留応力測定

1-8-7

Residual Stress Measurements beneath the Surface of Laser Peened Steel

K. Akita, H. Tanaka, K. Takahashi, Y. Sano¹, H. Suzuki² and A. Moriai²

Department of Mechanical Systems Engineering, Musashi Institute of Technology, Tokyo 158-8557

¹ Power and Industrial Systems Research and Development Center, Toshiba Corporation, Yokohama 235-8523

² Quantum Beam Science Directorate, Japan Atomic Energy Agency, Tokai, Ibaraki 319-1195

The laser peening introduces compressive residual stress in surface layer, and it is effective for the improvements of fatigue strength and the corrosion resistance and the prevention of stress corrosion cracking (SCC).

Intergranular strains are sometimes occurred in plastic deformed materials and it affects the accuracy of the stress measurements using the crystal diffraction technique. The intergranular strains may be occurred in the laser peened material because the material is deformed plastically. In this study, the intergranular effects generated in the laser peened surface of a ferritic steel were evaluated using neutron diffraction.

The material used for this study was a high tensile strength steel, JIS SHY685. The size of the specimen was $40 \times 40 \text{ mm}^2$ with the thickness of 15 mm. The fundamental wave of a Q-switched Nd:YAG laser was frequency-doubled to a water penetrable wave (wavelength = 532 nm). The specimen was driven to x - and y -directions in a water jacket during laser irradiation. The diameter of the laser spot was 0.8 mm. The pulse energy of the laser beam was 200 mJ. The coverage was 5000 %. Our laser peening process in this study did not use any coating materials.

The neutron diffractometer, RESA, in JRR-3 was used to measure the residual stresses. The direction of the measured strain was the surface normal direction. The measured diffraction planes were α -Fe 110, 211 and 200. The wavelength of neutron beam was 2.0725 Å. The residual stresses were cal-

culated using the strain in the surface normal direction under the assumption of equi-biaxial stress state.

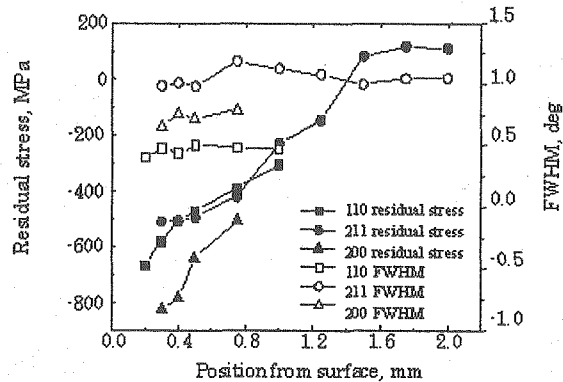


Figure 1: Depth profiles of residual stress and FWHM on laser peened sample (JIS SHY685).

Figure 1 shows the measured depth distributions of residual stress and full width at half maximum of diffraction profile (FWHM) beneath the laser peened surface. The residual stress distributions derived from the strains of the 110 and 211 reflections were in good agreement, while that of the 200 reflection, which is sensitive to the intergranular effect, indicated larger compressive stress by 100 MPa to 200 MPa in the surface layer until 0.8 mm depth from the surface. It is probably intergranular effect, so that the residual stress measurement with consideration of the intergranular effect may be required to evaluate the residual stress generated in the surface layer of the laser peened sample.

研究テーマ：中性子回折法によるアルミニウムエンジンの残留応力測定
 表題：揺動法を用いた中性子回折法による鋳造アルミニウム部品の応力測定

1-8-8

Stress Measurement of Cast Aluminum Components using the Neutron Diffraction Method with the Oscillation Technique

S. Yamashita, K. Onishi, M. Morikawa¹, H. Suzuki² and A. Moriai²

Measurement Engineering Department, NISSAN MOTOR CO., LTD. Okatsukoku, Atsugi-shi, Kanagawa 243-0192

¹Powertrain Evaluation and Test Department, NISSAN MOTOR CO., LTD. Tsurumi-ku, Yokohama-shi, Kanagawa 230-0053

²Quantum Beam Science Directorate, JAEA, Tokai, Ibaraki 319-1195

1. Introduction

The importance of internal residual stress measurement of vehicle components is growing in recent years in the automotive industry. The neutron diffraction method is known as a non-destructive evaluation and is a promising technique for the internal residual stress measurement. However the method is not available to the measurement of casting aluminum components due to the large crystal particle diameter. The oscillation technique, which makes the specimen rotate cyclically, is used to solve the problem in X-ray technique. The measurement result of casting aluminum components using neutron diffraction method in conjunction with oscillation technique is reported in this paper.

2. Observation of crystal particle diameter and direction using EBDP method

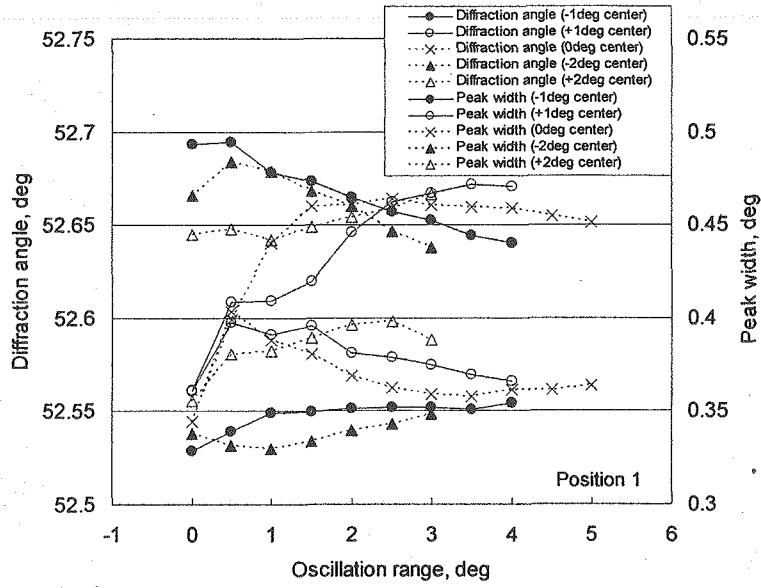
Before measuring the stress using the neutron diffraction method, the crystal particle diameter and direction was observed first using EBDP (Electron Backscatter Diffraction Pattern) to grasp the representative crystal circumstances of casting specimen that was fragment of engine. The measurement area was 600 square μm , and the spatial resolution was 1.5 μm . The measured particle diameter was 50-200 μm , and the direction was biased. This proved that the crystal circumstances were unsuitable for the measurement of neutron diffraction data due to few crystals in 3 mm³ gauged volume. A potential solution is the oscillation technique that will be able to increase the number of crystal in appearance.

3. Measurement of casting engine fragment using neutron diffraction in conjunction with oscillation technique

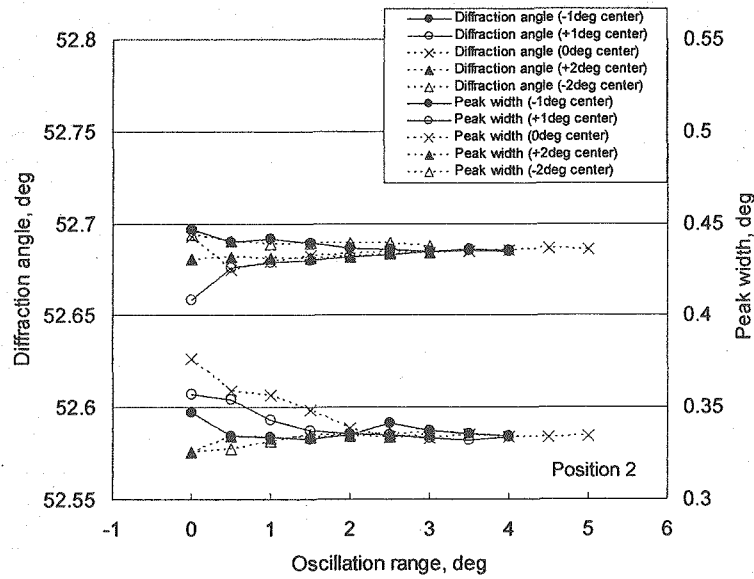
The neutron diffraction in conjunction with oscillation technique was tested using the RESA (RESidual Stress Analysis) being located in JRR-3 of JAEA. Two different areas on the casting aluminum engine were measured. The aluminum (111) was used, and the oscillation range of the specimen was ± 5 degrees. The diffraction angle and peak width was obtained as the following picture. The picture tells us that the diffraction angle (left axis) and peak width (right axis) at Position1 (a) were not converged on definite diffraction angle in ± 5 degrees oscillation range while both of them at Position2 (b) were converged on 52.69 degrees in ± 3 degrees oscillation range.

4. Conclusion

The result of Position 2, converging on constant in diffraction angle, verified that the oscillation technique was effective for the measurement of aluminum casting part. However the result of Position1, diverging in ± 5 degrees diffraction angle, clarified that the optimum oscillation angle differed with respect to various parts. It can be inferred that the optimum oscillation angle is depending on the shape and the crystal structure of aluminum casting part. The optimum oscillation condition will be clarified to ensure the measurement method of aluminum casting internal stress by using neutron diffraction.



(a) Position 1.




(b) Position 2.

Figure 1: Relation between oscillation angle and diffraction angle, peak width.
 (a) Position 1 (b) Position 2.

This is a blank page.

1. 中性子散乱 9) その他



1. Neutron Scattering 9) Others

This is a blank page.

研究テーマ：ナノ物質の創製とその構造機能研究

表題：位置敏感中性子回折による内部物質の結晶構造スキャン

1-9-1

Positional Structure Scanning by Neutron Diffraction Measurement

S. Shamoto, S. Iikubo, K. Kodama, H. Suzuki, H. Iikura,
A. Moriai, M. Matsubayashi and N. Igawa

Quantum Beam Science Directorate, JAEA, Tokai, Ibaraki 319-1195

The radiography is a technique to visualize inside of a material by radioactive ray transmission variation nondestructively. In the case of large metallic alloys such as bronze sculptures¹⁾, a white neutron beam is very powerful because of the high transmittance and the high total flux. On the other hand, by using a monochromatic neutron beam, refraction contrast and ultra small angle scattering property can be imaged, although the neutron flux is strongly reduced^{2,3)}. Here, we have studied the possibility of a positional structure imaging by using diffractometers at a continuous neutron source reactor, JRR-3. By using a diffraction technique, a positional structure scanning in a material was demonstrated.

The sample was a copper block with a cylindrical cavity where a SUS430 plate was inserted. Copper atom has 11.81 barn in the total neutron cross section, while SUS430 with about 83 at% iron and about 17 at% chromium has about 12.8 barn⁴⁾. The thickness of the SUS430 plate was reduced by a factor of 0.92 in comparison with the copper cavity depth, in order to match the attenuation of neutron beam. In other words, the thickness of SUS430 was set to be 7.4 mm in the copper cavity with 8.0 mm depth. Neutron radiography was measured at the Thermal Neutron Radiography Facility (TNR) installed at 7R beam port in JRR-3 in Japan, where the average neutron flux was about 1.5×10^8 n/cm²/sec. A radiography photo was taken for 4 sec. Neutron diffraction measurements were carried out at the Diffractometer for the Residual Stress Analysis (RESA)

at T2-1 and the High Resolution Powder Diffractometer (HRPD) at 1G in JRR-3. The neutron fluxes for both diffractometers were about 1×10^5 n/cm²/sec. The incident neutron wave lengths were 0.2073 nm and 0.1823 nm for RESA and HRPD, respectively. At the RESA, the sample was measured by $\Delta 2\theta = 0.1$ deg. step with slits of $W2 \times H15$ mm² before and after the sample for 100 and 220 sec on copper and SUS430, respectively. At the HRPD measurement, the sample was measured by 64 ³He detectors with $\Delta 2\theta = 0.05$ deg. step for 130 sec with a slit of $W4 \times H10$ mm² only before the sample. The collimation was Open (35')-20'-Sample-6'.

Figure 1 shows the front and side views of the test sample by the neutron radiography. The material difference between copper and SUS430 cannot be distinguished in both side and front views by the attenuation contrast regardless of the thickness. This kind of difficulty can be overcome by using a diffraction technique, which is very sensitive to the structure. For example, copper has a face-centered cubic (FCC) structure with a lattice parameter of 3.6149 Å, while SUS430 has a body-centered cubic (BCC) structure with $a = 2.803$ Å. Because of this structural difference, they were easily detected by the neutron diffraction patterns measured at HRPD and RESA, as shown in Figs. 2 and 3, respectively. Depending on the scattering area determined by incident and final neutron beams, the diffraction pattern changed drastically. Since only monochromatic neutron beam can be used for the neutron diffraction at the reactor source, the neutron flux at the sample position is re-

原子炉：JRR-3 装置：装置：RESA(T2-1),HRPD(1G),NRF(7R, C2-3-3-1) 分野：中性子散乱 (その他)

duced by 3 orders of magnitudes. Alternative way to get high intensity would be to use broad neutron spectrum at the sacrifice of the Q -resolution to specialize the diffraction measurement for the positional structure scanning.

This method can be used for x-ray, laser light, and sound diffraction measurements depending on the length scale or the material which one is interested in. Among the various beams, the neutron is the weakest. Therefore, there was little thought for the scanning. However, new coming pulse neutron source at J-PARC may provide us a chance to explore this type of scientific fields. So it is important to study the measuring time based on the experiments at an existing neutron source. Here, we showed a possibility of the positional structure scanning by neutron diffraction at existing diffractometers, RESA and HRPD at JRR-3. By using multi-detector such as positional sensitive detector, the efficiency can be dramatically improved even at the same diffractometer. Neutron magnetic lens can also increase the efficiency. Note that the synchrotron x-ray diffractometer with large area coverage of image-plate detectors is also a powerful tool for this kind of challenging measurements about the intensity⁵⁾. The present method would be useful for the short wavelength measurements, *i.e.*, high real space resolution about structural information together with a microscopic positional sensitivity.

References

- 1) E. H. Lehmann, "Neutron News", 17-1, 22 (2006).
- 2) W. Treimer, M. Strobl, A. Hilger, C. Seifert, and U. Feye-Treimer, Appl. Phys. Lett. 83, 398 (2003).
- 3) M. Strobl, W. Treimer, and A. Hilger, Appl. Phys. Lett., 85, 19 (2004).
- 4) Albert-Jose Dianoux, and Gerry Lander, "Neutron Data Booklet", Institute Laue-Langevin, Grenoble (2002).
- 5) P. J. Chupas, X. Qiu, J. C. Hanson, C. P. Grey, and S. J. L. Billinge, J. Appl. Crystallogr., 36, 1342 (2003).

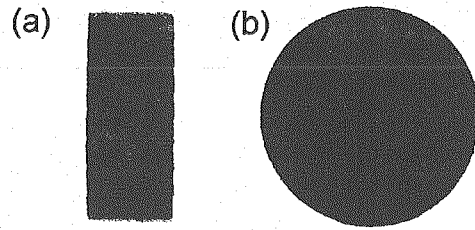


Figure 1: Radiography images (NRF) for the packed sample of 3 pieces. (a) the side view, (b) the front view.

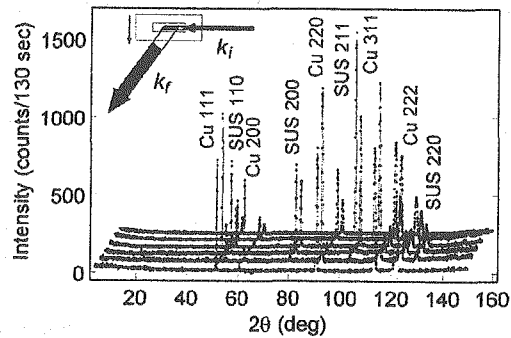


Figure 2: Neutron diffraction patterns (HRPD) of the sample measured from 1.5 mm to 21.5 mm in 4 mm step sliding along the gray axis in the inset. Inset: Incident and final neutron wavevectors, k_i and k_f , are shown by black arrows with beam widths relative to the sample size. Positional scanning was carried out by sliding the black parallelogram scattering volume along the gray axis.

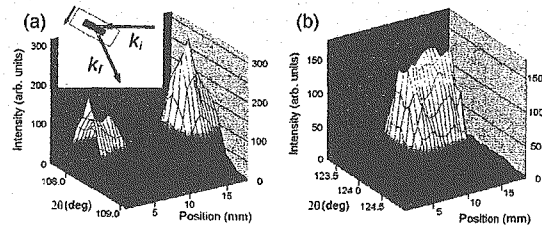


Figure 3: Three-dimensional neutron positional diffraction patterns of the sample (RESA). The diffraction area was scanned by 0.5 or 1 mm step from 1 to 18 mm along the gray axis in the inset of (a). (a) 220 reflection for the FCC copper block. (b) 211 reflection for the BCC SUS430 plate.

研究テーマ：中性子トポグラフィによる卵白リゾチーム結晶の転位の観察
表題：タンパク質結晶への中性子トポグラフィの応用

1-9-2

Application of Neutron Topography to Protein Crystals

H. Koizumi, N. Ohya, M. Koishi, M. Tachibana, K. Kojima, K. Kurihara¹ and R. Kuroki¹

International Graduate School of Arts and Sciences, Yokohama City University, Yokohama 236-0027

¹*Japan Atomic Energy Agency (JAEA), Tokai, Ibaraki 319-1195*

The characterization of defects, especially dislocations, in protein crystals is important for the understanding of their crystallization. The crystallization originating from dislocations has been investigated using atomic force microscopy (AFM). However, AFM is limited to only the local observation of the crystal surface. It is desired that the distribution of dislocations in the whole crystal could be observed.

Topograph technique (X-ray topography and neutron topography) is one of the most powerful tools for characterization of dislocation in the crystal. Therefore, we have performed the application of X-ray topography to protein crystals¹⁾, and consequently, we have succeeded in clearly observation of the dislocation images in hen egg-white (HEW) lysozyme crystals^{2,3)}.

On the other hand, the application of neutron topography to protein crystals has not been carried out so far. Especially, effect of water around dislocations only can be observed using neutron topography. Therefore, to obtain the interaction between intracrystalline water and dislocations in protein crystals, we tried to perform the application of neutron topography to lysozyme crystals.

The used orthorhombic HEW lysozyme crystals were grown by a liquid-liquid interfacial precipitation technique. To avoid the high background coming from the incoherent neutron scattering of hydrogen atoms, the crystallization experiments were carried out in D₂O solution. Neutron topography was carried out using LAUE on C2-3-3-4 at JRR-3. The camera length was 16 cm. Topographs

were recorded on imaging plate with exposure times of a few days.

Figure 1 shows Laue topographs which were recorded with the incident beam almost parallel to the [110] crystallographic direction of orthorhombic HEW lysozyme crystal. This is the first observation of neutron topography to protein crystals. It should be noticed that a topographic image corresponds to a shape of crystals of the lysozyme crystal using X-ray topography in spite of a bad resolution. In addition, this topographic contrast attributes to dislocations observed by X-ray topography. The more detail observation using film should be required to obtain fine structure.

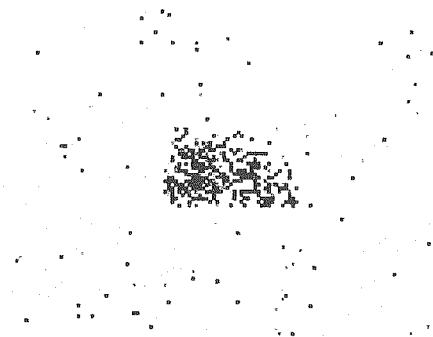


Figure 1: Topographic image of orthorhombic HEW lysozyme crystal obtained using neutron topography.

References

- 1) M. Tachibana and K. Kojima: "Current Topics in Crystal Growth Research", **6**, 35(2002).
- 2) M. Tachibana, H. Koizumi, K. Kojima: "J. Synchrotron Rad.", **10**, 416(2003).
- 3) H. Koizumi, M. Tachibana, I. Yoshizaki, K. Kojima: "Philos. Mag.", **85**, 3709(2005).

原子炉：JRR-3 装置：LAUE(T1-4-4,C2-3-3-4) 分野：中性子散乱（その他）

This is a blank page.

2. 中性子ラジオグラフィ



2. Neutron Radiography

This is a blank page.

研究テーマ：散乱中性子制御ハニカムコリメータを用いる定量的中性子ラジオグラフィシステムの開発と応用

表題：散乱中性子制御ハニカムコリメータを用いる定量的中性子ラジオグラフィシステムの開発と応用

2-1

Quantitative Neutron Radiography System with Honeycomb Collimator for Controls of Scattered Neutron and γ -ray Effects

M. Tamaki

Nuclear Engineering, Nagoya University, Furo-cho, Chikusa-ku, Nagoya 464-8603, JAPAN

1. Introduction

A wide dynamic range of the neutron radiography using digital imaging systems is preferred for quantitative analysis.

Based on the experiences and considerations, new combination of converters is designed, fabricated and examined. Present study reports some experimental results using the new converters and technical procedures.

2. Experimental Procedures

In the CCD-camera NR experiment, a set of new phosphor converters, honeycomb collimator (scattered neutron remover) and the test samples are set at specified locations of the TNRF I and II. For the direct exposure experimental setup, a pair of $Gd_2O_3 / ZnS:Ag$ converter and $ZnS:Ag$ screen are set with and without the position-controlled honeycomb collimator system. Image of (neutron+ γ -ray) by ($Gd_2O_3+ZnS:Ag$) and image of γ -ray by $ZnS:Ag$ are taken by the CCD-camera for exposure time of about 60s. For the indirect exposure experimental setup, the $Dy_2O_3 / ZnS:Ag$ converter and the test samples are set on the neutron beam line in the TNRF I irradiation room. After neutron irradiation, shielding shutter between TNRF I and II is open. The CCD-camera detects photons from the luminescent converter due to γ -ray and γ -ray of the $Dy-165$ and $-165m$ decays.

3. Results and Discussion

(1) For the direct exposure experiment, using $Gd_2O_3 / ZnS:Ag$ converter and $ZnS:Ag$ screen,

a pair of images of (neutron+ γ -ray) and γ -ray are taken by the CCD-camera, respectively. After sensitivity correction, γ -ray free neutron image is clearly obtained from the differential of the pair images. In addition, by combining the position-controlled honeycomb collimator system and the image processing, net neutron radiographic image (free from γ -ray, scattered neutron and honeycomb overlap) is obtained experimentally. This means that physical quantity such as neutron cross section and density of samples may be evaluated quantitatively from the NR image.

(2) The conventional CCD-camera imaging system is improved its quantitiveness by removing background of scattered neutrons from sample and surrounding exposure room using position-controlled honeycomb collimator. The neutron transmittances of the samples are fairly consistent with theoretical values, compared to ones by the conventional system. Honeycomb image overlapped on samples is erased by image processing of a series of relatively position-sifted images of the honeycomb and the samples. No degradations by image processing are observed in the transmittance and spatial resolution.

(3) Radiation damage in the CCD NR system is free by the indirect NR technique. In the indirect exposure experiment, the CCD-camera is isolated from neutron exposure. The system detects only photons from the luminescent converter due to the β -ray of the $Dy-165$ decay and the γ -ray of the $Dy-165m$ decay. Preliminary NR image is obtained, but very dark and high background due to geometrical and experimental limitations of the available system.

原子炉：JRR-3

装置：NRF(7R)

分野：中性子ラジオグラフィ（その他）

研究テーマ：中性子ラジオグラフィを用いた水素吸蔵合金タンクの水素濃度分布観察
 表題：中性子ラジオグラフィを用いた水素貯蔵合金タンク中の水素濃度分布観察

2-2 Observation of Hydrogen Distribution in Hydrogen Storage Alloys Tank by using Neutron-radiography Technique

H. Iikura, R. Yasuda, M. Matsubayashi, T. Ebisawa¹, H. Kawano², H. Arashima² and H. Ito²

Quantum Beam Science Directorate, JAEA, Tokai, Ibaraki 319-1195

¹*Machinery Research Laboratory Yokohama branch, The Japan Steel Works, Ltd., Yokohama, Kanagawa 236-0004*

²*Muroran Research Laboratory, The Japan Steel Works, Ltd., Muroran, Hokkaido 051-8505*

1. Introduction

It is considered that hydrogen storage alloys are remarkable for supply source of hydrogen gas to fuel cells, which are regarded as clean energy source in the next generation. However, it is important to optimize the structure of a hydrogen tank, a filling-up method of the alloys into the tank, and filling-up density of the alloys, because the hydrogen storage alloys expand the volume due to storing the hydrogen. In order to investigate hydrogen concentration distribution in the tank, we applied neutron radiography (NRG) to the investigation.

2. Result of observation of hydrogen storage alloy tanks in Last year

Last year, distribution of the alloys inside the tank after performing the release and storage process with 100 and 140 cycles was observed as shown in Fig. 1. In the projection images and tomographs (Fig. 1 a and b), the rich hydrogen region is observed near a gas injection port for the hydrogen release in both tanks. A movement of the alloy powder becomes the cause which transforms a tank. So, the trial to control the movement of the alloy was done.

3. Restriction of alloy movement in the tank

The schematic diagram of the experimental tank which simplifies a form and the NRG observation result are shown in Fig. 2. At the time, a La-Ni system alloy was used as the hydrogen storage alloy tanks. Also, foaming aluminum was inserted as a buffer to alloy movement, though the method was known to improve the heat-transfer property. In the projection images and tomographs in Fig. 2, a white part is an alloy and a black part is a buffer. The projection images and the tomographs showed that swelling of the tank was occurred

from the tank center to bottom. In this case, it was considered that an alloy moved through the gap in the convoluted buffer during the process of hydrogen absorbing and releasing. Therefore, the idea to control the movement of the alloy more tightly is necessary.

4. Future examination

Those results show that movement behavior of alloy particles under hydrogen release should be investigated to design new tank with stable performance. So, we will try to establish the in-situ observation technique to the inside of the tank.

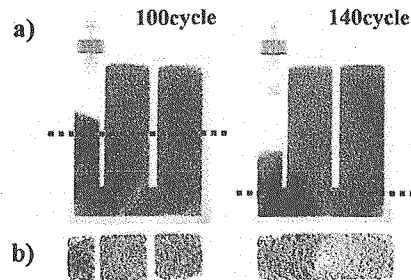


Figure 1: a) Projection images of the tanks. b) Tomographs of the dotted line in the projection images.

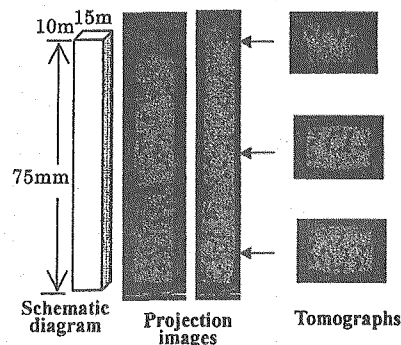


Figure 2: Schematic drawing of the hydrogen storage alloy tank and projection images, Tomography images.

研究テーマ：植物試料における水動態解析
 表題：中性子ラジオグラフィを用いたバラの水分動態解析

2-3

Water Movement Analysis in a Rose by Neutron Radiography

T. M. Nakanishi, Y. Ichimaru¹, H. Iikura² and M. Matsubayashi²

Graduate School of Agricultural and Life Science, the University of Tokyo, Bunkyo-ku, Tokyo 113-8657

¹Nagasaki Agricultural and Forestry Experiment Station, Kaizu-cho, Isahaya-shi, Nagasaki 854-0063

²Quantum Beam Science Directorate, JAEA, Tokai, Ibaraki 319-1195

1. Introduction

Water plays an important role for plant physiology. Since many biological process take place through water, it is important to study water movement within an intact plant. However little has been known for the role or kinetics of water in plants, mainly due to lacking the tools for the research.

In this research, we tried to analyze the change of water amount and distribution in roses during delivery process by neutron radiography (NRG) method. In the case of roses, so called, 'bent neck' phenomenon is a serious problem to ruin the commercial value of the cut flowers. Only flower part bends down during long delivery process. Though this phenomenon is estimated to be induced by the inhibition of water translocation to the flower part, the mechanism has not been known yet.

2. Materials and Methods

Roses (Rosa 'Rote Rose') grown in Nagasaki Prefecture were cut and transported to JAEA by a truck with two methods, packed in a paper box and given water in a bucket at low temperature. When they arrived at JAEA, the flowers were irradiated to get NRG images.

All the samples were set vertically to neutron beams from a research reactor, JRR-3, installed at JAEA. The irradiation was performed for 1.2 seconds and neutrons, converted to light through fluorescent converter (Kasei Optonix, Co.), were taken by a cooled charge coupled devices (CCD) camera (Hamamatsu Photonics, Co.) to get the image.

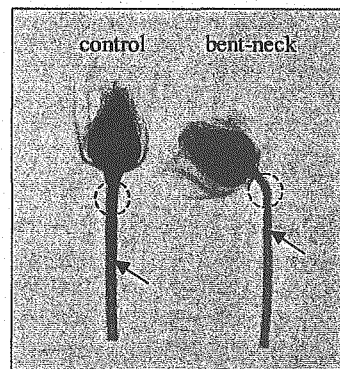


Figure. 1: The neutron image of rose.

The rose transported long distance caused 'bent neck' phenomenon (right).

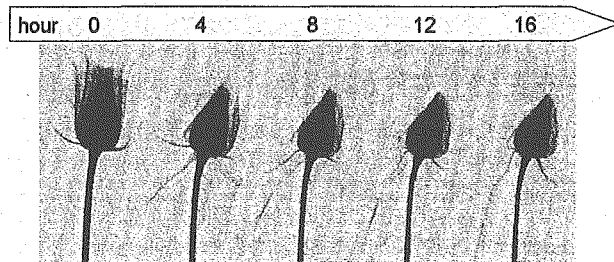


Figure. 2: The successive neutron image of rose.

The rose was cut the stem and not supplied with water at all. The same sample was irradiated every one hour (shown every four hours). Water content decreased by degrees, and the flower withered up gradually.

3. Results and Discussion

Neutron image of roses were shown in Fig. 1. Since there is a correlation between darkness in the neutron image and water amount¹⁾, the relative darkness in the figure was analyzed. Some roses packed in a paper box showed bent neck phenomena, and water content in bent neck plant was decreased. Especially at the bent stem, water content was found to be about 85 to 90% compared to that of control sample (indicated by circles). In addition, water decrease in the pith part of a stem was remarkable (indicated by arrows). It was suggested that the decrease of water pressure in each cells, induced by water-less stress, at the stem caused bent neck phenomenon.

We were able to find out the difference in bent neck sample of roses. Therefore, we tried to get the successive image during bent neck induction by water stress treatment (Fig. 2). The rose was cut the stem and not supplied with water at all. The same sample was irradiated every one hour. Water content of rose decreased by degrees, and the flower withered up gradually.

Figure 3 showed the profile of relative water amount along the center of the stem. At first, the water in Pith-A (low more than about 2 cm from the sepal) decreased remarkably for a few hours. The water in Pith-B (beneath the sepal) has begun to decrease conspicuously later for about 4 hours since cutting the stem (Fig. 3 dry). It was suggested that there is a structural and physiological difference between Pith-A and Pith-B.

Then, another rose was cut the stem and not supplied only for 4 hours. The water in Pith-A decreased rapidly, same as the rose (dry), for a few hours. But the water in Pith-B scarcely decreased (Fig. 3 +water). After 20 hours, this rose (+water) did not show the bent neck phenomenon. In order not to cause the phenomenon, we thought that it was necessary not to decrease water in the Pith-B of the stem.

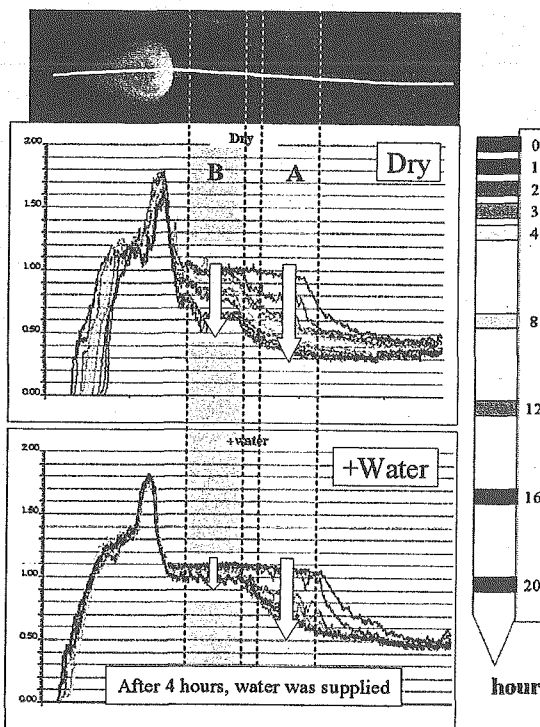


Figure 3: The change of water amount in rose.

The profiles were taken along the center line of a stem like the upper image. These two graphs show the change of relative water amount in the several parts of rose until 20 hours. The profile of rose, that was not supplied with water at all, was shown as the upper graph (Dry). The lower graph showed the one of rose that was supplied with water after 4 hours since cutting the stem (+water).

4. Acknowledgement

The present study is supported by the REIMEI Research Resources of JAEA.

References

- 1) T. M. Nakanishi, Y. Okuni, Y. Hayashi and H. Nishiyama: Water Gradient Profiles at Bean Plant Roots Determined by Neutron Beam Analysis, "J. Radioanal. and Nucl. Chem.", 264 No. 2, 313-317 (2005).

研究テーマ：原子力熱工学に関する研究
表題：稠密流路内沸騰流のボイド率計測

2-4

Brief Void Fraction Measurement of Boiling Flow in Tight-lattice Rod Bundle

M. Kureta

Nuclear Science and Engineering Directorate, JAEA, Tokai, Ibaraki 319-1195

1. Introduction

Neutron tomography void fraction measurement technique is developed originally in order to make clear the boiling phenomenon of boiling flow in tight-lattice rod bundles which simulate the FLWR, Innovative Water Reactor for Flexible Fuel Cycle, and to obtain the fine-mesh 3D void fraction database. In this review, the effect of power on void fraction distribution in tight-lattice 14-rod bundle test section is focused on. The experiments were carried out in the TNRF of JRR-3.

2. Experimental Setup

3D void fraction distribution is measured using the heated 14-rod tight-lattice bundle test section with gap of 1.3 mm, heater-rod diameter of 13.69 mm and heated length of 240mm under atmospheric pressure conditions. Inlet water temperature is set to 90 °C and power is controlled upon 60 kW. Test section is rotated upon 180 degree by 1 degree and the neutron radiography images were recorded by the cooled CCD camera. 3D void fraction is calculated using two-phase flow data with water-filled, gas-filled, shading and dark current data for calibration. Data was processed on the parallel high-speed computer with original software, NIPPON. For tomography processing, the FBP (filtered back-projection) and EM (expectation maximization) methods are examined.

3. Experimental Results

Effects of power input on the 3D void fraction distribution are parametrically investigated with the mass velocity as a parameter. Results were visualized such as the

cross-sectional view along the vertical center and transverse from the inlet to the exit *etc.* When the power input is low as 20 kW, high void fraction spots are generated at the rod gap near the inlet, and then the vapor tends to accumulate the center region of the rods and flow channel at the exit. When the power input increases as 60 kW, the region of high void fraction spots becomes small and center high void fraction region of exit part expands to the inlet. These tendencies are observed under wide range of mass velocity.

4. Summary

Void fraction of flow boiling of water in a 14-rod tight-lattice rod bundle was successfully measured and was very useful to the phenomenological understanding and also to verify the advanced thermal-hydraulic numerical analysis code. The FBP method has an advantage to calculation time but CT noise, artifact, obstructs the view. On the other hand, EM method has an advantage to the CT quality, that is, low artifact noise. But EM method needs very long calculation time if we request the high quality CT data. Therefore, as the next step, we are going to develop the high-speed EM algorithm.

原子炉：JRR-3 装置：NRF(7R, C2-3-3-1)

分野：中性子ラジオグラフィ（熱水力）

研究テーマ：中性子ラジオグラフィーによるエアコンコンプレッサー内の液面高さの可視化
 表題：中性子ラジオグラフィーによるエアコン・コンプレッサー内オイル挙動の可視化

2-5

Visualization of Oil Behavior Inside Air Conditioner Compressor by Neutron Radiography

S. Yamashita, K. Onishi, M. Matsubayashi¹ and H. Iikura¹

Measurement Engineering Department, NISSAN MOTOR CO., LTD. Okatsukoku, Atsugi-shi,
 Kanagawa 243-0192

¹Quantum Beam Science Directorate, JAEA, Tokai, Ibaraki 319-1195

1. Introduction

The Neutron Radiography is well-known as the non destructive evaluation method that has an ability to observe water and oil as well as metallic parts inside of the mechanical structure. And also the Neutron Radiography is expected to apply to the engineering field of vehicle development as a potential measurement technique for further quality improvement and development timing reduction.

This paper shows the result of the oil behavior inside the air conditioner compressor being in operation visualized by the Neutron Radiography.

2. Neutron Radiography Method

First we tried to obtain the static image of air conditioner using the facility of JRR-3 in JAEA. Static images were taken by a CCD camera.

Figure 1 showed the oil level clearly, and the structure that looks like the piston.

Figure 2 showed the compressor was operated by the electromotor mounted on the test-rig.

Figure 3 showed the dynamic images of which area was 24 square cm, frame rate was 30 Hz, and rpm was 360 approximately, which were taken by SIT camera.

3. Conclusion

It was proved that the behavior of operating oil and piston inside the compressor could be visualized. It will be required to make sure the feasibility in the actual operating conditions. In addition, it is worth to pursue other applications

such as oil behavior of transmission and another part of engine.

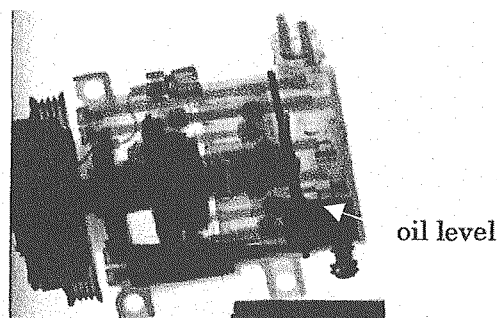


Figure 1 : Static image.

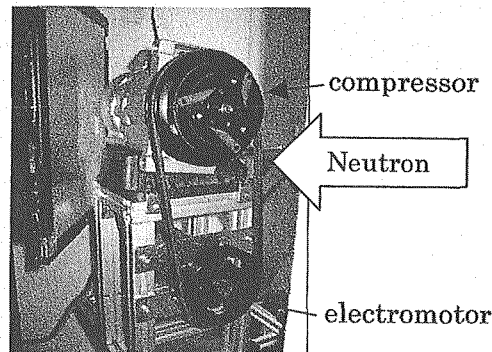


Figure 2 : Test-rig overview.



Figure 3 : Dynamic image.

研究テーマ：中性子産業利用技術の開発研究

表題：固体高分子型燃料電池のための中性子イメージング技術開発

2-6

Development of Neutron Imaging Techniques for Proton Exchange Membrane Fuel Cells (PEMFC)

M. Matsubayashi, H. Iikura and R. Yasuda

Quantum Beam Science Directorate, JAEA, Tokai, Ibaraki 319-1195

1. Introduction

The proton exchange membrane fuel cell (PEMFC) is a promising power source and has promising applications in transportation and consumer electronics because of its efficient energy conversion. This research used neutron imaging as a non-destructive investigation tool for a fuel cell, finally under operating condition.

2. Materials

The Japan Automobile Research Institute (JARI) standard type PEMFC is commercially available and applied to visualization experiments. The JARI standard type PEMFC consists of a piece of membrane-electrode-assembly (MEA) and pairs of fastening stainless steel plates, collector electrode plates, carbon separators and gaskets. A pair of fastening stainless steel plates were exchanged for a pair of aluminum plates prior to the experiment in terms of neutron transmission property and radioactivation.

3. Experiments and results

Visualization experiments were conducted at the JRR-3 thermal neutron radiography facility. Neutron images of the non-operated JARI standard type PEMFC for computed tomography (CT) were captured by a cooled CCD camera system.

Left side projection image in Fig. 1 clearly shows the serpentine flow channel created in the carbon separators. Right side projection image shows both flow channels of cathode and anode ones.

Figure 2 and Fig. 3 are 2-D vertical slices reconstructed from computed tomograms. The different flow channel pattern was observed in each image even though stainless steel made fastening bolts and nuts caused artifacts and blurred images.

4. Future examination

Those results show the capability of neutron imaging for non-operated PEMFC and also suggest that replacement of stainless parts with other low neutron cross section material improve computed tomograms.

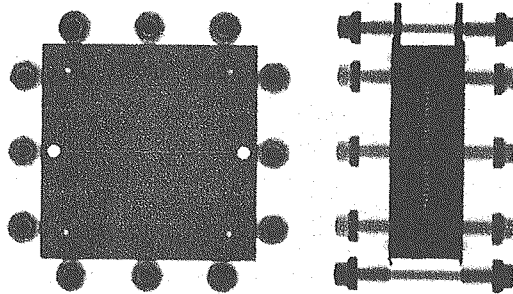


Figure 1: Projection images of JARI standard type PEMFC.

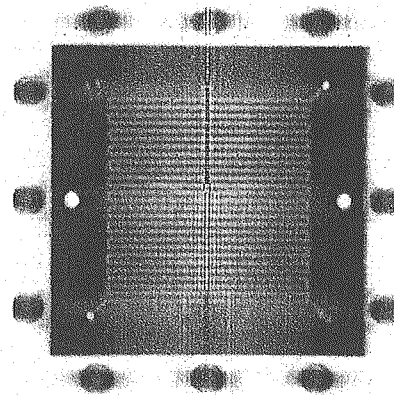


Figure 2: 2-D vertical slice reconstruction at the cathode side carbon separator.

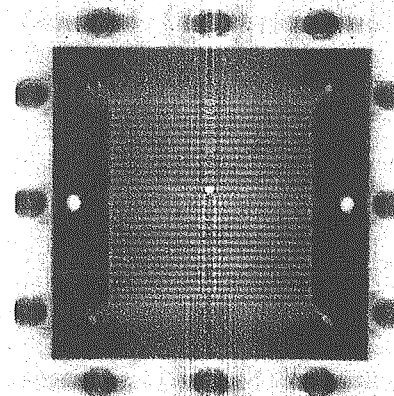


Figure 3: 2-D vertical slice reconstruction at the anode side carbon separator.

研究テーマ：中性子産業利用技術の開発研究

表題：JRR-3 冷中性子ラジオグラフィ装置への冷却型 CCD カメラ撮影システム導入

2-7

Installation of a Cooled-CCD Camera Imaging System at the JRR-3 Cold Neutron Radiography Facility

M. Matsubayashi, H. Iikura and R. Yasuda

Quantum Beam Science Directorate, JAEA, Tokai, Ibaraki 319-1195

1. Introduction

The JRR-3 cold neutron radiography facility (CNRF)¹⁾ was originally installed at the C2-3 beam line. The machine time of CNRF was shared among several neutron instruments. In order to increase the machine time and the number of instruments at the same beam line, neutron bender system was installed at the end of C2 beam line. This system worked well for increase the number of instruments but lost neutron flux. The neutron flux at the original CNRF position was more than 10^8 n/cm²s. After the installation of bender system, the neutron flux dropped by 1/100.

2. Comparison of imaging systems

Real-time neutron imaging using a silicon intensifier target (SIT) tube camera was originally available. Because the SIT tube camera system requires 10^6 n/cm²s order neutron flux at least, another imaging systems must be considered. As integration mode imaging systems, a neutron imaging plate and a combination of a fluorescent converter and a cooled charge coupled device (CCD) camera are promising replacements. Neutron imaging plates are expected to be most neutron sensitive.

3. Experiments and results

NE426 equivalent fluorescent converter (⁶LiF/ZnS:Ag) and Hamamatsu Photonics C4880 CCD camera was used. To reduce dark current noise, the CCD chip was cooled down to -30 °C. Conventional high-gain image acquire mode needs 6 min neutron exposure, super high-gain image acquire mode needs 90 s neutron exposure. Figure 1 shows neutron image without any samples. Artifacts due to the super mirror bender system were observed in the image. Because artifacts are convoluted in a captured image every time, shading correction (image arithmetic operation) is essential for improvement of images. Figure 2 shows raw neutron image

of a BNC connector, Fig. 3 shows shading corrected neutron image of the same sample. The artifact is well suppressed.

4. Future modification

Because 90 s exposure (high-gain mode) is too long to collect projection images for computed tomography, optimization of a fluorescent converter is highly required in addition to the modification of bender system.

Reference

- 1) M. Matsubayashi and A. Tsuruno: JRR-3 neutron radiography facility, "NEUTRON RADIOGRAPHY", 4, 415-422 (1994), Gordon and Breach Science Publishers.

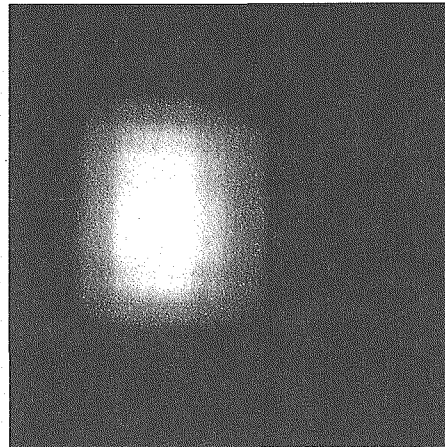


Figure 1: Neutron image without any samples.

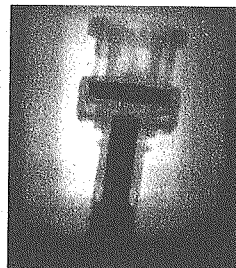


Figure 2: Raw neutron image of BNC connector.



Figure 3: Shading corrected image of BNC connector.

原子炉：JRR-3 装置：NRF(7R, C2-3-3-1) 分野：中性子ラジオグラフィ（その他）

研究テーマ：ガフクロミックフィルムの中性子に対する感度特性

表題：ガフクロミックフィルムを用いた中性子検出の試み

2-8

ガフクロミックフィルムを用いた中性子検出の試み

成山展照、¹大西世紀

(財) 高輝度光科学研究センター

¹ 海上技術安全研究所

ガンマ、X線線量計として用いられているガフクロミックフィルムの中性子イメージングへの応用可能性について調べるのが、本研究の目的である。HD-810 フィルムは放射線感受層がほとんど露出しているため、そこにコンバータを接触させれば、中性子感度を高めることができる。その効果を今回調べてみた。

照射は、JRR-4 の中性子ビーム設備照射筒にて行った。線源に対して希望の向きに試料をセットする方法がないため、回転による均一照射法を採用した。すなわち、試料を回転翼がついた円筒形容器に入れ、照射中、空気を送りつけることにより容器ごと軸周りに回転をさせた。ガフクロミックフィルムは、HD-810 と MD-55 を用いた。1cm × 5cm 程度に切り、感受面にポリエチレン(PE)、カドミニウム+ポリエチレン(Cd+PE)、スズ+ポリエチレン(Sn+PE)、窒化ホウ素(BN)を貼った。照射は、2時間と3時間47分の2通り行った。

油脂の付着などを考慮しなかったため、照射直後は幾らか放射化していたが、数週間後には測定可能なレベルになった。図1に、後半に照射したHD-810の濃淡を、スキャナーを用いて読み取った画像を示す。右から順番に裸、BN、PE、Sn+PE、Cd+PEを等間隔にセットした。Cdの位置は若干ずれている。BNの正方形部分が高いOD値(吸光度)を示したが、これは、(n,α)反応による熱中子子の影響と思われる。原子番号が低いため、2

次電子の影響は小さいと考えられる。Cdの丸部分が最も高いOD値を示したが、Snの部分がいずれも高くなかったことから、これはCdの(n,γ)反応によるガンマ線の影響と考えられる。OD値をガンマ線換算線量にしたところ、裸部が25Gy、BN部が35Gy、Cd部が100Gyの値であった。裸部でも予想されたγ線線量より大きかったのは、中子子の影響と思われる。

高速中子子に対しては、ポリエチレンで感度を確認できなかったが、熱中子子にはコンバータ付着時において感度を有することを確認できた。設備の関係上、回転させるしかなかったが、面の向きを固定できれば、感度は向上できると考えられる。放射化も予想通り問題ないレベルであった。ガンマ線との弁別が課題であるが、100kGy程度までの大線量に使えること、¹マイクロオーダーの高い位置分解能を有することから、その利用を期待できる。

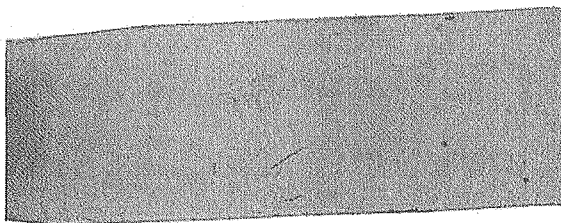


図1 HD-810 スキャン結果

参考文献

- 1) N. Nariyama, Appl. Radiat. Isot. 62, (2005) pp.693-697

This is a blank page.

3. 即発ガンマ線分析



3. Prompt Gamma-ray Analyses

This is a blank page.

研究テーマ：即発γ線ドップラー広がり法のホウ素の状態分析への応用

表題：リンゴ果実中のホウ素化学種の即発γ線ドップラー広がり法によるキャラクタリゼーション

3-1

Characterization of Boron Species in Apple Fruit by Doppler Broadening of Prompt γ-ray

Y. Sakai, Y. Watanabe, M. K. Kubo¹ and H. Matsue²

Daido Institute of Technology, Nagoya 457-8530, Japan

¹*International Christian University, Tokyo 181-8585, Japan*

²*Japan Atomic Energy Agency, Ibaraki 319-1195, Japan*

We revealed that the prompt γ-ray analysis (PGA) can be applied to characterization of boron-species states by probing the Doppler broadened line shape of 478-keV γ-ray from ⁷*Li produced in the ¹⁰B(n,α)⁷*Li reaction¹⁾. “Degradation constant” denoted by *D* was used as a key parameter, which reflects the elemental composition and the average density of a material where ⁷*Li ions move and lose their kinetic energy.

Boron is known to be one of the essential micronutrients for plants. In the present work, we investigated the boron species in various sections of an apple fruit by applying the Doppler broadening method. Prompt γ-ray measurement was carried out for fruit sections of an apple named “Fuji” as prepared in the followings;

- (1) The apple fruit was peeled using a knife, and cut into four slices. One of the fresh slices was submitted to the measurement as it was.
- (2) The second slice was crashed and grounded, and the resulting slurry fruit was

squeezed, being fractionated into residue and juice, the weight percentages of which were 26.3 % and 73.7 %, respectively.

- (3) The third and fourth slices were dried in air for a month and for a year, respectively.

The measurements were performed for several hours using the PGA system at the neutron-beam guide of JRR-3²⁾. We evaluated the *D* values and boron contents by our fitting procedure, which were summarized in Table 1. The *D* values of fresh slice, residue, and juice were obtained to be 1.1 to 1.2 × 10¹² s⁻¹, which are close to that for aqueous solution of boron species.

References

- 1) Y. Sakai *et al.* : “J. Radioanal. Nucl. Chem.”, **265**, 287 (2005).
- 2) C. Yonezawa *et al.* : “Nucl. Instrum. Methods. Phys. Res.”, **A329**, 207 (1993).

Table 1: Degradation constants (*D*) and boron contents in apple fruit

sample of apple fruit	Degradation constants (<i>D</i>)	boron contents	Remark
	10 ¹² s ⁻¹	ppm	
fresh slice	1.14 ± 0.14	6.5 ± 0.1	
residue	1.22 ± 0.05	10.2 ± 0.1	
juice	1.23 ± 0.13	4.2 ± 0.1	
dried slice(1)	1.48 ± 0.07	25.1 ± 0.3	dried in air for a month
dried slice(2)	1.63 ± 0.23	30.6 ± 0.2	dried in air for a year

原子炉：JRR-3 装置：PGA(T1-4-1,C2-3-2-2) 分野：即発γ線分析実験（農・水産物）

研究テーマ：中性子を利用した古代エジプトガラス遺物の非破壊分析

表題：中性子を利用した古代エジプトガラス遺物の非破壊分析

3-2

Non-destructive Analysis of the Ancient Egyptian Glass Relics by Neutron

S. Yoshida, K. Yamahana¹ and H. Matsue²

Department of Energy Science and Technology, Tokai University, Hiratsuka, Kanagawa 259-1292

¹Department of Asian Civilization, Tokai University, Hiratsuka, Kanagawa 259-1292

²Quantum Beam Science Directorate, JAEA, Tokai, Ibaraki 319-1195

Many glass relics called faience have been excavated in ancient Egyptian relics. Generally, these faience were mainly made from sand or stone containing rich silica (SiO_2), and fired a mixture with addition of a dash of lime (calcium oxide: CaO) and alkali (sodium oxide: Na_2O or potassium oxide: K_2O). And also, some kinds of natural coloring agent were used, such as blue, yellow and red was made by adding copper (CuO) or cobalt (CoO), lead (Pb) or antimony (Sb), and iron oxide (Fe_2O_3) or cuprite (Cu_2O).

At present, in the study of the ancient glass and faience, the scientific analysis of primary compositional element and a very small amount of element becomes essential. Neutron capture prompt gamma-ray analysis (PGA) which is one of the qualitative and quantitative analysis is in widespread use for the non-destructive evaluation of faience and sand of their raw materials. The purpose of this study is to investigate the characteristics of an age and an area by the measured distribution of minor elements content rates.

The distribution of Gd/Si , K/Si , Al/Si , Ti/Si , Fe/Si , Co/Si and Sm/Si rates of Iraqi and Egyptian sand and Egyptian faience were shown in Fig. 1 and Fig. 2. The relation between minor elements content rates in sand were shown some interesting associations with an area.

In the future, by further accumulation of measured data of sand and faience we are trying to estimate the producing area and the channel of trade.

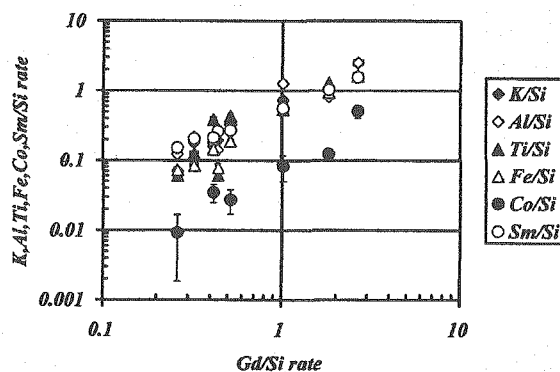


Figure 1: Gd/Si and $\text{K}, \text{Al}, \text{Ti}, \text{Fe}, \text{Co}, \text{Sm}/\text{Si}$ distribution of Iraqi and Egyptian sand.

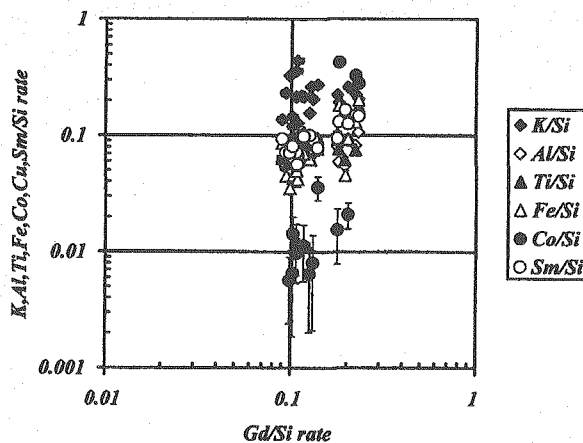


Figure 2: Gd/Si and $\text{K}, \text{Al}, \text{Ti}, \text{Fe}, \text{Co}, \text{Sm}/\text{Si}$ distribution of Egyptian faience.

原子炉：JRR-3 装置：PGA(T1-4) 分野：即発 γ 線分析実験（考古学）

研究テーマ：中性子インビームメスバウアー分光装置の開発

表題：中性子インビームメスバウアー分光装置の開発

3-3

Development of Neutron In-beam Mössbauer Spectrometer

M. K. Kubo, Y. Tsuruoka, Y. Kobayashi¹, Y. Yamada², Y. Watanabe³, Y. Sakai³, H. Shoji⁴,
W. Sato⁵ and H. Matsue⁶

Department of Chemistry, International Christian University, Tokyo 181-8585

¹*Applied Nuclear Physics Laboratory, RIKEN, Saitama 351-0198*

²*Department of Chemistry, Tokyo University of Science, Tokyo 162-8061*

³*Daido Institute of Technology, Nagoya 457-8530*

⁴*Graduate School of Science, Tokyo Metropolitan University, Tokyo 192-0039*

⁵*Department of Chemistry, Graduate School of Science, Osaka University, Osaka 560-0043*

⁶*Japan Atomic Energy Agency, Ibaraki 319-1195*

Emission Mössbauer spectroscopy is a useful tool in the investigation of the trace amount of chemical species formed by nuclear reactions and radioactive decays. The large transmission power of γ -ray used by the Mössbauer effect enables non-destructive analysis of the inside of solid materials in which nuclear events occur. We have been developing a new ^{57}Fe in-beam Mössbauer spectroscopic study in order to reveal the chemical and physical behaviors of the species produced after the neutron capture reaction of ^{56}Fe in materials. Continuing from last year, we studied iron disulfide¹). We chose marcasite, another polymorph of iron disulfide, this year.

Iron disulfide(FeS_2), a simple binary compound with relatively high iron concentration, has no magnetism at room temperature. In this compound, iron exists in its 2+ state and sulfur in S_2^{2-} form. In pyrite, Fe^{2+} and S_2^{2-} are arranged in the cubic rock salt type structure, while marcasite is orthorhombic of slightly distorted structure. A marcasite sample was prepared from a naturally occurring mineral collected in Hanover, Germany provided by Hori Mineralogy. A marcasite sample, a pressed powder disk of *ca.* $20 \times 20 \text{ mm}^2$ and about $100 \text{ mg}\cdot\text{cm}^{-2}$ in thickness, was placed at the target position of the PGA setup at the beam hall of the JRR-3 reactor.

The spectrum was analyzed and decom-

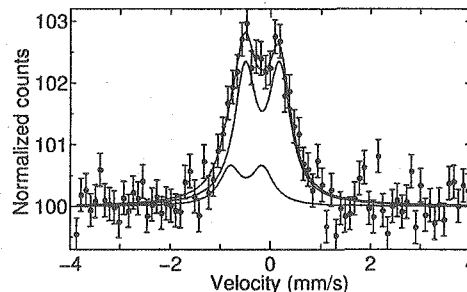


Figure 1: A neutron emission Mössbauer spectrum of marcasite at room temperature.

posed into two Lorentzian doublets (Fig. 1). The minor species had Mössbauer parameters similar to the parent marcasite. The other major product had larger *IS* and *QS* compared with marcasite and its yield was larger than the yield of the new species formed in pyrite. The chemical form of the new species in marcasite was not clear. We plan to establish a temperature variable measurement system to do more detailed investigation of iron disulfide and will apply it to study on other iron containing compounds.

References

- 1) M. K. Kubo, Y. Kobayashi, Y. Yamada, Y. Nemoto, T. Saito, Y. Sakai, H. Shoji, C. Yonezawa, H. Matsue, M. Nakada: "AIP Conference Proceedings", **765**, 348-351 (2005).

研究テーマ：中性子産業利用技術の開発研究
 表題：集光中性子ビームを利用した即発 γ 線分析
 3-4

Focusing Neutron Beam Induced Prompt Gamma-ray Analysis at JAEA

H. Matsue, M. Segawa, Y. Sekiya¹, S. Yamada, T. Shinohara, H. Sasao¹,
 T. Oku, J. Suzuki and H. M. Shimizu²

Quantum Beam Science Directorate, JAEA, Tokai, Ibaraki 319-1195

¹Radiation Application Development Association, Tokai, Ibaraki 319-1106

²Institute of Materials Structure Science, KEK, Tsukuba, Ibaraki 305-0801

1. Introduction

Neutron-induced prompt gamma-ray analysis (PGA) system of JRR-3 has been set at the thermal neutron port (T1-4-1). Instead of a 3 m vacuum tube upstream of the PGA system, we have recently installed a straight guide with a 3Qc mirror and a focusing guide in parallel. This modification allowed us to chose one of the two types of beam, high density focused beam or wide homogeneous beam, depending on the PGA experimental demands. In 2005, the focused and straight neutron beams became available on the PGA system^{1,2}.

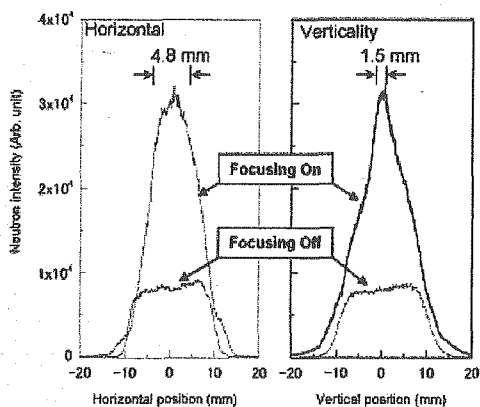


Figure 1: Beam profiles at PGA measurement position of the focusing and straight neutron beams (using $20 \times 20 \text{ mm}^2$ LiF collimator).

2. Characteristics on the focused neutron beam

The beam distribution profiles at the PGA

measurement position are shown in Fig. 1. Using the focusing guide, it is confirmed by a gold thin film activation method that the neutron beam size of $20 \times 20 \text{ mm}^2$ can be focused to $1.5 \times 4.8 \text{ mm}^2$ and neutron flux of the $1.6 \times 10^8 \text{ n}\cdot\text{cm}^{-2}\cdot\text{s}^{-1}$ at the focal point of beam position into $5.7 \times 10^8 \text{ n}\cdot\text{cm}^{-2}\cdot\text{s}^{-1}$. That means we have succeeded to take the 3.5 times higher neutron flux than the previous ones without using the focusing guide.

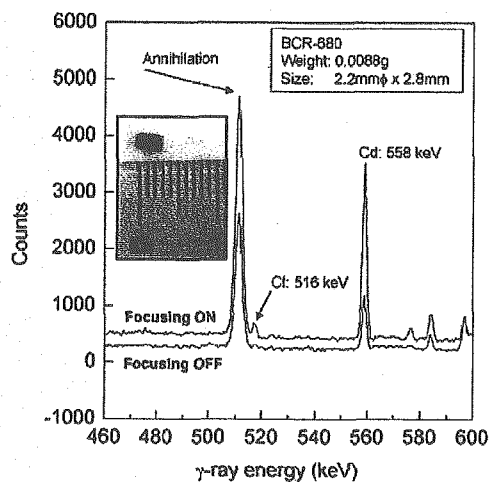


Figure 2: Prompt gamma-ray spectra from a BCR-680 sample measured by using the focusing and straight beams.

3. Prompt gamma-ray measurement for a small sample

The prompt gamma-ray spectra of a small sample (BCR-680) measured with usin of the focusing and straight beam are shown in Fig.

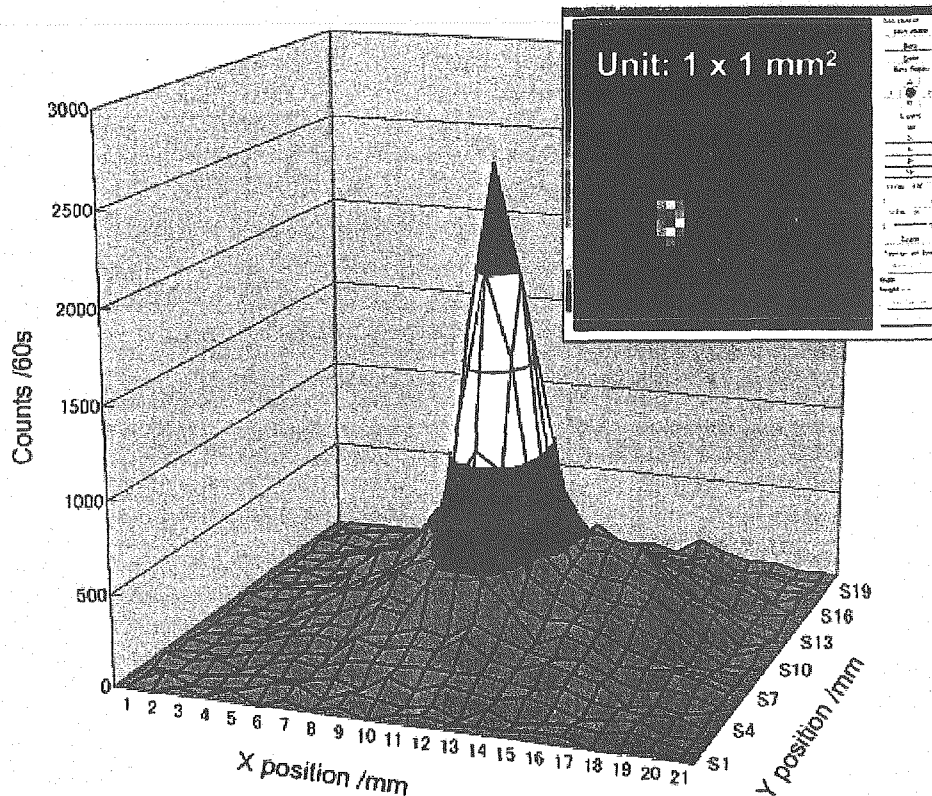


Figure 3: 2D distribution of the gamma-ray yields of B peak at 478 keV for a B metal point like sample (0.8 mg, 0.2mm ϕ).

2. The sample was a reference material of polyethylene containing heavy-elements such as Cd of 21.7 ppm. As shown in Fig. 2, the counting rate for Cd at the 558-keV gamma-ray peak was observed to increase by about 3 times using the focusing beam. The present results imply that the focusing beam should be effectual to PGA system using small samples.

4. Prompt gamma-ray 2D distribution measurement

The focused neutron beam can be used on the various fields. We developed the 2 dimensional (2D) movable sample holder of 0.5 mm in order to analyze various materials microscopically. In Fig. 3 is shown the 2D distribution of the gamma-ray yields of B peak at 478

keV for a B sample (0.8 mg, 0.2mm ϕ) for the purpose of evaluating ability of this system. We could succeed for the first time to measure samples by our 2D prompt gamma-ray analysis method, which has mm order spatial resolution.

References

- 1) H. Matsue, S. Yamada, J. Suzuki, T. Oku, H. Sasao, T. Shinohara, H. M. Shimizu: Focused Neutron Induced Prompt Gamma-Ray Analysis at JAEA, "J. Nucl. Radiochem. Sci.", 6, 164 (2005), (49th housyakagaku-touronkai youshisyuu).
- 2) S. Yamada, T. Shinohara, H. Sasao, T. Oku, J. Suzuki, H. Matsue, H. M. Shimizu: Development of a multichannel parabolic guide for thermal neutron beam focusing, "Physica B" in Print, (Proc. ICNS 2005).

研究テーマ：核物理・核化学的手法による原子核科学の研究

表題：MPGAにおけるデータ解析法の比較

3-5

Comparison of Data Sorting Methods in MPGA

Y. Toh, M. Oshima, M. Koizumi and A. Kimura

Nuclear Science and Energy Directorate, JAEA, Tokai, Ibaraki 319-1195

Most of nuclei emit two or more prompt gamma rays simultaneously in the neutron capture reaction. In multiple prompt gamma ray analysis (MPGA), the prompt gamma rays are simultaneously measured by two or more sets of gamma ray detectors, these gamma rays are reconstructed in the pair of two prompt gamma rays, and it is added to the two dimensional spectrum which sets two axes as the energy for every events. The gamma-ray distribution corresponding to the pair of the gamma ray which are emitted simultaneously will be obtained. By analyzing this two-dimensional gamma-ray peak, interference has the tendency to decrease^{1,2)}. Because the four crystals in a Clover Ge detector are packed very close, a Compton scattered gamma-ray from a crystal is often absorbed by one of the other three crystals. Consequently, summing up the all output signals from the four crystals, we can increase the photo efficiency of a Clover detector from about 100% to more than 120% for the 1.3-MeV gamma-ray. This method, which was called as "add-back" mode, improves the peak

to total ratio, as well. On the other hand, one can not neglect such events that one Clover detector catches more than two cascade gamma-rays, because the distance of the detector to the target is close. The add-back mode, therefore, sometimes makes a ghost peaks in a two-dimensional spectrum as seen in Fig. 1(b). In order to remove such unwanted ghost peak, we can analyze the same data with a method named "anti-coin mode", in which we discard the events that contain more than two data from a Clover detector. Namely, the anti-coin mode uses the other three Ge crystals as Compton suppressors. The result of the anti-coin mode analysis is shown in Fig. 1(c). Although this mode decreases the photo efficiency of a Clover detector, the peak to total ratio is improved significantly. If you have enough events, the data can be analyzed with the anti-coin mode.

References

- 1) Y.Toh *et. al.* : "Appl. Radiat. Isot.", **64**, 751 (2006).
- 2) Y.Toh *et. al.* : "J. of Nucl. Radiochem. Sci", **4**, 197 (2003).

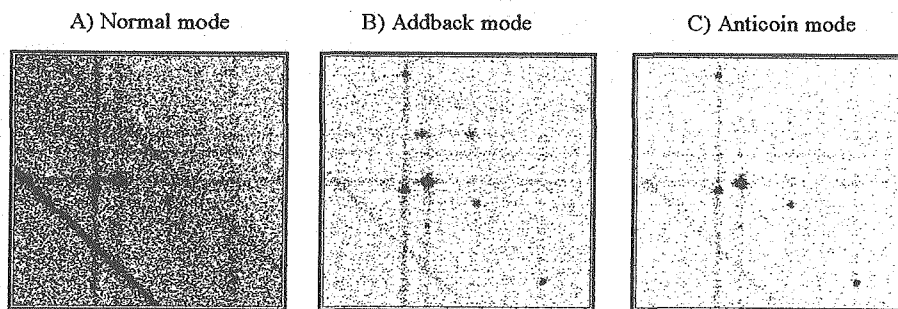


Figure 1: A part of two-dimensional spectrum: a) Normal b) Addback c) Anticoin.

原子炉：JRR-3

装置：MPGA(C2-3-2)

分野：即発 γ 線分析実験（その他）

4. 放射化分析



4. Neutron Activation Analyses

This is a blank page.

研究テーマ：フィッシュントラック法による環境試料中の核物質検出

表 題：フィッシュントラック法の保障措置環境試料パーティクル分析への応用

4-1

フィッシュントラック法の保障措置環境試料パーティクル分析への応用

李 致圭、井口一成、伊奈川潤、鈴木大輔、江坂文孝、間柄正明、桜井 聡、臼田重和
日本原子力研究開発機構 原子力基礎工学研究部門 環境・原子力微量分析研究グループ

フィッシュントラック (FT) - 表面電離質量分析 (TIMS) 法によるパーティクル分析法は、2次イオン質量分析器では測定が難しい粒径 $1 \mu\text{m}$ 以下の核分裂性物質を含む微小粒子に対しても同位体比分析が可能であることから、保障措置上有効な分析手法とされている。フィッシュントラック法では熱中性子照射により起こる核分裂の痕跡 (飛跡) から核分裂性物質を検出するので、高感度の検出が可能である。我々がこれまでに開発した FT-TIMS 法では、核分裂性物質を含む粒子を FT 検出器の中に閉じこめるもので (1層式 FT 試料調製法)、高い検出効率、試料調製の簡便さ、ウラン濃縮度別検出の可能性などの長所がある。しかし、検出器のエッチングの際、ウラン粒子の一部が溶解することがある。そこで、粒子を保持する層 (粒子層) と FT 検出器を分離した 2層式 FT 試料調製法の開発を行っている。この方法では粒子溶解の問題だけではなく粒子層と検出器の一端を固定することにより従来の 2層式 FT 試料で見られた検出器の FT と目的粒子との位置ずれを解決し、目的粒子の検出効率を向上させた。今回は、2層式 FT 試料作製法による FT-TIMS 分析法の開発状況について報告する。¹⁾

スワイプ試料からの粒子回収法については、1層式 FT 試料作製法と同様に粒子吸引法を用いた。粒子を捕集したポリカーボネート (PC) 製フィルターと溶剤 (1,2-ジクロロメタンとジク

ロロエタン混合液) を 1 mL 試験管にいれフィルターが完全に溶解するまでよく攪拌した後、石英ガラス板上で薄く伸ばして粒子層を作製する。その後、粒子層の上に厚さ $20 \mu\text{m}$ の PC 製の検出器を重ね、粒子層と検出器の一端を石英ガラス板上に固定し 2層式 FT 試料とした。2層式 FT 試料においては検出器での飛跡の形成は粒子層と検出器との間の密着度に大きく依存する。このため、粒子層と検出器にもう一枚の石英ガラス板を重ね、ポリエチレン製照射用治具を用いてこれを密着させた (図 1 (a))。熱中性子照射後の検出器のエッチングには、検出器のみをエッチングするために石英製の治具を作製し用いた (図 1 (b))。これによりエッチング工程による影響を及ぼさずに検出器だけを簡便にエッチングすることが出来た。検出器の熱中性子照射・エッチング後、核分裂性粒子の同定は検出器を元に戻すことで容易に判別することが出来る (図 1 (c))。本法の有効性を環境試料中のウラン粒子の検出の例で示す。図 2 (a) に示すように粒子層だけではウランと他の粒子との区別は出来ない。粒子層上にエッチングを行った検出器を重ねたのが図 2 (b) で、飛跡とウラン粒子の位置は正確に一致していることが分かる。

本法は、保障措置環境試料で予想される核分裂性粒子以外の粒子あるいは埃などが多数含まれている試料に対しても、飛跡の検出が容易にできる。その例を図 3 (a) と (b) に示す。

図はそれぞれ1層式と2層式FT試料において検出された飛跡で、図3 (a) のように埃などが多数含まれている試料の場合、1層式FT試料では飛跡の検出は非常に時間を要する。これに対して図3 (b) のような2層式FT試料では容易に検出することが出来る。

以上のように、2層式FT試料の開発により、1層式FT試料の欠点を解決し、かつ、ウラン粒子の検出が簡便で正確にできることが示された。

参考文献

- 1) C. G. Lee *et al.*, Jan. J. Appl. Phys. 45 (2006) L294.

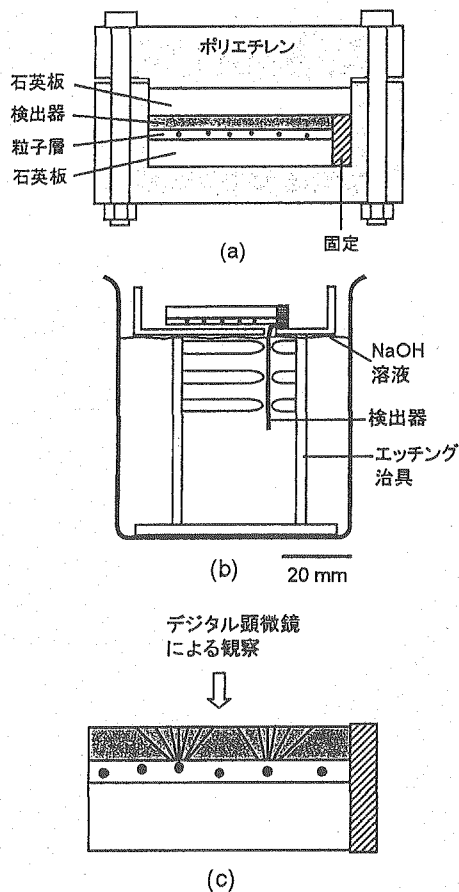


図1 2層式FT試料法による核分裂性粒子検出法。(a) 熱中性子照射、(b) 検出器のエッチング、(c) 目的粒子の同定

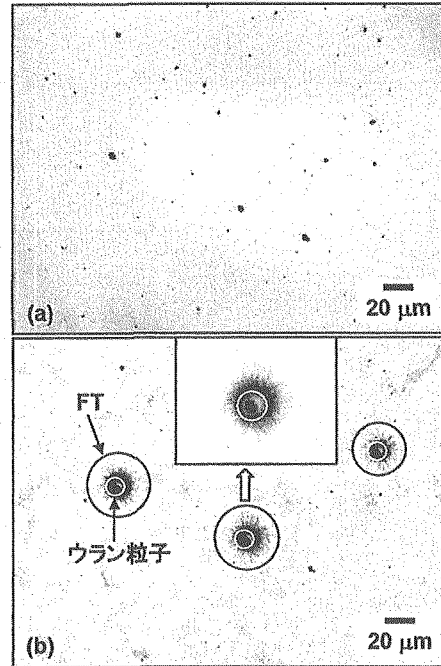


図2 2層式FT試料において飛跡からウラン粒子の検出法。(a) 粒子層、(b) 粒子層上に検出器を重ねた後

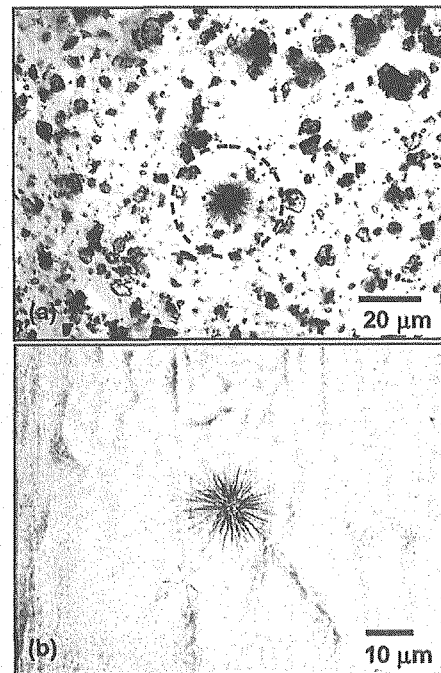


図3 FT試料作製法による飛跡。(a) 1層式FT試料による飛跡 (飛跡は点線の中に存在)、(b) 2層式FT試料による飛跡

研究テーマ：関東甲信静地方における浮遊粒子状物質中の金属成分濃度の把握
 表題：関東における大気エアロゾルのキャラクターゼーション（第25報）

4-2

内藤季和、米持真一¹

千葉県環境研究センター

¹埼玉県環境科学国際センター

関東地方環境対策推進本部大気環境部会浮遊粒子状物質調査会議

本研究では、関東地方の1都9県において浮遊粒子状物質の汚染実態を把握し、その濃度や組成等の動向を知ることを目的とした。

[調査方法] 平成16年7月26～30日(夏期)と12月6～10日(冬期)に18地点で行い、石英ろ紙およびポリフロンろ紙を装着したアンダーセンサンプラーにより、粒子を粒径2.1～11 μ m(粗大粒子)と2.1 μ m未満(微小粒子)に分級捕集した。捕集したろ紙試料は秤量後、日本原子力研究開発機構の原子力科学研究所(茨城県那珂郡東海村)のJRR-3原子炉において気送管(PN-3)での熱中性子放射化分析により、40秒照射・180秒測定で9種の短寿命核種(Mg, Al, Cl, Ca, Ti, V, Mn, Cu, Br)を分析した。イオンクロマトグラフ法により水溶性成分、CHNコーダー(熱分離法)により、炭素成分についても分析した。

[調査結果] (1)粒子状物質濃度：結果を図1に示した。平均値は粗大粒子が夏期、冬期ともに11 μ g/m³、微小粒子は夏期10 μ g/m³、冬期19 μ g/m³であった。微小粒子/(粗大粒子+微小粒子)の平均値は前年度までの0.7と比較して夏期が0.5、冬期は0.6と小さく、例年以上に粗大粒子の占める割合が多かった。

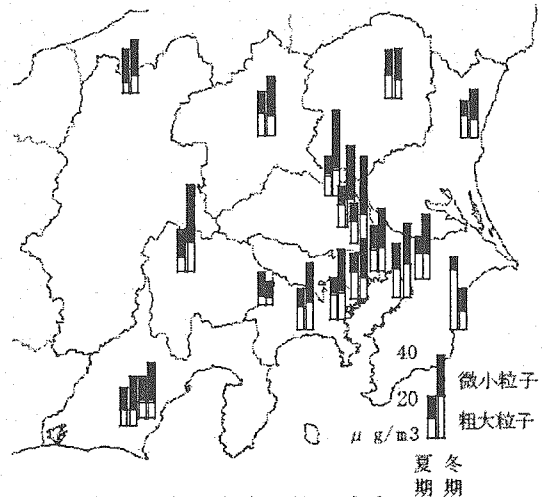


図1 平成16年度調査時の粒子濃度

(2) 金属成分：バナジウムは東京湾岸で高い傾向にあり、湾岸部で重油燃焼が多いことを示唆している。マンガンは冬期に東京湾岸で高くなる傾向があったが、理由は不明である。アルミニウムとカルシウムは粗大粒子に多く存在し、土壌粒子や道路粉じん由来と考えられる。ナトリウムと塩素は海に近い粗大粒子で濃度が高くなり、海塩粒子の影響と考えられた。臭素は例年微小粒子で濃度が高いが、今年度の結果では夏期の粗大粒子で高くなり、その原因は不明である。水溶性成分との比較では、ナトリウムと塩素はほぼ一致し、カルシウムとマグネシウムは放射化分析の結果が高く、非水溶性成分が多いと考えられる。

原子炉：JRR-3

装置：気送管

分野：放射化分析(環境)

研究テーマ：放射化分析による家畜・家禽の土壤摂取量推定

表題：家畜・家禽の土壤摂取が畜産物の生産に及ぼす影響

4-3

土壤混入率が異なる飼料を摂取した乳牛の乳汁中ダイオキシン類の濃度

西村宏一 木方展治¹

独立行政法人 農業・食品産業技術総合研究機構 畜産草地研究所

1 独立行政法人 農業環境技術研究所

家畜・家禽が土壤の付着した飼料を摂取するすると、表層土に吸着されている重金属や残留農薬等の有害物質が土壤を介して畜産物へ移行し、人体への汚染も危惧される。しかし、その影響は十分に検討されていない。平成 17 年度はスカンジウムを標準物質として用い、放射化分析法で泌乳牛の土壤摂取量と乳汁中のダイオキシン類の濃度を検討した。

飼料の調製条件（牧草の刈り取り時期の差異）から土壤混入率が高いと思われる TMR（穀実主体の配合飼料と牧草やサイレージ類の粗飼料を混合した飼料）と土壤混入率が低いと思われる TMR を、通常に飼養されている泌乳牛へ 45～60 日間給与し、高混入区（3 頭）と低混入区（2 頭）の分娩 6 日目の乳汁を採取した。TMR および粗飼料の生産圃場で採取した土壤を風乾・微粉碎して試料とした。TMR（300mg）、土壤（100mg）ならびに標準物質のスカンジウム水溶液を吸着させたろ紙をポリエチレン製袋に二重封入し、日本原子力研究開発機構 JRR-4 炉簡易照射筒（熱中性子束 $5.3 \times 10^{17} \times \text{m}^{-2}$ ）で、20 分間照射した。30～45 日間の冷却後、外側のポリエチレン製袋を交換し、 γ 線スペクトロメトリによって 500 秒間測定した。また、給与飼料（TMR）および乳汁中のダイオキシン類をキャピラリー高精度マススペクトルグラフ法で定量した。

飼料中の土壤含有率は表 1 のとおりであった。土壤混入率の差異は飼料調製時期の違いによるもので、牧草の草高の高低が土壤混入率に影響したものと思われた。

表 1 粗飼料の刈り取り時期と土壤含有率

刈り取り時期	土壤含有率
1 番刈り	0.19 %
3 番刈り	0.56 %

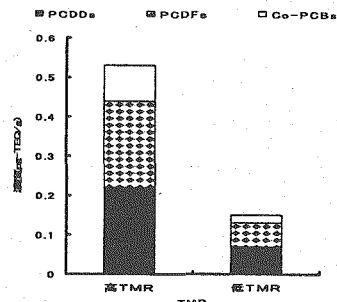


図1 TMRのダイオキシン類の濃度

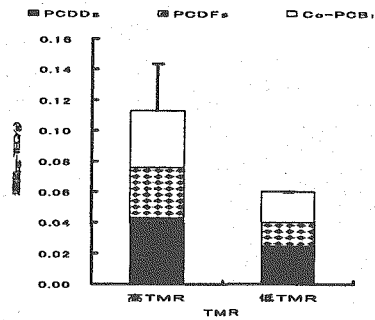


図2 牛乳中ダイオキシン類の濃度

また、土壤高混入 TMR と土壤低混入 TMR のダイオキシン類の濃度は図 1 のとおりであり、これを摂取した泌乳牛の乳汁中ダイオキシン類は図 2 のとおりであった。

飼料に付着した土壤中ダイオキシン類は牛体を通して乳汁へ移行した。

原子炉：JRR-4 装置：簡易照射筒

放射化分析：（農・水産物）

研究テーマ：核破砕核種に対する線量評価法の開発
 表題：水銀中生成トリチウムの性状解明

4-4

リチウムアマルガムの照射実験

真辺健太郎、横山須美、遠藤章

独立行政法人日本原子力研究開発機構 茨城県那珂郡東海村白方白根 2-4

J-PARC の物質・生命科学実験施設には、水銀を標的に用いた核破砕中性子源が設置される。この水銀ターゲット中には、大強度陽子による水銀の核破砕反応によって水素からビスマスまでの多種多様な放射性核種が生成する¹⁾。これら放射性核種のうち、トリチウムや希ガス放射性同位体などは液体である水銀ターゲットから漏出する可能性がある。中でもトリチウムは、水銀ターゲットに蓄積する放射性同位体のうちの約6割を占めると見積もられている¹⁾。またトリチウムは、その化学形によって線量係数が一万倍も異なる核種であり、被ばく防護及び線量評価の観点から水銀中で生成するトリチウムの性状や気相移行挙動に関する知見が極めて重要である。しかし現在のところ、水銀中生成トリチウムの性状等に関する研究はほとんど行われていない。

本研究は、大強度陽子により誘導される水銀の核破砕反応で水銀中に生成するトリチウムの化学形や気相移行挙動を明らかにすることを目的とする。大強度陽子誘導トリチウムを模擬するために、水銀に少量のリチウムを溶解して液体アマルガムとし、これを熱中性子照射することにより水銀中にトリチウムを生成させる方法を考案した。大強度陽子誘導トリチウムと熱中性子誘導トリチウムは、生成直後の運動エネルギーに差はある²⁾がともにホットアトムであり、他の原子や分子と結合を形成するのは運動エネルギーが十分に減少してからであることを考慮すれば、本研究の手法で大強度陽子誘導トリチウムを模擬できていると言える。

照射試料は金属水銀に少量の金属リチウムを加えてよく混合することで調製した。含まれるリチウムの量は約1 mol%とし、試料量は約1 gとした。調製した試料は、後のトリチウム回収実験で使用する装置に接続可能な形状を備えた石英管に封入した。また、照射試料の位置における熱中性子フラックスを正確に求めるためにコバルトフラックスモニタを用意した。試料とコバルトフラックスモニタを JRR-4 中性子ビーム設備のビーム孔に設置し、熱中性子モード I (熱中性子フラックス約 $2 \times 10^9 \text{ s}^{-1} \text{ cm}^{-2}$) で6時

間照射した。照射後の試料は約3日間冷却し、その後トリチウム回収実験に用いた。

図1に回収装置の模式図を示す。トリチウムの化学形はトリチウムガス (HT) またはトリチウム水 (HTO) のいずれかであると考えられる。まず HTO を水バブラで回収する。水バブラを通過した HT ガスは、約 600 °C に加熱した酸化銅 (CuO) カラムを用いて HTO に酸化した後、水バブラで回収した。液体シンチレーションカウンタを用いて放射能測定を行った。また、コバルトフラックスモニタは Ge 半導体検出器を用いて放射能測定を行い、これよりフラックスは約 $1.6 \times 10^9 \text{ s}^{-1} \text{ cm}^{-2}$ と求まった。

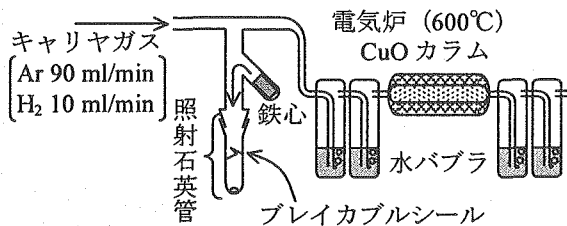


図1 照射石英管とトリチウム回収装置

本実験の結果、化学形の比 HTO/HT が 2 ~ 7 となり、HT よりも HTO が多く存在することが明らかとなった。不純物として水銀に溶存している酸素や水などの影響によるものと考えられる。

本研究は H18 年度も継続し、照射石英管の形状を改良するなどして収率の向上を図り、気相移行率を求める予定である。

参考文献

- 1) 小林薫, 神永雅紀, 羽賀勝洋, 木下秀孝, 麻生智一, 勅使河原誠, 日野竜太郎. JAERI-Tech 2002-005 (2002).
- 2) M. Enke, C.-M. Herbach, D. Hilscher, U. Jahnke, O. Schapiro, A. Letourneau, J. Galin, F. Goldenbaum, B. Lott, A. Péghaire, D. Filges, R.-D. Neef, K. Nünighoff, N. Paul, H. Schaal, G. Sterzenbach, A. Tietze and L. Pienkowski, Nucl. Phys. A 657 (1999) 317-339.

研究テーマ：RI・放射線技術者の養成

表題：実習 放射化分析

4-5

玄米およびゴマ中の微量元素分析

Neutron Activation Analysis of Trace Elements in Rice and Sesame

櫛田浩平

所 属 原子力研修センター

原研機構・原子力研修センターでは国内向けの各種研修コースの他、タイ、インドネシア、ベトナムなどの東南アジア諸外国を対象に原子力・放射線に関する研修協力事業を行っている。本実験はその中の「指導教官研修」としてベトナムからの研修生を対象として行った研修実験である。

研修生は現在あるいは将来自国における指導教官となるべき立場の人であり、本実験を通して放射化分析の基本理論と実験の具体的プロセスを体験し理解してもらうことを目指している。また本実験を通して非密封放射性同位元素の安全取扱いに習熟することも重要な課題である。

この実験では身近な環境試料として玄米およびゴマを選んだ。試料はポリエチレン袋に二重に封入し、JRR-4 PN パイプで 10 秒照射した。試料と共に中性子フラックスモニター（金箔）および Mn 標準試料も照射した。

照射後の試料は JRR-4 付属の実験室ですぐに開封し、Ge 測定器で放射能を測定した。

開封作業は研修生がゴム手袋等の防護具をつけ、養生したフードの中を行った。これは典型的な非密封 RI 取扱い作業であり、汚染や被ばくの低減を図りながら実施した。

今回分析対象とする元素は短寿命核種であり、2分から 30 分程度の冷却時間をおいて Ge 測定器でそれぞれ 300 秒測定した。測定距離は 5 cm。

この照射孔の中性子束は公称 $3.2 \times 10^{13}/\text{cm}^2\text{s}$ であるが、モニターによる測定では $3.73 \times 10^{13}/\text{cm}^2\text{s}$ という値を得た。

実験データの解析の結果、 ^{24}Na 、 ^{27}Mg 、 ^{28}Al 、

^{38}Cl 、 ^{42}K 、 ^{56}Mn 、 ^{59}Fe 、 ^{66}Cu などを検出した。主な元素の定量結果を表 1 に示す。

表 1 含有微量成分定量結果

	玄米	ゴマ
Mg	749	1982
Al	6.63	-
Na	5.21	-
Cl	123	24.6
K	1496	4610
Mn	15.9	48.6
Cu	-	16.4

金属としては Mg および K が多く含まれ、Mn も比較的にかかった。

以前の実験では玄米と白米を分析し、米中の微量元素は白米にしたときよりも玄米の方が割合として多く含まれることが分かったが、今回米（玄米）とゴマとを比較すると、一般的傾向として米よりもゴマの方が微量元素の含有割合が多いことが分かる。特にカリウムの含有割合が多かった。

米およびゴマ中の微量元素含有量を一般的に議論するにはさらに多くのデータ収集が必要であるが、ここでは研修実験として、本実験を通して研修生が放射化分析の基本理論と実験上の主要なプロセスを理解することができたと思われる。

原子炉：JRR-4

装置：気送管

分野：放射化分析（その他）

研究テーマ:中性子放射化分析法による環境試料の分析
 表題 :大気エアロゾル粒子のキャラクタリゼーション

4-6 大気エアロゾル粒子中の元素状カルシウムと水溶性カルシウムの濃度比

伊藤憲男 溝畑 朗
 大阪府立大学先端科学イノベーションセンター〒599-8570 大阪府堺市中区学園町1-2

研究目的

大気中に浮遊している粒子(大気エアロゾル粒子)の物理的および化学的特質を知るために、堺市において大気エアロゾル粒子を連続して観測している。捕集された試料のほとんどについてイオン成分(Cl^- , NO_3^- , SO_4^{2-} , Na^+ , NH_4^+ , K^+ , Mg^{2+} , Ca^{2+})の分析がおこなわれている。このなかで、土壌粒子の影響が大きい Ca^{2+} については、次の点が不明である。
 1)水溶性である Ca^{2+} がどのような化合物で存在しているか。
 2)全体のカルシウム、つまり元素状カルシウムに対してどの程度水溶性カルシウム(Ca^{2+})が存在しているか。
 以上の点を明らかにするために、捕集したエアロゾル粒子の元素状カルシウムの量を中性子放射化分析法で定量し、イオンクロマトグラフィーで分析した Ca^{2+} と比較し、カルシウムの元素状と水溶性の割合を求めた。さらに、イオン成分の分析結果より、 Ca^{2+} の化学形について推定した。

試料の採取方法

大気エアロゾル粒子を、堺市の大阪府立大学で捕集している。捕集条件は、次の表のとおりである。メンブレンフィルターは、放射化分析用、石英繊維フィルターはイオン成分分析用の試料を採取するために使用した。

捕集時間	吸引スピード	フィルター
24 時間(0-24 時)	20l/min	25mmφ メンブレンおよび石英繊維

放射化分析の分析条件

今回の実験は、蛍光 X 線分析で分析した Al の分析値の比較を行うため、蛍光 X 線の分析を行った試料から主に 2000 年と 2004 年に捕集された試料について放射化分析を行った。

以下の条件で中性子の照射を行い、放射化された試料は約 5 分間放射能が減衰するのを待ち、Ge 半導体検出器でガンマー線スペクトルを測定した。

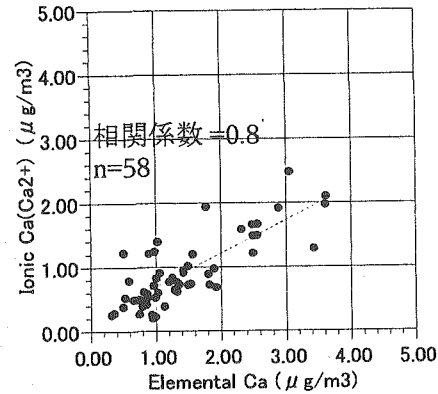
項目	条件
原子炉	JRR-3
照射孔	PN-3
照射時間	30 秒

結果

放射化分析で分析した元素状カルシウムとイオンクロマトグラフィーで分析した水溶性カルシウム(Ca^{2+})を比較した図を以下に示す。

原子炉 :JRR-3
 原子炉 :JRR-4

装置:放射化分析用照射設備
 装置:T パイプ



グラフ上の点は、傾き 0.52 の直線状にほぼ分布し、相関係数は 0.8 となった。良い相関関係はみとめられたが、元素状カルシウムに対する水溶性カルシウム(Ca^{2+})の割合($[\text{Ca-el}]/[\text{Ca}^{2+}]$)の平均値、標準偏差、最小値、最大値は、次のとおりであった。

	n	平均	標準偏差	最小	最大
$[\text{Ca-el}]/[\text{Ca}^{2+}]$	58	0.66	0.21	0.22	1.0

平均値は 0.66 であったが、0.22 ~ 1.0 の間で変化した。この割合の変化の季節的特徴は、試料数が少ないので、認められなかった。

陰イオンと陽イオンのモル濃度比で比較した場合、 Ca^{2+} に対する陰イオンとして NO_3^- が存在している可能性が示唆された。このことより、もともとの水溶性の割合が少ないカルシウムに対して、エアロゾル粒子表面でガスまたは粒子状の硝酸が反応して、 $\text{Ca}(\text{NO}_3)_2$ が生成されている可能性が認められた。

分野:放射化分析(環境)
 分野:放射化分析(環境)

This is a blank page.

5. ラジオアイソトープ製造



5. Production of Radio Isotopes

This is a blank page.

研究テーマ：溶融固化体に対する放射能測定手法の簡易・迅速化

表題：¹⁴C 分離法の検討

5-1 溶融固化体に対する放射能測定手法の簡易・迅速化 —¹⁴C 分離法の検討—

石森 健一郎 大木 恵一¹ 亀尾 裕 高泉 宏英¹ 中島 幹雄 大木 善之² 磯貝 啓介²

日本原子力研究開発機構バックエンド推進部門廃棄物確認技術開発グループ

¹ 日本原子力研究開発機構バックエンド技術部放射性廃棄物管理技術課² 日本分析センター

溶融固化体からの¹⁴C 分離法として、アルカリ融解法の適用について検討した。¹⁴C を含有する模擬溶融固化体試料の分析について従来法と比較した結果、アルカリ融解法は¹⁴C の定量的回収が可能で優れた分離法であることが分かった。

キーワード：溶融固化体、¹⁴C、アルカリ融融、放射能測定

緒言 日本原子力研究開発機構（原子力機構）では、所内施設で発生する低レベル放射性雑固体廃棄物を溶融固化体に成形してから処分することを計画している。処分を行うためには溶融固化体に含まれる放射性核種の合理的な評価手法の確立が求められ、現在、安全評価上重要となる核種について簡易かつ迅速な分析手法の構築を進めている。従来、固体試料からの¹⁴C 分離法には、O₂ 雰囲気中で強熱し CO₂ として回収する燃焼法¹⁾が用いられている。しかし、多元素の複合酸化物である多種多様な溶融固化体から効率的に¹⁴C を分離するためには、固化体の安定な化学構造を完全に分解できる試料処理法の選択が望ましいと考えられる。そこで溶融固化体からの¹⁴C 分離法としてアルカリ融解法の適用について検討し、¹⁴C を含有する模擬溶融固化体試料の分析結果について従来法との比較を行った。

実験 《¹⁴C 含有模擬溶融固化体試料の作製》 Si₃N₄ (17.5wt%)、SiO₂ (57.7wt%)、CaO (16.5wt%)、Al₂O₃ (8.2wt%) を混合してアルミナ坩堝に入れ、N₂ 雰囲気下 1600°C の電気炉内で溶融した。放冷した溶融物 (N 含有量 7wt%) を粒径 150 μm 以下に調製後、原子力機構 JRR-3 で熱中性子照射し ¹⁴N (n, p) ¹⁴C 反応により ¹⁴C を含有する模擬溶融固化体試料を作製した。

《アルカリ融解法を用いた¹⁴C 分析》溶融固化体試料 0.1g と NaOH 2.0g を Ni 坩堝に計り取り、550°C の電気炉内で 30 分間加熱してアルカリ融解した。

放冷後溶融物を純水に溶解し、N₂ パージしながら希 HNO₃ を加えて pH1 以下とした。溶液から発生した CO₂ はフェネチルアミン (PA)-メタノール溶液 (v/v=1) に吸収させて液体シンチレーションカウンターにより放射能を測定した。

結果 PA 溶液へ CO₂ の吸収について時間依存性を確認するため、既知量の¹⁴C 放射能基準 (Na₂CO₃) 溶液を用いて検討した。回収時間 120 分間で¹⁴C が 99% 以上回収されることが分かり、以後回収時間は 180 分間とした。次に¹⁴C 分離における溶融固化体マトリックスの影響について検討した。中性子照射前の Si₃N₄ 含有溶融固化体に¹⁴C 放射能基準を既知量混合し、アルカリ融融して PA 溶液に CO₂ を回収したところ回収率は 80% となった。この回収率の低下を防ぐために溶融固化体試料 0.1g 対し担体 Na₂CO₃ 0.1g を添加すると、回収率は 101% に向上し¹⁴C を定量的に回収できることが分かった。以上の検討をもとに、熱中性子照射により作製した¹⁴C 含有模擬溶融固化体試料の分析を行った (Table 1)。アルカリ融解法を用いた場合、¹⁴C の定量値は 1.26 × 10³ Bq/g となり、生成放射能の計算値 (1.2 × 10³ Bq/g) とほぼ一致した。一方、O₂ 気流下 900°C で 1 時間加熱する燃焼法では、定量値はアルカリ融融法の半分以下であった。

結言 本報告ではアルカリ融解法を用いることで溶融固化体からの定量的な¹⁴C の回収が可能となり、従来法よりも優れた¹⁴C 分離分析法を確立できた。


[1] 浅井他, JAERI-TECH, 2003-071 (2003).

Table 1 ¹⁴C 含有模擬溶融固化体試料の分析

分離法	定量値 (Bq/g)
アルカリ融解法	(1.26 ± 0.02) × 10 ³
燃焼法 ¹⁾	(5.79 ± 0.08) × 10 ²
計算値: 1.2 × 10 ³ (Bq/g)	

This is a blank page.

6. 原子炉燃料材料



6. Irradiation Test of Reactor Materials

This is a blank page.

研究テーマ：中性子照射により生成する鉛ビスマス合金中のポロニウム挙動に関する研究
 表題：JRR-4 中性子ビーム設備による鉛・ビスマス合金試料の中性子照射

6-1

鉛ビスマスから生成されるポロニウムのニッケルに対する付着特性

小原 徹、古賀 健¹、三浦照光¹、関本 博
 東京工業大学原子炉工学研究所
¹東京工業大学大学院理工学研究科

鉛ビスマス共晶合金(LBE)を冷却材等として用いた原子炉システムでは、ビスマスの中性子捕獲によりポロニウムが生成される。ポロニウム安全対策技術開発のための基礎的知見を得ることを目的として、ポロニウムの金属表面に対する吸着特性についての実験を行った。材料腐食実験からNiが鉛ビスマス合金に対して溶け出すということが知られている⁽¹⁾。そこで本実験ではNi金属を用いての吸着実験を行い、SUS316での実験結果と比較した。

5gのLBEに対し日本原子力研究開発機構のJRR-4中性子ビーム施設を用いて熱中性子照射を行い、ポロニウムを含んだLBE試料を作成した。その試料を加熱吸着試験装置⁽²⁾で加熱し、Ni金属板に吸着させた。実験条件を表1に示す。実験前後にNi金属板、鉛ビスマス試料の重さを測定し、実験後にNi金属板から放出されるα線の計

数(20hour)をα線スペクトロメーターで測定した。

実験の結果を表2に示す。LBE温度630℃の場合は550℃の場合と比べてLBEの蒸発量、Ni金属板への付着物の量が多くなっている。しかしながらポロニウムの量はLBE温度550℃の場合の方が630℃の場合よりも多くなっていることが確認できた。金属板材料の違いによる付着特性の違いは本実験では現れなかった。更に詳細な実験を行い材料の違いによる付着特性の変化についての検討を行う予定である。

参考文献

- 1) M Kondo et al, Journal of Nuclear Materials 343 (2005) 349-359.
- 2) 三浦、他；日本原子力学会「2004年春の年会要旨集」O-11

表2 実験結果

金属板材料	LBE 温度 (°C)	金属板温度 (°C)	金属板重量 増加(mg)	LBE 重量 減少(mg)	実験後のα線計数(Counts/20hr)
Ni	630	280	61	793	24
		320	13	566	34
	550	255	15	72	5835
		295	3	16	1121
		310~360	13	82	5272
SUS316	550	280	1	20	1652
		230	8	57	11148
		245	1	24	931

表1 実験条件

金属板材料	Ni, SUS316
温度保持時間	1hour
容器内圧力	0.5~1Pa
LBE加熱温度	550, 630°C
金属板温度	230~350°C

原子炉：JRR-4 装置：中性子ビーム設備 分野：原子炉燃料・材料（高速炉）

This is a blank page.

7. その他



7. Others

This is a blank page.

7-1

再発頭頸部癌に対するホウ素中性子捕捉療法

粟飯原輝人¹、平塚純一²、森田倫正¹、熊田博明³、小野公二⁴、原田保¹¹川崎医科大学耳鼻咽喉科学教室²川崎医科大学放射線医学教室（治療）³日本原子力研究開発機構⁴京都大学原子炉実験所

【はじめに】

頭頸部癌治療は、外科的治療、放射線治療、抗癌剤治療の3者を至適に組み合わせる方法が主流である。各治療法の技術は改良され治療率は向上してきているが、発見が遅れた進行癌や治療後の再発癌では、ほとんどの症例が従来の治療法での完全治癒を期待することは難しい。頭頸部が機能上・美容上その温存が大変重要な領域であり、従来の治療法では、制御困難と思われる進行病巣・再発病巣を正常臓器を損なうことなく治療できれば、患者の大きな負担は勿論のこと治療後の高いQOLが期待できる。そのような治療法開発は重要かつ急務である。

アミノ酸代謝が亢進した癌細胞に特異的に集積する p-boronophenylalanine (BPA)を用いた中性子捕捉療法 (BNCT) は、主に癌組織に集積した硼素 (¹⁰B) と熱中性子との核反応で生じる高 LET 放射線 (α 粒子) により癌細胞だけにエネルギーを集中させる事が可能であり癌治療の理想である¹⁾。また BPA の腫瘍集積は ¹⁸F-BPA PET での定量が可能で、その結果から抗腫瘍効果が予測可能である²⁾。

我々は上記理論に基づいて、2003年10月から川崎医科大学倫理委員会承認のもと、進行頭頸部癌患者に中性子捕捉療法を行っており、その詳細を報告する。

【対象と方法】

対象は2003年10月から2006年8月までの間に、(1)頭頸部癌標準治療にて制御困難、(2)PS \leq 2、(3)遠隔転移を認めない、または認めても予後に大きく関与しない、(4)¹⁸F-BPA PET 検査にて腫瘍/正常組織集積比が2.5以上、(5)文章で

同治療法について同意が得られた、のすべて条件を満たした再発頭頸部癌13例である。

性別は男性9例・女性4例、年齢は31歳から77歳(平均62.2)であった。

組織型は扁平上皮癌7例、悪性黒色腫3例、未分化癌1例、乳頭状腺癌1例、高悪性度粘表皮癌1例であった。全症例の観察期間は、6-42ヶ月(平均14.4)であった。

照射方法は照射前に病変部を画像(CTまたはMRI)撮影したものを、BNCT専用治療計画ソフト (SERA 又は JCDS) を用いて評価し、皮膚線量が15Gy-Eq、眼球線量が10Gy-Eq以下と設定し、腫瘍最低線量を20Gy-Eq以上とした。

照射日にBPA500mg/kgを2-3時間かけて点滴静注を行い、終了直後に照射体位のセッティングを行った。照射直前に血中ホウ素濃度を測定し、その血中ホウ素濃度から推定した各組織のホウ素濃度と、15分間の中性子線量から最終的な照射時間を決定した。

【結果】

全13症例の治療効果は、CR:3例、PR:8例、NC:2例であり、奏効率は84.5%であった。生存6例の現在までの平均観察期間は17.3ヶ月であり、死亡は7例であった。死亡例の内訳は、現病死6例、他因死1例であり、平均生存期間は11.8ヶ月であった。

照射に伴うGradeII以上の治療が必要とされる合併症は、放射線皮膚・粘膜炎が2例に認められたのみであり、その他の合併症は認められなかった。現在のところ晩期放射線障害は認められていない。

Case	原発巣	年齢/性	組織型	効果	合併症:放射性皮膚炎 (RTOG/EORTCscore)	観察期間	経過
1	顎下線	49/F	MC(HG)	CR	GI	42M	有病生存
2	中咽頭	73/M	SCC	NC	GI	19M	局所再発
3	舌	39/F	SCC	PR	GI	11M	遠隔転移
4	鼻根部	71/M	SCC	NC	GI	12M	遠隔転移
5	甲状腺	71/M	PAC	PR	GI	27M	有病生存
6	不明	77/M	SCC	CR	GI	20M	遠隔転移
7	中咽頭	73/M	SCC	PR	GI	11M	局所再発
8	喉頭	64/M	SCC	CR	GI	7M	敗血症
9	前頭洞	31/M	UC	PR	GI	3M	遠隔転移
10	口腔底	57/M	SCC	PR	GII	11M	有病生存
11	涙嚢	74/F	MM	PR	GI	9M	有病生存
12	口唇	66/M	MM	PR	GII	9M	有病生存
13	鼻腔	73/F	MM	PR	GI	6M	有病生存

MC: mucoepidermoid carcinoma, SCC:squamous cell carcinoma, UC:undifferentiated cancer, PA:papillary adenocarcinoma, MM:Malignant Melanoma, CR:complete response, PR:partial response, NC:no change

図1) 当科でBNCTを行った症例一覧

[考察とまとめ]

標準の頭頸部癌治療で制御不可能な症例に対して行った本治療では、奏効率 84.5%と非常に高いものであった。しかし、進行および再発癌の場合は、明らかな病変以外に微小転移が隠れている事が否定できず、我々の症例でも治療後に出現した転移病巣が予後を大きく左右した。しかしながら、標準治療施行後の再発病変に対する二次治療としての有効性は我々の最初の症例³⁾や本臨床研究結果から明らかであり、加藤らもその有効性を高く評価している⁴⁾。これまでの結果を踏まえ我々はBNCTを頭頸部癌治療の補助療法の一つ(Neoadjuvant therapy)に組み込むことができると考えている。現在我々は当大学倫理委員会承認のもと、頭頸部癌の初期治療にBNCTを開始しており、その治療効果を検討中である。

参考文献

- 1) Y Mishima. Neutron capture treatment of malignant melanoma using ¹⁰B-chlorpromazine. *Pigment Cell Res.* 1:215-221, 1973
- 2) Y Imahori, S Ueda, Y Ohmori, T Kusuki, K Ono, R Fujii and T Ido. Fluorine-18-labeled fluoroboronophenylalanine PET in patients with glioma. *J. Nucl. Med.* 39:325-333, 1998
- 3) Teruhito Aihara, Junichi Hiratsuka, Norimasa Morita, et al: First clinical case of boron neutron capture therapy for head and neck malignancies utilizing ¹⁸F-BPA PET. *Head and Neck.* -DOI 10 850-855 2006
- 4) I Kato, K Ono, Y Sakurai, M Ohmae, A Maruhashi, Y Imahori, M Kirihata, M Nakazawa and Y Yura. Effectiveness of BNCT for recurrent head and neck malignancies. *Applied Radiation and Isotopes* 61:1069-1073, 2004

研究テーマ：フィッション・トラック年代測定

表題：FT年代測定のためのディテクターの開発

7-2

フィッション・トラック法に用いるDAPプラスチックディテクターの改良(その2)

岩野英樹¹・檀原 徹¹・小林啓一²・鶴田隆雄³

¹: (株)京都フィッション・トラック ²: 山本光学㈱ ³: 近畿大学原子力研究所

近年、フィッション・トラック (FT) 年代測定法の外部ディテクターとしてジアルリフタレート (diallyl phthalate : DAP) 樹脂^{1,2,3,4,5,6)}が用いられている。これまで白雲母が使われてきたが、照射後の誘導放射能がかなり大きいことが問題になっていた⁹⁾。このことから放射線障害防止の観点上、放射能の小さいDAP樹脂への変更が進んでいる⁷⁾。一方、従来のDAP樹脂にはBrが不純物として含まれることが明らかになった⁸⁾。Br-82の半減期は35時間と比較的短い、照射直後から数日間は比較的高い放射能をもつ。放射化による試料の取り扱いに関する諸問題と従事者の被ばくの軽減の解決には、このような不純物を含まないディテクターが望まれる。

DAP樹脂の主原料は、DAPモノマーで、その製法には2種類ある：①アリルクロライドをフタル酸ソーダと反応させる、②アリルアルコールを無水フタル酸と反応させる。従来のDAP樹脂(以下Q-DAPと呼ぶ)は製法①のモノマーであったが、今回製法②のDAPモノマーを使って新しい樹脂(以下S-DAPと呼ぶ)を作成した。

JRR-4炉気送管(3.5MW)において熱中性子照射を120~180秒間行い、S-DAPおよびQ-DAPの照射後の表面線量の変化を比較した。測定にはGMサーベイメータを用い、この時の検出限界(BGレベル)は80cpmであった。図1にDAP試料の表面線量の減衰の様子を示した。

これまでの研究により、Q-DAPの表面線量率

は白雲母のその100分の1以下であることが明らかにされている⁹⁾。今回新しく作成したS-DAPは、Q-DAPよりさらに線量率が小さく(図1)、およそQ-DAPの3分の1程度であった。上記の照射条件の場合、表面線量が完全にBGレベルまで減衰するまでの経過時間は、Q-DAPでは最長6ヶ月であったのに対し、S-DAPは1~2ヶ月であった。

放射化の観点から見た場合、S-DAP樹脂は従来のものより優れた材料である。S-DAPの利用により、FT年代測定がさらに安定した手法として改良することができるであろう。

参考文献

- 1) Tsuruta, T. (1999) Radiat. Meas., 31, 99-102.
- 2) Tsuruta, T. (2000) Radiat. Meas., 32, 289-297.
- 3) Tsuruta, T. (2001a) Radiat. Meas., 34, 167-170.
- 4) Tsuruta, T. (2001b) American Society for Testing and Materials, 100, 789-796.
- 5) 小口・鶴田 (2001) 第1回先進放射線応用シンポジウム(大阪大学), 103-106.
- 6) 吉岡哲・鶴田隆雄・岩野英樹・檀原徹 (2002) FT ニュースレター, 第15号, 1-8.
- 7) Danhara, T., Iwano, H., Yoshioka, T. and Tsuruta, T. (2003) Jour. Geol. Soc. Japan, 109, 665-668.
- 8) Yoshioka, T., Tsuruta, T., Iwano, H. and Danhara, T. (2006) Radiat. Meas., 41, 513-519.

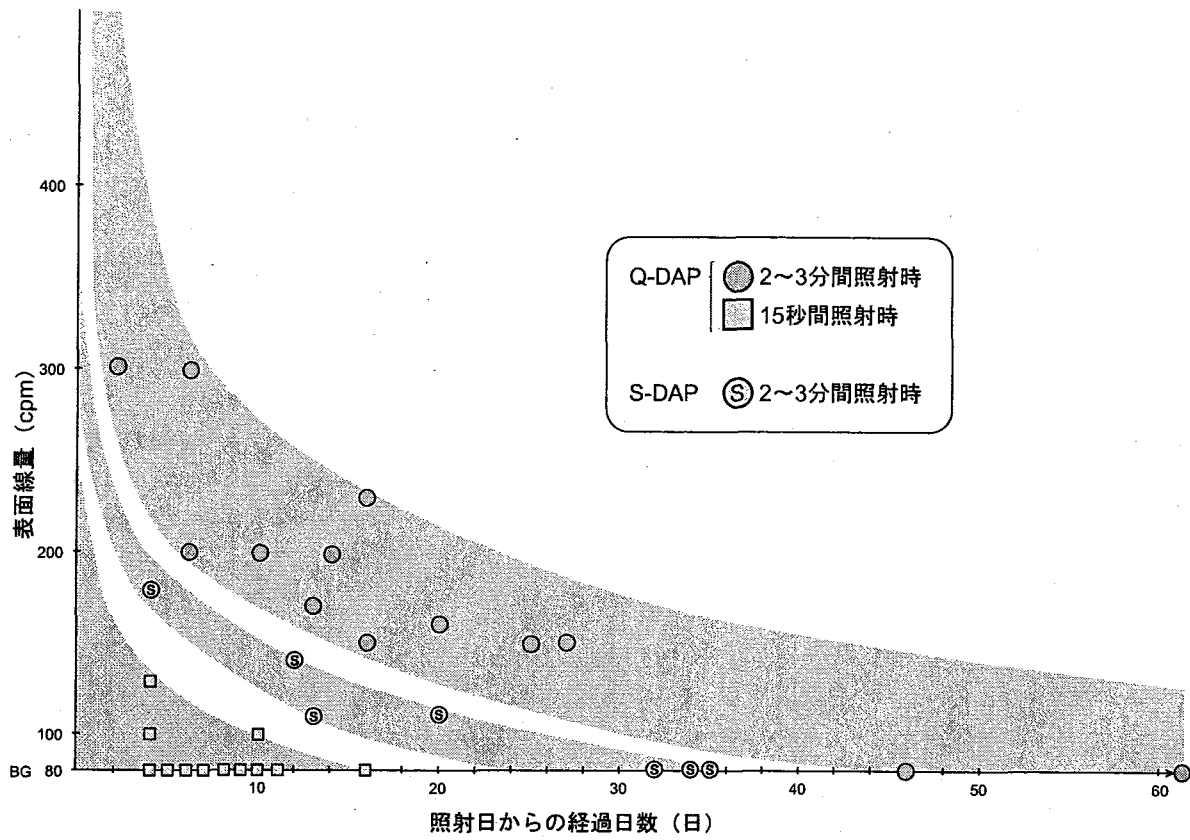


図1. JRR-4炉気送管(3.5Mw時)において2~3分照射した時のQ-DAPおよびS-DAPの表面線量経時変化. Q-DAPの15秒照射時のデータも合わせて示した.

おわりに

本報告書は、研究炉（JRR-3、JRR-4）を利用した利用者の協力を基に、研究炉の成果を提出して頂き、研究炉利用課で編集したものであります。この成果を公表する事で、研究炉の今後の有効利用並びに利用拡大に役立つ事を期待します。

なお、毎年度多大なるご協力頂いていた、『東京大学原子力研究総合センター』及び『東京大学物性研究所』の研究成果につきましては、それぞれの機関で研究成果を取りまとめているため、本報告書に掲載されておりません。

編集委員

編集委員メンバー

楠 剛（研究炉利用課長）

堀 直彦（研究炉利用課）

高橋 俊行（研究炉利用課）

渡辺 広子（研究炉利用課）

謝 辞

本報告書の発刊にあたり、多くの皆様から多大なご協力を頂きました。

原稿を提出して頂いた利用者の皆様のご協力に感謝するとともに、今後も研究炉が有効に利用され、種々の研究がさらに進展されることを期待します。

編集に際し、ご協力頂いた、研究炉加速器管理部長 山下清信氏、研究炉加速器管理部次長 竹内末広氏、JRR-3管理課長 村山洋二氏に深く感謝致します。

付 録



Appendixes

This is a blank page.

付録

原科研研究炉の利用設備一覧

1. JRR-3

1) 実験設備

実験孔	実験装置
1G	高分解能粉末中性子回折装置 (HRPD)
1G-A	生体高分子用中性子解析装置 (BIX-III)
1G-B	生体高分子用中性子解析装置 (BIX-IV)
2G	三軸型中性子分光器 (TAS-1)
3G	中性子トポグラフィ及び精密光学実験装置 (PNO)
4G	汎用三軸型中性子分光器 (GPTAS)
5G	偏極中性子散乱装置 (PONTA)
6G	東北大学中性子散乱分光器 (TOPAN)
7R	中性子ラジオグラフィ装置 (TNRF)
T1-1	中性子偏極回折装置 (HQR)
T1-2	単結晶中性子回折装置 (KSD)
T1-3	粉末中性子回折装置 (KPD)
T1-4-1	即発ガンマ線分析装置 (PGA)
T1-4-2	多重即発ガンマ線分析装置 (MPGA)
T1-4-3	TOF型中性子反射率計 (TOF)
T1-4-4	中性子ラウエ回折装置 (LAUE)
T1-4-5	中性子ベータ崩壊基礎測定装置
T2-1	残留応力測定中性子回折装置 (RESA)
T2-2	中性子4軸回折装置 (FONDER)
T2-3	多目的単色熱中性子ビームポート (MUSASHI)
T2-4	高分解能三軸型中性子分光器 (TAS-2)
C1-1	高エネルギー分解能三軸型中性子分光器 (HER)
C1-2	二次元位置測定小角散乱装置 (SANS-U)
C1-3	超高分解能後方散乱装置 (ULS)
C2-1	冷中性子散乱実験デバイス開発装置 (LTAS)
C2-2	高Q領域対応中性子反射率計 (SUIREN)
C2-3-1	中性子スピンエコー分光器 (NSE)
C2-3-2-1	多重即発ガンマ線分析装置 (MPGA)
C2-3-2-2	即発ガンマ線分析装置 (PGA)
C2-3-3-1	冷中性子ラジオグラフィ (CNRF)
C2-3-3-2	パルス中性子機器開発装置 (CHOP)
C2-3-3-3	TOF型中性子反射率計 (TOF)
C2-3-3-4	中性子ラウエ回折装置 (LAUE)
C3-1-1	高分解能パルス冷中性子分光器 (AGNES)
C3-1-2-1	中性子光学システム評価装置 (NOP)
C3-1-2-2	多層膜中性子干渉計/反射率計 (MINE)
C3-2	中性子小角散乱装置 (SANS-J)

2) 照射設備

水 力 照 射 設 備	HR-1, 2
気 送 照 射 設 備	PN-1, 2
放射化分析用照射設備	PN-3
均 一 照 射 設 備	SI-1
回 転 照 射 設 備	DR-1
垂 直 照 射 設 備	VT-1, RG-1~4 BR-1~4, SH-1

2. JRR-4

1) 実験設備

プ ー ル
中性子ビーム設備
散乱実験設備
冷却水循環ループ
医療照射設備 (BNCT)
即発ガンマ線分析装置

2) 照射設備

簡 易 照 射 筒	Tパイプ (水力)
	Sパイプ
	Dパイプ
	Nパイプ
気送管照射設備	PN

国際単位系 (SI)

表1. SI 基本単位

基本量	SI 基本単位	
	名称	記号
長さ	メートル	m
質量	キログラム	kg
時間	秒	s
電流	アンペア	A
熱力学温度	ケルビン	K
物質の量	モル	mol
光の度	カンデラ	cd

表2. 基本単位を用いて表されるSI組立単位の例

組立量	SI 基本単位	
	名称	記号
面積	平方メートル	m ²
体積	立方メートル	m ³
速度	メートル毎秒	m/s
加速度	メートル毎秒毎秒	m/s ²
波数	毎メートル	m ⁻¹
密度 (質量密度)	キログラム毎立方メートル	kg/m ³
質量体積 (比体積)	立法メートル毎キログラム	m ³ /kg
電流密度	アンペア毎平方メートル	A/m ²
磁界の強さ (物質量の) 濃度	アンペア毎メートル (モル毎立方メートル)	A/m (mol/m ³)
輝度	カンデラ毎平方メートル	cd/m ²
屈折率	(数の) 1	1

表5. SI 接頭語

乗数	接頭語	記号	乗数	接頭語	記号
10 ²⁴	ヨタ	Y	10 ⁻¹	デシ	d
10 ²¹	ゼタ	Z	10 ⁻²	センチ	c
10 ¹⁸	エクサ	E	10 ⁻³	ミリ	m
10 ¹⁵	ペタ	P	10 ⁻⁶	マイクロ	μ
10 ¹²	テラ	T	10 ⁻⁹	ナノ	n
10 ⁹	ギガ	G	10 ⁻¹²	ピコ	p
10 ⁶	メガ	M	10 ⁻¹⁵	フェムト	f
10 ³	キロ	k	10 ⁻¹⁸	アト	a
10 ²	ヘクト	h	10 ⁻²¹	ゼプト	z
10 ¹	デカ	da	10 ⁻²⁴	ヨクト	y

表3. 固有の名称とその独自の記号で表されるSI組立単位

組立量	SI 組立単位			
	名称	記号	他のSI単位による表し方	SI基本単位による表し方
平面角	ラジアン ^(a)	rad		m ² ・m ⁻¹ =1 ^(b)
立体角	ステラジアン ^(a)	sr ^(c)		m ² ・m ⁻² =1 ^(b)
周波数	ヘルツ	Hz		s ⁻¹
力	ニュートン	N		m ² ・kg ² ・s ⁻²
圧力, 応力	パスカル	Pa	N/m ²	m ⁻¹ ・kg ² ・s ⁻²
エネルギー, 仕事, 熱量	ジュール	J	N・m	m ² ・kg ² ・s ⁻²
工率, 放射束	ワット	W	J/s	m ² ・kg ² ・s ⁻³
電荷, 電気量	クーロン	C		s ² ・A
電位差 (電圧), 起電量	ボルト	V	W/A	m ² ・kg ² ・s ⁻³ ・A ⁻¹
静電容量	ファラド	F	C/V	m ⁻² ・kg ⁻¹ ・s ⁴ ・A ²
電気抵抗	オーム	Ω	V/A	m ² ・kg ² ・s ⁻³ ・A ⁻²
コンダクタンス	ジーメン	S	A/V	m ⁻² ・kg ⁻¹ ・s ³ ・A ²
磁束密度	ウェベア	Wb	V・s	m ² ・kg ² ・s ⁻² ・A ⁻¹
磁束	テスラ	T	Wb/m ²	kg ² ・s ⁻² ・A ⁻¹
インダクタンス	ヘンリー	H	Wb/A	m ² ・kg ² ・s ⁻² ・A ⁻²
セルシウス温度	セルシウス度 ^(d)	°C		K
光照射度	ルクスメーン	lm	cd・sr ^(c)	m ² ・m ⁻² ・cd=cd
(放射核種の) 放射能	ベクレル	Bq	lm/m ²	m ² ・m ⁻⁴ ・cd=m ⁻² ・cd
吸収線量, 質量エネルギー当量	グレイ	Gy		s ⁻¹
線量当量, 周辺線量当量, 方向性線量当量, 個人線量当量, 組織線量当量	シーベルト	Sv	J/kg	m ² ・s ⁻²

- (a) ラジアン及びステラジアンの使用は、同じ次元であっても異なった性質をもった量を区別するときの組立単位の表し方として利点がある。組立単位を形作る際のいくつかの用例は表4に示されている。
 (b) 実際には、使用する時には記号rad及びsrが用いられるが、習慣として組立単位としての記号“1”は明示されない。
 (c) 測光学では、ステラジアンの名称と記号srを単位の表し方の中にそのまま維持している。
 (d) この単位は、例としてミリセルシウス度m°CのようにSI接頭語を伴って用いても良い。

表4. 単位の中に固有の名称とその独自の記号を含むSI組立単位の例

組立量	SI 組立単位		
	名称	記号	SI 基本単位による表し方
粘力のモーメント	パスカル秒	Pa・s	m ⁻¹ ・kg ² ・s ⁻¹
表面張力	ニュートン毎メートル	N・m	m ² ・kg ² ・s ⁻²
角速度	ラジアン毎秒	rad/s	m ² ・m ⁻¹ ・s ⁻¹ =s ⁻¹
角加速度	ラジアン毎平方秒	rad/s ²	m ² ・m ⁻¹ ・s ⁻² =s ⁻²
熱流密度, 放射照度	ワット毎平方メートル	W/m ²	kg ² ・s ⁻³
熱容量, エントロピー	ジュール毎ケルビン	J/K	m ² ・kg ² ・s ⁻² ・K ⁻¹
質量熱容量 (比熱容量), 質量エンタルピー (比エンタルピー)	ジュール毎キログラム毎ケルビン	J/(kg・K)	m ² ・s ⁻² ・K ⁻¹
熱伝導率	ワット毎メートル毎ケルビン	W/(m・K)	m ² ・kg ² ・s ⁻³ ・K ⁻¹
体積エネルギー	ジュール毎立方メートル	J/m ³	m ⁻¹ ・kg ² ・s ⁻²
電界の強さ	ボルト毎メートル	V/m	m ² ・kg ² ・s ⁻³ ・A ⁻¹
体積電荷	クーロン毎立方メートル	C/m ³	m ⁻³ ・s ² ・A
電気変位	クーロン毎平方メートル	C/m ²	m ⁻² ・s ² ・A
誘電率	ファラド毎メートル	F/m	m ⁻³ ・kg ⁻¹ ・s ⁴ ・A ²
透磁率	ヘンリー毎メートル	H/m	m ² ・kg ² ・s ⁻² ・A ⁻²
モルエネルギー	ジュール毎モル	J/mol	m ² ・kg ² ・s ⁻² ・mol ⁻¹
モルエンタルピー, モルエンタルピー, 照射線量 (X線及びγ線)	ジュール毎モル毎ケルビン	J/(mol・K)	m ² ・kg ² ・s ⁻² ・K ⁻¹ ・mol ⁻¹
吸収線量	クーロン毎キログラム	C/kg	kg ⁻¹ ・s ² ・A
放射強度	グレイ毎秒	Gy/s	m ² ・s ⁻³
放射輝度	ワット毎ステラジアン	W/sr	m ⁴ ・m ⁻² ・kg ² ・s ⁻³ =m ² ・kg ² ・s ⁻³
放射輝度	ワット毎平方メートル毎ステラジアン	W/(m ² ・sr)	m ² ・m ⁻² ・kg ² ・s ⁻³ =kg ² ・s ⁻³

表6. 国際単位系と併用されるが国際単位系に属さない単位

名称	記号	SI 単位による値
分	min	1 min=60s
時	h	1h=60 min=3600 s
日	d	1 d=24 h=86400 s
度	°	1°=(π/180) rad
分	'	1'=(1/60)°=(π/10800) rad
秒	"	1"=(1/60)'=(π/648000) rad
リットル	l, L	1l=1 dm ³ =10 ⁻³ m ³
トン	t	1t=10 ³ kg
ネーパ	Np	1Np=1
ベル	B	1B=(1/2) ln10 (Np)

表7. 国際単位系と併用されこれに属さない単位でSI単位で表される数値が実験的に得られるもの

名称	記号	SI 単位であらわされる数値
電子ボルト	eV	1eV=1.60217733(49)×10 ⁻¹⁹ J
統一原子質量単位	u	1u=1.6605402(10)×10 ⁻²⁷ kg
天文単位	ua	1ua=1.49597870691(30)×10 ¹¹ m

表8. 国際単位系に属さないが国際単位系と併用されるその他の単位

名称	記号	SI 単位であらわされる数値
海里	海里	1海里=1852m
ノット	ノット	1ノット=1海里毎時=(1852/3600)m/s
アール	a	1a=1 dam ² =10 ² m ²
ヘクタール	ha	1ha=1 hm ² =10 ⁴ m ²
バル	bar	1bar=0.1MPa=100kPa=1000hPa=10 ⁵ Pa
オングストローム	Å	1Å=0.1nm=10 ⁻¹⁰ m
バイン	b	1b=100fm ² =10 ⁻²⁸ m ²

表9. 固有の名称を含むCGS組立単位

名称	記号	SI 単位であらわされる数値
エルグ	erg	1 erg=10 ⁻⁷ J
ダイン	dyn	1 dyn=10 ⁻⁵ N
ポアズ	P	1 P=1 dyn・s/cm ² =0.1Pa・s
ストークス	St	1 St=1cm ² /s=10 ⁻⁴ m ² /s
ガウス	G	1 G=10 ⁴ T
エルステッド	Oe	1 Oe=(1000/4π) A/m
マクスウェル	Mx	1 Mx=10 ⁻⁸ Wb
スチルブ	sb	1 sb=1cd/cm ² =10 ⁴ cd/m ²
ホト	ph	1 ph=10 ⁴ lx
ガリ	Gal	1 Gal=1cm/s ² =10 ⁻² m/s ²

表10. 国際単位に属さないその他の単位の例

名称	記号	SI 単位であらわされる数値
キュリー	Ci	1 Ci=3.7×10 ¹⁰ Bq
レントゲン	R	1 R=2.58×10 ⁻⁴ C/kg
ラド	rad	1 rad=1cGy=10 ⁻² Gy
レム	rem	1 rem=1 cSv=10 ⁻² Sv
X線単位	X unit	1 X unit=1.002×10 ⁻⁴ nm
ガンマ	γ	1γ=1 nT=10 ⁻⁹ T
ジャンスキー	Jy	1 Jy=10 ⁻²⁶ W・m ⁻² ・Hz ⁻¹
フェルミ	fm	1 fm=10 ⁻¹⁵ m
メートル系カラット		1 metric carat = 200 mg = 2×10 ⁻⁴ kg
トル	Torr	1 Torr = (101 325/760) Pa
標準大気圧	atm	1 atm = 101 325 Pa
カロリー	cal	
マイクロ	μ	1 μ=10 ⁻⁶ m